

**Liposomal and polymeric nanoparticles for targeted  
delivery of hydrophobic and hydrophilic drugs**

Shima Gholizadeh

2017

Paranimfen: Sama Gholizadeh  
Daniel Stellwagen

ISBN: 978-94-6332-240-9

Copyright © 2017 Shima Gholizadeh Soltani. All rights reserved. No part of this thesis may be reproduced or transmitted in any form or by any means, without written permission by the author and the publisher holding the copyrights of the published articles.

Cover design: Hadieh Shafie (<http://www.hadiehsafie.com>)

Printed by GVO drukkers & vormgevers B.V.

**Liposomal and polymeric nanoparticles for targeted delivery of hydrophobic and hydrophilic drugs**

Liposomale en polymere nanodeeltjes voor de gerichte afgifte van hydrofobe en hydrofiele geneesmiddelen

(met een samenvatting in het Nederlands)

Proefschrift

ter verkrijging van de graad van doctor aan de Universiteit Utrecht op gezag van de rector magnificus, prof.dr. G.J. van der Zwaan, ingevolge het besluit van het college voor promoties in het openbaar te verdedigen op maandag 2 oktober 2017 des middags te 4.15 uur

door

Shima Gholizadeh Soltani

geboren op 27 juni 1985 te Urmia, Iran

Promotor: Prof. dr. Ir. W.E. Hennink

Copromotoren: Dr. R. J. Kok  
Dr. J.A.A.M. Kamps

This thesis was (partly) accomplished with financial support from NanoNextNL, a micro and nanotechnology consortium of the government of The Netherlands and 130 partners (project 03D.07).

**Do not go gentle into that good night  
Rage, rage against the dying of the light**

*Dylan Thomas*

**To my Family**

# Contents

<b>Chapter 1</b> .....	<b>7</b>
General introduction	
<b>Chapter 2</b> .....	<b>29</b>
Diverse origins of the myofibroblast - implications for kidney fibrosis	
<b>Chapter 3</b> .....	<b>63</b>
E-selectin targeted immunoliposomes for rapamycin delivery to activated endothelial cells	
<b>Chapter 4</b> .....	<b>93</b>
Targeting rapamycin to podocytes using a vascular cell adhesion molecule-1 (VCAM-1)- harnessed SAINT-based lipid carrier system	
<b>Chapter 5</b> .....	<b>123</b>
PLGA-PEG nanoparticles for targeted delivery of an mTOR/PI3kinase inhibitor, NVP-BEZ235, to inflamed endothelium	
<b>Chapter 6</b> .....	<b>174</b>
Anti-GD2 immunoliposomes for delivery of the survivin inhibitor Sepantronium bromide (YM155) to neuroblastoma tumor cells	
<b>Chapter 7</b> .....	<b>208</b>
Summary and perspectives	
<b>Appendices</b> .....	<b>223</b>
Nederlandse samenvatting	
Acknowledgement	
Curriculum vitae	
List of publications	

# **Chapter 1**

## **General introduction**

## Introduction

The use of nanotechnology has become widespread throughout society starting about two decades ago, and since then it has heavily influenced every field of modern science [1, 2]. The major impact of nanotechnology on life sciences, particularly regarding the topic of drug delivery, is briefly discussed in this chapter.

The ultimate goal of drug (nano-)carrier systems (also referred to as nanomedicines) is to deliver an active pharmaceutical ingredient (API) to the target tissue (i.e. specific cell types) in a manner that controls the timing of the API delivery as well as the effective local API dose [2, 3]. Drug loaded nanocarrier systems consist of submicron-sized particles, typically in the range between 20 and 200 nm, containing one or more therapeutic agents that are dispersed, adsorbed, or covalently bound in encapsulating vesicles, capsules, or polymer matrices [4, 5]. The advantage of such drug loaded nanocarrier systems is that they can be specifically designed to improve bioavailability and pharmacokinetics of the encapsulated API, which can eventually contribute to reducing the side effects [5, 6].

Thus far, several nanocarrier systems have advanced towards preclinical and clinical trials for disease diagnosis and therapy [7, 8]. Because of the huge potential of applying nanotechnology in the field of drug delivery, nanomedicine development has attracted big investments from both private and public sectors in the past two decades [8, 9]. However, despite the rapid development of nanocarrier technology for targeted drug delivery, many fundamental aspects of this technology still remain relatively poorly understood. This is not surprising, considering the huge number of potential 'drug + nanocarrier' combinations that can be explored. While the required characteristics of the nanocarrier formulation are largely dependent on the target tissue (e.g. tumor or inflammation site) on which the drug molecules have to act, it is important to realize that the final properties and efficacy of the formulation are largely determined by the chemical nature of the drug molecules (e.g. hydrophilic/lipophilic balance, electrical charge, functional groups chemistry, log P value, etc.) and the type of nanocarrier (e.g. liposome, polymeric nanoparticle, etc.). In this thesis we illustrate the



potential and diversity of nanocarriers, since we have chosen several different types of formulations, testing the influence of drug type, nanocarrier type and surface (antibody) functionalization on the performance (efficacy).

Three different drugs were investigated and evaluated as in nanocarrier formulations based on either lipids or biodegradable polymers. The studied drugs are: rapamycin (sirolimus), dactolisib (NVP-BEZ235) and sepantronium bromide (YM155) (see figure 1). Rapamycin and NVP-BEZ235 are hydrophobic drugs that inhibit mTOR and mTOR/PI3K signaling pathways, respectively [10], resulting in anti-inflammatory and anti-proliferative effects. In this thesis rapamycin and NVP-BEZ235 are used as anti-proliferative compounds that act on inflammation activated endothelial cells. Sepantronium bromide is a hydrophilic drug that promotes apoptosis of tumor cells via its action on anti-apoptotic signaling pathways [11]. This compound has been targeted to neuroblastoma tumor cells. Dependent on the drug molecule's physicochemical characteristics, different types of drug-loaded nanocarrier systems were prepared and evaluated, such as liposomes and polymeric nanoparticles. Overall, this thesis illustrates the flexibility of nanocarrier formulations and gives mechanistic insights into their efficacy.

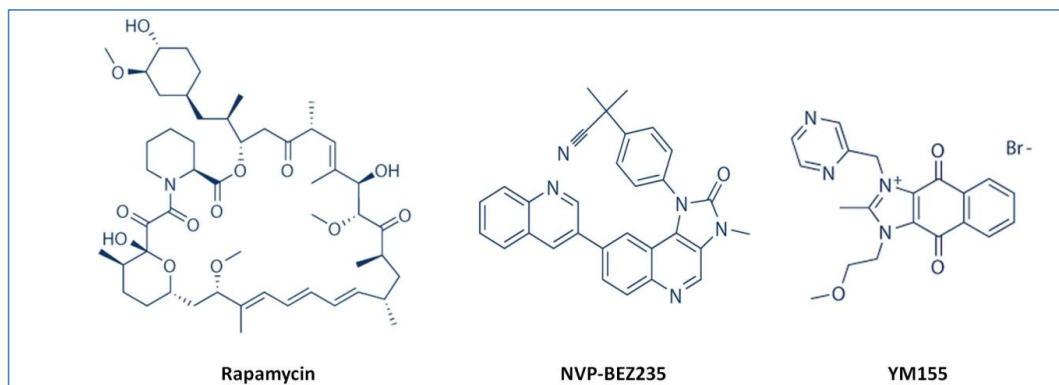


**Figure 1.** Chemical structures of small drug molecules used in this thesis.

## Inflammatory disorders and kinase inhibitors

An inflammatory response is a complex defense mechanism of a host tissue to injury or infection or more generally, the loss of cell or tissue homeostasis [12]. When studying the response mechanism in more detail, two types of inflammatory states can be identified [12]. One is the acute inflammatory response, which is mediated by tissue specific (localized) macrophages and mast cells and leads to the production of various inflammatory mediators such as chemokines and cytokines. The acute inflammatory response is characterized by regulated recruitment of various blood cells, particularly leukocytes, to the infected or injured region [12, 13]. In case that the elimination of pathogens cannot be achieved by the acute inflammatory response (as is the case in for example in diabetic nephropathy, arthritis, bowel disease, etc.), the inflammatory process changes to a state which is referred to as chronic inflammation [12, 14]. Chronic inflammation is characterized by the onset of cellular processes that result in the healing and/or destruction of (parts of) the affected tissue, eventually resulting in the formation of fibrotic tissue. Besides the typical acute and/or chronic inflammatory responses that normally appear, another type of inflammatory response can be triggered in certain diseased conditions [14]. This is so-called systemic inflammatory disorder/condition which results from general over-activation of the immune system [14, 15]. This type of behavior does not seem to fit into the classical mechanism of transition from acute inflammation to a chronic inflammation [14]. Such an inflammatory condition is particularly of interest because it accompanies many of the diseases typical of industrialized countries, including obesity, type 2 diabetes, chronic kidney disease (CKD), atherosclerosis, neurodegenerative diseases, and cancer [14].

Many of the current therapeutic approaches are based on attempts to control leukocyte activation, such as applying immune modulatory drugs (first-line therapies) to treat immune-mediated inflammatory diseases [16]. However, most of those therapies involve (cytotoxic) immunosuppressive drugs without any selectivity, which are usually associated with side effects [17, 18]. After long term administration, many patients develop resistance against such therapies and

become unresponsive [16]. Therefore, there is a large unmet need for effective treatment of inflammatory-mediated diseases. This has prompted a search for new drug targets, such as specific cell signaling proteins that are pivotal in pathways that are activated upon inflammation [16].

Protein phosphorylation, conducted by protein kinases, is one of the major types of post translational modification, and as such it is a fundamental mechanism for cell signaling [19-21]. Protein kinases control cell growth and proliferation, as well as the initiation and regulation of immunological responses [16, 22, 23]. Deregulation of protein kinase activities has been found to be the cause (directly or indirectly) of over 400 diseases [16, 24]. Not surprisingly, protein kinases are still considered to be one of the most important classes of drug targets [25]. Small (i.e. low molecular weight) drugs and drug candidates can be used to inhibit kinase activity [26]. The mechanism of action of these small inhibitory compounds is either through interfering with adenosine triphosphate (ATP)-kinase binding, or by interfering with kinase-protein interactions [16]. One important kinase target in inflammation is the mTOR signaling cascade, which has a crucial role in growth, proliferation, polarity, differentiation and development of cells [27, 28]. Deregulation of mTOR has been related to the progression of inflammatory disorders [29]. Therefore, mTOR is considered to be an interesting therapeutic target to prevent the progression of inflammatory disorders, using either mTOR inhibitors (e.g. rapamycin) or dual inhibitors of the mTOR/phosphoinositide 3-kinase (PI3K) pathways (e.g. NVP-BEZ235) [30]. Dual inhibitors of PI3K and mTOR block both upstream and downstream of the kinase Akt, thus avoiding the problem of Akt activation following blocking of the mTORC1 via negative feedback loop which is known to occur with rapamycin or structurally related inhibitors [29, 31].

### **Neuroblastoma and YM155**

The most commonly occurring extracranial solid tumor during childhood is neuroblastoma (NB). This type of tumor is well known for its broad variation in clinical behavior [32, 33]. Some NB tumors

spontaneously differentiate from malignant ganglioneuroma into benign forms, or vice versa from benign to malignant forms [34-36].

In general, treatment of children suffering from stage 1 and 2 of NB can stay limited to surgery [37, 38], while infants less than 1 year old suffering from stage 1 and 2 of NB have a bigger chance of getting cured following a combination of chemotherapy and surgery [39-41]. However, most of the children older than 1 year old who suffer from progressive NB (i.e. stage 4) have little chance to survive, even when undergoing multimodal therapy [41-43]. Although NB treatment techniques are continuously being refined, survival rates of neuroblastoma patients have not significantly changed over the past decade.

Based on previous studies, it has been reported that several biological factors affect the clinical treatment outcome of NB, such as patient age, tumor stage, tumor histology and genetic abnormalities [44-46]. Recently, studies are mainly focused on finding a correlation at the molecular level between variability of tumor growth and responsiveness to therapy [47-49].

The principle aim of cancer therapy is to completely eradicate or at least stop the proliferation and migration of malignant cells, ideally without affecting healthy cells. Conventional chemotherapy attacks the rapidly dividing cancer cells by blocking the cell cycle. Because of rapid proliferation of the cancer cells, chemotherapy is to some extent selectively toxic to tumor tissue. However, not only cancer cells divide rapidly, but hematopoietic cells and hair follicles also have rapid turnover, explaining the common side effects of chemotherapy.

Great progress had been made in the last two decades towards gaining more molecular level insight into tumor biogenesis. Acquired knowledge on (patho-)physiological cascades involved in cancer cell formation and progress, has resulted in the development of novel anticancer agents such as “targeted therapeutics”, including growth factor receptor inhibitors, histone deacetylase inhibitors and (tyrosin) kinase inhibitors which specifically interfere with certain growth features of tumor cells [50-52]. Due to their pharmacologically specific mechanism of action, these types of

therapeutics have been shown to be more selective towards cancer cells, both in vitro and in vivo [52-54].

Sepantronium bromide, also known as YM155, is a small molecular inhibitor of the anti-apoptosis protein survivin that has been selected from a high throughput screening assay using a survivin promoter luciferase [55]. In preclinical experimentations, the dose and time-dependent characteristics of inhibition of survivin expression (i.e. at mRNA and protein levels) by YM155 were identified. [56]. Inhibition of survivin expression by YM155 resulted in activation of caspases and induction of apoptosis in a wide array of human tumor cell lines [57]. More recent findings have suggested significant synergy between sepantronium bromide and other types of chemotherapeutic agents, such as platinum-compounds and taxanes [58, 59]. Phase I/II clinical trials on YM155 combined with paclitaxel or docetaxel have been applied on patients suffering from different types of malignancies [59, 60].

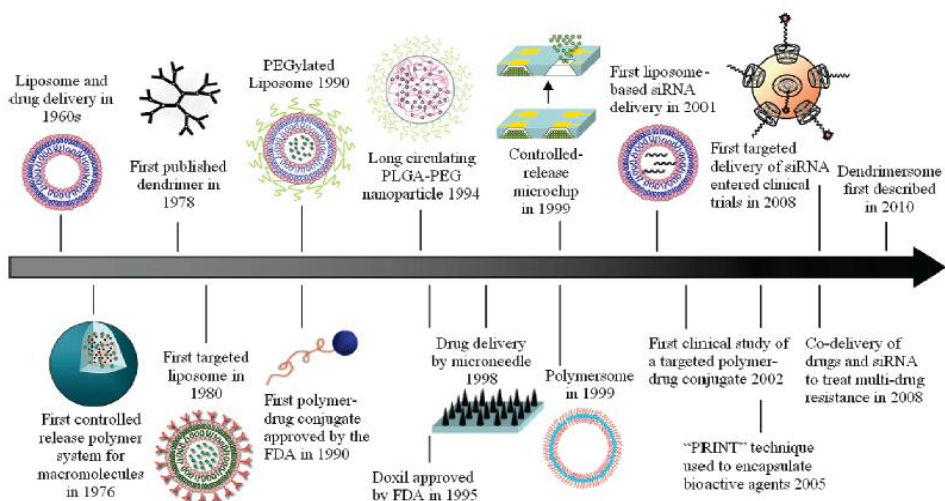
### **Nanomedicines**

Despite the ongoing rise of biotherapeutics, small drug molecules (i.e. molecular weight  $\leq 900$  Da) still represent the majority of drug products developed and marketed by the pharmaceutical industry.

However, many of these small drug products are facing inherent pharmacological challenges, such as unfavorable pharmacokinetics, or sub-optimal tissue distribution. Typically, small (hydrophilic) drug molecules are rapidly eliminated from blood circulation via renal filtration, hindering their accumulation in the target tissue (e.g. tumor cells). Furthermore, small drug molecules may also have a large volume of distribution due to their size and/or their hydrophobicity, thereby risking potentially undesirable effects due to accumulation in other tissues [61, 62]. An increasing number of tailored and specialized drug formulations is being developed that incorporate the concepts of advanced drug delivery. The aim of these new products is to overcome the challenges that are inherent to the use of small drug molecules, and to thereby provide more convenient treatment

regimens for the patients [61,62]. Encapsulation of the drug molecules in a colloidal delivery system (i.e. nanocarrier) is an efficient approach to modify the physicochemical and biopharmaceutical properties of drugs [2]. The ability of drug carrier systems to alter the pharmacokinetics of small drug molecules and to improve their efficacy/toxicity balance has been shown for many different nanocarrier systems, ranging from liposomes [63], and polymeric nanoparticles [64] to micelles [65].

These colloidal delivery systems can consist of a broad range of different particulate suspensions (dispersed systems), including polymeric and lipid nanoparticles, micelles and liposomes, in which the drug molecules are either dissolved, dispersed, or covalently coupled with a linker to the carrier [66, 67]. The incorporation of a drug into a colloidal delivery system can protect the drug against degradation and can achieve sustained and localized drug release (increasing efficacy and limiting side effects), resulting in increased patient comfort by avoiding repetitive bolus injections or the use of perfusion pumps [66-68]. The availability of effective drug delivery systems has encouraged a re-investigation into small molecular compounds that were previously considered to be pharmaceutically suboptimal and undevelopable.



**Scheme 1.** Timeline of nanotechnology based drug delivery platforms. Delivery systems that serve as important milestones throughout the history have been highlighted. Adapted with permission from reference [71]. Copyright 2010, American Chemical Society.

Among the different types of carrier systems reported thus far, lipid and polymer based particulate systems are the most well-known. Liposomes were first proposed as drug carrier system in the 1970s by Gregoriadis and coworkers, and over the past decades various different polymers have been used for encapsulation and coating of active pharmaceutical ingredients (API) [69-71]. A timeline showing a brief historical overview of the developments regarding drug nanocarrier systems is shown in scheme 1. It is important to note that from a formulation point of view, the loading efficiency of (small) drug molecules and the stability of the formulated final product are two challenging aspects that need to be carefully considered before and during preparation steps of the drug loaded carrier system. The loading methods are typically adapted to the structural characteristics of the active pharmaceutical ingredient (API) and the type of carrier systems that are applied in the formulation. Table 1 shows an overview of nanocarriers, each representing a relevant example of typical formulation and encapsulation strategies adapted for each type of molecule.

**Table 1.** Examples of loaded bioactive molecules with different physicochemical properties in liposomal or polymeric nanoparticles

Physicochemical characteristic	Bioactive agent	Carrier systems	Loading methodology
Hydrophilic	Dexamethasone disodium phosphate [72]	liposomes	thin-layer hydration (TLH)
	Prednisolone disodium Phosphate [73]	liposomes	thin-layer hydration (TLH)
	rCramoll (Lectin) [74]	liposomes	TLH followed by freeze–thaw (FT) cycles
	Riboflavin [75]	liposomes	dehydration–rehydration

	Cytarabine [76]	liposomes	reverse-phase evaporation
	Ascorbic acid [77]	Chitosan nanoparticles	nanoprecipitation method
Amphiphilic	Doxorubicin [78]	liposomes	remote loading Ammonium phosphate/sulphate/acetate
	Diclofenac sodium [79]	liposomes	gradient Calcium acetate gradient
	Imatinib mesylate [80]	PLGA nanoparticles	emulsion-solvent evaporation
	Doxorubicin [81]	PLGA nanoparticles	emulsion-solvent evaporation
	Sunitinib [82]	Chitosan nanoparticles	nanoprecipitation method
Hydrophobic	Paclitaxel [83]	liposomes	drug /lipid film hydration
	Rapamycin [84]	liposomes	drug /lipid film hydration
	Paclitaxel [85]	PLGA nanoparticles	emulsion-solvent evaporation
	Curcumin [86]	PLGA nanoparticles	emulsion-solvent evaporation



### Passive and active targeted drug delivery

Thus far, several nanotechnology based therapeutic products have been approved for clinical use by the American Food and Drug Administration (FDA) and many systems are currently in clinical trials [87, 88]. The majority of the systems are based on passively-targeted PEGylated nanomedicines (e.g. liposomes and polymeric nanoparticles) that are loaded with drugs or drug candidates, which are also referred to as second generation nanomedicines (considering first generation to be nanoparticles with non-stealth surface chemistry) [89]. These nanocarrier systems have advantages of prolonged circulation half-life, improved drug solubility, potentially reduced immunogenicity and/or ability to release the drug molecules in a sustained or stimuli-responsive fashion. These properties are generally considered as important determinants of the drug dosing regimen.

More advanced versions of nanomedicines are based on actively targeted (i.e. molecular recognition processes via ligand-receptor interactions) nanomedicines that are decorated with targeting ligands on their surface to increase target specificity. This approach aims for: I) strong binding of nanocarrier (delivery) system to target cells and prolonged retention at the site of the target cells; II) receptor-mediated internalization of the nanocarrier into the target cells, and III) cytosol routing of the loaded drug compound [90, 91]. It is generally assumed that actively targeted drug carrier systems are retained longer in the target tissue than their passively targeted counterparts due to increased cellular interaction and internalization. However, it is important to note that such a targeted approach does not always result in increased accumulation of the drug carrier in the target tissue/cells compared to passively-targeted nanomedicines [92-95]. Such results are generally related to physicochemical characteristics of the carrier systems, or to the type of targeting ligand used on the surface of nanoparticles. Nevertheless, the value of using an actively targeted drug carrier should always be carefully examined and properly verified.

Vascular cells (e.g. endothelial cells) have been proposed as attractive targets for drug targeting for several decades already. Uses include imaging in disease diagnostics, delivery of therapeutic (anti-inflammatory) agents, and anti-thrombotic interventions in highly vascularized tissues [96, 97].

Certain molecules, such as adhesion molecules (i.e. selectins, VCAM-1, etc.) are normally absent on the vascular lumen but are exposed on inflammation-affected endothelium, making them excellent targets for drug delivery in inflammatory disorders. For example, anti E-selectin antibodies are attractive moieties for the delivery of therapeutic agents to activated endothelium [98]. It is important to note that there are multitude of parameters that have an impact on the successful targeted delivery of nanomedicines to the vascular endothelial cells. For example, items to consider include: affinity of the targeting ligand for the receptor, ligand density on the surface of the nanocarrier system, the distribution density of target determinants on the target cell surface and their accessibility to the nanocarriers, flow parameters, size and geometry of the nanocarriers.

For targeted delivery to the tumor cells, nanocarriers first need to reach the tumor tissue interstitium via extravasation via the enhanced permeability and retention (EPR) effect. The EPR effect is the result of two distinct phenomena, convection and diffusion, which are the main driving forces for passive nanomedicine transport to the tumor tissue [99, 100]. As described in the previous paragraph, nanocarriers need to be optimized with respect to certain features, such as shape, size, surface charge and environmental susceptibility, in order for the passive delivery of the therapeutics to the tumor tissue to take place. To date, studies of active targeting of tumor tissue have shown comparable results (*in vivo*) to their passively targeted counterparts regarding accumulation of cytotoxic drugs at the target site. Most likely, the initial accumulation of the nanocarriers in the tumor is caused by the EPR effect (i.e. extravasation from the circulation into the tumor), before active targeting can take place [101, 102]. Regardless, most of the studies of actively targeted nanomedicine have shown increased efficacy, both *in vitro* and *in vivo*, compared to their passively targeted counterparts [103-107]. However, for most studies thus far it has been difficult to unambiguously determine whether this improved efficacy is related to the presence of the targeting ligands, because (information on) proper control experiments with passive targeting are typically lacking.

Various types of targeting ligands have thus far been reported for active tumor targeting, including proteins, nucleic acid based ligands and (small) molecular ligands. One example is the use of monoclonal antibodies (mAbs) as a targeting ligands that can be conjugated to the surface of nanocarrier system, specifically aimed at target antigens or receptors that are over expressed on the surface of the tumor cells [108].

One of the mAb targets with a high clinical relevance is the disialoganglioside (GD2) antigen [109]. GD2 is known to be a specific antigen for malignant neuroblastoma cells, and is therefore an attractive option for active drug targeting of tumor tissues with neuroectodermal origin. In earlier studies, anti-GD2 antibodies have been successfully used as targeting motif on the surface of liposomal carrier systems, either to stimulate immune responses by direct interaction of immune cells (i.e. macrophages, B cells and NK cells) with the anti-GD2 targeted liposomes, or to enable active targeted delivery of the liposomal carrier systems (containing active pharmaceutical ingredients) to the neuroblastoma cells [110, 111].

### **Aim of the thesis**

Taking the above insights and efforts into account, the present thesis focuses on the development of targeted particulate carrier systems, based on lipids or biodegradable aliphatic polyesters, for cell specific delivery of low molecular weight hydrophilic or hydrophobic drug compounds. We aimed to:

- Design, synthesize/formulate and characterize various lipid- or polymer-based targeted carrier systems, loaded with different classes of drug molecules (i.e. rapamycin, dactolicib (NVP-BEZ235), and sepantronium bromide (YM155)).
- Validating the efficacy of E-selectin, vascular cell adhesion protein 1 (VCAM-1) and GD2 targeted drug loaded delivery systems on specific cell types.
- Investigate the pharmacokinetic and bio-distribution of one of the developed formulations (YM155 loaded anti-GD2 immunoliposomes) in tumor bearing mice.

## Outline of the thesis

**Chapter 2** reviews kidney fibrosis, which is the common end point of chronic kidney disease. The mechanistic pathways behind fibrosis tissue formation in the kidney and the major contributors of myofibroblast progenitors in the kidney fibrosis are discussed. Further, the current status of pre-clinical and clinical anti-fibrotic therapy are discussed, together with targeting strategies that might be helpful to support resident or circulating cells in maintaining or regaining their original functional differentiation state. The topic of this review chapter is based on the original project proposal, which was focused on targeted drug delivery for treatment of kidney disease (glomerulonephritis). However, due to various setbacks, the experimental part of the project was restructured, instead focusing on a more general study of targeted drug delivery and its potential in the treatment of inflammation and neuroblastoma.

The results of the experimental work done in this project can be found in **Chapters 3-6** of this thesis.

**Chapter 3** describes the formulation of E-selectin targeted, rapamycin loaded, immunoliposomes and their characterization. The prepared formulations were characterized for their physicochemical properties and their interaction (i.e. binding and uptake) with E-selectin expressing (TNF- $\alpha$  activated) endothelial cells. In addition, their ability to block activation of the targeted cellular pathway (i.e. mTOR) and the resulting inhibition of endothelial cell migration and proliferation were studied.

In **Chapter 4** VCAM-1 was identified as a targeting molecule that is expressed on the surface of TNF- $\alpha$  activated podocytes (cell type that is abundantly present in the glomeruli of the kidney). Hence, we explored the possibilities of using VCAM-1 as a cell-surface receptor to deliver the potent immunosuppressant rapamycin to activated podocytes, using a lipid-based nanocarrier system 'Saint-O-Somes'. Anti-VCAM-1 rapamycin-Saint-O-Somes were prepared and characterized, and their in vitro efficacy on activated podocytes was studied using a cell migration assay.

In **Chapter 5** poly(D,L-lactide-co-glycolide) (PLGA) and poly(D,L-lactide-co-glycolide)-poly(ethylene glycol)-2000 (PLGA-PEG), copolymers were used to formulate NVP-BEZ235 loaded nanoparticles. The

effect of copolymer ratios as well as different drug load contents on the physicochemical properties and release kinetics of the obtained nanoparticles (NPs) were investigated. Furthermore, SATA modified anti-E-selectin antibody was attached covalently to the surface of the NPs, in order to render the formulated NPs cell specific. The targeted formulations were further optimized (in vitro), based on Ab density on the surface of NPs. Finally, specific delivery (uptake) and efficacy of the E-selectin targeted, BEZ loaded, nanoparticles were evaluated in vitro in TNF- $\alpha$  activated endothelial cells by cell migration and western blot analysis.

**Chapter 6** describes the formulation of GD2-targeted, YM155 loaded, immunoliposomes. The prepared formulations were characterized based on their physicochemical properties, stability, and release kinetics under various conditions (i.e. different release media). The in vitro therapeutic efficacy of the YM155 loaded immunoliposomes was compared to free YM155 and non-targeted YM155 loaded liposomes on GD2-positive neuroblastoma cells (KCNr). Additionally, the pharmacokinetic behavior and the tumor accumulation of the immunoliposomes were also studied in KCNr tumor xenografted NMRI female mice.

Finally, in **Chapter 7** the results of the research presented in this thesis is summarized, and the feasibility of targeted nanocarrier systems is discussed for (future) use in therapeutic applications, followed by general discussion on nanotechnology risk assessment.

## References

1. Juliano R., Nanomedicine- is the wave cresting? *Nat Rev Drug Discov*, 2013. 12(3): p. 171–172.
2. Babu A, Templeton AK, Munshi A, Ramesh R., Nanodrug Delivery Systems: A Promising Technology for Detection, Diagnosis, and Treatment of Cancer. *AAPS PharmSciTech*, 2014. 15(3): p. 709–721.
3. Bourzac K., Nanotechnology: Carrying drugs. *Nature*, 2012. 491(7425): p. S58-60.

4. Cho K, Wang X, Nie S, Chen ZG, Shin DM., Therapeutic nanoparticles for drug delivery in cancer. *Clin Cancer Res*, 2008. 14(5): p. 1310-6.
5. Cerqueira BB, Lasham A, Shelling AN, Al-Kassas R. Nanoparticle therapeutics: Technologies and methods for overcoming cancer. *Eur J Pharm Biopharm*, 2015. 97: p. 140–151.
6. De Jong WH and Borm PJA., Drug delivery and nanoparticles: Applications and hazards. *Int J Nanomedicine*, 2008. 3(2): p. 133–149.
7. Davis ME, Chen Z. et al., Nanoparticle therapeutics: an emerging treatment modality for cancer. *Nature Reviews Drug Discovery*, 2008. 7: p. 771-782.
8. Hare JI, Lammers T, Ashford MB, Puri S, Storm G, Barry ST. Challenges and strategies in anti-cancer nanomedicine development: An industry perspective. *Advanced Drug Delivery Reviews*, 2017. 108: p. 25–38.
9. Farokhzad OC, Langer R., Impact of nanotechnology on drug delivery. *ACS Nano*, 2009. 3(1): p. 16-20.
10. Zheng Y, Jiang Y., mTOR Inhibitors at a Glance. *Mol Cell Pharmacol*, 2015. 7(2 ): p. 15-20.
11. Satoh T, Okamoto I, Miyazaki M, Morinaga R, Tsuya A, et al., Phase I study of YM155, a novel survivin suppressant, in patients with advanced solid tumors. *Clin Cancer Res*, 2009. 15(11): p. 3872-80.
12. Medzhitov R., Origin and physiological roles of inflammation. *Nature* 2008. 454: p. 428-435.
13. Serhan CN, Brain SD, et al., Resolution of inflammation: state of the art, definitions and terms. *FASEB J.* , 2007. 21(2): p. 325-32.
14. Medzhitov R., Inflammation 2010: new adventures of an old flame. *Cell*, 2010 140(6): p. 771-6.
15. Pohl D, Benseler S., Systemic inflammatory and autoimmune disorders. *Handb Clin Neurol.* , 2013. 112: p. 1243-52.
16. Patterson H, Nibbs R, et al., Protein kinase inhibitors in the treatment of inflammatory and autoimmune diseases. *Clin Exp Immunol*, 2014. 176(1): p. 1-10.
17. Balagué C, Kunkel SL, Godessart N. Understanding autoimmune disease: new targets for drug discovery. *Drug Discov Today*, 2009. 14: p. 926–34.
18. Steinman L, Merrill JT, et al., Optimization of current and future therapy for autoimmune diseases. *Nat Med*, 2012. 18: p. 59–65.
19. Grant SK., Therapeutic protein kinase inhibitors. *Cell Mol Life Sci*, 2009. 66: p. 1163–77.
20. Ubersax JA, Ferrell JE Jr., Mechanisms of specificity in protein phosphorylation. *Nat Rev Mol Cell Biol* 2007. 8: p. 530–41.

21. Kontzias A, Laurence A, et al., Kinase inhibitors in the treatment of immune-mediated disease. *F1000 Med Rep*, 2012. 4(5): p. 1-8.
22. Asadullah K, Gaestel M., Protein kinase inhibitors for the treatment of inflammation – an overview. *Anti-inflamm & Anti-allergy Agents in Med Chem*, 2007. 6: p. 3–4.
23. Shen K, Hines AC, et al., Protein kinase structure and function analysis with chemical tools. *Biochim Biophys Acta*, 2005. 1754: p. 65–78.
24. Melnikova I, Golden J., Targeting protein kinases. *Nat Rev Drug Discov*, 2004. 3: p. 993–4.
25. Vlahovic G, Crawford J., Activation of tyrosine kinases in cancer. *Oncologist*, 2003. 8: p. 531–8.
26. Gaestel M, Mengel A, et al., Protein kinases as small molecule inhibitor targets in inflammation. *Curr Med Chem*, 2007. 14: p. 2214–34.
27. Laplante M, Sabatini DM., mTOR signaling at a glance. *Journal of cell science*, 2009. 122: p. 3589-3594.
28. Laplante M, Sabatini DM., mTOR signaling in growth control and disease. *Cell*, 2012. 149(2): p. 274–293.
29. Weichhart T, Hengstschläger M, Linke M., Regulation of innate immune cell function by mTOR. *Nature Reviews Immunology*, 2015. 15: p. 599–614.
30. Müller S, Chaikuad A, et al., The ins and outs of selective kinase inhibitor development. *Nature Chemical Biology* 2015. 11: p. 818–821.
31. Dienstmann R, Rodon J, Serra V, Tabernero J. Picking the Point of Inhibition: A Comparative Review of PI3K/AKT/mTOR Pathway Inhibitors. *Mol Cancer Ther*, 2014. 13(5): p. 1021–31.
32. Miller RW, Y.J.J., Novakovic B., *Childhood cancer*. *Cancer Biol Ther*, 1994. 75: p. 395–405.
33. Pizzo PA, Poplack DG., *Principles and Practice of Pediatric Oncology*. 6th Edition. Philadelphia: Lippincott Williams And Wilkins, 2010: p. 895–937.
34. Evans AE, Gerson J, Schnauer L., Spontaneous regression of neuroblastoma. *Natl Cancer Inst Monogr*, 1976. 44: p. 49–54.
35. D'Angio GJ, Evans AE, Koop CE., Special pattern of widespread neuroblastoma with a favourable prognosis. *Lancet*, 1971. 1: p. 1046–1049.
36. Haas D, Ablin AR, et al., Complete pathologic maturation and regression of stage IVS neuroblastoma without treatment. *Cancer Biol Ther*, 1988. 62: p. 818–825.
37. Alvarado CS, London WB, et al., Natural history and biology of stage A neuroblastoma: a Pediatric Oncology Group study. *J Pediatr Hematol Oncol*, 2000. 22: p. 197–205.
38. Perez CA, Matthay KK, et al., Biologic variables in the outcome of stages I and II neuroblastoma treated with surgery as primary therapy: a Children's Cancer Group study. *J Clin Oncol*, 2000. 18: p. 18–26.

39. Bowman LC, Castleberry RP, et al., Genetic staging of unresectable or metastatic neuroblastoma in infants: a Pediatric Oncology Group study. *J Natl Cancer Inst*, 1997. 89: p. 373–380.
40. Schmidt ML, Lukens JN, et al., Biologic factors determine prognosis in infants with stage IV neuroblastoma: a prospective Children's Cancer Group study. *J Clin Oncol*, 2000. 18: p. 1260–1268.
41. Matthay KK, George RE, Yu AL., Promising therapeutic targets in neuroblastoma. *Clin Cancer Res*, 2012. 18(10): p. 2740-53.
42. Matthay KK, Villablanca JG, et al., Treatment of high-risk neuroblastoma with intensive chemotherapy, radiotherapy, autologous bone marrow transplantation, and 13-cis-retinoic acid. *N Engl J Med*, 1999. 341: p. 1165–1173.
43. Izbicka E, Izbicki T., Therapeutic strategies for the treatment of neuroblastoma. *Curr Opin Investig Drugs*, 2005. 6(12): p. 1200-14.
44. Brodeur GM, Pritchard J, et al., Revisions of the international criteria for neuroblastoma diagnosis, staging, and response to treatment. *J Clin Oncol*, 1993. 11: p. 1466–1477.
45. Evans AE, D'Angio GJ, et al., Prognostic factors in neuroblastoma. *Cancer Biol Ther*, 1987. 59: p. 1853–1859.
46. Shimada H, Umehara S, et al., The International Neuroblastoma Pathology Classification (the Shimada system). *Cancer Biol Ther*, 1999. 86: p. 364–372.
47. Weinstein JL, Katzenstein HM, Cohn SL., Advances in the Diagnosis and Treatment of Neuroblastoma. *The Oncologist*, 2003. 8(3): p. 278-292.
48. Yang R, Niepel M, Mitchison TK, Sorger PK. Dissecting Variability in Responses to Cancer Chemotherapy Through Systems Pharmacology. *Clin Pharmacol Ther*, 2010. 88(1): p. 34–38.
49. Diaz-Cano SJ., Tumor Heterogeneity: Mechanisms and Bases for a Reliable Application of Molecular Marker Design. *Int J Mol Sci*, 2012. 13(2): p. 1951-2011.
50. Hanahan D, Weinberg RA., The hallmarks of cancer. *Cell*, 2000. 100(1): p. 57-70.
51. Arora A, Scholar EM., Role of Tyrosine Kinase Inhibitors in Cancer Therapy. *Journal of Pharmacology and Experimental Therapeutics*, 2005. 315(3): p. 971-979.
52. Lammers T, Kiessling F, Hennink WE, Storm G., Drug targeting to tumors: Principles, pitfalls and (pre-) clinical progress. *Journal of Controlled Release*, 2012. 161(2): p. 175–187.
53. Krause DS, Van Etten RA., Tyrosine kinases as targets for cancer therapy. *N Engl J Med*, 2005. 353(2): p. 172-87.
54. Collins I, Workman P., New approaches to molecular cancer therapeutics. *Nature Chemical Biology*, 2006. 2: p. 689 - 700.



55. Zhang C, Cao X, et al., Silencing of survivin by YM155 induces apoptosis and growth arrest in hepatocellular carcinoma cells. *Oncology letters*, 2015. 10(3): p. 1627-1631.
56. Tolcher AW, Mita A, Lewis LD, Garrett CR, et al., Phase I and pharmacokinetic study of YM155, a small-molecule inhibitor of survivin. *J Clin Oncol.* , 2008. 26(32): p. 5198-203.
57. Nakahara T, Kita A, Yamanaka K, Mori M, et al., YM155, a novel small-molecule survivin suppressant, induces regression of established human hormone-refractory prostate tumor xenografts. *Cancer Res*, 2007. 67(17): p. 8014-21.
58. Iwasa T, Okamoto I, et al., Marked anti-tumour activity of the combination of YM155, a novel survivin suppressant, and platinum-based drugs. *Br J Cancer Biol Ther*, 2010. 103(1): p. 36-42.
59. Kelly RJ, Rajan A, et al., A phase I/II study of sepantronium bromide (YM155, survivin suppressor) with paclitaxel and carboplatin in patients with advanced non-small-cell lung cancer. *Ann Oncol*, 2013. 10: p. 2601-6.
60. Kudchadkar R, Emst S, et al., A phase 2, multicenter, open-label study of sepantronium bromide (YM155) plus docetaxel in patients with stage III (unresectable) or stage IV melanoma. *Cancer Med*, 2015. 4(5): p. 643-650.
61. Lammers T, Subr V, Ulbrich K, HPMa-based polymer therapeutics improve the efficacy of surgery, of radiotherapy and of chemotherapy combinations. *Nanomedicine (Lond)*. 2010. 5(10): p. 1501-23.
62. Kidane A, Bhatt PP., Recent advances in small molecule drug delivery. *Current Opinion in Chemical Biology*, 2005. 9: p. 347-351.
63. Szebeni J, Fülöp T, Dézsi L, Metselaar B, Storm G., Liposomal doxorubicin: the good, the bad and the not-so-ugly. *J Drug Target*, 2016. 24(9): p. 765-767.
64. Kamaly N, Xiao Z, Valencia PM, Radovic-Moreno AF, Farokhzad OC., Targeted polymeric therapeutic nanoparticles: design, development and clinical translation. *Chem Soc Rev*, 2012. 41(7): p. 2971-3010.
65. Caral H, Kataoka K, Progress of drug-loaded polymeric micelles into clinical studies. *J Control Release*, 2014. 190: p. 465-76.
66. Vignaud S, Benoit JP, Saulnier P., Strategies for the nanoencapsulation of hydrophilic molecules in polymer-based nanoparticles. *Biomaterials*, 2011. 33: p. 8593-604.
67. Khadka P, Ro J, Kima H, Kima I, et al., Pharmaceutical particle technologies: An approach to improve drug solubility, dissolution and bioavailability. *Asian Journal of Pharmaceutical Sciences*, 2014. 9(6): p. 304-316.
68. Eloy JO, Claro de Souza M, Petrilli R, Barcellos JP, Lee RJ, Marchetti JM., Liposomes as carriers of hydrophilic small molecule drugs: Strategies to enhance encapsulation and delivery. *Colloids and Surfaces B: Biointerfaces*, 2014. 123: p. 345-363.

69. Monteiro N, Martins A, et al., Liposomes in tissue engineering and regenerative medicine. *J R Soc Interface*, 2014. 11(101).
70. Liechty WB, Kryscio DR, et al., Polymers for Drug Delivery Systems. *Annu Rev Chem Biomol Eng.*, 2010. 1: p. 149–173.
71. Shi J, Votruba AR, et al., Nanotechnology in Drug Delivery and Tissue Engineering: From Discovery to Applications. *Nano Lett*, 2010. 10(9): p. 3223–3230.
72. Asgeirsdóttir SA, Zwiers PJ, et al., Inhibition of proinflammatory genes in anti-GBM glomerulonephritis by targeted dexamethasone-loaded AbEsel liposomes. *Am J Physiol Renal Physiol*, 2008. 294(3): p. 554-61.
73. Schiffelers RM, Metselaar JM, et al., Liposome-Encapsulated Prednisolone Phosphate Inhibits Growth of Established Tumors in Mice. *Neoplasia*, 2005. 7(2): p. 118-27.
74. Cunha CRA, Silva LCN, et al., Encapsulation into Stealth Liposomes Enhances the Antitumor Action of Recombinant Cratylia mollis Lectin Expressed in Escherichia coli. *Front Microbiol*, 2016. 7(1355).
75. Zadi B, Gregoriadis G., A Novel Method for High-Yield Entrapment of Solutes into Small Liposomes. *Journal of liposome research*, 2008. 10: p. 73-80.
76. Szoka F Jr, Papahadjopoulos D, et al., Procedure for preparation of liposomes with large internal aqueous space and high capture by reverse-phase evaporation. *Proc Natl Acad Sci*, 1978. 75(9): p. 4194–4198.
77. Jang KI, Lee HG., Stability of chitosan nanoparticles for L-ascorbic acid during heat treatment in aqueous solution. *J Agric Food Chem.*, 2008. 56(6): p. 1936-41.
78. Fritze A, Hens F, et al., Remote loading of doxorubicin into liposomes driven by a transmembrane phosphate gradient. *Biochimica et Biophysica Acta (BBA) - Biomembranes*, 2006. 1758(10): p. 1633–1640.
79. Hwang SH, Maitani Y, et al., Remote loading of diclofenac, insulin and fluorescein isothiocyanate labeled insulin into liposomes by pH and acetate gradient methods. *International Journal of Pharmaceutics*, 1999. 179(1): p. 85-95.
80. Marslin G, Revina AM, et al., Delivery as nanoparticles reduces imatinib mesylate-induced cardiotoxicity and improves anticancer activity. *Int J Nanomedicine*, 2015. 10: p. 3163–3170.
81. Betancourt T, Brannon-Peppas L., Doxorubicin-loaded PLGA nanoparticles by nanoprecipitation: preparation, characterization and in vitro evaluation. *Nanomedicine (Lond)*, 2007. 2: p. 219-32.
82. Joseph JJ, Sangeetha D, Gomathi T., Sunitinib loaded chitosan nanoparticles formulation and its evaluation. *Int J Biol Macromol*, 2016. 82: p. 952-8.
83. Kan P, Tsao CW, et al., A Liposomal Formulation Able to Incorporate a High Content of Paclitaxel and Exert Promising Anticancer Effect. *Journal of Drug Delivery*, 2010. 2011: p. 1-9

84. Onyesom I, Lamprou DA, et al., Sirolimus Encapsulated Liposomes for Cancer Therapy: Physicochemical and Mechanical Characterization of Sirolimus Distribution within Liposome Bilayers. *Mol. Pharmaceutics*, 2013. 10(11): p. 4281–4293.
85. Danhier F, Lecouturier N, et al., Paclitaxel-loaded PEGylated PLGA-based nanoparticles: In vitro and in vivo evaluation. *Journal of Controlled Release*, 2009. 133(1): p. 11–17
86. Mukerjee A, Vishwanatha JK., Formulation, characterization and evaluation of curcumin-loaded PLGA nanospheres for cancer therapy. *Anticancer Res*, 2009. 29: p. 3867-3876.
87. Zhang L, Gu FX, et al., Nanoparticles in medicine: therapeutic applications and developments. *Clin Pharmacol Ther*, 2008. 83(5): p. 761-9.
88. Weissig V, Pettinger TK, Murdock N, Nanopharmaceuticals (part 1): products on the market. *International Journal of Nanomedicine*, 2014. 15(9): p. 4357-4373.
89. Albanese A, Tang PS, Chan WC., The effect of nanoparticle size, shape, and surface chemistry on biological systems. *Annu Rev Biomed Eng.* , 2012. 14: p. 1-16.
90. van der Meel R, Vehmeijer LJ, Kok RJ, Storm G, van Gaal EV., Ligand-targeted particulate nanomedicines undergoing clinical evaluation: current status. *Adv Drug Deliv Rev* , 2013. 65(10): p. 1284-98.
91. Bi Y, Hao F, et al., Progress on Actively Targeted Nanoparticles for Drug Delivery to Tumor. *Curr Drug Metab*, 2016. 17(8): p. 763-782.
92. Choi CH, Alabi CA, et al., Mechanism of active targeting in solid tumors with transferrin-containing gold nanoparticles. *Proc Natl Acad Sci U S A*, 2010. 107: p. 1235–40.
93. Kirpotin DB, Drummond DC, et al., Antibody targeting of long-circulating lipidic nanoparticles does not increase tumor localization but does increase internalization in animal models. *Cancer Research*, 2006. 66: p. 6732-40.
94. Toy R, Hayden E, et al., Multimodal in vivo imaging exposes the voyage of nanoparticles in tumor microcirculation. *ACS Nano*, 2013. 7: p. 3118-29.
95. Kunjachan S, Pola R, Gremse F, Theek B, et al., Passive vs. Active Tumor Targeting using RGD- and NGR-modified Polymeric Nanomedicines. *Nano Lett*, 2014. 14(2): p. 972–981.
96. Chacko AM, Hood ED, et al., Targeted nanocarriers for imaging and therapy of vascular inflammation. *Curr Opin Colloid Interface Sci*, 2011. 16(3): p. 215-227.
97. Simone E, Ding BS and Muzykantov v., Targeted delivery of therapeutics to endothelium. *Cell and Tissue Research*, 2009. 335(1): p. 283-300.
98. Muzykantov VR., Targeted Drug Delivery to Endothelial Adhesion Molecules. Hindawi Publishing Corporation, 2013. p. 1-27.
99. Bertrand N, Wu J, et al., Cancer Nanotechnology: The impact of passive and active targeting in the era of modern cancer biology. *Adv Drug Deliv Rev*, 2014. 66: p. 2–25.

100. Maeda H., Tumor-Selective Delivery of Macromolecular Drugs via the EPR Effect: Background and Future Prospects. *Bioconjugate Chem.*, 2010. 21(5): p. 797–802.
101. Danhier F, Feron O, Pr at V., To exploit the tumor microenvironment: Passive and active tumor targeting of nanocarriers for anti-cancer drug delivery. *J Control Release*, 2010. 148(2): p. 135-46.
102. Maeda H., Vascular permeability in cancer and infection as related to macromolecular drug delivery, with emphasis on the EPR effect for tumor-selective drug targeting. *Proc Jpn Acad Ser B Phys Biol Sci*, 2012. 88(3): p. 53-71.
103. Mamot C, Ritschard R, et al., Tolerability, safety, pharmacokinetics, and efficacy of doxorubicin-loaded anti-EGFR immunoliposomes in advanced solid tumours: a phase 1 dose-escalation study. *Lancet Oncol*, 2012. 13(12): p. 1234-41.
104. Ishida O, Maruyama K, et al., Liposomes bearing polyethyleneglycol-coupled transferrin with intracellular targeting property to the solid tumors in vivo. *Pharm Res*, 2001. 18(7): p. 1042-8.
105. Suzuki R, Takizawa T, et al., Effective anti-tumor activity of oxaliplatin encapsulated in transferrin-PEG-liposome. *Int J Pharm*, 2008. 346(1-2): p. 143-50.
106. Glasgow MD, Chougule MB., Recent Developments in Active Tumor Targeted Multifunctional Nanoparticles for Combination Chemotherapy in Cancer Treatment and Imaging. *J Biomed Nanotechnol*, 2015. 11: p. 1859–1898.
107. Falagan-Lotsch P, Grzincic EM., and Murphy CJ., New Advances in Nanotechnology-Based Diagnosis and Therapeutics for Breast Cancer: An Assessment of Active-Targeting Inorganic Nanoplatfoms. *Bioconjugate Chem*, 2017. 28(1): p. 135–152.
108. P rez-Herrero E, Fern ndez-Medarde A., Advanced targeted therapies in cancer: Drug nanocarriers, the future of chemotherapy. *Eur J Pharm Biopharm*, 2015. 93: p. 52-79.
109. Fleurence J, F.S., Bahri M, Cochonneau D, Cl menceau B, Paris F, Heczey A, Birk  S., Targeting O-Acetyl-GD2 Ganglioside for Cancer Immunotherapy. *J Immunol Res*, 2017: p. 1-16
110. Adrian JE, Wolf A, et al., Targeted delivery to neuroblastoma of novel siRNA-anti-GD2-liposomes prepared by dual asymmetric centrifugation and sterol-based post-insertion method. *Pharm Res*, 2011. 28(9): p. 2261-72.
111. Brignole C, Pastorino F, et al., Immune cell-mediated antitumor activities of GD2-targeted liposomal c-myc antisense oligonucleotides containing CpG motifs. *J Natl Cancer Inst*, 2004. 96(15): p. 1171-80.

## **Chapter 2**

### **Diverse origins of the myofibroblast - implications for kidney fibrosis**

Lucas L. Falke, Shima Gholizadeh, Roel Goldschmeding, Robbert J. Kok and Tri Q. Nguyen, *Nat Rev Nephrol.* 2015, 11(4): 233-44.

## Abstract

Fibrosis is the common end point of chronic kidney disease. The persistent production of inflammatory cytokines and growth factors leads to an ongoing process of extracellular matrix production that eventually disrupts the normal functioning of the organ. During fibrosis, the myofibroblast is commonly regarded as the predominant effector cell. Accumulating evidence has demonstrated a diverse origin of myofibroblasts in kidney fibrosis. Proposed major contributors of myofibroblasts include bone marrow-derived fibroblasts, tubular epithelial cells, endothelial cells, pericytes and interstitial fibroblasts; the published data, however, have not yet clearly defined the relative contribution of these different cellular sources. Myofibroblasts have been reported to originate from various sources, irrespective of the nature of the initial damage responsible for the induction of kidney fibrosis. Here, we review the possible relevance of the diversity of myofibroblast progenitors in kidney fibrosis and the implications for the development of novel therapeutic approaches. Specifically, we discuss the current status of preclinical and clinical antifibrotic therapy and describe targeting strategies that might help support resident and circulating cells to maintain or regain their original functional differentiation state. Such strategies might help these cells resist their transition to a myofibroblast phenotype to prevent, or even reverse, the fibrotic state.

## Key points

- Myofibroblasts involved in kidney fibrosis might originate from diverse origins, including bone marrow-derived fibroblasts, tubular epithelial cells, endothelial cells, pericytes and interstitial fibroblasts
- Independent studies have shown that myofibroblasts can be derived from either one or more sources, irrespective of the nature of the initial damage responsible for the induction of kidney fibrosis
- The diversity of myofibroblast progenitors in kidney fibrosis might be relevant for the development of novel therapies
- Systemic therapies have been developed that can inhibit myofibroblast accumulation and fibrotic development; however, the efficacy and safety of these therapies in chronic kidney disease is not clear

- Targeting strategies to support resident and circulating cells in maintaining or regaining their original functional differentiation state and resisting transition to a myofibroblast phenotype might prevent or reverse fibrosis

## Introduction

The process of fibrosis or scar formation involves a complex interplay between multiple pleiotropic genes, including transforming growth factor  $\beta$  (*TGF- $\beta$* ), vascular endothelial growth factor (*VEGF*), platelet derived growth factor (*PDGF*), epidermal growth factor and connective tissue growth factor [1, 2]. The proliferative response of fibroblasts following injury provides an initial advantage, by helping to maintain tissue integrity and reduce the chance of infection; however, the regenerative potential of the tissue is ultimately limited by this response and the functions of the injured organ are further reduced [3]. The proliferative response possibly reflects an ancient evolutionary pressure that has skewed the tissue response to injury towards fibrosis; this process would protect the damaged organ against hazardous external factors, at the expense of long-term regeneration. Less challenging environmental and societal conditions and improved health care make regeneration favorable compared to quick fibrotic repair, as well as the increase in the mean age and lifespan. Understanding the mechanisms behind fibrosis is essential for the development of therapies that can correct or adjust this balance, so as to reduce unnecessary scar formation in pathologies such as kidney disease. The therapeutic potential of interventions that target known profibrotic factors has been extensively studied; [1, 4] however, these studies have not yet resulted in the establishment of effective clinically-available antifibrotic therapies [5]. Exploration of alternative intervention points for the management of kidney fibrosis is therefore warranted. Myofibroblasts are the key effector cell-type during fibrotic disease; they are the main producers of extracellular matrix (ECM), crosslinking enzymes, and inhibitors of matrix degrading metalloproteinases, [6] and increase in number during fibrosis. The exact origin of the myofibroblast during chronic kidney disease (CKD) is widely debated. The purpose of this Review is to summarize the

evidence for the various potential origins of myofibroblasts in the context of kidney fibrosis. We also discuss the possible clinical implications of the distinct myofibroblast progenitors with respect to drug-targeting strategies.

### **Wound healing response**

Kidney injury, for example caused by trauma, toxic exposure, or immune complexes, initiates a wound healing response. The early stage of wound healing is characterized by the rupture of platelets and the subsequent formation of a fibrin mesh, which leads to blood coagulation. This mesh recruits neutrophils and monocytes that become polarized macrophages. Macrophages can be polarized towards numerous different subtypes; major subtypes include M1 polarized pro-inflammatory macrophages and M2 polarized wound healing-associated macrophages [7]. The later stage of the wound healing response can be further subdivided into three phases [8]. During the first phase, the macrophage population shifts from an M1 to an M2 phenotype, and from promoting an inflammatory response to promoting tissue regeneration [9].

M2 macrophages secrete high levels of growth factors, such as TGF- $\beta$ 1, PDGF, and pro-epidermal growth factor, which induce cellular proliferation and synthesis of the ECM. Under the influence of these growth factors, myofibroblasts become highly abundant in the second phase, start to produce ECM components, and exert tensile forces to facilitate wound closure [10, 11]. Upon repetitive injury, as observed in CKD, the second stage of the wound healing response fails to resolve and fibrosis might ensue during a third phase. The third phase is characterized by protracted excessive deposition of ECM, increased crosslinking of collagen fibers, and decreased degradation of the ECM.10 Figure 1 summarizes the main sequence of events with regard to fibroblast activation. A full overview of the involvement of inflammatory cells, the myofibroblast differentiation sequence and proliferation promoting signals, is provided elsewhere [12–14].



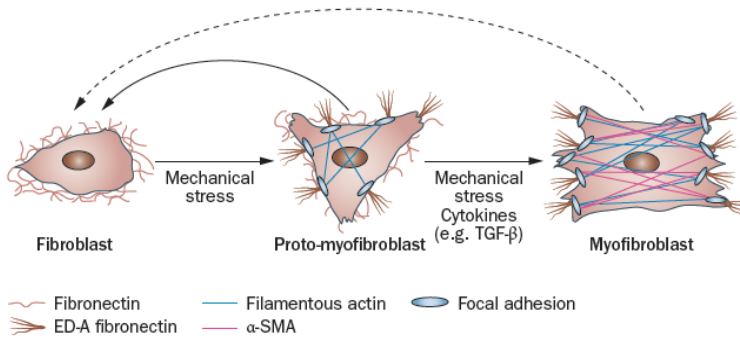


**Figure 1.** Differentiation steps of fibroblasts towards myofibroblast subtypes. Interstitial fibroblasts are characterized by the production of fibronectin and the absence of filamentous-actin,  $\alpha$ SMA and ED-A fibronectin. The protomyofibroblast produces ED-A fibronectin, contains stress fibers and focal adhesions, but does not yet contain the contractile  $\alpha$ SMA thus representing an immature myofibroblast. Mature myofibroblasts show abundant production of ED-A fibronectin and F-actin and are characterized by the presence of  $\alpha$ SMA. The transition from fibroblasts to protomyofibroblasts is reversible (solid line), but it is not known whether myofibroblasts can also re-differentiate into fibroblasts (dotted line).

### Techniques to study myofibroblasts

Several approaches can be used to determine the origin of myofibroblasts during disease. The two main methods involve studying the expression of differentiation markers and/or labelling of progenitor cells followed by lineage tracing. The following sections describe both the technical aspects of the methods used and the results that have been obtained thus far with regard to the origins of myofibroblasts during kidney injury. A glossary of terms used throughout this Review can be found in Box 1.

**Box 1 | Glossary**

- **Biologic agents:** medical term for therapeutic proteins or peptides manufactured in or isolated from a biological source
- **Humanized antibody:** immunoglobulins that are generated in animals with a full human amino acid sequence, thereby preventing a xenimmune response
- **Immunofluorescence/immunohistochemistry:** a technique that uses antibodies against specific molecular structures (usually proteins) to identify markers of interest. These antibodies can be detected by using fluorescent or chemical markers.
- **Lineage tracing:** a method used to trace the progeny of a single cell. Furthermore, donor cells or organs *ex vivo* can be labelled and injected into a non-genetically modified wild-type animal. This would be considered as fate tracing of the originally labelled (but not genetically altered) donor cells or organ. For more information see figure 3.
- **Marker:** an identifiable component expressed on the surface or within a cell that enables specific identification of the cellular subtype. Usually the marker is a specific protein, the expression of which can be identified using either immunofluorescence/immunohistochemistry or immunoelectron microscopy
- **Tyrosine kinase inhibitors:** small molecules that inhibit the signal domain of receptors on the cell surface

**Expression of differentiation markers**

Numerous studies have attempted to describe the expression of myofibroblast markers and to document any overlap with markers considered to be specific for renal cells (mesenchymal, epithelial, or endothelial) and cells of extra-renal origin [15]. A clear definition of the myofibroblast is yet to be agreed on, and therefore researchers currently use distinct but overlapping definitions. The myofibroblast was first identified as a cell type in fibrotic contractures, with features reminiscent of both fibroblasts and smooth muscle cells; [16] cell biologists have now generally accepted that a myofibroblast is a differentiated cell that shows both of these characteristics. A myofibroblast is defined by its ultrastructural features, such as large and expanded endoplasmatic reticula and a fibronexus containing intracellular myofilaments [17]. Preparing samples for electron microscopy to visualize such features, however, is labor intensive, time consuming, and costly and therefore immunohistochemical analysis followed by light microscopy of cell-surface markers is often used as an alternative to identify myofibroblasts. Myofibroblasts produce substantial amounts of ECM while additionally exhibiting contractile properties mediated by intermediary filament proteins, such as vimentin (VIM) and aortic smooth muscle actin (ACTA2, commonly known as  $\alpha$ SMA) [18].

Myofibroblasts express high levels of  $\alpha$ SMA, a stress fiber protein that facilitates increased contractility; as such,  $\alpha$ SMA is generally accepted as a definitive marker that is capable of identifying all myofibroblasts present in the studied tissue [19]. Approximately 75% of collagen-producing cells express  $\alpha$ SMA, indicating that this marker can be used to identify the majority of fibrotic mediator cells, but it is not fully sensitive [20]. During fibrosis, interstitial mesenchymal cells and myofibroblasts might comprise a heterogeneous group of cells that shift during disease progression, both in terms of marker expression and function [15]. Table 1 provides an overview of the cellular function of these precursor cells and the expression of their defining markers. The expression of most markers overlaps between these interstitial cell types, and consequently it should be noted that no marker has yet been identified that is fully specific for the individual precursors. The majority of fibroblasts express  $\alpha$ SMA, but not all  $\alpha$ SMA-positive cells produce large amounts of collagen. These  $\alpha$ SMA-positive ECM-negative cells might represent leucocytes, thus impairing the specificity of  $\alpha$ SMA as a marker of myofibroblasts. Alternatively, non-ECM-producing  $\alpha$ SMA-positive cells might represent a subset of myofibroblasts that are predominantly contractile [21].

Other markers that have been used to identify myofibroblasts include protein S100-A4 (S100A4), VIM, platelet derived growth factor receptor  $\beta$  (PDGFR $\beta$ ) and 5'-nucleotidase (NT5E) [15, 22, 23]. S100A4 and VIM were initially considered to be myofibroblast specific; however, these markers have subsequently been identified in macrophages, and thus cannot be used to specifically identify myofibroblasts [24, 25]. Figure 2 illustrates that there is only partial overlap in the cellular expression of  $\alpha$ SMA, VIM and PDGFR $\beta$  during kidney fibrosis; studies of myofibroblasts that employ only one cellular marker should therefore be interpreted with caution. Furthermore, scoring of marker expression using techniques such as immunohistochemistry can be subjective and provides only indirect evidence regarding myofibroblast origin, being at best a static snapshot of the very dynamic fibrotic process.

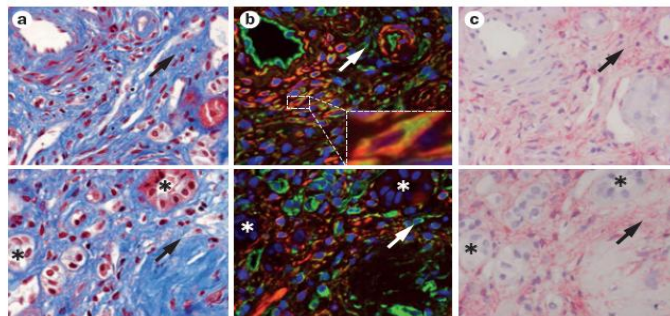


**Figure 2.** Expression of fibroblast markers only partially overlap in kidney fibrosis. A human kidney biopsy sample from a patient with allograft nephropathy was analyzed by three staining methods to determine overlap in fibroblast marker expression. The upper and lower panels show a different field of view. **(a)** Masson trichrome staining illustrates the extent of interstitial fibrosis. **(b)** Co-immunofluorescence for  $\alpha$ SMA (red, TRITC) and VIM (green, FITC). The arrow indicates interstitial cells that are positive for VIM but negative for  $\alpha$ SMA. The insert shows a myofibroblast that is positive for both  $\alpha$ SMA and VIM. **(c)** Immunohistochemistry for PDGFR $\beta$  expression in the corresponding areas to parts a and b. All areas show severe collagen deposition, suggesting that interstitial cells can produce large quantities of extracellular matrix, despite lacking expression of  $\alpha$ SMA. The arrows indicate the same position in consecutive microscopic images, as shown in panel b. The asterisks mark tubules. Despite severe interstitial fibrosis, no positive expression for  $\alpha$ SMA, VIM or PDGFR $\beta$  is observed. All images were taken in the same field of view at a magnification of  $\times 400$ . Abbreviations:  $\alpha$ SMA, aorta smooth muscle actin; FITC, fluorescein isothiocyanate; PDGFR $\beta$ , platelet derived growth factor  $\beta$ ; TRITC, tetramethylrhodamine; VIM, vimentin.

### Permanent labelling and lineage tracing

Direct evidence regarding the contribution of specific cell types to the myofibroblast pool during fibrotic kidney disease has been obtained from lineage tracing in animal studies using genetic labelling techniques. Lineage tracing of kidney cells relies on the permanent labelling of parent cells and their subsequent progeny cells, based on the transient expression of specific markers for distinct cell types or cellular compartments [26]. This technique can be performed either during development or during the postnatal period of the genetically labelled animals [27]. Studies have used *Sox2* to label epithelial cells; *Foxd1*, to label mesenchymal cells; *Tie2*, to label endothelial cells; and *PO* (also known as *Mpz*) to label neural crest cells [28–30]. Using the Cre recombinase system, transient expression can be used to permanently induce tracer protein expression, such as green

fluorescent protein (GFP), in these distinct cell types and their progeny [31]. An example of how this system could be used to trace *Foxd1*-positive cells is illustrated in figure 3.

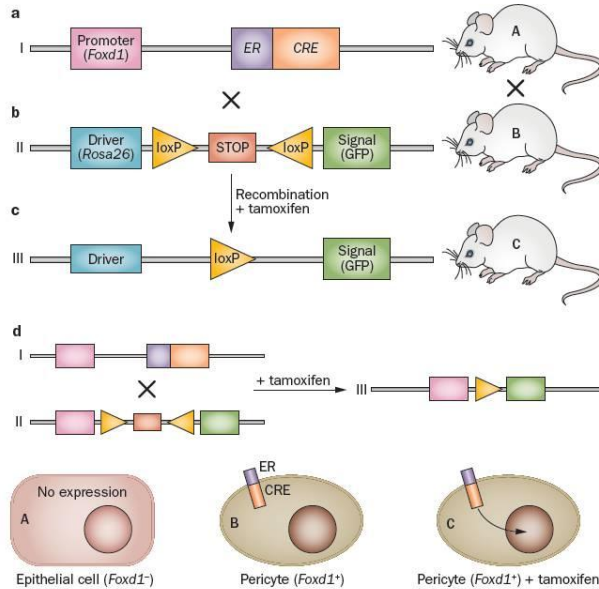


**Figure 3.** Schematic of the Cre–lox system used to trace FOXD1-positive pericytes. **(a)** Transgenic mouse “A” contains Cre recombinase capable of recognizing *loxP* sites, under the control of a specific tracer–marker promoter (in this case *Foxd1*). The Cre recombinase is only expressed in cells that are positive for the marker. **(b)** Transgenic mouse “B” contains a signaling sequence (in this case GFP) that is driven by a ubiquitous driver sequence (*Rosa26*) that is normally prematurely terminated by an inserted stop codon. The stop sequence is flanked by *loxP* sites. **(c)** Crossbreeding mouse “A” and “B” can produce transgenic mouse “C” in which the tracer or marker promoter driven Cre recombinase recognizes the *loxP* sites flanking the stop sequence, upon which the latter is excised. This excision allows the driver sequence to complete transcription and translation of the signaling cassette, thus allowing for specific lineage tracing. **(d)** An epithelial cell not expressing *Foxd1* does not have a tamoxifen-specific modified oestrogen receptor Cre recombinase (ER/Cre) fusion protein expressed at the cell membrane. Consequently, activation of the ER with tamoxifen does not occur and does not lead to fusion protein translocation to the nucleus and signal protein expression by recombining the stop sequence out of the DNA. In pericytes, however, *Foxd1* driven ER/Cre fusion protein expression does occur. Subsequently, tamoxifen injection ultimately leads to permanent signal protein expression allowing for timed FOXD1 specific tracing of pericytes. Abbreviations: FOXD1, forkhead box D1; GFP, green fluorescent protein.

## Origin of interstitial myofibroblasts

### Interstitial cells of mesodermal origin

The definition of kidney interstitial mesenchymal cells or fibroblasts is not straightforward as it is based on ill-defined morphology, nonspecific marker expression and the absence of markers that define specific cellular functions [15]. Pericytes and resident interstitial fibroblasts show overlapping basal expression of several markers that were previously described as being specific for either cell type [15]. Table 2 lists the utilized markers of embryonic mesodermal lineage and of differentiated mature cell populations that are relevant for research into the origins of myofibroblasts.

A series of observations have converged on the concept that pericytes—resident interstitial mesenchymal cells supporting capillary endothelial cells—are the main source of myofibroblasts in kidney fibrosis. In an experimental rat model of obstructive nephropathy, an inverse correlation between expression of *αSma* and *Nt5e* was observed, suggesting the conversion of interstitial mesenchymal cells into myofibroblasts [32]. The majority of fibroblasts in a rat model of angiotensin II-induced kidney fibrosis were found to be derived from resident renal interstitial cells [33]. These interstitial cells were later identified as perivascular pericytes, which trans-differentiated into collagen-producing myofibroblasts [20]. Subsequent *Foxd1*-driven lineage tracing in mice has provided further support for the notion that pericyte-derived cells account for the vast majority of  $\alpha$ SMA-positive cells in kidney fibrosis [29]. Another murine lineage tracing study that used *PO*-driven Cre recombinase, indicated that a large proportion of the interstitial myofibroblast pool is derived from erythropoietin (EPO)-producing interstitial mesenchymal cells, which are derived from the neural crest during embryogenesis [28]. Under conditions of cellular stress, these cells were observed to lose expression of EPO and subsequently transformed into myofibroblasts. Furthermore, a subset of these cells additionally expressed forkhead box protein D1 (FOXD1). An overlap between *PO* and *FOXD1* was shown in this study, and therefore common ancestry has been suggested. Further elaboration of this observation is made elsewhere [18].

Contradictory to these findings, other studies have suggested that myofibroblasts might be derived from interstitial fibroblasts that are not expressing pericyte markers. Moreover, although pericytes accumulate in the interstitium during CKD, they have not been shown to contribute to the pool of myofibroblasts that express  $\alpha$ SMA or collagen in several genetic mouse models of kidney fibrosis [34]. Irrespective of the numerical contribution of pericyte transformation into myofibroblasts, the sequence of pericyte detachment from endothelial cells leading to capillary instability (and an associated subsequent increase in fibrosis), seems to be a hallmark of CKD [35, 36].

Mesangial cells are commonly regarded as glomerular pericytes [37]. Research both *in vitro* and *in vivo*, has shown that mesangial cells are capable of transforming into  $\alpha$ SMA-positive cells under profibrotic conditions [38–40]. Furthermore, a positive correlation between glomerular  $\alpha$ SMA expression, mesangial expansion, and glomerular type IV collagen expression has been observed in rats with diabetic nephropathy [41].

### Epithelial cells

Epithelial-to-mesenchymal transition (EMT) is a physiological process characterized by the differentiation of epithelial cells towards a more mesenchymal phenotype [42]. During development, EMT occurs during gastrulation, whereby ectodermal cells differentiate to form new cells of the mesodermal germ layer [43]. Phenotypically, EMT is usually defined as the loss of typical epithelial markers, such as E-cadherin and tight junction protein ZO-1 (TJP1), while gaining mesenchymal markers, such as VIM,  $\alpha$ SMA, and S100A4. Outside of its function during development, EMT contributes to tumor progression and fibrogenesis in various organs, including the lungs, liver, kidneys, and heart.

EMT has been proposed to be important mechanism responsible for the accumulation of interstitial myofibroblasts and collagen production during kidney fibrosis [43]. Expression of  $\alpha$ SMA has been detected in tubular and glomerular epithelia in association with disease progression, in

both a remnant kidney model and during experimental glomerulonephritis [44, 45]. Furthermore, it has been proposed that the EMT might be responsible for the loss of podocytes that occurs in diabetic kidney disease; [46] features of EMT have also been observed in human tissue samples obtained by biopsy of patients with various other renal diseases [47–49]. Bone morphogenetic protein 7 (BMP7), hepatocyte growth factor (HGF) and EPO are known inhibitors of EMT *in vitro* [50]. Injections of BMP7, HGF, and EPO *in vivo* inhibited the increased expression of mesenchymal markers by tubular epithelial cells in murine models of unilateral ureteral obstruction (UUO) and nephrotoxic nephritis-induced CKD [51–53]. The possible transition of these cells into interstitial myofibroblasts, however, was not addressed in these studies.

In an early lineage tracing study,  $\gamma$ -GT-driven GFP expression in a murine model of UUO indicated that cells of tubular epithelial origin undergoing EMT contributed 36% to the tubulointerstitial myofibroblast pool [54]. A later study from the same researchers, using essentially the same mouse model, reported a much smaller contribution of these cells (5%) without providing a clear explanation for the observed difference [34]. Subsequent studies have attempted, but not succeeded, to reproduce the first observation in similar and other *in vivo* models, although EMT of tubular epithelial cells *in vitro* has been confirmed by numerous independent groups [29]. An epithelial tracing study using the *Cdh16* promoter in a model of obstructive nephropathy failed to identify a contribution of the tubular epithelium to the myofibroblast pool by undergoing EMT [55]. An additional report showed that epithelial overexpression of TGF- $\beta$ , driven by *Pax8*, resulted in tubular autophagy and induced interstitial fibrosis [56]. No induction of *S100A4* expression, as a marker of fibroblast differentiation, or migration of tubular epithelial cells into the interstitium, however, was observed at an ultrastructural level; in this case it is most likely that interstitial fibrosis occurred by paracrine signaling. Other markers of possible *in situ* EMT, such as *Snai1*, *Twist1*, or *Snai2*, [57] were not addressed in this study [56].

The role of EMT in the context of loss of epithelial and acquisition or reacquisition of certain mesenchymal features and markers by tubular epithelial cells in CKD is largely undisputed. However,



the direct contribution of this EMT reminiscent process to the interstitial myofibroblast pool seems unlikely [58, 59].

Numerous studies have demonstrated that EMT is involved in glomerular disease. Extra-capillary lesions that occur in crescentic glomerulonephritis are derived from parietal epithelial cells of the Bowman capsule [60]. The contribution of podocytes to glomerulosclerosis has not been studied extensively, although successful podocyte-tracing methods have been described during glomerular injury [61–63]. The association between podocytes and glomerulosclerosis has not yet been addressed using a lineage tracing approach, however. Podocyte-mediated production of *VEGF* is required for glomerular endothelial and mesangial stability; therefore, loss of healthy podocytes might lead to capillary collapse and glomerulosclerosis [64]. Furthermore, it has been suggested that  $\alpha$ SMA might not be an appropriate marker for monitoring the fibrotic transition of glomerular epithelial cells. Transgelin could prove to be a more suitable marker for fibrotic effector cell research in glomerulopathies as it seems to be more sensitive and specific than  $\alpha$ SMA with regard to glomerular injury and fibrotic cell activation [65].

### Endothelial cells

The endothelia can transdifferentiate towards a more mesenchymal phenotype, in a similar manner to epithelial cells. This process is known as endothelial-to-mesenchymal transition (EndoMT) [66]. EndoMT has been suggested to contribute to the increased number of myofibroblasts during kidney disease [30]. Cells, double labelled with the pan endothelial marker platelet endothelial cell adhesion molecule 1 (PECAM-1) and  $\alpha$ SMA, and *Tie2*-YFP lineage-traced cells, were counted in three different rodent models of kidney disease [30]. From these experiments, the contribution of EndoMT was calculated to be ~40%. Consistent with this observation, EndoMT was subsequently found to give rise to a large proportion of myofibroblasts during experimental diabetic kidney disease [67]. In *Tie2*-GFP mice, cells that are derived from a lineage that once expressed endothelial-specific *Tie2*, permanently express GFP. Following streptozotocin injection to induce diabetic nephropathy in

*Tie2*–GFP mice, ~10% of  $\alpha$ SMA-positive cells were positive for enhanced GFP, and were thus considered to have derived from *Tie2* lineage cells [67]. By analysing GFP overlap with PECAM-1, the specificity of the *Tie2* based lineage tracing approach was determined. An additional 80% of this subpopulation of cells was also positive for the expression of PECAM-1, resulting in an 8% computed contribution of endothelial cells to the interstitial myofibroblast pool. *Crim1* mutant mice develop renal cysts and fibrosis owing to aberrant capillary formation. Fate tracing of *Tie2*-positive cells in this mouse model showed that these cells contributed 31% of the interstitial myofibroblasts, composed of 6% cells of monocyte origin, and 25% cells of endothelial origin [68].

These studies suggest that endothelium-derived cells contribute to the myofibroblast pool during fibrotic disease. The magnitude of this contribution may vary depending on the model used. Interestingly, in a porcine model of ischaemia–reperfusion injury, an association between complement system activation and EndoMT was identified [69]. Accessibility of both the endothelium and the complement system make this an interesting finding for further development of targeted therapeutics; however, causality has yet to be established.

### Cells of extra-renal origin

In addition to resident kidney cells, circulating cells might also contribute to the interstitial myofibroblast pool in kidney fibrosis. Both mesenchymal stem cells and fibrocytes derived from haematopoietic stem cells are capable of differentiating into collagen-expressing  $\alpha$ SMA-positive myofibroblasts *in vitro* under profibrotic conditions [70–72]. Studies in bone marrow-depleted mice injected with GFP-positive donor bone marrow have indicated that ~15% of myofibroblasts may originate from circulating cells [54].

Transplantation of bone marrow harboring a red fluorescent protein transgene under the control of the  *$\alpha$ Sma* promoter indicated that ~35% of interstitial myofibroblasts originated from the bone marrow in both a murine model of obstructive nephropathy and a genetic murine model of Alport syndrome [34]. Furthermore, these bone marrow-derived (myo)fibroblasts, actively contributed to

fibrosis [73]. Data from a rat model of ischaemia–reperfusion injury showed similar results. Injection of human alkaline phosphatase-expressing bone marrow cells showed that >30% of these cells contribute to the interstitial kidney myofibroblast pool [74]. Other studies, however, show contradictory data. In human sex-mismatched kidney-allograft recipients [75] and experimental chronic kidney allograft nephropathy, circulating recipient progeny cells were observed as interstitial myofibroblasts [76]. Consistently, a mouse model of obstructive nephropathy showed that subsequent to transplantation of sex-mismatched bone marrow, only 9% of myofibroblasts originated from bone marrow cells [77]. The same study, however, used *Col1a2* promoter-driven luciferase to show that circulating cells did not contribute to collagen production. Transplantation of bone marrow cells expressing GFP under the control of the *Col1a2* promoter additionally did not support a contribution of bone marrow-derived cells to collagen production in kidney fibrosis [20]. In another study performed by the same research group, mice transplanted with *Col1a1*-GFP chimeric bone marrow failed to show a direct contribution of bone marrow cells to kidney fibrosis [78]. Taken together, these latter two studies show that the direct contribution of bone marrow cells to the interstitial myofibroblast pool, other than through paracrine or endocrine signaling, seems highly unlikely.

### **Caveats to lineage experiments**

Although much research has been performed to study the origin of the myofibroblast during CKD, numerous discrepancies exist in the reported data. Several general factors that potentially influence the reliability of the results should be noted and great care should be taken to ensure that future studies are comparable. The choice of mouse strain can be a large influence on fibrotic development [79] as can the duration and severity of the model used. It has been postulated that only during very late and severe stages of kidney disease is the tubular basal membrane sufficiently damaged to allow epithelial cells to infiltrate the interstitium and contribute to the fibrotic process. The infiltration of

epithelial cells could be a factor that affects *in vitro* data, as no basal membrane is present in most culture systems.

Caveats in the use of non-inducible Cre–*lox* recombination systems have been identified primarily with regard to the sensitivity and specificity of the genetic tracing constructs used. First, it must be shown that the transiently-expressed specific promoter used for tracing experiments is not reactivated later in life or during disease progression, as this process would reduce the specificity of the tracing. By using an inducible Cre, such as an estrogen receptor fusion protein, specific subsets of cells can express Cre recombinase only when tamoxifen is co-administered. This approach leaves only a small window of opportunity for recombination to occur and thereby increases specificity. In addition, it is essential to demonstrate that artificially truncated or randomly inserted versions of the transgenes are not expressed differentially when compared to the endogenous gene, by assessing both transgenes under physiological and pathological conditions.

The specificity of the promoters used for tracing experiments must be demonstrated. TIE2 is commonly regarded as a marker specific for endothelium; however, it should be noted that although TIE2 is sensitive for endothelial cells, it is not specific as it also marks myeloid-derived cells, such as monocytes [80]. In addition, TIE2 is expressed in cells of mesenchymal origin that ultimately give rise to vascular smooth muscle cells and pericytes [81]. Numerous cell types that express overlapping markers can bias tracing study results. Critical reviews describing these shortcomings and discrepancies can be found elsewhere [15, 18, 59, 82, 83].

### **Anti-fibrotic therapy**

Targeting myofibroblasts is the cornerstone of rational antifibrotic therapy owing to the pivotal role of this cell type in the production of profibrotic mediators and in the deposition of ECM components [84]. Molecular medicine has yielded a wide range of targeted agents, including kinase inhibitors and biologic therapies, which can be used for antifibrotic therapy [85, 86]. These agents

have proven effective in the preclinical setting; however, they have failed to advance into clinical practice, primarily due to a poor balance between antifibrotic efficacy and adverse effects.

### **Direct targeting**

Targeted accumulation of antifibrotic therapeutic agents in the kidney, and especially in kidney myofibroblasts, may improve their therapeutic index. Such accumulation can be achieved with the use of nanomedicines, such as nanoparticulate carriers or conjugates that bind to cell-surface receptors on myofibroblasts. Using this approach, nanocarriers can deliver a drug load inside myofibroblast cells when internalization is triggered by binding to the receptor. Hypothetically, this process will increase local antifibrotic activity with lowered systemic drug exposure. Such a strategy has not yet been described for kidney disease, but other studies in liver fibrosis describe nanocarrier-based strategies that might be feasible for targeting kidney myofibroblasts [87, 88].

### **Nanocarriers**

Indirect targeting relies upon the delivery of antifibrotic agents into other resident kidney cells, which then subsequently release these drugs in the kidney parenchyma, to provide localized antifibrotic activity on a tissue level rather than a cellular level. Table 3 details the nanocarrier strategies that can be employed for delivering antifibrotic compounds to the kidney through recognition by various cell surface receptors.

One of the most appealing approaches to deliver therapeutic compounds to the kidney is through the targeting of tubular epithelial cells. The proximal tubular epithelium is highly active in accumulating compounds from the filtered urine via the multitude of receptors in the luminal brush-border [89]. Among these, low density lipoprotein receptor-related protein 2 (commonly known as megalin/cubulin), and folate receptor 1 $\alpha$  have been exploited successfully for drug targeting purposes [90, 91]. These receptors can be reached only by filtered compounds, which justifies the investigation of relatively small drug-carrier conjugates that can pass through the glomerular filtration barrier.

These drug-targeting approaches rely on the internalization of the nanocarrier and subsequent processing in the lysosomal compartment. This strategy is primarily feasible for small molecule agents that can diffuse over intracellular membranes and further redistribute once liberated from the carrier. Kinase inhibitor–lysozyme conjugates that can perturb the TGF- $\beta$ , p38 MAPK, or Rho kinase signalling pathways have been shown to elicit downstream antifibrotic responses, such as reduced expression of inflammatory and profibrotic mediators (including CCL2 and TGF- $\beta$ 1), when evaluated in rat models of renal inflammation (unilateral renal ischaemia) and fibrosis (UUO) [90, 92]. Protection against tubular damage was reported following tubular cell-directed delivery of the Rho kinase inhibitor, Y27632, [90] as well as following tubular delivery of immunosuppressive agents, such as mycophenolic acid and prednisolone, by means of 2-glucosamine-based conjugates [93, 94]. Although long-term follow-up studies are lacking, these initial studies show the potential of antifibrotic therapeutic drug delivery in resident kidney cells and the subsequent modulation of profibrotic and antifibrotic mediators.

PDGFR $\beta$  is expressed by the majority of resident cell types in the kidney, and both PDGF ligands and PDGF receptors are overexpressed during fibrosis [95]. Higher expression levels of PDGFR $\beta$  on the myofibroblast cell surface compared to normal kidney parenchyma make it an attractive route through which antifibrotic compounds can be accumulated into cells. Interferon- $\gamma$  conjugates have been delivered to PDGFR $\beta$ -expressing fibroblasts by means of cyclic peptide ligands that contain a PDGFR $\beta$  peptide epitope. Chemical conjugation of peptide epitopes, or recombinant expression of a chimeric protein that comprises targeting peptides and the effector domain of interferon- $\gamma$ , are techniques that have been used successfully [87]. Targeting myofibroblasts in this way has not yet been explored in kidney fibrosis, but impressive results have already been demonstrated in the context of liver fibrosis. PDGFR $\beta$ -targeted interferon- $\gamma$  derivatives accumulate in activated myofibroblasts upon intravenous administration in mice with CCl<sub>4</sub>-induced liver fibrosis, which subsequently inhibited both early and progressive stages of liver fibrosis [87]. In a similar approach, cyclic PDGF $\beta$  peptides and manno-6-phosphate carbohydrate tethers were used to modify human

serum albumin, thus obtaining albumin-based nanocarriers directed to fibroblasts [96]. This approach has proved successful for the delivery of small molecule antifibrotic agents, such as 15-deoxy-delta12,14-prostaglandin J2, [88] the angiotensin-receptor blocker losartan and an inhibitor of TGF $\beta$ R1 [97, 98].

### **Manipulation of myofibroblast activity**

Indirect approaches to influence renal myofibroblast activity can also be envisioned. Enhancing the production of antifibrotic mediators by kidney resident cells or, inversely, inhibiting the production of profibrotic growth factors or other local mediators, are two possible approaches [1, 84]. Fibrosis may also be attenuated by interfering with the recruitment of immune cells into the renal interstitium [12]. Several kidney cell types, such as tubular epithelia or endothelia, can be the focus of an indirect myofibroblast targeting strategy, and have been described in more detail in other recent reviews [99–101].

### **Clinical trials**

Numerous preclinical and clinical studies using systemic therapy have been successful in inhibiting myofibroblast accumulation and attenuating kidney fibrosis. An important component of these successful preclinical therapies has been the use of strategies to target the profibrotic TGF- $\beta$  signalling pathway [4], including with the use of microRNA-29.102 The pan-TGF- $\beta$  antibody, fresolimumab, has been shown to be well tolerated in a phase I trial among patients with focal segmental glomerulosclerosis [103]. The efficacy of this therapy was not studied, but a phase II trial is currently underway among patients with a steroid-resistant form of this condition [104].

Another approach for inhibiting myofibroblast accumulation and attenuating kidney fibrosis is by targeting connective tissue growth factor, a key mediator of profibrotic TGF- $\beta$  activity, using a humanized monoclonal antibody. This human IgGk antibody (known as FG-3,019) has been tested in a phase I clinical trial among patients with microalbuminuric diabetes, and administration of this antibody proved to be well tolerated and significantly decreased albuminuria [105]. A trial using the

drug nintedanib, a multikinase inhibitor that acts on PDGFR, VEGF receptor and fibroblast growth factor receptor (FGFR) tyrosine kinases, reduced disease progression among patients with idiopathic pulmonary fibrosis [106]. Nintedanib was well tolerated and approved by the FDA for idiopathic pulmonary fibrosis in October 2014. Nintedanib may therefore be another potential therapy for kidney fibrosis. Gefitinib, an epidermal growth factor tyrosine kinase inhibitor, has shown promise in the treatment of experimental kidney disease [107]. A number of trials assessing the safety and efficacy of gefitinib are currently underway, and if well tolerated, trials studying the therapeutic feasibility in kidney disease might be initiated. A clinical trial investigating the effects of the PDGFR tyrosine kinase inhibitor imatinib, has also shown promising results in patients with nephrogenic systemic fibrosis [108].

Despite some promising data, considerations regarding the limitations of systemic antifibrotic therapy need to be taken into account. Sparse reports exist describing the reversal of renal fibrosis, but it is generally accepted that prevention of ECM deposition is more likely to result in successful treatment. As such, high doses of antifibrotic therapeutics administered during the onset and progression of disease might provide the best results in terms of morbidity and mortality. High drug doses, however, are associated with off target effects and adverse events [109, 110]. Indeed, with current therapeutic dosage, adverse events are seen with the majority of tyrosine kinase inhibitors [109, 110]. A meta-analysis has shown that targeting VEGF receptors with tyrosine kinase inhibitors increases mortality [111]. Long-term exposure to tolerated doses of biologic therapies might, alternatively, lead to drug resistance as seen during the treatment of oncological disease. Targeting VEGFR leads to a PDGFR/FGFR-mediated escape [112]. In addition, long-term exposure of carcinoma cell lines to TGF $\beta$ R I and/or II inhibitors induces drug resistance associated with a more invasive phenotype [113]. Whether long-term exposure to antifibrotic drugs, such as tyrosine kinase inhibitors and monoclonal antibodies, during fibrotic kidney disease is well tolerated and effective, remains to be investigated. Emerging data indicates that specific targeting of high-dose antifibrotic therapy to the kidney is preferable over long-term systemic treatment.



Anti-fibrotic small molecule drugs can be accumulated in kidney myofibroblasts or other kidney cell types by the above-discussed targeting strategies. To exemplify, the biologic agents galunisertib, indetanib, gefitinib, and imatinib have structural properties that render them good candidates for nanocarrier-based formulations, either using drug-carrier conjugates or by encapsulation in nanoparticles [114, 115]. Furthermore, delivery of antisense or nucleic acid-based therapeutics might also benefit from nanocarrier-based delivery systems, as such hydrophilic agents typically cannot cross cellular or organelle membranes. For example, delivery of microRNA-29 into the kidney has been achieved by local transgene expression following ultrasound microbubble-mediated gene transfer [102].

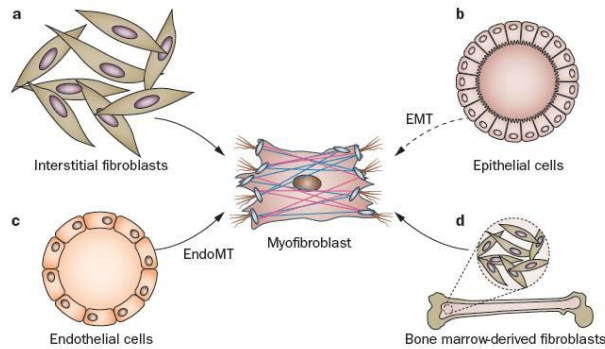


**Figure 4.** Potential origins of myofibroblast progenitors. **(a)** Interstitial mesenchymal (fibroblast) cells are commonly regarded as the most profound contributor to the myofibroblast pool during disease. **(b)** Epithelial cells were historically indicated as a potential source of myofibroblasts by EMT; however previous research has contradicted this evidence and epithelial progeny has become unlikely. **(c)** Endothelial cells have been shown to contribute to some extent to myofibroblasts that contribute to fibrotic development by EndoMT. **(d)** Bone marrow derived cells have been shown to incorporate and contribute to myofibroblast numbers. Abbreviations: EMT; epithelial-to-mesenchymal transition; EndoMT, endothelial-to-mesenchymal transition.

Finally, antibodies or recombinant proteins that target TGF- $\beta$  family members or their receptors are directed to extracellular pharmacological targets; enhancing their accumulation in the kidney should avoid internalization of the therapeutic modality. By contrast, for small molecule inhibitors of TGF- $\beta$  signaling, localized release within the kidney parenchyma seems most appropriate. Renal

delivery of recombinant proteins has been investigated recently for the delivery of the antifibrotic protein BMP-7, by means of an injectable hydrogel depot [116].

**Table 1.** Features of different types of interstitial cells in the kidney

Feature	Cell type			
	Fibroblast	Myofibroblast	Pericyte	VSMC
ACTA2	✗	✓	✓	✓
PDGFR $\beta$	✓	✓	✓	✓
S100A4	✓	✓	✗	✓
NT5E	✓	✓	✓	✗
DES	✗	✗	✓	✓
VIM	✓	✓	✓	✓
<b>Function</b>	ECM maintenance and structural support to the parenchyma	Wound contraction Tissue healing response	Vascular stability Production of VEGF-A Chemical and/or mechanical sensation	Regulating vascular wall tonus
<b>Location</b>	Interstitial In contact with the epithelium and epithelial basal membrane	Absent under physiological conditions Present in the interstitium under pathological conditions	Interstitial In contact with the endothelium and endothelial basement membrane	Medial layer of blood vessels

\*Owing to the overlap of marker expression, only ultrastructural analysis can discriminate between these four interstitial cell types. Other cell types, such as leucocytes, also express these markers. Abbreviations:  $\alpha$ SMA, aorta smooth muscle actin; DES, desmin; ECM, extracellular matrix; NT5E, 5'-nucleotidase (CD73); PDGFR $\beta$ , platelet-derived growth factor receptor,  $\beta$ ; S100A4, S100 calcium binding protein A4; VEGF, vascular endothelial growth factor A; VIM, vimentin; VSMC, vascular smooth muscle cell.

**Table 2.** All published lineage trace experiments to date

Cell type	Traced marker method	Model	Results	Study
Interstitial fibroblasts (derived from neural crest cells)	<i>PO</i>	UUO	~100% of cortical and medullary resident fibroblasts were of MPZ origin.  Reduced EPO production	Asada, N. <i>et al.</i> (2011)[28]
Pericytes and interstitial fibroblasts	<i>Pdgfr<math>\beta</math></i>	UUO COL4A3-KO	Cellular proliferation, with no contribution to fibrosis	Lebleu, V.S. <i>et al.</i> (2013)[34]
Pericytes and interstitial fibroblasts	NG-2	UUO COL4A3-KO	Cellular proliferation, with 6% contribution to fibrosis	Lebleu, V.S. <i>et al.</i> (2013)[34]
Pericytes, perivascular fibroblasts, VSMCs, and mesangial cells	FOXD1	UUO I R	100% co-expression of FOXD1 and PDGFR $\beta$ in pericytes.  ~25% co-expression of ACTA2 and FOXD1 lineage	Humphreys, B.D. <i>et al.</i> (2010)[29]
Epithelial cells	$\gamma$ GT	UUO	5% contribution to myofibroblasts	Lebleu, V.S. <i>et al.</i> (2013)[34]
Epithelial cells	$\gamma$ GT	UUO	36% contribution to myofibroblasts	Iwano, M. <i>et al.</i> (2002)[54]
Epithelial cells	SIX2	UUO I R	No contribution to myofibroblasts	Humphreys, B.D. <i>et al.</i> (2010)[29]
Collecting duct and urothelial cells	HOXB7	UUO I R	No contribution to myofibroblasts	Humphreys, B.D. <i>et al.</i> (2010)[29]
Endothelial cells	CDH5	UUO	10% contribution to myofibroblasts	Lebleu, V.S. <i>et al.</i> (2013)[34]

Endothelial cells (and a subpopulation of monocytes)	TIE2 (and CD31 co-expression)	UUO IR COL4A3-KO	30–50% contribution to myofibroblasts	Zeisberg, E.M. <i>et al.</i> (2008)[30]
Endothelial cells (and a subpopulation of monocytes)	TIE2	Streptozotocin-induced diabetic nephropathy	28% contribution to myofibroblasts	Li, J. <i>et al.</i> (2009)[67]
Endothelial cells (and a subpopulation of monocytes)	TIE2	CRIM1-KO (VEGFA deficiency)	31% co-expression of TIE2 and ACTA2 6% coexpression of TIE2, ACTA2 and F4/80	Phua, Y.L. <i>et al.</i> (2013)[68]
Cells of extrarenal origin and/or bone marrow cells	$\alpha$ -SMA bone marrow transplant	UUO	35% contribution to myofibroblasts. Contribution to fibrosis is independent of proliferation	Lebleu, V.S. <i>et al.</i> (2013)[34]
Cells of extrarenal origin cells and/or bone marrow cells	S100A4 bone marrow transplant	Physiologic conditions UUO	12% contribution to interstitial fibroblasts, without fibrogenic stress. 15% contribution to myofibroblasts during stress	Iwano, M. <i>et al.</i> (2002)[54]
Cell of extrarenal origin and/or bone marrow cells	Sex mismatch bone marrow transplant using COL1A2-luciferase	UUO	8.6% contribution of bone marrow-derived cells to myofibroblasts No contribution to COL1A2 synthesis	Roufosse, C. <i>et al.</i> (2006)[75]
T and B leukocytes	RAG1-KO	COL4A3-KO	Reduced interstitial fibrosis	Lebleu, V.S. <i>et al.</i> (2008)[117]

Abbreviations:  $\alpha$ SMA, aorta smooth muscle actin;  $\gamma$ GT,  $\gamma$ -glutamyl transpeptidase; CDH5, cadherin 5, type 2 (vascular endothelium); COL1A2, collagen type 1,  $\alpha$  2; COL4A3, collagen, type IV,  $\alpha$  3 (Goodpasture antigen); EPO, erythropoietin; FOXD1, forkhead box D1; HOXB7, homeobox B7; IR, ischaemia–reperfusion; KO, knockout; NG-2, neural–glial antigen 2; PO, myelin protein zero; PDGFR $\beta$ , platelet-derived growth factor receptor,  $\beta$  polypeptide; RAG1, recombination activating

**Table 3.** Drug targeting to myofibroblasts via surface receptors on kidney cells

Target cell	Target receptor	Nanocarrier system	Validation
Proximal tubular epithelial cells	Megalin	Y27632-lysozyme conjugate	Unilateral IR in rats [90]
		SB201290-lysozyme conjugate	Unilateral IR in rats [92]
		LY-364947-lysozyme conjugate	UUO in rats [115]
	Megalin	Imatinib-lysozyme conjugate	Healthy mice, UUO mice [114]
		EPAC activator 007-lysozyme conjugate	Unilateral IR in mice [118]
		Mycophenolate-glucosamine conjugate	Unilateral IR in rats [94, 119]
Proximal tubular epithelial cells	Megalin	Prednisolone-glucosamine conjugate	Unilateral IR in rats [93]
		Prednisolone-low-molecular weight chitosan conjugate	Healthy mice [120]
		Folate receptor 1	Rapamycin-folate conjugate
Proximal tubular epithelial cells	Unknown target	Arg-vasopressin-alkylglycoside conjugate	Healthy rats [121]
		alfa8 integrin	Dye loaded anti-alfa8 immunoliposomes
Mesangial cells	Thy 1.1.	Mycophenolate loaded OX-7 immunoliposomes	Rats with anti-Thy 1.1. induced glomerulonephritis [123]
		Endothelial cells	E-selectin
podocytes	Podocyte specific antigen*	Anti-podocyte targeted siRNA-protamine polyplexes	Uninephrectomized rats [125]

\*Nanocarriers directed to these receptors have been developed for rodents only; human receptor homologues have not yet been identified. Abbreviations: GBM, glomerular basement membrane; IR, ischaemia-reperfusion; OX7, mouse monoclonal anti-Thy1 antibody; PKD, polycystic kidney disease; siRNA, small interfering RNA; Thy1.1, thymocyte differentiation antigen 1.1; UUO, unilateral ureteral obstruction.

## Conclusions

This review summarizes the evidence for a diverse population of myofibroblast progenitors in kidney fibrosis. Data from various research groups have yielded differing results about the nature of the progenitor cells (Figure 4), leading to controversy in this field. Consequently, a clear understanding of the relative contribution of the different cellular sources to renal myofibroblasts has not yet been achieved. These discrepancies can be explained by several factors, including differences in injury models, the use of different Cre-*lox* recombination systems, the specificity of chosen promoters, and the lack of a specific myofibroblast cell marker.

Targeting myofibroblasts is the cornerstone of rational antifibrotic therapy, in view of the pivotal role of this cell type in the production of profibrotic mediators and its role in the deposition of ECM components. Direct targeting strategies might include support of resident and circulating cells, to help them maintain or regain their original functional differentiation state and resist their transition to a myofibroblast phenotype. In addition, molecular medicine has yielded a wide range of targeted agents, such as kinase inhibitors and biologic therapies, which can be used in antifibrotic approaches. Although clinical trials in patients with kidney fibrosis are scarce, initial studies have shown the potential of antifibrotic therapeutics delivered to resident kidney cells to modulate profibrotic and antifibrotic mediators.

## References

1. Kok, H.M., Falke, L.L., Goldschmeding, R. & Nguyen, T.Q. Targeting CTGF, EGF and PDGF pathways to prevent progression of kidney disease. *Nat Rev Nephrol* (2014).
2. Hakrroush, S. et al. Effects of increased renal tubular vascular endothelial growth factor (VEGF) on fibrosis, cyst formation, and glomerular disease. *Am J Pathol* 175, 1883-95 (2009).

3. Thannickal, V.J. Aging, antagonistic pleiotropy and fibrotic disease. *Int J Biochem Cell Biol* 42, 1398-400 (2010).
4. Akhurst, R.J. & Hata, A. Targeting the TGFbeta signalling pathway in disease. *Nat Rev Drug Discov* 11, 790-811 (2012).
5. Ryu, J.H. & Daniels, C.E. Advances in the management of idiopathic pulmonary fibrosis. *F1000 Med Rep* 2, 28 (2010).
6. Novak, M.L. & Koh, T.J. Macrophage phenotypes during tissue repair. *J Leukoc Biol* 93, 875-81 (2013).
7. Strutz, F. & Muller, G.A. Mechanisms of renal fibrogenesis. . *Immunological Renal Diseases* 2nd edition, 73 - 101 (2001).
8. Sica, A. & Mantovani, A. Macrophage plasticity and polarization: in vivo veritas. *J Clin Invest* 122, 787-95 (2012).
9. Wynn, T.A. & Ramalingam, T.R. Mechanisms of fibrosis: therapeutic translation for fibrotic disease. *Nat Med* 18, 1028-40 (2012).
10. Micallef, L. et al. The myofibroblast, multiple origins for major roles in normal and pathological tissue repair. *Fibrogenesis Tissue Repair* 5 Suppl 1, S5 (2012).
11. Duffield, J.S., Lupper, M., Thannickal, V.J. & Wynn, T.A. Host responses in tissue repair and fibrosis. *Annu Rev Pathol* 8, 241-76 (2013).
12. Meng, X.M., Nikolic-Paterson, D.J. & Lan, H.Y. Inflammatory processes in renal fibrosis. *Nat Rev Nephrol* 10, 493-503 (2014).
13. Tomasek, J.J., Gabbiani, G., Hinz, B., Chaponnier, C. & Brown, R.A. Myofibroblasts and mechano-regulation of connective tissue remodelling. *Nat Rev Mol Cell Biol* 3, 349-63 (2002).
14. Meran, S. & Steadman, R. Fibroblasts and myofibroblasts in renal fibrosis. *Int J Exp Pathol* 92, 158-67 (2011).
15. Boor, P. & Floege, J. The renal (myo-)fibroblast: a heterogeneous group of cells. *Nephrol Dial Transplant* 27, 3027-36 (2012).
16. Gabbiani, G. & Majno, G. Dupuytren's contracture: fibroblast contraction? An ultrastructural study. *Am J Pathol* 66, 131-46 (1972).
17. Eyden, B. The myofibroblast: phenotypic characterization as a prerequisite to understanding its functions in translational medicine. *J Cell Mol Med* 12, 22-37 (2008).
18. Duffield, J.S. Cellular and molecular mechanisms in kidney fibrosis. *J Clin Invest* 124, 2299-306 (2014).
19. Hinz, B. et al. The myofibroblast: one function, multiple origins. *Am J Pathol* 170, 1807-16 (2007).
20. Lin, S.L., Kisseleva, T., Brenner, D.A. & Duffield, J.S. Pericytes and perivascular fibroblasts are the primary source of collagen-producing cells in obstructive fibrosis of the kidney. *Am J Pathol* 173, 1617-27 (2008).

21. Hinz, B. The myofibroblast: paradigm for a mechanically active cell. *J Biomech* 43, 146-55 (2010).
22. Strutz, F. et al. Identification and characterization of a fibroblast marker: FSP1. *J Cell Biol* 130, 393-405 (1995).
23. Leader, M., Collins, M., Patel, J. & Henry, K. Vimentin: an evaluation of its role as a tumour marker. *Histopathology* 11, 63-72 (1987).
24. Osterreicher, C.H. et al. Fibroblast-specific protein 1 identifies an inflammatory subpopulation of macrophages in the liver. *Proc Natl Acad Sci U S A* 108, 308-13 (2011).
25. Mor-Vaknin, N., Punturieri, A., Sitwala, K. & Markovitz, D.M. Vimentin is secreted by activated macrophages. *Nat Cell Biol* 5, 59-63 (2003).
26. Lewandoski, M. Conditional control of gene expression in the mouse. *Nat Rev Genet* 2, 743-55 (2001).
27. Dressler, G.R. Advances in early kidney specification, development and patterning. *Development* 136, 3863-74 (2009).
28. Asada, N. et al. Dysfunction of fibroblasts of extrarenal origin underlies renal fibrosis and renal anemia in mice. *J Clin Invest* 121, 3981-90 (2011).
29. Humphreys, B.D. et al. Fate tracing reveals the pericyte and not epithelial origin of myofibroblasts in kidney fibrosis. *Am J Pathol* 176, 85-97 (2010).
30. Zeisberg, E.M., Potenta, S.E., Sugimoto, H., Zeisberg, M. & Kalluri, R. Fibroblasts in kidney fibrosis emerge via endothelial-to-mesenchymal transition. *J Am Soc Nephrol* 19, 2282-7 (2008).
31. Sauer, B. Inducible gene targeting in mice using the Cre/lox system. *Methods* 14, 381-92 (1998).
32. Picard, N., Baum, O., Vogetseder, A., Kaissling, B. & Le Hir, M. Origin of renal myofibroblasts in the model of unilateral ureter obstruction in the rat. *Histochem Cell Biol* 130, 141-55 (2008).
33. Faulkner, J.L., Szykalski, L.M., Springer, F. & Barnes, J.L. Origin of interstitial fibroblasts in an accelerated model of angiotensin II-induced renal fibrosis. *Am J Pathol* 167, 1193-205 (2005).
34. Lebleu, V.S. et al. Origin and function of myofibroblasts in kidney fibrosis. *Nat Med* 19, 1047-53 (2013).
35. Khairoun, M. et al. Renal ischemia-reperfusion induces a dysbalance of angiopoietins, accompanied by proliferation of pericytes and fibrosis. *Am J Physiol Renal Physiol* 305, F901-10 (2013).
36. Kida, Y. & Duffield, J.S. Pivotal role of pericytes in kidney fibrosis. *Clin Exp Pharmacol Physiol* 38, 467-73 (2011).
37. Schlondorff, D. The glomerular mesangial cell: an expanding role for a specialized pericyte. *FASEB J* 1, 272-81 (1987).
38. Sam, R. et al. Glomerular epithelial cells transform to myofibroblasts: early but not late removal of TGF-beta1 reverses transformation. *Transl Res* 148, 142-8 (2006).



39. Whiteside, C. et al. Regulation of mesangial cell alpha-smooth muscle actin expression in 3-dimensional matrix by high glucose and growth factors. *Nephron Exp Nephrol* 109, e46-56 (2008).
40. Alpers, C.E., Hudkins, K.L., Gown, A.M. & Johnson, R.J. Enhanced expression of "muscle-specific" actin in glomerulonephritis. *Kidney Int* 41, 1134-42 (1992).
41. Matsubara, T. et al. Expression of Smad1 is directly associated with mesangial matrix expansion in rat diabetic nephropathy. *Lab Invest* 86, 357-68 (2006).
42. Lamouille, S., Xu, J. & Derynck, R. Molecular mechanisms of epithelial-mesenchymal transition. *Nat Rev Mol Cell Biol* 15, 178-96 (2014).
43. Kalluri, R. & Weinberg, R.A. The basics of epithelial-mesenchymal transition. *J Clin Invest* 119, 1420-8 (2009).
44. Ng, Y.Y. et al. Glomerular epithelial-myofibroblast transdifferentiation in the evolution of glomerular crescent formation. *Nephrol Dial Transplant* 14, 2860-72 (1999).
45. Ng, Y.Y. et al. Tubular epithelial-myofibroblast transdifferentiation in progressive tubulointerstitial fibrosis in 5/6 nephrectomized rats. *Kidney Int* 54, 864-76 (1998).
46. Yamaguchi, Y. et al. Epithelial-mesenchymal transition as a potential explanation for podocyte depletion in diabetic nephropathy. *Am J Kidney Dis* 54, 653-64 (2009).
47. Bariety, J. et al. Glomerular epithelial-mesenchymal transdifferentiation in pauci-immune crescentic glomerulonephritis. *Nephrol Dial Transplant* 18, 1777-84 (2003).
48. Rastaldi, M.P. et al. Epithelial-mesenchymal transition of tubular epithelial cells in human renal biopsies. *Kidney Int* 62, 137-46 (2002).
49. Vongwiwatana, A., Tasanarong, A., Rayner, D.C., Melk, A. & Halloran, P.F. Epithelial to mesenchymal transition during late deterioration of human kidney transplants: the role of tubular cells in fibrogenesis. *Am J Transplant* 5, 1367-74 (2005).
50. Chen, C.L. et al. Erythropoietin suppresses epithelial to mesenchymal transition and intercepts Smad signal transduction through a MEK-dependent mechanism in pig kidney (LLC-PK1) cell lines. *Exp Cell Res* 316, 1109-18 (2010).
51. Tasanarong, A., Kongkham, S. & Khositseth, S. Dual inhibiting senescence and epithelial-to-mesenchymal transition by erythropoietin preserve tubular epithelial cell regeneration and ameliorate renal fibrosis in unilateral ureteral obstruction. *Biomed Res Int* 2013, 308130 (2013).
52. Yang, J. & Liu, Y. Blockage of tubular epithelial to myofibroblast transition by hepatocyte growth factor prevents renal interstitial fibrosis. *J Am Soc Nephrol* 13, 96-107 (2002).
53. Zeisberg, M. et al. BMP-7 counteracts TGF-beta1-induced epithelial-to-mesenchymal transition and reverses chronic renal injury. *Nat Med* 9, 964-8 (2003).
54. Iwano, M. et al. Evidence that fibroblasts derive from epithelium during tissue fibrosis. *J Clin Invest* 110, 341-50 (2002).
55. Li, L., Zepeda-Orozco, D., Black, R. & Lin, F. Autophagy is a component of epithelial cell fate in obstructive uropathy. *Am J Pathol* 176, 1767-78 (2010).

56. Koesters, R. et al. Tubular overexpression of transforming growth factor-beta1 induces autophagy and fibrosis but not mesenchymal transition of renal epithelial cells. *Am J Pathol* 177, 632-43 (2010).
57. Thiery, J.P., Acloque, H., Huang, R.Y. & Nieto, M.A. Epithelial-mesenchymal transitions in development and disease. *Cell* 139, 871-90 (2009).
58. Galichon, P., Finianos, S. & Hertig, A. EMT-MET in renal disease: should we curb our enthusiasm? *Cancer Lett* 341, 24-9 (2013).
59. Kriz, W., Kaissling, B. & Le Hir, M. Epithelial-mesenchymal transition (EMT) in kidney fibrosis: fact or fantasy? *J Clin Invest* 121, 468-74 (2011).
60. Smeets, B. et al. Tracing the origin of glomerular extracapillary lesions from parietal epithelial cells. *J Am Soc Nephrol* 20, 2604-15 (2009).
61. Hackl, M.J. et al. Tracking the fate of glomerular epithelial cells in vivo using serial multiphoton imaging in new mouse models with fluorescent lineage tags. *Nat Med* 19, 1661-6 (2013).
62. Schulte, K. et al. Origin of parietal podocytes in atubular glomeruli mapped by lineage tracing. *J Am Soc Nephrol* 25, 129-41 (2014).
63. Burford, J.L. et al. Intravital imaging of podocyte calcium in glomerular injury and disease. *J Clin Invest* 124, 2050-8 (2014).
64. Eremina, V. et al. Vascular endothelial growth factor a signaling in the podocyte-endothelial compartment is required for mesangial cell migration and survival. *J Am Soc Nephrol* 17, 724-35 (2006).
65. Sakamaki, Y. et al. Injured kidney cells express SM22alpha (transgelin): Unique features distinct from alpha-smooth muscle actin (alphaSMA). *Nephrology (Carlton)* 16, 211-8 (2011).
66. Piera-Velazquez, S., Li, Z. & Jimenez, S.A. Role of endothelial-mesenchymal transition (EndoMT) in the pathogenesis of fibrotic disorders. *Am J Pathol* 179, 1074-80 (2011).
67. Li, J., Qu, X. & Bertram, J.F. Endothelial-myofibroblast transition contributes to the early development of diabetic renal interstitial fibrosis in streptozotocin-induced diabetic mice. *Am J Pathol* 175, 1380-8 (2009).
68. Phua, Y.L., Martel, N., Pennisi, D.J., Little, M.H. & Wilkinson, L. Distinct sites of renal fibrosis in *Crim1* mutant mice arise from multiple cellular origins. *J Pathol* 229, 685-96 (2013).
69. Curci, C. et al. Endothelial-to-mesenchymal transition and renal fibrosis in ischaemia/reperfusion injury are mediated by complement anaphylatoxins and Akt pathway. *Nephrol Dial Transplant* 29, 799-808 (2014).
70. Bellini, A. & Mattoli, S. The role of the fibrocyte, a bone marrow-derived mesenchymal progenitor, in reactive and reparative fibroses. *Lab Invest* 87, 858-70 (2007).
71. Lee, C.H., Shah, B., Moioli, E.K. & Mao, J.J. CTGF directs fibroblast differentiation from human mesenchymal stem/stromal cells and defines connective tissue healing in a rodent injury model. *J Clin Invest* 120, 3340-9 (2010).

72. Yang, L. et al. Bone marrow-derived mesenchymal stem cells differentiate to hepatic myofibroblasts by transforming growth factor-beta1 via sphingosine kinase/sphingosine 1-phosphate (S1P)/S1P receptor axis. *Am J Pathol* 181, 85-97 (2012).
73. Reich, B. et al. Fibrocytes develop outside the kidney but contribute to renal fibrosis in a mouse model. *Kidney Int* 84, 78-89 (2013).
74. Broekema, M. et al. Bone marrow-derived myofibroblasts contribute to the renal interstitial myofibroblast population and produce procollagen I after ischemia/reperfusion in rats. *J Am Soc Nephrol* 18, 165-75 (2007).
75. Roufosse, C. et al. Bone marrow-derived cells do not contribute significantly to collagen I synthesis in a murine model of renal fibrosis. *J Am Soc Nephrol* 17, 775-82 (2006).
76. Grimm, P.C. et al. Neointimal and tubulointerstitial infiltration by recipient mesenchymal cells in chronic renal-allograft rejection. *N Engl J Med* 345, 93-7 (2001).
77. Rienstra, H. et al. Donor and recipient origin of mesenchymal and endothelial cells in chronic renal allograft remodeling. *Am J Transplant* 9, 463-72 (2009).
78. Lin, S.L., Castano, A.P., Nowlin, B.T., Lupper, M.L., Jr. & Duffield, J.S. Bone marrow Ly6Chigh monocytes are selectively recruited to injured kidney and differentiate into functionally distinct populations. *J Immunol* 183, 6733-43 (2009).
79. Eddy, A.A., Lopez-Guisa, J.M., Okamura, D.M. & Yamaguchi, I. Investigating mechanisms of chronic kidney disease in mouse models. *Pediatr Nephrol* 27, 1233-47 (2012).
80. De Palma, M. et al. Tie2 identifies a hematopoietic lineage of proangiogenic monocytes required for tumor vessel formation and a mesenchymal population of pericyte progenitors. *Cancer Cell* 8, 211-26 (2005).
81. Chang, L. et al. Differentiation of vascular smooth muscle cells from local precursors during embryonic and adult arteriogenesis requires Notch signaling. *Proc Natl Acad Sci U S A* 109, 6993-8 (2012).
82. Eddy, A.A. The origin of scar-forming kidney myofibroblasts. *Nat Med* 19, 964-6 (2013).
83. Zeisberg, M. & Duffield, J.S. Resolved: EMT produces fibroblasts in the kidney. *J Am Soc Nephrol* 21, 1247-53 (2010).
84. Tampe, D. & Zeisberg, M. Potential approaches to reverse or repair renal fibrosis. *Nat Rev Nephrol* 10, 226-37 (2014).
85. Distler, J.H. & Distler, O. Tyrosine kinase inhibitors for the treatment of fibrotic diseases such as systemic sclerosis: towards molecular targeted therapies. *Ann Rheum Dis* 69 Suppl 1, i48-51 (2010).
86. Prakash, J. et al. Novel Therapeutic Targets for the Treatment of Tubulointerstitial Fibrosis. *Current Signal Transduction Therapy* 3, 97-111 (2014).
87. Bansal, R., Prakash, J., De Ruyter, M. & Poelstra, K. Targeted recombinant fusion proteins of IFNgamma and mimetic IFNgamma with PDGFbetaR bicyclic peptide inhibits liver fibrogenesis in vivo. *PLoS One* 9, e89878 (2014).
88. Hagens, W.I. et al. Targeting 15d-prostaglandin J2 to hepatic stellate cells: two options evaluated. *Pharm Res* 24, 566-74 (2007).

89. Christensen, E.I., Birn, H., Storm, T., Weyer, K. & Nielsen, R. Endocytic receptors in the renal proximal tubule. *Physiology (Bethesda)* 27, 223-36 (2012).
90. Prakash, J. et al. Inhibition of renal rho kinase attenuates ischemia/reperfusion-induced injury. *J Am Soc Nephrol* 19, 2086-97 (2008).
91. Shillingford, J.M., Leamon, C.P., Vlahov, I.R. & Weimbs, T. Folate-conjugated rapamycin slows progression of polycystic kidney disease. *J Am Soc Nephrol* 23, 1674-81 (2012).
92. Prakash, J. et al. Intracellular delivery of the p38 mitogen-activated protein kinase inhibitor SB202190 [4-(4-fluorophenyl)-2-(4-hydroxyphenyl)-5-(4-pyridyl)1H-imidazole] in renal tubular cells: a novel strategy to treat renal fibrosis. *J Pharmacol Exp Ther* 319, 8-19 (2006).
93. Lin, Y. et al. Targeted drug delivery to renal proximal tubule epithelial cells mediated by 2-glucosamine. *J Control Release* 167, 148-56 (2013).
94. Wang, X. et al. Effects of mycophenolic acid-glucosamine conjugates on the base of kidney targeted drug delivery. *Int J Pharm* 456, 223-34 (2013).
95. Floege, J., Eitner, F. & Alpers, C.E. A new look at platelet-derived growth factor in renal disease. *J Am Soc Nephrol* 19, 12-23 (2008).
96. Greupink, R. et al. Mannose-6-phosphate/insulin-Like growth factor-II receptors may represent a target for the selective delivery of mycophenolic acid to fibrogenic cells. *Pharm Res* 23, 1827-34 (2006).
97. Moreno, M. et al. Reduction of advanced liver fibrosis by short-term targeted delivery of an angiotensin receptor blocker to hepatic stellate cells in rats. *Hepatology* 51, 942-52 (2010).
98. van Beuge, M.M. et al. Enhanced effectivity of an ALK5-inhibitor after cell-specific delivery to hepatic stellate cells in mice with liver injury. *PLoS One* 8, e56442 (2013).
99. Dolman, M.E., Harmsen, S., Storm, G., Hennink, W.E. & Kok, R.J. Drug targeting to the kidney: Advances in the active targeting of therapeutics to proximal tubular cells. *Adv Drug Deliv Rev* 62, 1344-57 (2010).
100. Leeuwis, J.W., Nguyen, T.Q., Dendooven, A., Kok, R.J. & Goldschmeding, R. Targeting podocyte-associated diseases. *Adv Drug Deliv Rev* 62, 1325-36 (2010).
101. Scindia, Y.M., Deshmukh, U.S. & Bagavant, H. Mesangial pathology in glomerular disease: targets for therapeutic intervention. *Adv Drug Deliv Rev* 62, 1337-43 (2010).
102. Qin, W. et al. TGF-beta/Smad3 signaling promotes renal fibrosis by inhibiting miR-29. *J Am Soc Nephrol* 22, 1462-74 (2011).
103. Trachtman, H. et al. A phase 1, single-dose study of fresolimumab, an anti-TGF-beta antibody, in treatment-resistant primary focal segmental glomerulosclerosis. *Kidney Int* 79, 1236-43 (2011).
104. A Study of Fresolimumab in Patients With Steroid-Resistant Primary Focal Segmental Glomerulosclerosis (FSGS). <http://clinicaltrials.gov/ct2/show/NCT01665391?term=fresolimumab&rank=3> (2014).
105. Adler, S.G. et al. Phase 1 study of anti-CTGF monoclonal antibody in patients with diabetes and microalbuminuria. *Clin J Am Soc Nephrol* 5, 1420-8 (2010).

106. Richeldi, L. et al. Efficacy and safety of nintedanib in idiopathic pulmonary fibrosis. *N Engl J Med* 370, 2071-82 (2014).
107. Liu, N. et al. Genetic or pharmacologic blockade of EGFR inhibits renal fibrosis. *J Am Soc Nephrol* 23, 854-67 (2012).
108. Elmholdt, T.R., Buus, N.H., Ramsing, M. & Olesen, A.B. Antifibrotic effect after low-dose imatinib mesylate treatment in patients with nephrogenic systemic fibrosis: an open-label non-randomized, uncontrolled clinical trial. *J Eur Acad Dermatol Venereol* 27, 779-84 (2013).
109. Illouz, F., Braun, D., Briet, C., Schweizer, U. & Rodien, P. Endocrine side-effects of anti-cancer drugs: thyroid effects of tyrosine kinase inhibitors. *Eur J Endocrinol* 171, R91-9 (2014).
110. Hartmann, J.T., Haap, M., Kopp, H.G. & Lipp, H.P. Tyrosine kinase inhibitors - a review on pharmacology, metabolism and side effects. *Curr Drug Metab* 10, 470-81 (2009).
111. Hong, S. et al. Risk of treatment-related deaths with vascular endothelial growth factor receptor tyrosine kinase inhibitors: a meta-analysis of 41 randomized controlled trials. *Onco Targets Ther* 7, 1851-67 (2014).
112. Casanovas, O., Hicklin, D.J., Bergers, G. & Hanahan, D. Drug resistance by evasion of antiangiogenic targeting of VEGF signaling in late-stage pancreatic islet tumors. *Cancer Cell* 8, 299-309 (2005).
113. Connolly, E.C. et al. Outgrowth of drug-resistant carcinomas expressing markers of tumor aggression after long-term TbetaRI/II kinase inhibition with LY2109761. *Cancer Res* 71, 2339-49 (2011).
114. Dolman, M.E. et al. Imatinib-ULS-lysozyme: a proximal tubular cell-targeted conjugate of imatinib for the treatment of renal diseases. *J Control Release* 157, 461-8 (2012).
115. Prakash, J. et al. Cell-specific delivery of a transforming growth factor-beta type I receptor kinase inhibitor to proximal tubular cells for the treatment of renal fibrosis. *Pharm Res* 25, 2427-39 (2008).
116. Dankers, P.Y. et al. Hierarchical formation of supramolecular transient networks in water: a modular injectable delivery system. *Adv Mater* 24, 2703-9 (2012).
117. Lebleu, V.S., Sugimoto, H., Miller, C.A., Gattone, V.H., 2nd & Kalluri, R. Lymphocytes are dispensable for glomerulonephritis but required for renal interstitial fibrosis in matrix defect-induced Alport renal disease. *Lab Invest* 88, 284-92 (2008).
118. Stokman, G. et al. Epac-Rap signaling reduces oxidative stress in the tubular epithelium. *J Am Soc Nephrol* 25, 1474-85 (2014).
119. Wang, X. et al. Mechanistic studies of a novel mycophenolic Acid-glucosamine conjugate that attenuates renal ischemia/reperfusion injury in rat. *Mol Pharm* 11, 3503-14 (2014).
120. Yuan, Z.X. et al. Randomly 50% N-acetylated low molecular weight chitosan as a novel renal targeting carrier. *J Drug Target* 15, 269-78 (2007).
121. Suzuki, K. et al. Specific renal delivery of sugar-modified low-molecular-weight peptides. *J Pharmacol Exp Ther* 288, 888-97 (1999).
122. Scindia, Y., Deshmukh, U., Thimmalapura, P.R. & Bagavant, H. Anti-alpha8 integrin immunoliposomes in glomeruli of lupus-susceptible mice: a novel system for delivery of

- therapeutic agents to the renal glomerulus in systemic lupus erythematosus. *Arthritis Rheum* 58, 3884-91 (2008).
123. Suana, A.J. et al. Single application of low-dose mycophenolate mofetil-OX7-immunoliposomes ameliorates experimental mesangial proliferative glomerulonephritis. *J Pharmacol Exp Ther* 337, 411-22 (2011).
  124. Asgeirsdottir, S.A. et al. Inhibition of proinflammatory genes in anti-GBM glomerulonephritis by targeted dexamethasone-loaded AbEsel liposomes. *Am J Physiol Renal Physiol* 294, F554-61 (2008).
  125. Hauser, P.V. et al. Novel siRNA delivery system to target podocytes in vivo. *PLoS One* 5, e9463 (2010).

## **Chapter 3**

### **E-selectin targeted immunoliposomes for rapamycin delivery to activated endothelial cells**

Shima Gholizadeh, Ganesh Ram R. Visweswaran, Gert Storm, Wim E. Hennink, Jan. A. A. M. Kamps, Robbert J. Kok, submitted for publication.

**Abstract**

Activated endothelial cells play a pivotal role in the pathology of inflammatory disorders and thus present a target for therapeutic intervention by drugs that intervene in inflammatory signaling cascades, such as rapamycin (mTOR inhibitor). In this study we developed anti-E-selectin immunoliposomes for targeted delivery to E-selectin over-expressing (TNF- $\alpha$  activated) endothelial cells. Liposomes composed of DPPC, Cholesterol, and DSPE-PEG-Mal were loaded with rapamycin via lipid film hydration, after which they were further functionalized by coupling SATA-modified mouse anti human E-selectin antibodies to the distal ends of the maleimidyl (Mal)-PEG groups. In cell binding assays, these immunoliposomes bound specifically to TNF- $\alpha$  activated endothelial cells. Upon internalization, rapamycin loaded immunoliposomes inhibited proliferation and migration of endothelial cells, as well as expression of inflammatory mediators. Our findings demonstrate that rapamycin-loaded immunoliposomes can specifically inhibit inflammatory responses in inflamed endothelial cells. Therefore, the use of immunoliposomes for targeted delivery is expected to improve the therapeutic efficacy/safety profile of this class of drugs.



## 1. Introduction

The mammalian target of the drug rapamycin is a 289-kDa serine/threonine kinase, typically known as mTOR. This mTOR kinase is a component of two different cellular signaling regulating complexes, known as mTOR complex 1 and 2 (mTORc1 and mTORc2) [1-4]. The aforementioned proteins interact with specific downstream targets that are responsible for the interconnection of mTOR to different downstream signaling pathways such as Akt, SGK1 and 4E-BP1 that are involved in a variety of cellular processes such as cell survival, proliferation and cytoskeletal organization. Recent studies have highlighted the pivotal role of the mTOR pathways in inflammatory disorders [5-8]. Also, a significant effect of mTOR on the progression of chronic kidney disease (CKD) has recently been suggested in several pre-clinical studies [9, 10]. Other pre-clinical studies using animal models (e.g. rat models of CKD) have shown that the inhibition of mTOR signaling pathways by rapamycin resulted in a significant reduction of the influx of inflammatory cell into the diseased area [11, 12]. The inhibition of mTOR signaling pathways by rapamycin was also shown to significantly reduce the release of pro-inflammatory and pro-fibrotic cytokines, as well as fibrotic tissue formation, thus improving overall kidney function [11, 12].

Rapamycin is a macrolide compound with hydrophobic characteristics (Log P: 4.3) [13] resulting in poor water solubility, slow dissolution rate and consequential low oral bioavailability [13, 14]. Nanocarrier formulations can overcome the problems associated with the poor biopharmaceutical characteristics of rapamycin, and thus can contribute to an improved safety and efficacy profile [15-17]. Several rapamycin formulations have been reported in literature, based on various types of nanocarrier systems such as polymeric blend nanoparticles composed of the diblock copolymer polyethylene glycol–poly-L-lactic acid (mPEG–PLA) mixed with acid terminated PLA [15]; micelles composed of mixed diblock copolymers mPEG-b-P(HPMA-Lac-co-His) and mPEG-b-PLA [16]; and liposomes composed of soy phosphatidylcholine (SPC), cholesterol (Chol) and 1,2-distearoyl-sn-glycero-3-phosphoethanolamine-*N*-[amino(polyethyleneglycol)-2000] (DSPE-PEG) [18].

While many of the current anti-inflammatory therapeutic approaches are focused on attempts to suppress the activity of immune effector cells, recently there has been a growing interest toward understanding the role of endothelial cells in leukocyte recruitment into inflamed tissues [19, 20]. Endothelial cells are in direct contact with the blood which makes these cells attractive targets for nanocarrier delivery strategies. Selective delivery to inflamed endothelial cells is possible by targeting adhesion molecules (e.g. E-selectin, P-selectin, intercellular adhesion molecule (ICAM) and vascular cell adhesion molecule-1 (VCAM-1)) on their surface. Adhesion molecules are selectively (over)expressed in the presence of inflammatory stimulants such as interleukin-1 (IL-1), lipopolysaccharides (LPS) and tumor necrosis factor- $\alpha$  (TNF- $\alpha$ ) [21].

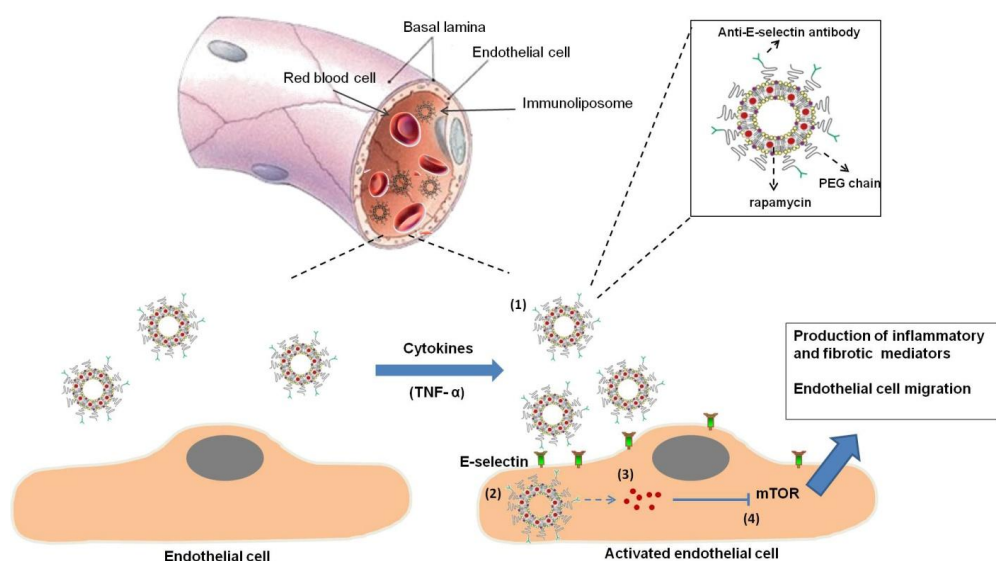


**Figure 1.** Concept of targeted delivery of rapamycin to TNF- $\alpha$  activated (i.e. inflamed) endothelial cells. **(1)** Schematic representation of E-selectin targeting liposomes loaded with rapamycin. **(2)** Interaction of immunoliposomes with E-selectin adhesion molecules expressed on the cell surface. **(3)** Active uptake and intercellular delivery /cytosolic release of rapamycin molecules from liposomes. **(4)** Inhibiting effect of rapamycin on activated mTOR pathway. Adapted with permission from ref [23]. Copyright 2012, Pearson education Inc.

Proper cell selective delivery of potent anti-inflammatory agents may provide an important tool to both increase the efficacy and reduce the side effects of such therapeutic compound (i.e. rapamycin) in the treatment of inflammatory disorders [22].

In this study, we have developed anti-E-selectin antibody (Ab) coupled immunoliposomes, loaded with rapamycin, for targeted delivery to TNF- $\alpha$  activated endothelial cells (Figure 1). This work discusses the characterization and formulation of the immunoliposomes, while their cell binding and uptake properties by TNF- $\alpha$  activated endothelial cells are also investigated. To evaluate the pharmacologic effects of the rapamycin containing immunoliposomes, cell proliferation and motility, phosphorylation of mTOR kinases, and inflammatory gene expression levels were analyzed.

## 2. Materials and methods

### 2.1 Materials

1,2-Distearoyl-*sn*-glycero-3-phosphoethanolamine-N-[methoxy(polyethyleneglycol)-2000]-maleimide (Mal-PEG<sub>2000</sub>-DSPE), 1,2-dipalmitoyl-*sn*-glycero-3-phosphocholine (DPPC) and 1,2-dimyristoyl-*sn*-glycero-3-phosphoethanolamine-N-(lissamine rhodamine B sulfonyl) (Rho-PE) were obtained from Avanti Polar Lipids (Alabaster AL, USA). Cholesterol (Chol) and N-succinimidyl-S-acetylthioacetate (SATA) were purchased from Sigma-Aldrich (St. Louis MO, USA). Rapamycin (Sirolimus) was purchased from LC laboratories. 4',6-Diamidino-2-phenylindole (DAPI) was obtained from Roche (Woerden, The Netherlands) and paraformaldehyde from Fluka (Zwijndrecht, The Netherlands). All chemicals used were of analytical grade unless otherwise stated.

### 2.2 Preparation of Rapamycin loaded, E-selectin targeted and non-targeted liposomes

Liposomes were prepared from a mixture of DPPC, Cholesterol and Mal-PEG<sub>2000</sub>-DSPE in the respective molar ratio of 65: 25: 10 which equals to respective amounts of 43, 9 and 27 mg in 3 ml of chloroform: methanol (9:1, v/v) to a final concentration of 30 mM total lipid (TL). Fluorescently

labeled liposomes were prepared by adding Rhodamine-PE to the lipid mixture at 0.2 mol% of total lipid. Rapamycin was dissolved with the lipid mixture at a concentration of 20 nmol/ $\mu$ mol TL, which is equivalent to 1.7 mg rapamycin. Organic solvents were removed using a rotary evaporator and subsequent drying under a nitrogen flow. The resulting drug-lipid film was hydrated by adding 3 ml of HBS buffer pH 7.4 (10 mM Hepes containing 135 mM NaCl), followed by sonication in an ice-bath using a tip sonicator (Bandelin Sonopuls) for 10 min and incubation for 1 h at room temperature. Unilamellar liposomes were prepared by multiple extrusion steps using a Lipex<sup>TM</sup> Extruder (Northern Lipids, Burnaby, BC, Canada) over polycarbonate membranes (Nuclepore, Pleasanton, CA, USA) at different pore size range (from 0.4  $\mu$ m to 0.1  $\mu$ m). Mouse anti-human E-selectin (IgG2a) was purified from supernatant produced by hybridoma H18/7 kindly provided by Dr. M. Gimbrone Jr. (Harvard Medical School, Boston, MA,) and modified with S-acetylthioacetyl (SATA) (8:1 SATA:Ab mol:mol ratio) as described before [24]. SATA-modified anti-human E-selectin antibody (2 mg/ml in HBS buffer) was treated with hydroxylamine 0.5 M for 45 min to deprotect the thioacetyl groups and subsequently reacted to the maleimidyl groups on the liposomes at 15  $\mu$ g/ $\mu$ mol TL as described before [24]. Non-reacted antibody and non-encapsulated rapamycin were removed by passing liposomes over a PD10 desalting column (GE Healthcare Life Sciences<sup>TM</sup>) followed by ultrafiltration using Vivaspin centrifugal concentrators (Sartorius AG, Aubagne, France) with a molecular weight cut-off membrane of 300-kDa.

### 2.3 Characterization of liposomes

Liposome sizes and polydispersities were measured using dynamic light scattering (DLS) on an ALV CGS-3 system (Malvern Instruments, Malvern, UK). Zeta- $\zeta$  potential of liposomes was measured using a Malvern Zetasizer Nano-Z (Malvern Instruments, Malvern, UK) with universal ZEN 1002 dip cells and DTS (Nano) software. Rapamycin content of the liposomes was determined in 100  $\mu$ l aliquots which were disrupted by diluting in 300  $\mu$ l of acetonitrile. Rapamycin content was determined by high performance liquid chromatography on a Waters Acquity HPLC system (Waters

Corporation, Milford, MA, USA) equipped with a Sunfire C18 column (5  $\mu\text{m}$  bead size; 4.6 x 150mm) thermostated at 60°C and a UV detector operated at 290 nm. The isocratic mobile phase (1 ml/min) was composed of 70% acetonitrile and 30% water. The total lipid concentration was determined according to Rouser *et al* [25]. Conjugation of Ab to the surface of liposomes was confirmed with dot blot assay, using HRP conjugated Goat-anti-Mouse IgG (H+L) Secondary Antibody (Thermo Fischer Scientific). Liposomes were further characterized by determining the concentration of surface coupled Ab, using mouse IgG (Sigma Aldrich) as a standard via Micro-BCA assay (Pierce Biotechnology, Rockford, IL, USA).

The number of antibody molecules coupled per liposome ( $p$ ) was calculated by geometric arguments according to formula (1) below, as described previously by Adrian and co-workers [26].

$$p = \pi/6 \times C_{Ab} \times (3d_{bl} \times R^2 - 3R \times d_{bl}^2 + d_{bl}^3) \times M_{Ab}^{-1} \times V_{Ls}^{-1} \quad (1)$$

In which ( $C_{Ab}$ ) is measured concentration of antibody (gram per mol of lipid), ( $R$ ) is the average diameter (nanometers) of the spherical liposomes, ( $V_{Ls}$ ) and ( $d_{bl}$ ) represent specific lipid volume and lipid bilayer thickness, respectively, and ( $M_{Ab}$ ) is the molecular mass of the antibody.

## 2.4 Cell lines and culture conditions

Human umbilical vein endothelial cells (HUVEC cells) were obtained from Lonza (Breda, The Netherlands). Cells were grown in endothelial cell growth medium-2 (EGM-2) (Lonza, Breda, The Netherlands), consisting of endothelial basal medium-2 (EBM-2) supplemented with growth factors and antibiotics (EGM-2 SingleQuots kit, Lonza). The cells were kept in culture at 37 °C in a humidified atmosphere containing 5% CO<sub>2</sub>/95% air. Experiments were performed with cells of passage 3-7.

## 2.5 Binding and uptake of fluorescent labeled liposomes

Binding of liposomes was studied by incubating TNF-activated endothelial cells with rhodamine-labeled liposomes at 4°C. HUVEC cells were seeded at 8000 cells/well in 6-well chamber slides (Lab-Tek® supplier). After 24 h, the cells were activated with TNF- $\alpha$  (recombinant human tumor necrosis

factor- $\alpha$ ; Boehringer, Mannheim, Germany), at concentration of 10 ng/ml for 4 h at 37°C and subsequently incubated with rhodamine labeled liposomes at 4°C (0.5 mM TL; 1 h at 4 °C). Cells were washed with PBS and fixed with 4% paraformaldehyde in PBS. Nuclei were stained with DAPI (1  $\mu$ g/ml; 5 min at room temperature) and washed again with PBS. Slides were mounted on glass cover slide using fluorSave (Calbiochem, San Diego, CA, USA) and analyzed for binding of labeled liposomes with a Keyence microscope (BZ-9000 BioRevo, Keyence®).

Uptake of Rhodamine labeled liposomes by TNF-activated endothelial cells was determined by flow cytometry. HUVEC cells were added at concentration of 10,000 cells/well in U-bottom shaped 96-well plates (Becton & Dickinson, Mountain View, CA, USA), activated with TNF $\alpha$  (10 ng/ml; 4 h at 37°C) and subsequent incubated with rhodamine labeled liposomes in a concentration range of 0.02 – 3  $\mu$ M TL in EGM-2 cell culture medium for 3 h at 37 °C in the dark. After removal of culture medium and excess of liposomes the cells were washed three times with cold PBS containing 0.3% BSA. Cells were collected by centrifugation for 5 min at 500 g at 20°C and washed with an acidic buffer (200 mM glycine containing 150 mM NaCl, pH 3.0) to remove cell surface bound liposomes. Next, cells were fixed with 10% formalin solution. Uptake of Rhodamine labeled liposomes by the cells was quantified via flow cytometry with BD FACSCanto (Becton & Dickinson). Per sample 10,000 events were collected and the samples were prepared in triplicate. Data were analyzed with BD FACSDiva™ software (Becton & Dickinson) and expressed as mean fluorescence intensity.

## **2.6 Effects of rapamycin loaded liposomes on cultured cells**

### **2.6.1 Effect of rapamycin on cell viability**

The cell viability upon incubation with rapamycin at different concentrations was evaluated via MTS assay, which measures the mitochondrial (metabolic) activity of the cells. HUVEC cells were seeded into 96-well plates: 8000 cells were seeded per well. After 24 h of seeding the medium was refreshed with fresh medium containing TNF- $\alpha$  (10 ng/ml), and 50  $\mu$ l of rapamycin dilutions in medium prepared from a stock solution of rapamycin in DMSO was added to the cells,

corresponding to a final concentration of 2.5-50  $\mu$ M. After 48 h of incubation, MTS assay (Promega, Leiden, The Netherlands) was performed according to manufacturer's protocol.

### 2.6.2 Effect of rapamycin liposomes on migration of endothelial cells

HUVEC cells were seeded in 6 well plates at a density of 80,000 cells per well. After overnight adherence of the cells to the well plates in full EGM-2 medium, cells were activated with TNF- $\alpha$  (10 ng/ml; 4 h at 37°C), followed by treatment with either free rapamycin or different liposomal formulations equivalent to 10  $\mu$ M rapamycin. After 12 h, a scratch wound was made in the cell monolayer with a p20 pipet tip. Cells and dimensions of the scratch wound were imaged and recorded at 20x magnification with a Nikon TE2000 microscope. Cells were washed once with PBS and incubated for an additional 16 h with fresh medium before imaging of the scratch wound areas. Scratch wound surface area was analyzed using NIH ImageJ software, and expressed relative to the initial scratch wound area.

### 2.6.3 Effect of rapamycin liposomes on proliferation of endothelial cells

The effect of rapamycin and liposomes containing rapamycin on endothelial cell proliferation was analyzed in two different experimental setups, using either short-term exposure followed by a recovery period or long-term continuous exposure. In detail, HUVEC cells were seeded at a density of 5000 cells/well in 96-well plates. After overnight adherence to the plates, cells were activated with TNF- $\alpha$  as described above (10 ng/ml for 4 h at 37°C) after which the medium was replaced by fresh culture medium containing either free rapamycin or liposomal rapamycin in a concentration range of 25 nM - 40  $\mu$ M. For short term exposure, the medium was refreshed with drug-free medium after 4 h followed by an additional 44 h incubation period, while long-term exposure involved one continuous 48 h period of incubation with drug-containing medium. Next, culture media were replaced by drug-free medium containing BrdU reagent (Roche Applied Science, Penzberg, Germany), after which cells were cultured for an extra 24 h (in total 72 h). Cell proliferation was assayed by BrdU-colorimetric immunoassay according to the supplier's protocol. A

standard curve was created in order to convert sample optical density (OD) values into proliferating cell numbers per well. Sequential dilutions of cells were prepared from a stock solution to obtain a calibration curve for the response of various concentrations of cells (781, 1563, 3125, 6250 and 125000 cells per well), as a double linear plot of absorbance values (OD) against proliferating cell number. Cells were seeded and cultured for 24 h. Cells were incubated with BrdU reagent for an extra 24 h and incorporation of BrdU was detected with a BrdU cell proliferation ELISA kit. The total number of cells required to construct the curve in triplicate was  $2.4 \times 10^6$ , which is a quantity that can be harvested from a 70% confluent T175 flask (175 cm<sup>2</sup>).

#### **2.6.4 Effect of rapamycin liposomes on mRNA expression and intracellular signaling**

The effect of rapamycin liposomes on inflammatory signaling was investigated by Q-PCR mRNA expression analysis. HUVEC cells were seeded in 12 well plates at 50,000 cells per well and allowed to adhere overnight before activation with TNF- $\alpha$  for 4 h at 37°C, followed by incubation for 24 h at 37°C with medium containing either 10  $\mu$ M rapamycin or its equivalent in liposomal rapamycin. RNA was isolated using RNeasy® Mini Plus Kits (Qiagen, Venlo, the Netherlands) according to the manufacturer's protocol. The concentration of RNA was determined by both NanoDrop® ND-1000 spectrophotometer (Wilmington, DE) and by agarose (1%) gel electrophoresis. Complementary DNA (cDNA) to respective RNA samples was generated by a 20  $\mu$ l mixture containing SuperScript™ III RNaseH-Reverse Transcriptase (Invitrogen, supplied by Life Technologies, Bleiswijk, the Netherlands), RNaseOut inhibitor (40 U) (Invitrogen) and 250 ng random hexamers (Promega, Leiden, the Netherlands). cDNA solutions were diluted to 10 ng/ml with MilliQ, and 1  $\mu$ l was used for each PCR reaction.

Human GAPDH (Hs99999905\_m1), E-selectin (Hs00174057\_m1), VCAM-1(Hs00365486\_m1), VEGF-A (Hs00173626\_m1), hTIE2 (Hs00176096\_m1), TGF-b (Hs00171257\_m1) and mTOR (Hs01042424\_m1) primer probes were purchased as Assay-on-Demand from Applied Biosystems (Nieuwerkerk a/d IJssel, the Netherlands). These primer probes together with Absolute QPCR Rox



Mix (Thermo Fischer Scientific) were used for real-time PCR analysis performed on an ABI PRISM 7900HT Sequence Detector (Applied Biosystems). The mean of obtained threshold cycle values ( $C_t$ ) were analyzed by the comparative  $C_t$  method. The respective genes were normalized to human GAPDH, resulting in  $\Delta C_t$  values. Average  $\Delta C_t$  values of non-activated cells were deducted from the values of the TNF- $\alpha$ -activated cells and the relative mRNA levels were calculated by  $2^{-\Delta C_t}$  for the respective genes. Experiments were performed in duplicate with two independently prepared formulations (each time samples were analyzed in duplo).

Effects of rapamycin on signaling events downstream from mTOR were also investigated by anti-phospho-Western blotting. For phospho-Western blotting, HUVEC cells were seeded at 100,000 cells per well in 6-well plates and allowed to adhere overnight before activation with TNF- $\alpha$  for 4 h at 37°C and incubation with free rapamycin or liposomal rapamycin formulations at concentration of 10  $\mu$ M rapamycin for another 4 h at 37°C. Finally, cells were stimulated by addition of 0.5% insulin for 10 min. Insulin is a known stimulator of the mTOR signaling cascade and activation of the insulin receptor results in phosphorylation of both mTOR (at Ser 2448) and S6-ribosomal protein (at Ser 235/236) kinases [27]. After washing with cold PBS, the cells were lysed in radioimmunoprecipitation assay (RIPA) buffer, containing phosphatase/kinase inhibitor cocktail (Thermo Fischer Scientific), (120  $\mu$ l/well), on ice for 30 min and centrifuged at 14,000 g at 4°C for 15 min. The obtained supernatants were stored at -20°C until further evaluation. The protein concentration of the samples was determined by micro-BCA assay. Aliquots corresponding to 15  $\mu$ g of the protein cell lysate were subjected to SDS-PAGE on 4-12% gradient NuPAGE Novex Bis-Tris mini-gels and electro-transferred onto nitrocellulose membranes via an iBlot Dry Blotting system. Membranes were blocked with 5% BSA in Tris-buffered saline containing 0.1% Tween-20 (TBS-T) for 2 h at room temperature, followed by staining overnight at 4°C for phospho-mTOR (Ser 2448) and phospho-S6 ribosomal protein (Ser235/236) using rabbit polyclonal antibodies (Cell Signaling Technology, Inc.).  $\beta$ -Actin (Cell Signaling Technology, Inc.) was stained as control. Antibodies were diluted 1:1000 in 5% BSA in TBS-T according to the manufacturer's protocol. After three times washing with TBS-T, membranes were

incubated for 1 h at room temperature with goat anti-rabbit peroxidase-conjugated secondary antibody diluted 1:1000 in 5% BSA in TBS-T. Proteins were detected using supersignal west femto chemiluminescent substrate (Thermo Fischer Scientific) and visualized using a Gel Doc imaging system equipped with a XRS camera and Quantity one analysis software (Bio-Rad, Hercules, CA, USA). Densitometric analysis was done using NIH Image J software. Phosphorylation intensity of mTOR and S6 protein of cells exposed to different formulations were normalized versus insulin activated control cells. Experiments were performed in duplicate with two independently prepared formulations.

## 2.7 Statistical analysis

For the cell-based (*in vitro*) experiments, statistical analysis of the data was performed using Graphpad Prism software (Graphpad software 5.0, San Diego CA, USA), using analysis of variance (ANOVA). Values for the experiments are represented  $\pm$  SEM, unless stated otherwise. Differences were considered to be significant at values of  $P < 0.05$ .

## 3. Results and discussions

### 3.1 Preparation and characterization of rapamycin loaded immunoliposomes

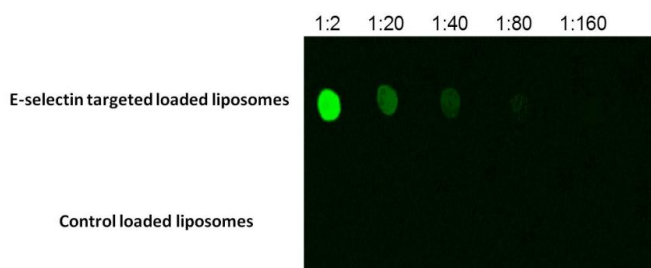
PEGylated (immuno)-liposomes loaded with rapamycin were prepared by lipid film hydration and extrusion. Mouse monoclonal anti-human-E-selectin antibodies were conjugated to the maleimidyl-PEG-DSPE anchor after the extrusion steps. The physicochemical properties of the different types of liposomes are given in Table 1. The average liposome size defined by DLS method was 125 nm with a polydispersity index of 0.1. It has been reported that under certain conditions micelles could be an unwanted byproduct in the formulation of liposomes with high-PEG content [28]. In this work the volume-weighted Gaussian distribution (not shown) derived from the DLS analysis showed no micelle formation under the liposomal preparation conditions applied in this work [29]. The prepared liposomes showed a negative zeta-potential of -15 mV, most likely due to the localized negative charges on the phospholipid head groups within the liposomal bilayer [30].

**Table 1.** Physicochemical properties of liposomal formulations used in this study

Samples	size (nm)	PDI <sup>a</sup>	Zeta potential (mV)	Total lipid recovery (%)	Rapamycin (mg/ml)	Drug/TL <sup>b</sup> (Mol%)	EE <sup>c</sup> (%)	Ab/ Lipo <sup>d</sup>
Control liposomes (drug free)	120 ± 9	0.07 ± 0.03	-12.6 ± 3.2	85 ± 2	n/a <sup>e</sup>	n/a	n/a	n/a
Control liposomes (rapamycin loaded)	122 ± 2	0.05 ± 0.02	-11.1 ± 5.0	88 ± 3	0.44 ± 0.01	1.85 ± 0.01	80 ± 3	n/a
Rhodamine-labeled control liposomes (drug free)	125 ± 4	0.09 ± 0.08	-17.3 ± 2.0	90 ± 3	n/a	n/a	n/a	n/a
E-selectin targeted loaded liposomes (rapamycin loaded)	134 ± 5	0.13 ± 0.06	-14.1 ± 6.2	86 ± 4	0.45 ± 0.01	1.96 ± 0.04	82 ± 1	6 <sup>f</sup>
Rhodamine-labeled E-selectin targeted liposomes (drug free)	138 ± 2	0.15 ± 0.07	-15.1 ± 0.9	89 ± 1	n/a	n/a	n/a	6

Data are presented as mean values ± SD of 2-3 preparations. <sup>a</sup> Polydispersity index. <sup>b</sup> Drug/TL mole % determined after liposomal disruption. (The initial Drug/TL mole % prior to liposomal formulation was calculated to be 2). <sup>c</sup> Encapsulation efficiency = (rapamycin loaded in lipid bilayer)/(rapamycin added). <sup>d</sup> Number of attached antibody molecules per liposome. <sup>e</sup> Not applicable. <sup>f</sup> The lipid bilayer thickness is corrected for loaded rapamycin, see main text for details.

Based on HPLC analysis of destructed liposomes, rapamycin encapsulation efficiency of the liposomes was determined to be approximately 80%, resulting in a formulation with a rapamycin concentration of 0.45 mg/ml. Dot blot analysis of the liposomes clearly showed the presence of antibody on the surface of targeted liposomes (Figure 2).

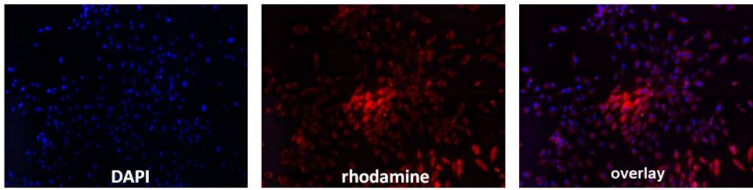
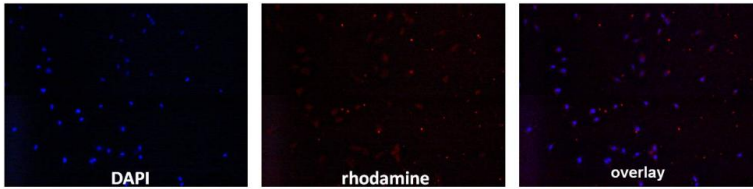
**Figure 2.** Dot Blot analysis on liposomal formulations (E-selectin targeted liposomes and control liposomes) at different dilution ranges.

From the micro BCA assay the coupling efficiency of the anti-E-selectin to the liposomes was determined to be  $77 \pm 3\%$  (SD, n=2), corresponding to  $13.4 \pm 0.14$  (SD, n=2)  $\mu\text{g}$  of anti E-selectin Ab per  $\mu\text{mol}$  of total lipid. Combining formula (1) given in section specific lipid volume ( $V_{LS}$ ) of 1.25

$\text{nm}^3$  and liposome bilayer thickness ( $d_{bl}$ ) of 3.7 nm [31], plus the molecular weight of anti E-selectin Ab (approximately 150 kDa), results in a calculated average of 5.6 Ab molecules coupled per liposome (i.e. 6 Ab molecules/liposome). However, intercalation of the loaded hydrophobic drug compound (i.e. rapamycin) into the hydrocarbon chain region in the lipid bilayer could lead to variations in bilayer thickness, due to changes in the molecular conformation of the intercalated (drug) compound [32]. This effect has previously been reported to result in a 10% increase in liposome bilayer thickness ( $d_{bl}$ ) of DPPC domains loaded with the drug Atorvastatin [33]. Assuming a similar increase in liposome bilayer thickness ( $d_{bl}$ ), formula (1) described above (section 2.3) yields a calculated average of 5.9 Ab molecules, or 6 Ab molecules per liposome, regardless. 2.3 with the literature values for

### 3.2 Cellular handling of E-selectin targeted liposomes by activated endothelial cells

The ability of anti-E-selectin targeted liposomes in binding and uptake by TNF- $\alpha$ -activated endothelial cells was studied by fluorescent microscopy and flow cytometry measurements, respectively. The interaction of immunoliposomes with activated HUVEC cells was visualized by means of fluorescent microscopy (Figure 3). Anti-E-selectin immunoliposomes were effectively internalized by the activated endothelial cells, while control liposomes showed significantly less internalization (Figure 4).

**A:** rhodamine labeled E-selectin targeted liposomes**B:** rhodamine labeled control liposomes

**Figure 3.** Wide-field fluorescence microscopy pictures of TNF- $\alpha$  activated HUVEC cells incubated (4 h) with rhodamine labeled liposomes. **(A):** rhodamine labeled E-selectin targeted liposomes; **(B):** rhodamine labeled control liposomes. Objective lens magnification of 20x. Rhodamine is depicted as red, DAPI (nuclear staining) as blue.

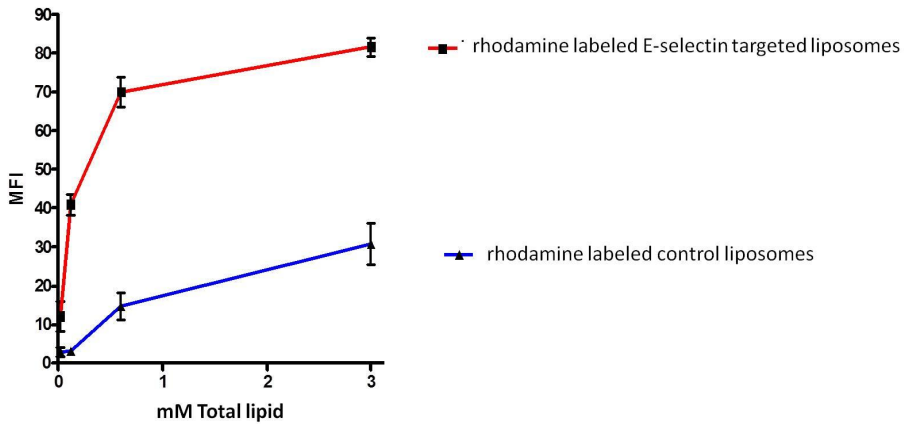


**Figure 4.** Internalization of E-selectin targeted liposomes by activated endothelial cells. Mean Fluorescence Intensity (MFI) of cells incubated with rhodamine labeled E-selectin targeted liposomes (■) and rhodamine labeled control liposomes (▲) after 3 h incubation at 37 °C. Cells were treated with an acid wash (pH: 3.0) after incubations to remove surface bound liposomes. Data are presented as mean  $\pm$  SEM of three experiments using the same formulation.

### 3.3 Pharmacological activity of rapamycin loaded liposomes

#### 3.3.1 Cell viability assessment

TNF- $\alpha$  activated HUVEC cells treated with different concentrations of rapamycin for 48 h did not show reduced viability at concentrations of rapamycin up to 25  $\mu$ M. A sharp decrease in cell viability was found at a rapamycin concentration of 50  $\mu$ M (Figure 5). Combining this data with results from previous studies [34, 35], 10  $\mu$ M rapamycin was chosen as a non-toxic concentration at which anti-inflammatory and other pharmacological effects of targeted liposomal rapamycin formulations can be evaluated.

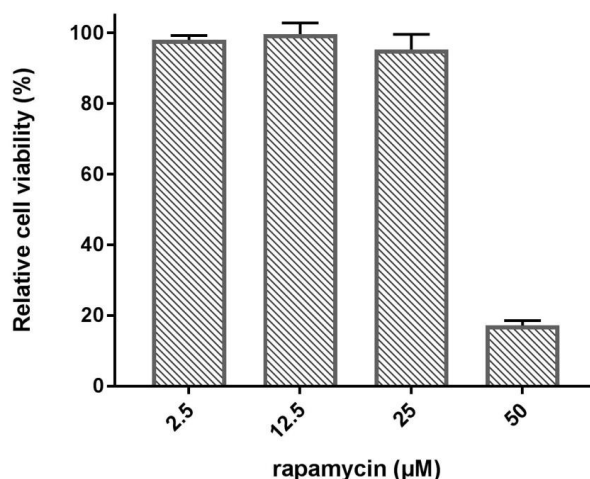


**Figure 5.** MTS cell viability assay on TNF- $\alpha$  activated HUVEC cells. Cells were exposed to solutions containing different concentrations of rapamycin for 48 h. Data are normalized compared to control (non-treated) cells. Results are presented as mean  $\pm$  SEM of three experiments.

#### 3.3.2 Effects of rapamycin liposomes in scratch wound assay

The mTOR signaling cascade controls a wide range of cellular responses, including cell migration [36]. To investigate the pharmacological activity of rapamycin-loaded liposomal formulations the migration of endothelial cells was studied in a scratch wound assay.

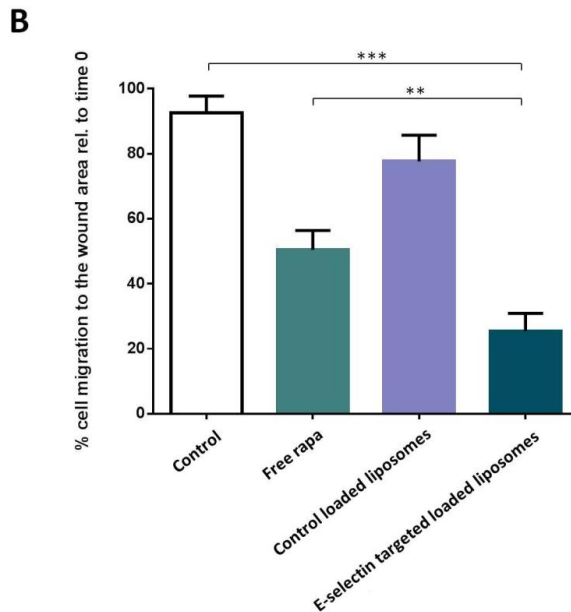
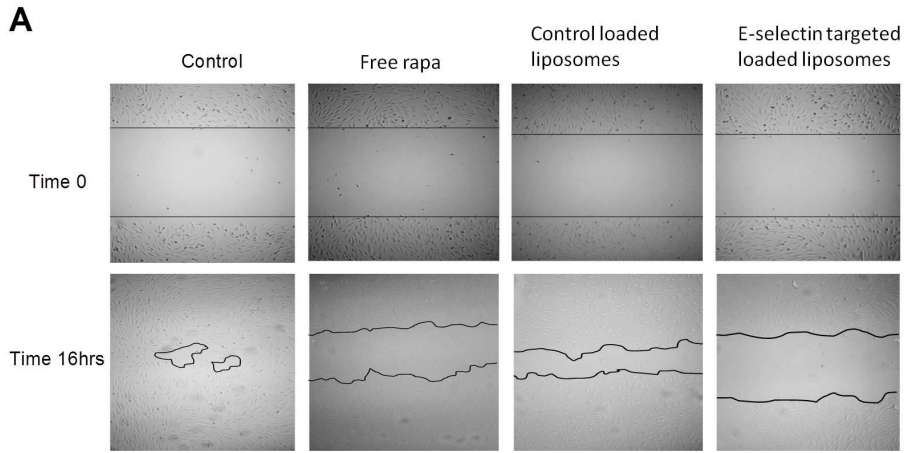


**Figure 6.** Effect of rapamycin loaded liposomes on migration of TNF- $\alpha$  activated endothelial cells. Repopulation of endothelial cells in a scratch wound was investigated with TNF- $\alpha$  activated HUVEC cells that had been pre-incubated with rapamycin formulations at 10  $\mu$ M for 12 h. **(A):** Images were taken right after the wound scratch (T=0) and 16 h after scratching (T=16). Wound closure was quantified by analysis of the scratch wound area with Imaj software. **(B):** Semi-quantitative analysis of closure of the scratch wound area, as calculated from the images taken at t=0 h and t=16 h. Data are plotted as mean values  $\pm$  SEM of three experiments with the same formulations; \*\*p<0.01, \*\*\*p<0.001 compared to free rapamycin and control.

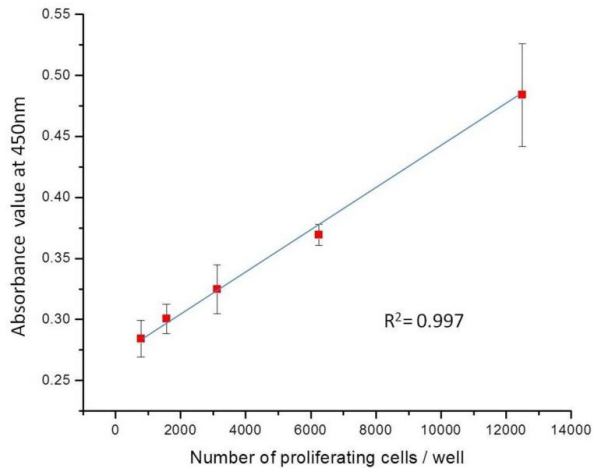
Semi-quantitative analysis of the scratch wound area revealed that TNF-treated endothelial cells (control) repopulated the cell-free area for more than 90% in 16 h. Treatment with free rapamycin reduced the closure of the scratch area to 50% in 16 h (Figure 6 A and B). Non-targeted liposomes showed a slight reduction of the scratch wound area closure compared to the control, which was most likely caused by unspecific uptake of the liposomes by the cells within the set exposure time (Figure 6). Importantly, E-selectin targeted liposomes loaded with rapamycin showed significantly enhanced inhibition of cell migration, with a reduction of up to 60% compared to untreated endothelial cells. One way to explain the mechanisms behind the inhibition of cell migration and cell motility induced by cytokines such as TNF- $\alpha$  is that inhibition of mTOR also blocks the action of vascular endothelial cell growth factor A (VEGF), which is a critical regulator of angiogenesis and endothelial cell migration through both inhibition of VEGF synthesis and its signal transduction [37, 38]. Another way to explain the phenomena is that rapamycin has an inhibitory effect on mTORc1 by preventing the interaction of mTOR with the raptor protein scaffold [39].

### 3.3.3. Effects of rapamycin formulations on proliferation of activated endothelial cells

Both endothelial migration and proliferation can contribute to closure of the scratch wounds, as discussed in the previous paragraph. Although we studied the scratch wound healing at incubation times shorter than the doubling time of HUVEC cells (approximately 48 h) (ACEA Biosciences Inc.) overnight repopulation of the scratch wound area cannot be fully attributed to endothelial cell migration only. We therefore studied the potential inhibitory effects on endothelial cell proliferation in two different setups, using either prolonged exposure for a period of 48 h or short-term exposure for 4 h followed by a 44 h recovery (i.e. treatment-free) period. The latter experimental conditions mimic *in vivo* drug exposure, in which drug peak levels are alternated with drug-free periods. To investigate the correlation between absorption value (BrdU incorporation) and number of proliferating cells, a calibration curve was made out of serial dilutions of HUVEC cells per well. In this way, the absolute absorbance values obtained for control cells and each of the treatments could be



converted to the number of proliferating cells per well (Figure 7A). In the short term exposure study (Figure 7B) neither free rapamycin, nor the control loaded liposomal formulation of rapamycin significantly affected endothelial cell proliferation in the studied dose range. Only the highest concentration of E-selectin loaded targeted liposomes (25  $\mu\text{M}$ ) showed slight reduction ( $\sim 10\%$ ) in endothelial cell proliferation from average 5722 cells/well (control) down to 5081 (cells/well). After long-term exposure of 48 h (Figure 7C), both free rapamycin and E-selectin targeted liposomes loaded with rapamycin inhibited endothelial cell proliferation, while control loaded liposomes showed less anti-proliferative activity. The contribution of E-selectin directed uptake of rapamycin loaded liposomes was most prominently observed at 1 and 5  $\mu\text{M}$  concentrations, which highlights the added value of targeted liposomes for intracellular delivery of rapamycin. At high concentrations of rapamycin (25  $\mu\text{M}$ ), passive uptake of free rapamycin and receptor-mediated uptake of rapamycin loaded immunoliposomes resulted in similar effects of the delivered drug within the target cells, which can be attributed to saturation of the E-selectin uptake pathway and to overall saturation of the mTOR inhibition by rapamycin under those conditions.

**A**

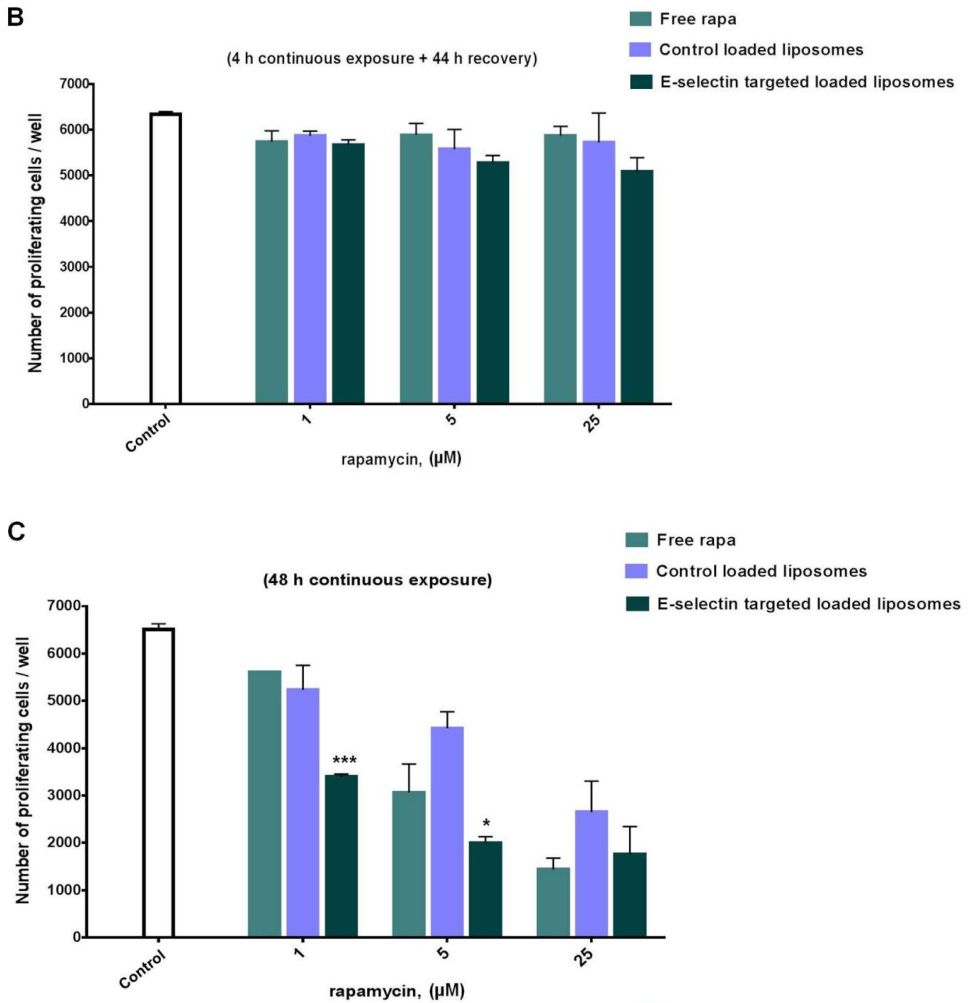


**Figure 7.** Cell proliferation was determined in TNF- $\alpha$  activated HUVEC cells by BrdU-incorporation after 48 h of total incubation period. **(A):** Effect of proliferating cell number on absorbance at 450 nm, measured using BrdU incorporation assay. **(B):** Cells were exposed for 4 h to rapamycin formulations followed by recovery period of 44 h in fresh medium. **(C):** Cells were exposed for 48 h to rapamycin formulations continuously. Data are plotted as mean values  $\pm$  SEM of three experiments with the same formulations; \* $p < 0.05$ , \*\*\* $p < 0.001$  compared to free rapa treatment.

The results obtained from this experiment correlate well with the previously discussed inhibiting effect of rapamycin on cell migration and motility. It can be concluded that within the 16 h time frame at concentration of 10  $\mu\text{M}$ , the rapamycin inhibiting effect on the repopulation of the scratch

wound area is not entirely due to its effect on cell motility and migration, but can also be attributed to its anti-proliferative effect.

#### 3.3.4. Effects of rapamycin liposomes on gene expression

Real time q-PCR analysis was used to examine whether rapamycin and its liposomal formulations affect mRNA expression of proteins related to inflammation under TNF- $\alpha$  activated and/or non-activated conditions. In total 6 genes were studied, including: inflammation induced adhesion molecules (VCAM-1 and E-selectin); angiogenesis mediators (TIE2 receptor and VEGF); fibrosis cytokine (TGF- $\beta$ ) and mTOR itself. The results of the gene expression assays are shown in Figure 8.

First, the effect of TNF- $\alpha$  on the gene expression of the selected genes was evaluated. The activated cells showed a strong (>100 fold) increase in gene expression of both VCAM-1 and E-selectin (Figure 8A and B). Expression of adhesion molecules, especially E-selectin, plays a main role in this study as specific binding of the immunoliposomes to E-selectin mediates liposome uptake. The cell binding assays discussed in section 3.2 (see also Figure 3) showed that E-selectin expression is already elevated at t=4 h (i.e. the time point for adding the liposomal formulations to the cells). The results on the gene expression of adhesion molecules shown in Figure 8 indicate that their expression is enhanced in presence of TNF- $\alpha$  even at t=24 h. In general, these findings are consistent with previous studies in which it was shown that exposure to TNF- $\alpha$  either after 4 or 24 h induces the expression of E-selectin and VCAM-1 mainly via activation of NF- $\kappa$ B pathway [40, 41].

Upon activation of the cells with TNF- $\alpha$ , a 4.4 and 5.6 fold increase in gene expression of angiogenesis mediators was observed, compared to resting cells, for the TIE2 angiopoietin receptor and the VEGF ligand respectively (Figure 8C and D). However, the precise role of TNF- $\alpha$  in angiogenesis has been a subject of debate in scientific literature [42]. Several *in vitro* studies have shown that TNF- $\alpha$  can be either proangiogenic or antiangiogenic, depending mainly on cell environmental factors [39]. With the experimental conditions used in this work, we demonstrated that TNF- $\alpha$  induced gene expression of both the TIE2 receptor and the VEGF ligand. These findings

are in good agreement with previous studies that also reported that TNF- $\alpha$  induced these above mentioned gene expressions (TIE2 and VEGF), both of which are reported to be mediated through the NF- $\kappa$ B pathway [43-46].

TGF- $\beta$  is a pleiotropic cytokine which has either inflammatory or anti-inflammatory activities, depending on the cellular environment. In this study, we could not detect changes in TGF- $\beta$  gene expression upon cell activation with TNF- $\alpha$  (Figure 8E). Using different cell types, a study by Chen and coworkers reported that TNF- $\alpha$  expression induced TGF- $\beta$  secretion in macrophages and vice versa [47], while another study by Sullivan and coworkers demonstrated that TNF- $\alpha$  plays significant role in regulating TGF- $\beta$  in lung fibroblasts through AP-1 activation *in vitro* [48]. However, under the experimental conditions we could not detect any change in TGF- $\beta$  gene expression between the cells activated with TNF- $\alpha$  and the non-activated resting cells.

The results obtained in this work show an approximately 2-fold increase in mTOR gene expression for the TNF- $\alpha$  activated cells compared to the resting cells (Figure 8F). This is consistent with previous studies which showed that TNF- $\alpha$  up-regulates mTOR gene expression by activation of the NF- $\kappa$ B pathway [49, 50].

When introduced to TNF- $\alpha$  activated cells, both free rapamycin and immunoliposomes loaded with rapamycin significantly reduced the gene expressions of VCAM-1, E-selectin, VEGF and TIE2, as shown in figure 8A-D. However, no effect was detected for mTOR and TGF- $\beta$  gene expressions (Figure 8E, F). Control (i.e. non-targeted) liposomes loaded with rapamycin showed less effect on the overall gene expression as compared to their (targeted) counterparts. Taken together, the data suggest that targeted liposomes loaded with rapamycin are most effective, as their introduction resulted on average in a 50% decrease in gene expression of VCAM-1, E-selectin, VEGF and TIE2 compared to TNF- $\alpha$  activated (control +) cells. Free rapamycin also caused a significant decrease in the expression of these same genes compared to TNF- $\alpha$  activated (control +) cells, but the data from figure 8 show that the targeted liposomes were (at least) 15% more effective in inhibiting gene expression than free rapamycin. When comparing their impact on the expression of E-selectin

(Figure 8B), the difference between targeted liposomes loaded with rapamycin and free rapamycin is even more pronounced. Similar results regarding the effectiveness of the targeted liposomes are also observed in cell migration and proliferation assays. Most likely, the active delivery of rapamycin by the targeted liposomes resulted in the highest intracellular concentrations within the designated time period.

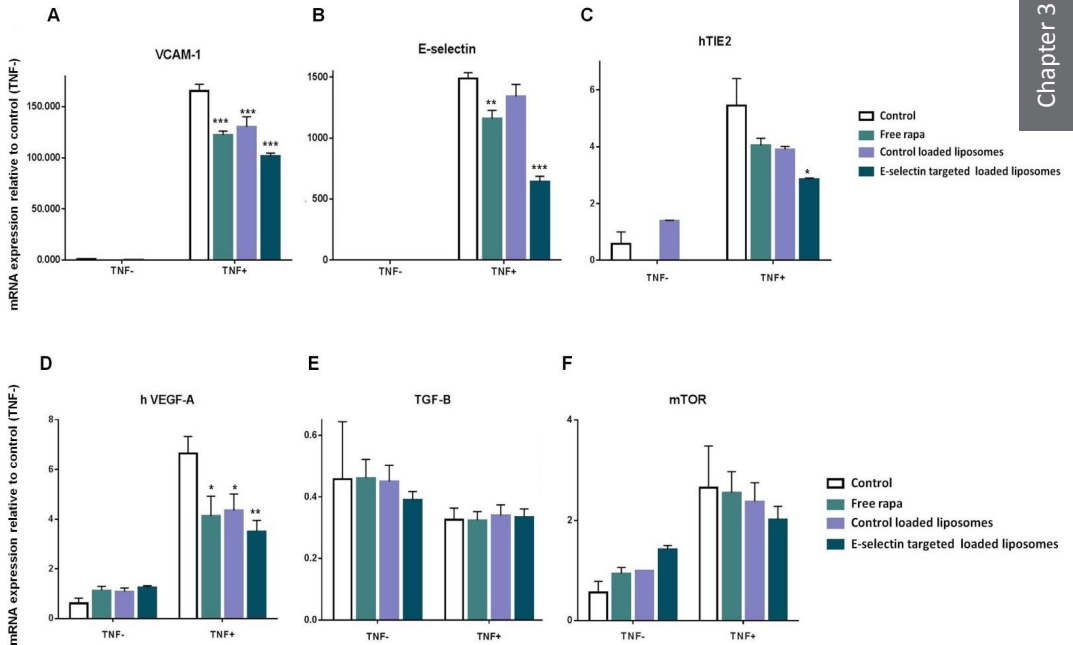
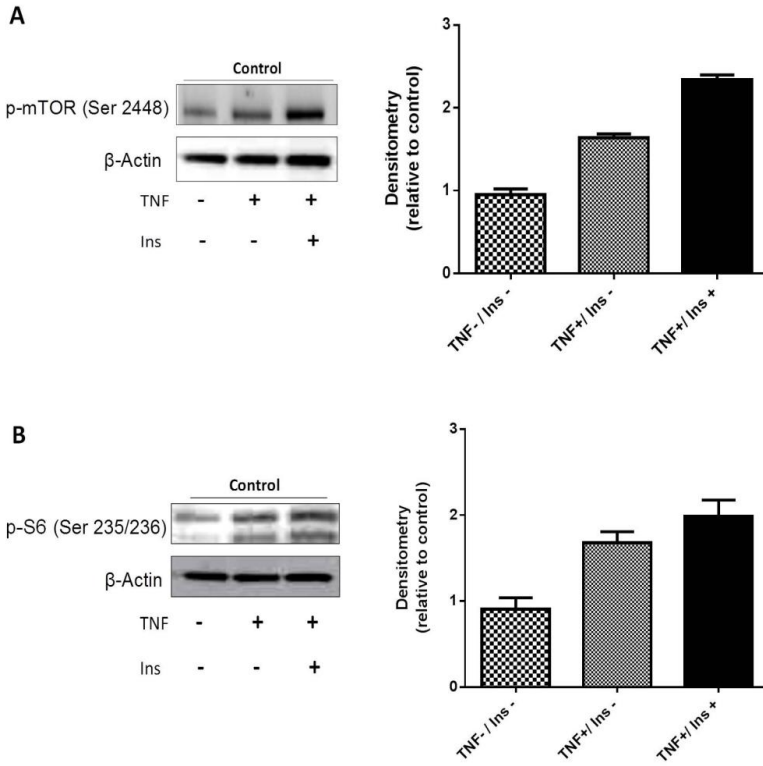


**Figure 8.** TNF- $\alpha$  activated and non-activated HUVEC cells were treated with rapamycin and its liposomal formulations for 24hrs. **(A)** VCAM-1, **(B)** E-selectin, **(C)** hTIE2, **(D)** h VEGF-A, **(E)** TGF- $\beta$  **(F)** mTOR gene expressions determined by q-PCR analyses. Total mRNA input was corrected for the housekeeping gene hGAPDH. Quantitative change in expression was calculated relative to resting cells (TNF-). Data are plotted as mean values  $\pm$  SEM of two independent experiments; \* $p$  < 0.05, \*\* $p$  < 0.01, \*\*\* $p$  < 0.001 compared to TNF- $\alpha$  activated control cells (TNF+).

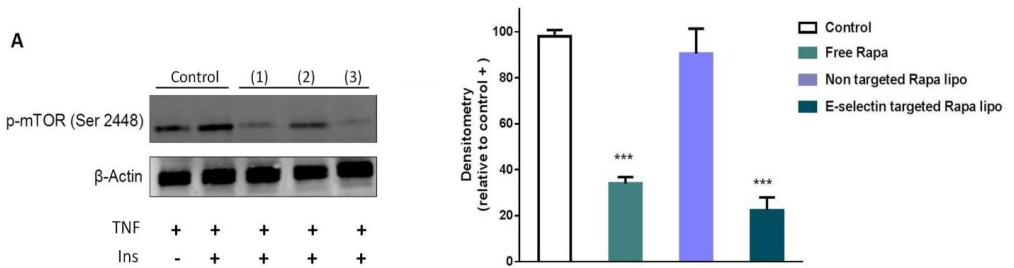
### 3.3.5. Effects of rapamycin liposomes on mTOR signaling cascade

To induce E-selectin over-expression on the surface of the HUVEC cells, they were first exposed to TNF- $\alpha$  for 4 h. As shown previously, this step is essential for active binding and uptake of E-selectin targeted liposomes, while TNF- $\alpha$  is also one of the inflammatory cytokines that affects cell signaling pathways, such as activation of mTOR in HUVEC cells [51]. Insulin is known to strongly modulate downstream effectors in the mTOR pathway [52]. For more details on the effects of insulin on the mTOR pathway, the reader is referred to the works of Garami et al. and Nave et al. (53, 54). Therefore, several experiments were performed to determine whether incubating HUVEC cells with solely TNF- $\alpha$  or with a combination of TNF- $\alpha$  and insulin would have an effect on the phosphorylation of Ser<sup>235/236</sup> of the S6 ribosomal protein and Ser<sup>2448</sup> of mTOR. Activation with only TNF- $\alpha$  induced a 72% and 85% increase in the degree of phosphorylation of mTOR and S6 proteins respectively, compared to resting cells (control). Exposure of the cells to insulin in the presence of TNF- $\alpha$  resulted in an increase versus control of 146% and 120% in phosphorylation of mTOR and S6 proteins respectively, as shown in figure 9A and B. While previous studies have reported an increase in phosphorylation of mTOR and S6 proteins through a PI3kinase-Akt dependent pathway upon exposure to insulin, such an effect has not yet been reported in the presence of TNF- $\alpha$  [53, 55-56].

Both free rapamycin and E-selectin targeted liposomes loaded with rapamycin inhibited phosphorylation of mTOR and S6 after a 4h incubation at a concentration of 10  $\mu$ M of rapamycin, while control (i.e. non-targeted) liposomes loaded with rapamycin showed almost no inhibitory effect (Figure 10A and B). These findings are in good agreement with our results from the cell migration, proliferation and gene expression assays, in which E-selectin targeted liposomes loaded with rapamycin showed a more pronounced inhibiting effect than its non-targeted counterparts. It should be noted that the conditions in this experiment differed slightly from the cell migration, proliferation and gene expression assays described in earlier paragraphs, because insulin was applied as an additional stimulating factor for the short-lived activation of the mTOR pathway upon treatment with rapamycin.



**Figure 9.** Effect of stimulation with TNF- $\alpha$  and combined stimulation with TNF- $\alpha$  and insulin on phosphorylation of mTOR **(A)** and S6 ribosomal protein **(B)** in HUVEC cells. Data are plotted as mean values  $\pm$  SEM of two experiments with two separately prepared formulations.



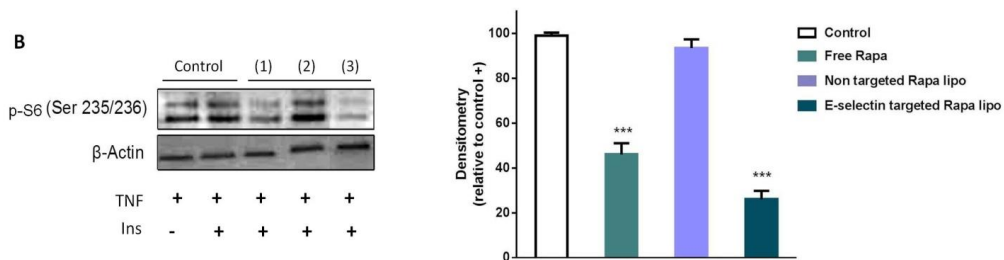


**Figure 10.** Effect of rapamycin and its liposomal formulations (equivalent to 10  $\mu$ M rapamycin) on phosphorylation of mTOR (**A**) and S6 ribosomal protein (lower band) (**B**) in HUVEC cells. **(1)** represents free rapamycin; **(2)** control loaded liposomes and **(3)** E-selectin targeted loaded liposomes. Data are plotted as mean values  $\pm$  SEM of two experiments with two separately prepared formulations; \*\*\* $p$ <0.001 compared to control +.

#### 4. Conclusion

Free rapamycin is a potent and efficacious drug in the treatment of inflammatory disorders; its use is however associated with side effects. The present approach involving its encapsulation in immunoliposomes will provide for a more selective activity of the drug targeted to a specific cell type. Anti-E-selectin immunoliposomes were shown to be attractive nanocarrier systems for targeted delivery of rapamycin to TNF- $\alpha$  activated endothelial cells. Further studies to evaluate in vivo efficacy of rapamycin loaded immunoliposomes are necessary to fully address their value for anti-inflammatory therapy.

#### 5. Acknowledgments

This work has been supported by NanoNextNL, a micro and nanotechnology consortium of the government of The Netherlands and 130 partners (project 03D.07). The authors would like to thank Mies van Steenbergen (Utrecht University) for his expert technical assistance.



## 6. References

1. Kim DH, S.D., Ali SM, King JE, Latek RR, Erdjument-Bromage H, Tempst P, Sabatini DM., mTOR interacts with raptor to form a nutrient-sensitive complex that signals to the cell growth machinery. *Cell*, 2002. 110: p. 163-75.
2. Sarbassov DD, A.S., Kim DH, Guertin DA, Latek RR, Erdjument-Bromage H, Tempst P, Sabatini DM., Rictor, a novel binding partner of mTOR, defines a rapamycin-insensitive and raptor-independent pathway that regulates the cytoskeleton. *Curr Biol*, 2004. 14: p. 1296-302.
3. Jacinto E, L.R., Schmidt A, Lin S, Rüegg MA, Hall A, Hall MN., Mammalian TOR complex 2 controls the actin cytoskeleton and is rapamycin insensitive. *Nat Cell Biol*, 2004. 6: p. 1122-8.
4. Wullschlegel S, Loewith R, Hall MN., TOR signaling in growth and metabolism. *Cell*, 2006. 124: p. 471-484.
5. Cejka D, H.S., Niederreiter B, Sieghart W, Fuereder T, Zwerina J, Schett G., Mammalian target of rapamycin signaling is crucial for joint destruction in experimental arthritis and is activated in osteoclasts from patients with rheumatoid arthritis. *Arthritis Rheum.*, 2010. 62: p. 2294-302.
6. Li D, Wang C., Yao Y, Chen L, Liu G, Zhang R, Liu Q, Shi FD, Hao J, mTORC1 pathway disruption ameliorates brain inflammation following stroke via a shift in microglia phenotype from M1 type to M2 type. *FASEB J*, 2016.
7. Xie L, Sun F, Wang J, Mao X, Xie L, Yang SH, Su DM, Simpkins JW, Greenberg DA, Jin K., mTOR signaling inhibition modulates macrophage/microglia-mediated neuroinflammation and secondary injury via regulatory T cells after focal ischemia. *J Immunol*, 2014. 192(12): p. 6009-19.
8. Weichhart T, Hengstschläger M, Linke M., Regulation of innate immune cell function by mTOR. *Nature Reviews Immunology*, 2015. 15: p. 599-614.
9. Lieberthal W, Levine J.S., The role of the mammalian target of rapamycin (mTOR) in renal disease. *J Am Soc Nephrol*, 2009. 20: p. 2493-502.
10. Lieberthal W, Levine J.S., Mammalian target of rapamycin and the kidney. II. Pathophysiology and therapeutic implications. *Am J Physiol Renal Physiol*, 2012. 15: p. 180-91.
11. Bonegio RG, Wang Z, Valeri CR, Andry C, Salant DJ, Lieberthal W., Rapamycin ameliorates proteinuria-associated tubulointerstitial inflammation and fibrosis in experimental membranous nephropathy. *J Am Soc Nephrol*, 2005. 16: p. 2063-72.
12. Wu MJ, Wen MC, Chiu YT, Chiou YY, Shu KH, Tang MJ., Rapamycin attenuates unilateral ureteral obstruction-induced renal fibrosis. *Kidney Int*, 2006. 69: p. 2029-36.
13. Simamora P, Yalkowsky SH., Solubilization of rapamycin. *Int J Pharm*, 2001. 213: p. 25-9.
14. Hu X, Chen D, Zhang J, Liu Z, Wu W. et al., Sirolimus solid self-microemulsifying pellets: Formulation development, characterization and bioavailability evaluation. *Int J Pharm*, 2012. 438: p. 123-33.

15. Woo HN, Ju EJ, Jung J, Kang HW, Lee SW et al., Preclinical evaluation of injectable sirolimus formulated with polymeric nanoparticle for cancer therapy. *Int J Nanomedicine*, 2012. 7: p. 2197–2208.
16. Chen YC, Lin YF, Hsiue GH., Rapamycin encapsulated in dual-responsive micelles for cancer therapy. *Biomaterials* 2013. 34: p. 1115–1127.
17. Shah M, Janga SR, Shi P, Dhandhukia J, Liu S et al., A rapamycin-binding protein polymer nanoparticle shows potent therapeutic activity in suppressing autoimmune dacryoadenitis in a mouse model of Sjogren’s syndrome. *J Control Release*, 2013. 171: p. 269–279..
18. Eloy JO, Petrilli R, Topan JF, Antonio HM, et al., Co-loaded paclitaxel/rapamycin liposomes: Development, characterization and in vitro and in vivo evaluation for breast cancer therapy. *Colloids Surf B Biointerfaces.*, 2016. 41: p. 74-82.
19. Panés J, Perry M, Granger DN., Leukocyte-endothelial cell adhesion: avenues for therapeutic intervention. *Br J Pharmacol*, 1999. 126: p. 537–550.
20. Muller WA., Leukocyte-endothelial-cell interactions in leukocyte transmigration and the inflammatory response. *Trends Immunol*, 2003. 24: p. 327-34.
21. Cook-Mills JM, Deem TL., Active participation of endothelial cells in inflammation. *J Leukoc Biol*, 2005. 77(4): p. 487–495.
22. Koning GA, Wauben MH, Kok RJ, Mastrobattista E, Molema G, ten Hagen TL, Storm G., Targeting of angiogenic endothelial cells at sites of inflammation by dexamethasone phosphate-containing RGD peptide liposomes inhibits experimental arthritis. *Arthritis Rheum*, 2006. 54(4): p. 1198-208.
23. Martini FH, et al., *Fundamentals of Anatomy & Physiology*. Pearson education Inc., 2012.
24. Everts M, Kok RJ, Asgeirsdóttir SA, Vestweber D, Meijer DK, Storm G, Molema G., In vitro cellular handling and in vivo targeting of E-selectin-directed immunoconjugates and immunoliposomes used for drug delivery to inflamed endothelium. *Pharm Res*, 2003. 20(1): p. 64-72.
25. G. Rouser, A. Yamamoto., Two dimensional thin layer chromatographic separation of polar lipids and determination of phospholipids by phosphorus analysis of spots. *Lipids*, 1970. 5: p. 494–496.
26. Adrian JE, Scherphof GL, Meijer DK, van Loenen-Weemaes AM, Reker-Smit C, Terpstra P, Poelstra K., A novel lipid-based drug carrier targeted to the non-parenchymal cells, including hepatic stellate cells, in the fibrotic livers of bile duct ligated rats. *Biochim Biophys Acta.*, 2007. 1768(6): p. 1430-9.
27. Pellegatta F, Catapano AL, Luzi L, Terruzzi I., In Human Endothelial Cells Amino Acids Inhibit Insulin-induced Akt and ERK1/2 Phosphorylation by an mTOR-dependent Mechanism. *Journal of Cardiovascular Pharmacology*, 2006. 47(5): p. 643-649.
28. Johnsson M, Edwards K., 2003. Liposomes, disks, and spherical micelles: aggregate structure in mixtures of gel phase phosphatidylcholines and poly(ethylene glycol)-phospholipids. *Biophys J*. 85(6), 3839-47

29. Weissig V, Whiteman KR, Torchilin VP., 1998. Accumulation of protein-loaded long-circulating micelles and liposomes in subcutaneous lewis lung carcinoma in mice. *Pharm Res.* 15(10), 1552-6.
30. Garbuzenko, O., Zalipsky, S., Qazen, M., Barenholz, Y., 2005. Electrostatic of PEGylated micelles and liposomes containing charged and neutral lipopolymers. *Langmuir.* 21(6), 2560-8.
31. Enoch HG, Strittmatter P., Formation and properties of 1000-Å-diameter, single-bilayer phospholipid vesicles. *Proc Natl Acad Sci.*, 1979. 76: p. 145–149.
32. Sun Y, Lee CC, Hung WC, Chen FY, Lee MT, Huang HW., The bound states of amphipathic drugs in lipid bilayers: study of Curcumin. *Biophysical Journal*, 2008. 95: p. 2318–2324.
33. Redondo-Morata L, Lea Sanford R, Andersen OS, Scheuring S., Effect of statins on the nano-mechanical properties of supported lipid bilayers. *Biophysical Society*, 2016. 111(2): p. 363-372.
34. Ping Yang, Lei Zhao, Jun Yuan, Yao Chen, Zac Varghese, John F. Moorhead, Yaxi Chen, and Xiong Z. Ruan., Paradoxical effect of rapamycin on inflammatory stress-induced insulin resistance in vitro and in vivo. *Sci Rep*, 2015. 5: p. 149-59.
35. Salas-Prato M, Mehdi AZ, Duperré J, Thompson P, Brazeau P., Inhibition by rapamycin of PDGF- and bFGF-induced human tenon fibroblast proliferation in vitro. *J Glaucoma*, 1996. 5(1): p. 54-9.
36. Berven LA, Crouch MF., Role of the p70(S6K) pathway in regulating the actin cytoskeleton and cell migration. *Exp Cell Res*, 2004. 296: p. 183–195.
37. Del Bufalo D, Trisciuglio D, Desideri M, Cognetti F, Zupi G, Milella M., Antiangiogenic potential of the Mammalian target of rapamycin inhibitor temsirolimus. *Cancer Research*, 2006. 66(11): p. 5549-54.
38. Guba M, Steinbauer M, Koehl G, Flegel S, Hornung M, et al., Rapamycin inhibits primary and metastatic tumor growth by antiangiogenesis: involvement of vascular endothelial growth factor. *Nat Med*, 2002. 8(2): p. 128-35.
39. Arsham AM, Neufeld TP., Thinking globally and acting locally with TOR. *Curr Opin Cell Biol* 2006. 18(6): p. 589–597.
40. Rahman A, Kefer J, Bando M, Niles WD, Malik AB., E-selectin expression in human endothelial cells by TNF- $\alpha$ -induced oxidant generation and NF- $\kappa$ B activation. *the American Physiological Society*, 1998.
41. Wagener FA, Feldman E, de Witte T, Abraham NG., Heme induces the expression of adhesion molecules ICAM-1, VCAM-1, and E selectin in vascular endothelial cells. *Proc Soc Exp Biol Med.* , 1997. 216(3): p. 456-63.
42. Sainson RC, Johnston DA, Chu HC, Holderfield MT, et al., TNF primes endothelial cells for angiogenic sprouting by inducing a tip cell phenotype. *Blood* 2008. 111: p. 4997-5007.
43. DeBusk LM, Nishishita T, Chen J, Thomas JW, Lin PC., Tie2 receptor tyrosine kinase, a major mediator of tumor necrosis factor alpha-induced angiogenesis in rheumatoid arthritis. *Arthritis Rheum*, 2003. 48(9): p. 2461-71.

44. Nagineni CN, William A, Detrick B, Hooks JJ., Regulation of VEGF expression in human retinal cells by cytokines: implications for the role of inflammation in age-related macular degeneration. *J Cell Physiol.*, 2012. 227(1): p. 116-26.
45. Yuan J, Fang W, Lin A, Ni Z, Qian J., Angiopoietin-2/Tie2 signaling involved in TNF-alpha induced peritoneal angiogenesis. *Int J Artif Organs*, 2012. 35(9): p. 655-62.
46. Chen JX, Chen Y, DeBusk L, Lin W, Lin PC. Dual functional roles of Tie-2/angiopoietin in TNF-alpha-mediated angiogenesis. *Am J Physiol Heart Circ Physiol*, 2004. 287: p. 187-95.
47. Chen Y, Liu FQ, Liu Y, Lui VC, Lamb JR, Tam PK., LPS-induced up-regulation of TGF-beta receptor 1 is associated with TNF-alpha expression in human monocyte-derived macrophages. *J Leukoc Biol*, 2008. 83(5): p. 1165-73.
48. Sullivan DE, Nguyen H, Abboud E, Brody AR., TNF-alpha induces TGF-beta1 expression in lung fibroblasts at the transcriptional level via AP-1 activation. *J Cell Mol Med*, 2009. 13(8): p. 1866-76.
49. Dan HC, Cooper MJ, Cogswell PC, Duncan JA, Ting JP, Baldwin AS., Akt-dependent regulation of NF- $\kappa$ B is controlled by mTOR and Raptor in association with IKK. *Genes Dev*, 2008. 22: p. 1490-1500.
50. Karonitsch T, Herdy B, Kandasamy K, Niederreiter B, et al., AB0075 MTOR: An Unexpected Role on the TNF-Regulated MRNA Transcriptome in Rheumatoid Fibroblast-Like Synoviocytes. *Ann Rheum Dis* 2015. 74: p. 915-916.
51. Glantschnig H, Fisher JE, Wesolowski G, Rodan GA, Reszka AA., M-CSF, TNF, and RANK ligand promote osteoclast survival by signaling through mTOR/S6 kinase. *Cell Death Differ.*, 2001. 10: p. 1165-1177.
52. Pellegatta F, Luzi L, Terruzzi I., In human endothelial cells amino acids inhibit insulin-induced Akt and ERK1/2 phosphorylation by an mTOR-dependent mechanism. *J Cardiovasc Pharmacol*, 2006. 47(5): p. 643-9.
53. Garami A, Zwartkruis FJ, Nobukuni T, Joaquin M, Rocco M, Stocker H, Kozma SC, Hafen E, Bos JL, Thomas G., Insulin Activation of Rheb, a Mediator of mTOR/S6K/4E-BP Signaling, is Inhibited by TSC1 and 2. *Molecular Cell*, Vol. 11, 1457-1466, 2003.
54. Nave, B.T., Ouwens, M., Withers, D. J., Alessi, D.R., and Shepherd, P.R., 1999. Mammalian target of rapamycin is a direct target for protein kinase B: identification of a convergence point for opposing effects of insulin and amino-acid deficiency on protein translation. *Biochem J*. 344, 427-31.
55. Reynolds TH, Bodine SC, Lawrence JC Jr. Control of Ser2448 phosphorylation in the mammalian target of rapamycin by insulin and skeletal muscle load. *J Biol Chem*, 2002. 277(20): p. 17657-62.
56. Scott PH, Brunn GJ, Kohn AD, Roth RA, Lawrence JC Jr., Evidence of insulin-stimulated phosphorylation and activation of the mammalian target of rapamycin mediated by a protein kinase B signaling pathway. *Proc Natl Acad Sci*, 1998. 95(13): p. 7772-7.

## **Chapter 4**

**Targeting Rapamycin to podocytes using a vascular cell adhesion molecule-1**

**(VCAM-1)-harnessed SAINT-based lipid carrier system**

Ganesh Ram R. Visweswaran, Shima Gholizadeh, Marcel H. J. Ruiters, Grietje Molema, Robbert J. Kok, Jan. A. A. M. Kamps. PLoS One. 2015, 10 (9): 1-17.

**Abstract**

Together with the mesangial cells, glomerular endothelial cells and the basement membrane, podocytes constitute the glomerular filtration barrier (GFB) of the kidney. Podocytes play a pivotal role in the progression of various kidney-related diseases such as glomerular sclerosis and glomerulonephritis that finally lead to chronic end-stage renal disease. During podocytopathies, the slit-diaphragm connecting the adjacent podocytes are detached leading to severe loss of proteins in the urine. The pathophysiology of podocytopathies makes podocytes a potential and challenging target for nanomedicine development, though there is a lack of known molecular targets for cell selective drug delivery. To identify VCAM-1 as a cell-surface receptor that is suitable for binding and internalization of nanomedicine carrier systems by podocytes, we investigated its expression in the immortalized podocyte cell lines AB8/13 and MPC-5, and in primary podocytes. Gene and protein expression analyses revealed that VCAM-1 expression is increased by podocytes upon TNF $\alpha$ -activation for up to 24 h. This was paralleled by anti-VCAM-1 antibody binding to the TNF $\alpha$ -activated cells, which can be employed as a ligand to facilitate the uptake of nanocarriers under inflammatory conditions. Hence, we next explored the possibilities of using VCAM-1 as a cell-surface receptor to deliver the potent immunosuppressant Rapamycin to TNF $\alpha$ -activated podocytes using the lipid-based nanocarrier system Saint-O-Somes. The anti-VCAM-1-rapamycin-SAINT-O-Somes more effectively inhibited the cell migration of AB8/13 cells than free Rapamycin and non-targeted Rapamycin-SAINT-O-Somes indicating the potential of VCAM-1 targeted drug delivery to podocytes.

## 1. Introduction

Kidney glomeruli are composed of four major components namely mesangial cells, fenestrated endothelium, glomerular basement membrane (GBM), and podocytes. These latter cells form the glomerular filtration barrier (GFB) of the kidney. Mesangial cells, present in the interstitium between the glomerular endothelial cells, are indirectly involved in the filtration process by controlling the glomerular surface area [1]. The glomerular endothelium is lined with 70-100 nm fenestrations which are actively involved in filtration [1]. The fenestrated endothelium is attached to one side of the GBM, which contain pores of around 250-350 nm. The GBM is sandwiched on the proximal side by visceral epithelial cells called podocytes. The adjacent podocytes are connected by slit diaphragms with a width of around 40 nm, forming podocyte foot processes mainly involved in filtration of proteins [1]. The slit diaphragm bridging the podocytes contains nephrin, podocin, CD2AP, and nephrin-like proteins NEPH1 and NEPH2. The contraction and relaxation of the podocytes regulate the glomerular filtration rate leading to ultrafiltration of water and ion salts into the urinary space. Apart from filtration, the podocytes synthesize the GBM, maintain the shape of the capillary tube, and provide growth factors for mesangial and endothelial cells. Recent findings demonstrate that cross-talk exists between the endothelial cells and podocytes, especially during glomerulopathies, indicating a significant role of these cells in glomerular disease [2].

Glomerulonephritis in the USA comprise 90% of patients that need kidney transplantation or dialysis and it is the underlying cause of end-stage renal failure in 30–50% of kidney transplant recipient [3] emphasizing the importance of the development of efficacious drugs to treat injured glomerular cells [4]. In glomerulopathies such as glomerular nephritis, glomerular sclerosis and diabetic nephropathy, especially the podocytes are severely affected leading to partial or complete loss of filtration function [1]. During these diseases, the fenestrations of the glomerular filtration barrier widen, leading to proteinuria, the hallmark of glomerular diseases. Further, detachment of the podocyte foot-processes and subsequent loss of the podocytes in urine dramatically increases proteinuria. To date, therapeutic intervention to treat podocytopathies is inadequate. Because of

their role in pathological processes of glomerular diseases and their accessibility through the blood stream of glomerular capillaries, podocytes could be targeted by systemically applied drug-targeting approaches employing molecular targets specifically expressed by the diseased podocytes. Although there are few preliminary studies involving delivery of siRNA and proteins to podocytes [5, 6], targeting small molecule therapeutics was never done. Rapamycin (or sirolimus), a mammalian target of Rapamycin (mTOR) inhibitor, is widely used in the clinic as immunosuppressant to treat patients after kidney transplantation. However, the prolonged use of Rapamycin on podocytes in kidney transplant patients results in severe proteinuria that leads to the progression of chronic kidney disease and renal failure [7]. Furthermore, it has been shown that mTOR complex 1(mTORC1) is involved in podocyte injury [8]. As Rapamycin is commonly used in the clinic and its effects as free drug on podocytes have been studied, it is relevant to investigate the role of Rapamycin on podocytes in an encapsulated formulation. Using targeted drug delivery systems such as liposomes, the dosage and the side effects of Rapamycin may potentially be optimized and minimized, respectively, and on the other hand the local drug concentration achieved could be increased.

In this study, we investigated whether podocytes express inflammation-induced cell adhesion molecules like vascular cell adhesion molecule-1 (VCAM-1). VCAM-1 is a surface expressed receptor that can facilitate receptor-mediated endocytosis of nanosized drug carriers. We used lipid-based nanocarriers called SAINT-O-Somes that were previously shown to have better intracellular drug release properties than conventional liposomes, and that can target a particular cell type when harnessed with an antigen-specific antibody [9, 10]. Here, we report that cultured podocytes express VCAM-1 when triggered with TNF $\alpha$  to mimic the inflammatory condition. Furthermore, as a conceptual proof of targeting drugs to podocytes, we demonstrated that these cells internalize this type of lipid-based nanocarriers and, finally, that Rapamycin incorporated into VCAM-1-SAINT-O-Somes effectively inhibited cellular responses in VCAM-1-expressing podocytes.



## 2. Materials and methods

### 2.1. Materials

Lipids 1,2-distearoyl-*sn*-glycero-3-phosphoethanolamine-N-[methoxy(polyethylene glycol)-2000]-maleimide (Mal-PEG<sub>2000</sub>-DSPE), 1-palmitoyl-2-oleoyl-*sn*-glycero-3-phosphocholine (POPC) and 2-distearoyl-*sn*-glycero-3-phosphoethanolamine-N-[methoxy(polyethylene glycol)-2000] (DSPE-PEG<sub>2000</sub>) were obtained from Avanti Polar Lipids (Alabaster AL, USA). Cholesterol (Chol) and N-succinimidyl-5-acetylthioacetate (SATA) were purchased from Sigma-Aldrich (St. Louis MO, USA). 1,1'-dioctadecyl-3,3',3'-tetramethylindocarbocyanine perchlorate (DiI) was from Molecular Probes (Leiden, the Netherlands) and 1-methyl-4-(*cis*-9-dioleyl)methyl-pyridinium-chloride (SAINT-C18) from Synvolux Therapeutics Inc. (Groningen, the Netherlands). All chemicals used were of analytical grade unless otherwise stated.

### 2.2. Cell culture

The generation of the human and mouse conditionally immortalized podocyte cell lines, AB8/13 and MPC-5, were previously described [11, 12]. AB8/13 podocytes were kindly provided by Dr. Moin A. Saleem (Bristol, UK); Dr. Peter Mundel (Charlestown, USA) kindly provided the MPC-5 cells. AB8/13 and MPC-5 cells were cultured at 33°C and the cells were differentiated in 5% CO<sub>2</sub> incubator at 37°C for 10-15 days as indicated. The cells were cultured in RPMI 1640 medium containing 1% 100 units/ml penicillin/streptomycin and 1% Insulin-Transferrin-Selenium (ITS) (Invitrogen, Breda, the Netherlands) and 10% fetal bovine serum. For MPC-5 cells, it was excluded and pyruvate (1%) and interferon (10 U IFN- $\gamma$ /ml) were added for cell proliferation. For differentiation of MPC-5 cells, medium without IFN- $\gamma$  was used and the cells were incubated at 37°C in collagen A (10%)-coated cell culture plates (BD Biosciences, Breda, the Netherlands). The medium was refreshed at 5-day intervals. On the day of the experiment, cells were incubated in the absence (quiescent cells) or presence of TNF $\alpha$  (Boehringer Ingelheim GmbH, Ingelheim am Rhein, Germany) at 10 ng/ml for 24 h, unless stated otherwise.

### 2.3. Isolation of primary podocytes

Male C57bl/6OlaHsd mice (18-23 g) were purchased from Harlan (Zeist, The Netherlands). Animals were group housed and maintained on a mouse chow diet, in a temperature and light-dark cycle controlled environment (24°C, 12:12 h). Mice were sacrificed under anesthesia (inhalation of isoflurane/O<sub>2</sub>), and organs were collected. All animal experiments were performed according to national guidelines and upon approval of the local Animal Care and Use Committee of Groningen University (DEC 6106).

Glomeruli from kidneys of 6-8 C57BL/6 mice were isolated based on previously described anti-CD31bead based endothelial cell preparations [13] with the following modifications. Cortices of the kidneys were minced for 3 min and next incubated at 37°C with collagenase-I (0.2 g% in Dulbecco's phosphate buffered saline (DPBS) with Ca<sup>2+</sup>/Mg<sup>2+</sup>; Worthington Biochemical Corp. Lakewood, NJ, USA) for 45 min. The collagenase/kidney mixture was pushed 15-17 times through a 14 G needle and dripped gently through a 70 µm cut-off cell strainer (BD Pharmingen, San Diego, CA). The eluate was spun down at 140 x g for 8 min and the pellet was resuspended in ~3 ml of bead wash solution (PBS with 0.1 % BSA and antibiotic/antimycotic (1:100) (Sigma) followed by incubation with rat anti mouse-CD31 (BD Pharmingen)-coated magnetic beads (pre-incubated overnight at 4°C with sheep anti-rat beads; Dynabeads, Life Technologies, Bleiswijk, the Netherlands) for 15 min at room temperature on a rotator. The anti-CD31 positive cells were separated using a Magnetic Particle Concentrator (Invitrogen) and the bead discard was sieved through a 40 µm cut-off cell strainer (BD Pharmingen) to isolate glomeruli. The glomeruli on cell strainer were washed with 25 ml of DPBS at 5 ml aliquots. The glomeruli were next treated with 1 ml of collagenase-I (Worthington Biochemical Corp.) in DPBS with Ca/Mg for 1 h followed by 10 times titration using an insulin syringe. The glomeruli were obtained by spinning down at 140 x g for 8 min and resuspended in Dulbecco's Modified Eagle Medium (DMEM)/F-12 supplemented with 10% FCS, 100 µg/ml streptomycin, 100 U/ml penicillin and Insulin-Transferrin-Selenium (ITS) (podocyte-specific medium) and seeded in gelatin-coated plates at 37°C for 4-5 days. To eliminate the endothelial cells from the glomerular

outgrowths, anti-ICAM-2 (BD Pharmingen)-coated magnetic beads (pre-incubated overnight at 4°C with sheep anti-rat beads; Dynabeads) were incubated with trypsin/EDTA detached glomerular outgrowth cells for 15 min at room temperature on a rotator. The ICAM-2 positive cells were removed from the glomerular outgrowth cells and the ICAM-2 negative fraction was seeded in podocyte-specific medium until confluent (2-3 days) at 37°C and RNA was next isolated for RT-qPCR analysis. Cytospots of the ICAM-2 negative fraction cells were made on microscope slides for immunostaining by releasing the cells from the tissue culture plates by trypsinization followed by suspending the cells in podocyte-specific medium.

#### 2.4. Gene expression studies by RT-qPCR

RNA was isolated from cells using the RNeasy® Mini Plus Kit (Qiagen, Venlo, the Netherlands) according to manufacturer's protocol. The concentration and integrity of RNA were determined by the NanoDrop® ND-1000 spectrophotometer (Wilmington, DE) and by agarose (1%) gel electrophoresis, respectively. Complementary DNA (cDNA) from respective RNA samples were generated using SuperScript™ III RNaseH-Reverse Transcriptase (Invitrogen), RNaseOut inhibitor (40 U) (Invitrogen) and 250 ng random hexamers (Promega, Leiden, the Netherlands) in 20 µl total volume. 1 µl of the cDNA product was used for each PCR reaction.

Human GAPDH (Hs99999905\_m1), E-selectin (Hs00174057\_m1), VCAM-1 (Hs00365486\_m1), WT-1 (Hs01103751\_m1) and mouse GAPDH (Mm99999915\_g1), synaptopodin (Mm03413333\_m1), WT-1 (Mm01337048\_m1) and VCAM-1 (Mm00449197\_m1) primer-probes were purchased as Assay-on-Demand from Applied Biosystems (Nieuwekerk a/d IJssel, the Netherlands). These primer-probes together with Absolute QPCR Rox Mix (Thermo Scientific, Landsmeer, the Netherlands) were used in Quantitative (q) PCR performed in ABI PRISM 7900HT Sequence Detector (Applied Biosystems), with two technical replicates per sample. RT-qPCR and data analysis were performed as described previously [10]. The threshold cycle values ( $C_t$ ) were obtained by the comparative  $C_t$  method and we averaged the two technical replicate  $C_t$  values. The respective genes were normalized to the

housekeeping gene glyceraldehyde-3-phosphate dehydrogenase (GAPDH), resulting in  $\Delta C_t$  values. The relative mRNA levels were calculated by  $2^{-\Delta C_t}$  for respective genes.

## 2.5. Western blot

AB8/13 cells, differentiated for 15 days at 37°C, treated with TNF $\alpha$  (10 ng/ml) for 4, 8 and 24 h were lysed by sonication in Radio-Immuno Precipitation Assay (RIPA) buffer (Sigma-Aldrich) for 1 min. Total protein concentration of the lysate was determined by BCA protein assay (Thermo Scientific) according to manufacturer's protocol and equal amounts of lysate were mixed with SDS-loading buffer. The protein samples were electrophoresed on a SDS-(10%) PAA gel and transferred to a nitrocellulose membrane followed by blocking with 5% skimmed milk in PBS for 1 h. The membrane was cut based on the molecular masses of the target proteins followed by incubation with primary antibodies rabbit- polyclonal anti-VCAM-1 (~100-kDa, Santa Cruz Biotechnology Inc. Heidelberg, Germany), mouse-anti-human synaptopodin (~74-kDa, Progen), rabbit-polyclonal anti-GAPDH (~37-kDa, Santa Cruz Biotechnology Inc.) and/or mouse anti-human actin (~42-kDa, Millipore, Amsterdam, the Netherlands) for 1 h at room temperature. The membranes were washed three times with PBST and incubated with relevant horseradish peroxidase (HRP)-conjugated secondary antibodies for 1 h. Finally, the membranes were washed and the proteins on the membrane were visualized and detected using Supersignal West Femto Chemiluminescent Substrate (Thermo Scientific) and a Gel Doc imaging system equipped with a XRS camera (Bio-Rad).

## 2.6. SAINT-O-Somes preparation

Dil-Saint-O-Somes (SAINT-O-Somes) were prepared from Mal-PEG<sub>2000</sub>-DSPE, DSPE-PEG<sub>2000</sub>, SAINT-C-18, POPC and cholesterol in a molar ratio of 1:4:18:37:40 in chloroform:methanol (9:1, v/v) as described previously [10]. Dil, a fluorescent label that incorporates in the liposome lipid bilayer, was added to the lipid mixture at 0.5 mol% of total lipid. In order to prepare rapamycin loaded-SAINT-O-Somes, desired amounts of rapamycin were simultaneously added to the lipid mixture based on the total amount of lipid (20 nmol rapamycin/ $\mu$ mol total lipid) and a drug-lipid film was created using a

rotary evaporator and subsequent drying under a nitrogen stream. The formed Lipid or drug/lipid films were hydrated by adding HBS buffer composed of 10 mM Hepes and 135 mM NaCl buffer pH 7.4. Followed by sonication for 10 min and incubation for 1h at room temperature. Unilamellar SAINT-O-Somes were prepared by multiple extrusion steps over polycarbonate membranes (Nuclepore, Pleasanton, CA, USA) at different pore size range (from 0.4  $\mu\text{m}$  to 0.1  $\mu\text{m}$ ). Part of the total SAINT-O-Somes preparation was conjugated with a specific antibody (targeted SAINT-O-Somes), the non-modified SAINT-O-Somes (non-targeted) were used as control. Mouse anti-human VCAM-1 (IgG1) was purified from supernatant produced by hybridoma E1/6aa2 as previously described for mouse anti-human E-selectin [9]. The monoclonal VCAM-1 antibody-producing hybridoma E1/6aa2 was kindly provided by Dr. M. Gimbrone Jr. (Harvard Medical School, Boston, MA, USA). The monoclonal mouse anti-human VCAM-1 antibody was thiolated by SATA and was coupled (15  $\mu\text{g}$  Ab / $\mu\text{mol}$  total lipid) to a maleimide group present at the distal end of the PEG chain as previously described [9]. The mixture was incubated for 1 hour at room temperature followed by incubation at 4°C overnight. The day after, free antibody and excess rapamycin exist within the samples, were removed by passing SAINT-O-Somes through a PD10 column followed by spinning in a Vivaspin centrifugal concentrator (Sartorius AG, Aubagne, France) with a molecular weight cut-off membrane of 300-kDa.

## 2.7. Characterization of SAINT-O-Somes

The phospholipid phosphate content of the SAINT-O-Somes was determined by phosphate assay [14, 15]. The mean particle size was measured using dynamic light scattering (DLS). Intensity-weighted average “z average” and the polydispersity index of the SAINT-O-Somes was determined by analyzing the correlation function (cumulants analysis) using Malvern software. All measurements were performed at a 90° angle. The zeta-( $\zeta$ ) potential of the SAINT-O-Somes was determined in 10mM Hepes buffer (pH: 7.4), by laser doppler electrophoresis using a Zetasizer Nano-Z (Malvern Instruments Ltd.).

Rapamycin content of the SAINT-O-Somes was determined by high performance liquid chromatography (Waters Acquity HPLC system, Waters Corporation, Milford, MA, USA) using a Sunfire C18, 5 $\mu$ m column (4.6 x 150mm) column, at a flow rate of 1 ml/min and a column temperature of 60°C. The isocratic mobile phase was composed of 70% acetonitrile and 30% water, UV detection was performed at 290 nm. Rapamycin encapsulation efficiency (EE) was calculated from the HPLC analysis.

$$EE = (\text{amount of measured Rapamycin} / \text{amount of added Rapamycin}) \times 100\%$$

Size, charge, polydispersity index, the amount of rapamycin encapsulated are listed in table 1. The coupling of anti-VCAM-1 antibody to rapamycin-SAINT-O-Somes was determined by Dot-blot as described before [16].

## 2.8. Flow cytometry

AB8/13 and MPC-5 cells differentiated for 15 days at 37°C were incubated with or without TNF $\alpha$  (10 ng/ml) for 24 h. The cells were detached from the plates by trypsinization and divided over FACS tubes and washed once with ice cold FACS buffer (PBS-containing 5% FCS). Next the cells were incubated with mouse anti-human-VCAM-1 (10  $\mu$ g/ml) (for AB8/13) and polyclonal rabbit anti-VCAM-1 antibodies (10  $\mu$ g/ml) (for MPC-5) for 45 min at 4°C followed by three washing steps with ice cold FACS buffer (PBS-containing 5% FCS). Control cells were incubated with mouse anti-rat-IgG2a (Clone OX35, hybridoma supernatant) (5  $\mu$ g/ml) antibodies (isotype) and quiescent cells were used as controls. Detection was established by incubation with a FITC-tagged rabbit anti-mouse IgG Fab<sub>2</sub> (Jackson immuno research, PA, USA) (for AB8/13) and alexa<sub>488</sub>-tagged goat-anti-rabbit (Life Technologies) (for MPC-5) secondary antibodies for 30 min at 4°C followed by washing three times with FACS buffer.

Similarly, to determine the association of the anti-VCAM-1-Dil-SAINT-O-Somes, quiescent or TNF $\alpha$  (10 ng/ml; 24 h)-activated AB8/13 cells were incubated with either anti-VCAM-1-Dil-SAINT-O-Somes or Dil-SAINT-O-Somes, all at a concentration of 80 nmol total lipid/ml for 4 h at 37°C. Quiescent cells

incubated with an equivalent volume of HN buffer were included as control. The cells were finally resuspended in 0.2 ml FACS buffer and analyzed by flow cytometry (Calibur, BD Biosciences, NJ, USA). The mean fluorescence intensity (MFI) was obtained after analysis with FlowJo™ software package (Tree Star Inc., OR, USA), version 7.6.5). The MFI values of the cells (TNF $\alpha$ -activated and quiescent) incubated with isotype control antibodies were subtracted from test samples. Results presented were determined from the mean of three independent experiments with duplicate incubations per experiment.

## 2.9. Fluorescence microscopy

For immunofluorescence detection of nephrin and Tie2, cytosots of primary podocytes were made on a microscope slide. To avoid nonspecific binding of antibodies, blocking with PBS-containing 1% BSA and 5% FCS was performed at room temperature. Guinea pig anti-mouse nephrin (Promega), rat anti-mouse Tie2 (Millipore) and rabbit-IgG (SouthernBiotech, Alabama, USA) (control) antibodies were added and incubated for 1 h at room temperature followed by incubation with respective secondary fluorescent antibodies Goat anti-guinea pig-FITC (SouthernBiotech), goat anti-rat-FITC (SouthernBiotech) and goat anti-rabbit-Alexa<sub>488</sub> (Life Technologies) for 30 min. The cells were washed three times with PBS after incubation with primary and secondary antibodies. Finally, the nuclei were stained with 4',6-diamidine-2'-phenylindole dihydrochloride (DAPI) in fluoroshield mounting medium (Abcam, Cambridge, UK). The cells were visualized and analyzed under a fluorescence microscope (DM RXA, Leica Microsystems AG, Wetzlar, Germany), and Leica Q600 Qwin software V01.06, respectively.

For fluorescence microscopy detection of Dil-SAINT-O-Somes, AB8/13 cells (16,000 cells/cm<sup>2</sup>) were seeded in Lab-Tek chamber slides (NUNC, Rochester, NY) and allowed for 15 days to differentiate at 37°C with medium refreshed every 5 days. Cells were activated with TNF $\alpha$  (10 ng/ml) for 24 h followed by incubation with anti-VCAM-1-Dil-SAINT-O-Somes and Dil-SAINT-O-Somes, both at a concentration of 80 nmol total lipid/ml for 4 h at 37°C. 10 min before the end of incubation, the

nuclei of the cells were stained with Hoechst 33342 (0.1 mg/ml in serum free medium; Invitrogen) followed by washing three times with ice cold PBS and one final wash with ice cold serum-free culture medium. The chamber was removed and a cover slip was placed on the slide followed by sealing with nail polish. The microscopic images were taken within 1 h.

### 2.10. Cell viability assay

Effects of rapamycin and rapamycin-SAINTO-Somes on cell viability of AB8/13 cells were determined by Sulforhodamine B (SRB) colorimetric assay [17]. AB8/13 cells (15 days differentiated at 37°C; 5000 cells/cm<sup>2</sup>) were either activated with TNF $\alpha$  (10 ng/ml) for 24 h or incubated in control medium (non-activated cells). Free rapamycin, rapamycin-SAINTO-Somes and anti-VCAM-1-rapamycin-SAINTO-Somes were added to triplicate wells at final concentrations of 8 or 32  $\mu$ M rapamycin after which the cells were incubated for an additional 24 h at 37°C. The cells were then fixed by addition of 10% (wt/vol) Trichloroacetic acid (TCA) at 4°C for 1 hour, followed by staining with 0.4% SRB stain in 1% acetic acid for 30min. Excess non-bound SRB dye was removed by multiple washings with 1% acetic acid after which the cells were dried at room temperature. The protein-bound dye was dissolved in unbuffered 10mMTris for 30 min and OD values were measured at 490–550 nm with a Spectrostar microplate reader. The values obtained were normalized versus control cells treated with TNF $\alpha$ .

### 2.11. Wound healing assay

Confluent 6-well culture plate with differentiated AB8/13 cells were incubated in the absence or presence of TNF $\alpha$  (10 ng/ml; 24 h) followed by treatment with free rapamycin, rapamycin-SAINTO-Somes and anti-VCAM-1-rapamycin-SAINTO-Somes at a concentration of 10 nmol/ml. After 12 h incubation with the different formulations, a scratch was made with a sterile 200  $\mu$ l pipette tip followed by a one-time wash with PBS after which cells were refreshed with fresh medium. The wound closure was followed in time for the next 24 h with images taken at 0, 6 and 24 h time points.



The extent of wound closure was determined by quantifying cell migration towards the wound using ImageJ.

## 2.12. Statistical analysis

Statistical analysis of the results was performed by two-tailed unpaired Student's *t*-test and one-way ANOVA. *p*-values <0.05 were considered to be significant. Data were analyzed with Graphpad prism (Graphpad software 5.0b, San Diego CA, USA).

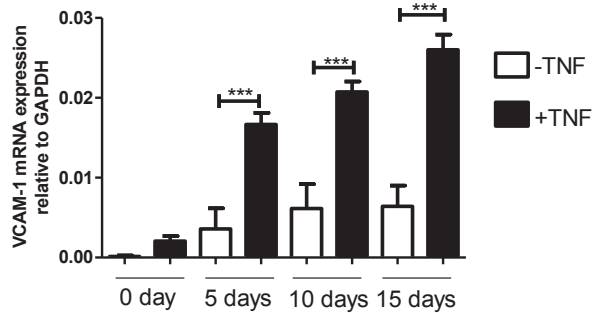
## 3. Results and Discussion

To investigate the possibilities of using VCAM-1 as a molecular target to deliver drugs specifically (in)to podocytes, we initiated an *in vitro* study using the human conditionally immortalized podocyte cell line AB8/13 [11]. These cells proliferate at 33°C and differentiate to the podocyte phenotype in 10-15 days at 37°C. In order to establish the differentiation of AB8/13 cells into a podocyte phenotype, mRNA and protein expression of the podocyte-specific markers (Wilms's Tumor-1 (WT-1) and synaptopodin) were analyzed after 15 days at 37°C. Differentiated AB8/13 cells expressed both WT-1 and synaptopodin, confirming AB8/13 as podocytes (Figure S1 and Figure S2).

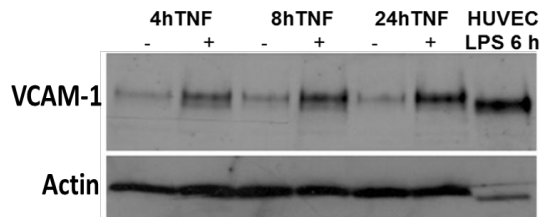
### 3.1. TNF $\alpha$ exposure induces the expression of VCAM-1 in differentiated AB8/13 podocytes

To study the prospects of using adhesion molecule VCAM-1 as a molecular target for podocyte-specific drug delivery purposes, mRNA was isolated from both TNF $\alpha$  (10 ng/ml; 4 h)-activated and quiescent AB8/13 cells up to 15 days of differentiation at 37°C. The concentration of TNF $\alpha$  (10 ng/ml) used in the present study was prior optimized in the laboratory for various cell type(s) (e.g. endothelial cells) and thus would enable to compare the podocytes data with other renal cells. Gene expression levels of VCAM-1 were compared to the housekeeping gene GAPDH. VCAM-1 was expressed by podocytes and the expression was significantly upregulated by TNF $\alpha$  (Figure 1A). Under the conditions studied, the expression of VCAM-1 gradually increased with the differentiation time of the cells and was at its maximum at 15 days of differentiation (Figure 1A).

A.



B.



C.

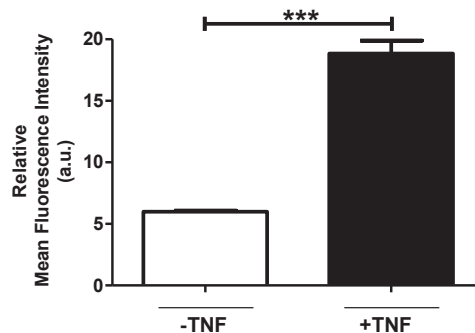


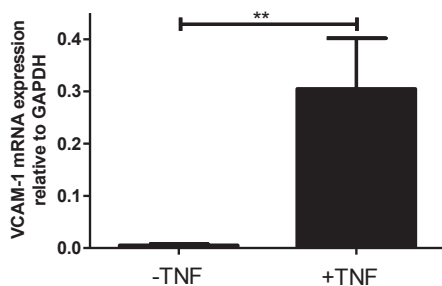
**Figure 1.** VCAM-1 is expressed in AB8/13 cells and the expression is increased upon TNF $\alpha$ -activation. (A) RT-qPCR analysis of human VCAM-1 mRNA expression. The AB8/13 cells were differentiated for 0, 5, 10, and 15 days at 37°C and treated with TNF $\alpha$  (10 ng/ml) for 4 h. (B) Western blot analysis of VCAM-1 (~110-kDa) and actin (~42-kDa) (loading control) proteins expression in cell lysate of AB8/13 cells, 15 days differentiated at 37°C in the absence (-) or presence (+) of TNF $\alpha$  for various time points. (C) FACS analysis of VCAM-1 protein in TNF $\alpha$ -activated (10 ng/ml; 24 h) and quiescent AB8/13 cells incubated with mouse antihuman-VCAM-1 for 45 min at 4°C followed by incubation with fluorescently-labelled secondary antibody. \* $p < 0.001$ .

An approximately 4-fold increase in VCAM-1 mRNA expression was observed in the presence of TNF $\alpha$  when compared to quiescent cells. Analysis of VCAM-1 protein expression in the differentiated AB8/13 cells corroborated the mRNA data that in the absence of TNF $\alpha$  there is basal expression of VCAM-1 and that the expression significantly increases in the presence of TNF $\alpha$  (Figure 1B and Figure 1C). To confirm the expression of VCAM-1 protein by podocytes, also flow cytometry was performed. Figure 1C shows that anti-VCAM-1 antibodies bound to both activated and quiescent cells. There is a 3-fold higher expression of VCAM-1 in TNF $\alpha$ -activated podocytes compared to quiescent cells (Figure 1C). The binding of VCAM-1 specific antibodies to quiescent cells can be attributed to the basal expression of VCAM-1 in this condition. These results indicate that VCAM-1 can be used as a molecular target to address inflammation activated podocytes using nanocarriers.

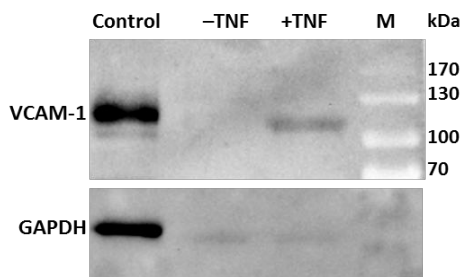
### **3.2. VCAM-1 is also expressed in a mouse podocyte cell line and primary mouse podocytes**

We investigated the expression of VCAM-1 both in a conditionally immortalized mouse podocyte cell line (MPC-5) that was differentiated for 12 days at 37°C and in primary mouse podocytes. TNF $\alpha$  was added to the incubation during the last 24 h before isolation of mRNA or protein. RT-qPCR analysis of podocyte-specific markers synaptopodin and WT-1 showed the expression of both genes confirming MPC-5 cells as podocytes (Figure S3). Similar to AB8/13 cells, MPC-5 cells expressed VCAM-1 and the expression was significantly upregulated in the presence of TNF $\alpha$  (Figure 2A). Western blot analysis and flow cytometry of MPC-5 cells are in accordance with the gene expression results, showing significant VCAM-1 protein levels in these cells upon activation with TNF $\alpha$  (Figure 2B and Figure 2C).

A.



B.



C.

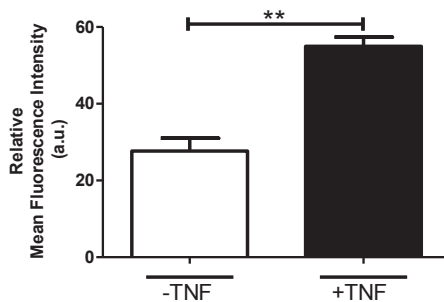


**Figure 2.** VCAM-1 is expressed by the mouse podocyte cell line MPC-5. (A) mRNA expression of VCAM-1 in the absence (-) or presence (+) of TNF $\alpha$  (10 ng/ml; 24 h) as analyzed by RT-qPCR analysis. (B) Western blot analysis of protein extracts of MPC-5 cells that were incubated in the absence (-) or presence (+) of TNF $\alpha$  (10 ng/ml; 24 h) prior to harvesting. M and control indicate respectively, pre-stained molecular weight marker and positive control (HUVEC cells activated with LPS for 6 h). (C) FACS analysis of VCAM-1 expression by MPC-5 cells using anti-VCAM-1 antibody by flow cytometry. \* $p < 0.001$ .

Primary mouse podocytes were grown from glomeruli isolated from kidneys of mice, as described in the material & methods section. After 4-5 days of incubation at 37°C in podocyte-specific medium, cells that sprouted from the glomeruli proliferated to confluency (Figure 3A). In order to separate the podocytes from the glomerular endothelial cells, anti-ICAM-2 antibody coated magnetic beads (which bind to ICAM-2, a surface marker exclusively expressed by endothelial cells) were used for the selection and removal of endothelial cells, and the cells that did not bind to the anti-ICAM-2 beads were seeded in podocyte-specific medium. Cytospots from these ICAM-2 negative fractions were stained with podocyte and endothelial cell-specific antibodies. Immunofluorescence analysis showed specific detection of the podocyte-specific marker nephrin confirming that the cultured cells had a podocyte-like phenotype (Figure 3B). In contrast, cytospots stained for Tie2 that is restrictedly expressed by endothelial cells showed no fluorescence indicating that there was no contamination with endothelial cells (Figure 3C and Figure 3D). Primary podocytes were either grown in quiescence or activated by TNF $\alpha$  for 6 h and RNA was isolated to determine the expression of podocyte and endothelial markers and VCAM-1. In accordance with the data obtained with AB8/13 cells and MPC-5 cells, VCAM-1 was also expressed in mouse primary podocytes and the expression was upregulated in the presence of TNF $\alpha$  (Figure 3E). RT-qPCR analysis showed the expression of podocyte-specific genes (WT-1 and synaptopodin) confirming these primary cells as podocytes (Figure S4). There is minute expression of the endothelial-specific genes CD31 and VEcadherin confirming that there is hardly any contamination of glomerular endothelial cells in the primary podocyte culture (Figure S4). Since the yield of primary podocytes after isolation from mouse kidneys is very limited, we only performed gene expression analysis and immunofluorescence of VCAM-1 in primary podocytes.

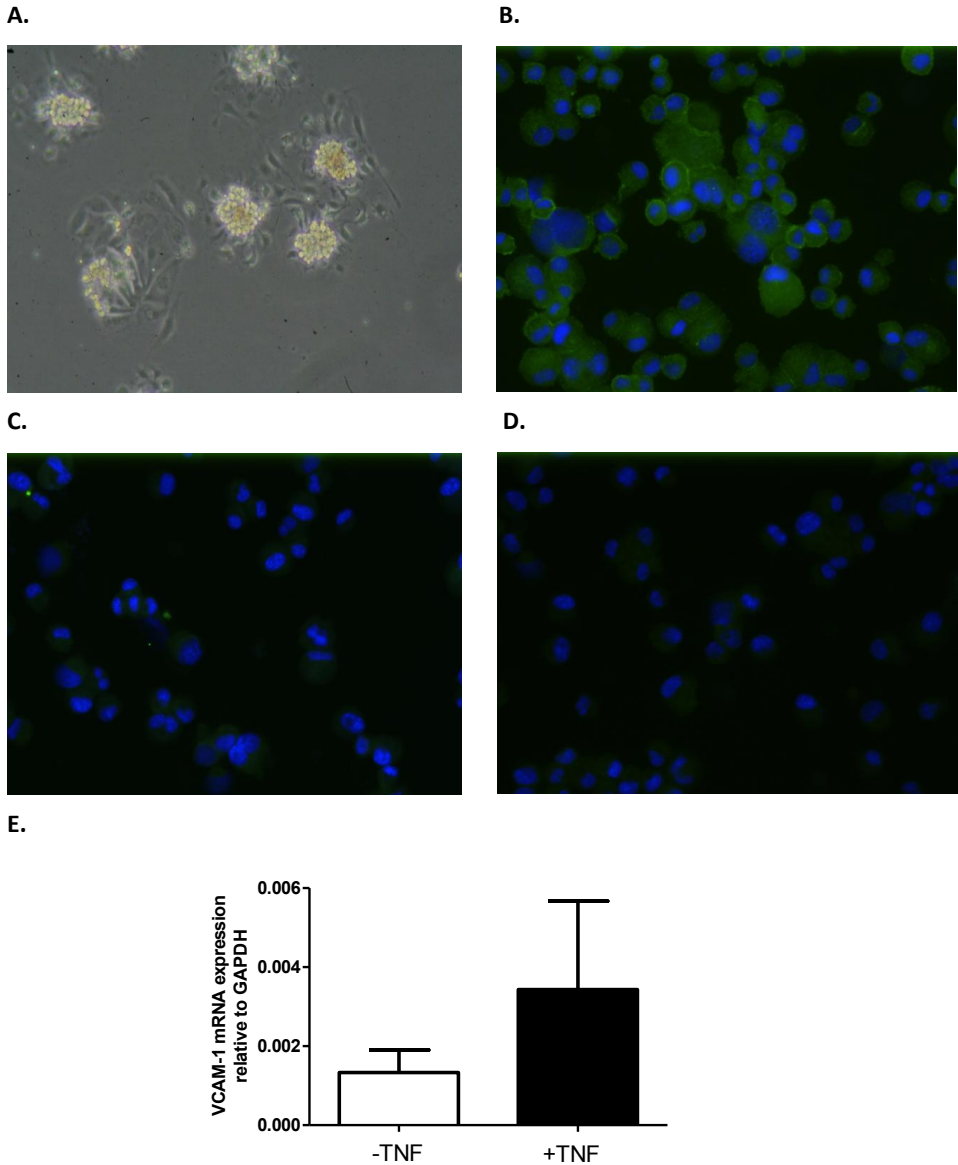


**Figure 3.** VCAM-1 is expressed in primary mouse podocytes. (A) Phase-contrast view of glomerular outgrowths of isolated glomeruli from mouse kidney, 2 days after seeding in podocyte-specific medium. Immuno-staining of cytospots of the ICAM-2 negative fraction after ICAM-2 re-beading, detecting nephrin (B), while the endothelial marker Tie2 (C) is not detected. Panel (D) shows background staining with control rabbit-IgG antibodies (and does not detect anything). Antibodies that specifically bound to the cells are stained in green. Nuclei were stained in blue with DAPI. (E) VCAM-1 mRNA expression in mouse primary podocytes in the absence (-) or presence (+) of TNF $\alpha$ , as determined by RT-qPCR. Data are presented as mean values  $\pm$  sd, n = 3 from three independent experiments.

Based on these *in vitro* gene and protein expression results in AB8/13, MPC-5, and primary mouse podocytes, we concluded that VCAM-1 is expressed by podocytes and that the expression was significantly upregulated by activation of the cells with the pro-inflammatory cytokine TNF $\alpha$ . This led us to hypothesize that VCAM-1 can be exploited as a molecular target to specifically deliver drugs (in) to podocytes using a nanocarrier system, especially since VCAM-1 receptors were shown to be internalized by cells *via* clathrin-mediated endocytosis [18]. This is a prerequisite for an efficient nanocarrier to successfully deliver its contents inside its target cell [19].

### 3.3. Association of anti-VCAM-1-Dil-Saint-O-Somes with inflammation activated AB8/13 podocytes

To deliver therapeutic compounds into podocytes, we used a SAINT-based lipid drug carrier system called SAINT-O-Somes as the carrier of choice. Anti-VCAM-1 antibodies were coupled to the distal end of the polyethylene glycol molecules of the SAINT-O-Somes to make them inflammation activated podocyte specific. To investigate the binding and association by the podocytes, SAINT-O-Somes were labeled with Dil in the lipid bilayer. The diameter of Dil-SAIN-O-Somes and anti-VCAM-1-Dil-SAIN-O-Somes was  $95\pm 2$  and  $115\pm 11$  nm, respectively.  $45\pm 3$   $\mu\text{g}$  of anti-VCAM-1 antibodies were coupled per  $\mu\text{mol}$  total lipid of SAINT-O-Somes, which was comparable to earlier studies in which siRNA was incorporated in anti-VCAM-1 antibody harnessed SAINT-O-Somes [9].

Anti-VCAM-1-Dil-SAIN-O-Somes (targeted) and Dil-SAIN-O-Somes (non-targeted) were incubated for 4 h with quiescent and TNF $\alpha$ -activated, 15 days differentiated AB8/13 cells at 37°C. Fluorescence microscopy analysis showed association of anti-VCAM-1-Dil-SAIN-O-Somes, both in quiescent and TNF $\alpha$ -activated podocytes, with the association with activated cells being much higher (Figure 4C and Figure 4D). In contrast, non-targeted-Dil-SAIN-O-Somes were hardly associated with either quiescent or TNF $\alpha$ -activated cells (Figure 4A and Figure 4B), indicating specificity of targeted-Dil-SAIN-O-Somes for podocytes.

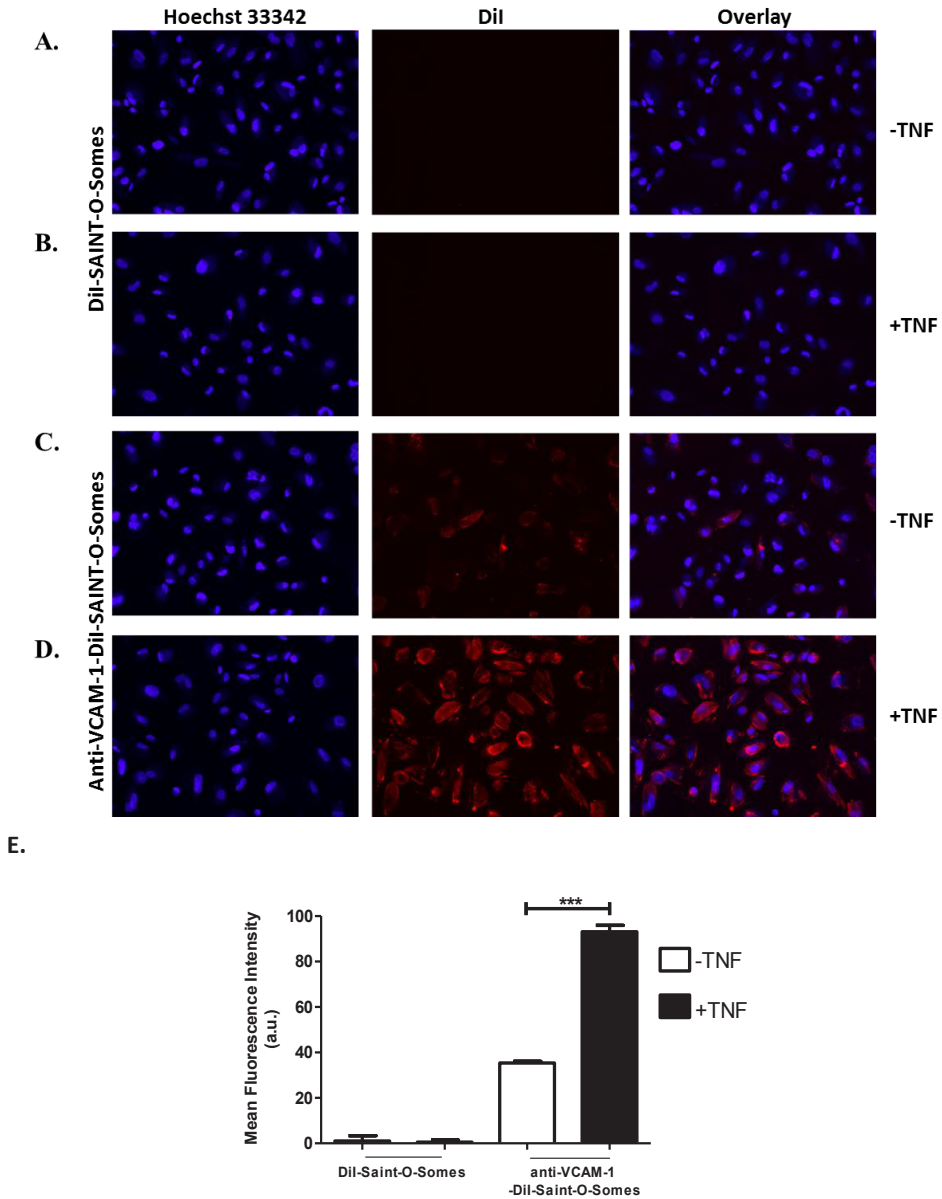


**Figure 4.** Anti-VCAM-1-Dil-Saint-O-Somes bind to AB8/13 cells. Dil-SAINT-O-Somes (A, B) and anti-VCAM-1-Dil-SAINT-O-Somes (C, D) were incubated for 4 h at 37°C with AB8/13 cells in the absence (-) (A, C) or presence (+) (B, D) of TNF $\alpha$  (10 ng/ml; 24 h). The nuclei were stained blue with Hoechst 33342. Original magnification 200x. (E) Quantification of binding of anti-VCAM-1-Dil-SAINT-O-Somes or Dil-SAINT-O-Somes to AB8/13 cells. Cells incubated in equal volumes of HN buffer were taken as controls and their values were subtracted from test samples. The mean fluorescence intensity (MFI) was determined by FACS and analyzed by FlowJoTM. \*p <0.001.



These results were supported by the flow cytometry results obtained at 37°C under similar experimental conditions. Association of anti-VCAM-1-Dii-SAINT-O-Somes to TNF $\alpha$ -activated podocytes was increased almost 3-fold and more than 150-fold compared to quiescent cells and cells incubated with non-targeted-SAINT-O-Somes, respectively (Figure 4E). The non-targeted-SAINT-O-Somes were hardly associated with the AB8/13 cells, either in the absence or presence of TNF $\alpha$ . These results demonstrate proof-of-concept of targeting podocytes using anti-VCAM-1 nanocarriers.

### 3.4. Characterization of Rapamycin-SAINT-O-Somes (VACM-1 targeted and non-targeted)

Physicochemical properties of SAINT-O-Somes are listed in table. 1. With DLS analyses we demonstrated that average SAINT-O-Some size was in range of 120-130 nm with corresponding polydispersity index below 0.1. The zeta potential was approximately +11mV which is due to the combined structural properties of SAINT-C18 and PEG2000-DSPE. The Rapamycin concentration in liposomal suspensions was determined by a high performance liquid chromatography-ultraviolet (HPLC-UV) method after disruption of liposomes in acetonitrile (see table. 1). The encapsulation of Rapamycin did not affect the physicochemical properties of the liposomes.

**Table 1.** Characterization of Rapamycin-SAINT-O-Somes

Samples	Size (nm)	Zeta potential (mV)	Polydispersity index	Rapamycin EE <sup>a</sup> (%)
Anti-VCAM-1-Rapamycin-SAINT-O-Somes	128 ± 4	10.8 ± 0.9	0.06 ± 0.01	73 ± 0.7
Rapamycin- SAINT-O-Somes	122 ± 2	11.0 ± 0.3	0.07 ± 0.01	71 ± 1.2

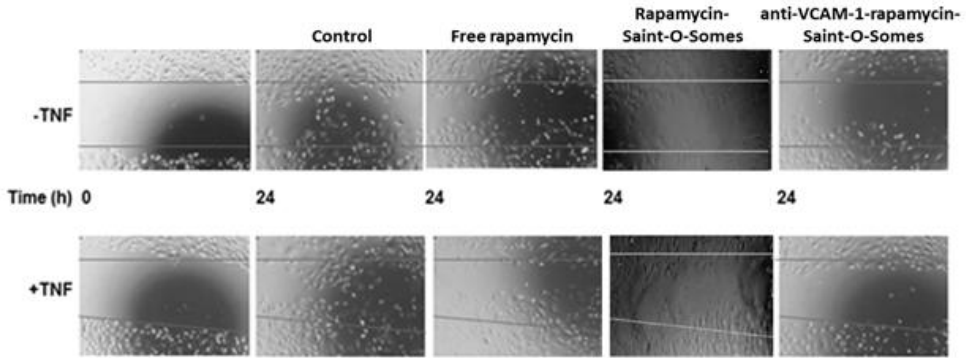
Data are represented as averages (± SD) of three independently made formulations. <sup>a</sup> Encapsulation efficiency.

### 3.5. Effect of anti-VCAM-1-rapamycin-SAINT-O-Somes on inflammation activated AB8/13 podocytes

It has been proposed that mTOR is involved in podocyte injury [8]. The delivery of mTOR inhibitor rapamycin to podocytes hence will be an attractive approach to treat podocyte injury. One of the techniques to study rapamycin effects in cells is studying migration of the cells. Rapamycin was encapsulated in the lipid-bilayer of the anti-VCAM-1-SAINT-O-Somes and control SAINT-O-Somes. The coupling of VCAM-1 specific antibody to rapamycin-SAINT-O-Somes was confirmed by Dot-blot assay using anti-VCAM-1 antibody detection of the protein (Figure S5).

To test the effects of drug loaded anti-VCAM-1-rapamycin-SAINT-O-Somes and compare these with drug loaded non-targeted-SAINT-O-Somes and free drug, a wound healing assay was performed. Light microscopic images from the wound healing assay show that AB8/13 cell migration was almost completely inhibited in TNF $\alpha$ -activated cells treated with anti-VCAM-1-rapamycin-SAINT-O-Somes indicating a cell migration inhibitory effect of rapamycin when applied in the SAINT-O-Somes formulation (Figure 5A). We also observed partial inhibition of cell migration in cells that had not been pretreated with TNF $\alpha$  which is most likely due to the basal expression of VCAM-1 in these cells (Figure 4). Free rapamycin and non-targeted-SAINT-O-Somes loaded with rapamycin showed partial response in TNF $\alpha$  pretreated cells, but these effects were less pronounced as compared to the anti-VCAM-1-rapamycin-SAINT-O-Somes (Figure 5A). Quantification of closure of the wound area showed a 3-fold inhibition of the wound closure in 24 h by the targeted formulation when compared to control cells (Figure 5B). The observed cell migration inhibitory effects are likely due to the inhibition of the actin cytoskeleton by rapamycin [20].

A.



B.

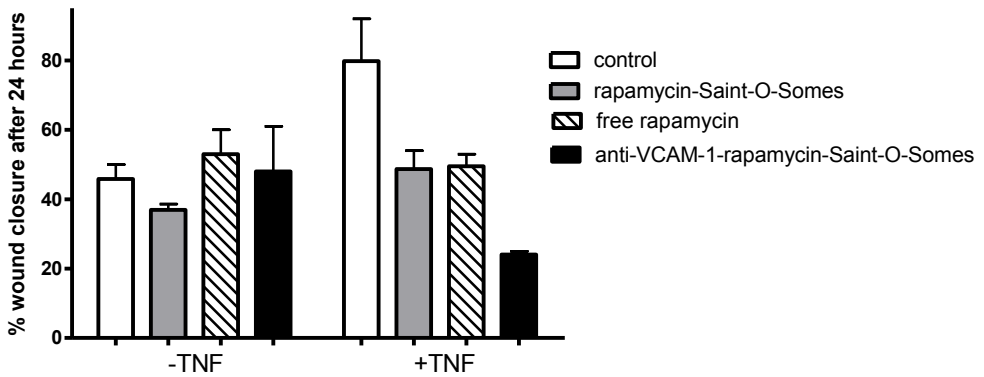


**Figure 5.** Effect of anti-VCAM-1-rapamycin-SAINT-O-Somes on AB8/13 cells. (A) A scratch was made into confluent cell cultures of AB8/13 in the absence (-) or presence (+) of TNF $\alpha$  (10 ng/ml; 24 h). These cells were first treated with HN buffer (control), free drug, rapamycin-SAINT-O-Somes and anti-VCAM-1-rapamycin-SAINT-O-Somes for 12 h, after which a wound was induced and the wound closure was followed in time up to 24 h. (B) The number of cells that had migrated into the scratch area (=) were quantified from two independent experiments by ImageJ.

Cell viability studies for 24h showed that rapamycin loaded SAINT-O-somes were not toxic (Figure S6; more than 80% cell viability up to concentrations equivalent to 30 nmol/ml rapamycin). Of note,

free rapamycin in combination with TNF $\alpha$  pretreatment reduced podocyte viability by 50%, but this is not observed in the wound healing assay which only lasted for 24h.

#### 4. Conclusion

Together these experiments provide conceptual proof that VCAM-1 could be employed as a molecular target to deliver therapeutic compounds into injured podocytes. As mentioned earlier, during podocytopathies the fenestrations of the GFB also widen enabling the passage of nanocarriers such as liposomes to reach the injured podocytes. In glomerular diseases, not only podocytes but rather all GFB cells, kidney arterioles and venules are injured leading to the expression of various adhesion molecules including VCAM-1. Earlier studies demonstrate that VCAM-1 expression is upregulated in vascular endothelial cells under inflammatory conditions [9, 21, 22]. Hence, one can expect that rapamycin loaded anti-VCAM-1-SAINTOsomes will be internalized by inflammation triggered endothelial cells, similar to previously reported siRNA loaded anti-VCAM-1-SAINTOsomes [9, 23]. The expression of VCAM-1 on (subsets of) endothelial cells and on activated podocytes has obviously implications for targeted drug delivery. Although one would like to differentiate between uptake in endothelial cell and podocytes from a scientific proof-of-concept point-of-view, such an exploration in animal models may pose several technical hurdles. First, renal function should largely be preserved in the early stages of the experimental animal model which infers that only a subset of glomeruli (and also the podocytes and endothelial cells) will be disease affected. Podocyte- and endothelium- associated expression of VCAM-1 will furthermore strongly depend on the progression of renal disease in the experimental model. We have earlier demonstrated that the expression of VCAM-1 in glomerular endothelial cells is low in experimental glomerulonephritis, likely because of high microRNA levels which have been shown to down regulate VCAM-1 protein expression [24]. Podocytes and endothelial cell only constitute a small percentage of the total kidney mass, and accumulation of anti-VCAM-1-SAINTOsomes in these respective cell types can be demonstrated by immunohistochemical staining. This strategy proved successful for

demonstrating *in vivo* glomerular endothelial cell targeting by anti-E-selectin liposomes [25]. Identification of the cell type involved in glomerular accumulation of the nanocarriers can be done by double staining with podocyte- or endothelium-specific cell markers to get answers on which cell type actually has accumulated the immunoliposomes. Moreover, since both these cell types play an important role in inflammatory processes in the kidney we hypothesize that drug delivery to these cell types may lead to additive therapeutic effects, providing that the delivered drug has beneficial effects in both cell types. Rapamycin may be a good candidate for such a nanocarriers-based approach. We presume that an anti-VCAM-1-coated nanocarrier could be an option to therapeutically address more than one cell type under inflammatory conditions in kidney diseases. Establishing podocyte targeting *in vivo* in a relevant disease model is an obvious and interesting perspective for future research.

## 5. Acknowledgements

This work is supported by NanoNextNL, a micro and nanotechnology consortium of the Government of the Netherlands and 130 partners (project 03D.07). The authors would like to thank Henk Moorlag Peter Zwiers and Henriëtte Morselt for expert technical assistance.

## Supplementary information

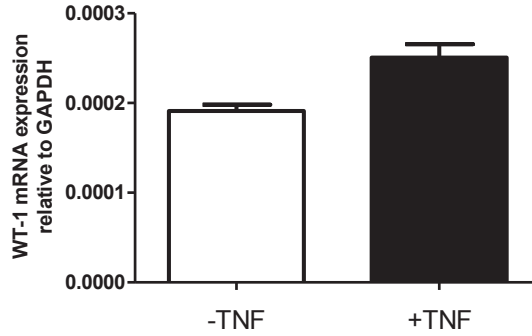


**Figure S1.** Wilm's Tumor-1 (WT-1) is expressed by AB8/13 cells. AB8/13 cells were allowed to differentiate for 15 days at 37°C and RNA was isolated from cells incubated in the absence or presence of TNF $\alpha$  (10 ng/ml, 24 h). WT-1 mRNA expression relative to GAPDH was analyzed by RT-qPCR. Data are presented as mean values  $\pm$  SD, n = 3 from three independent experiments.

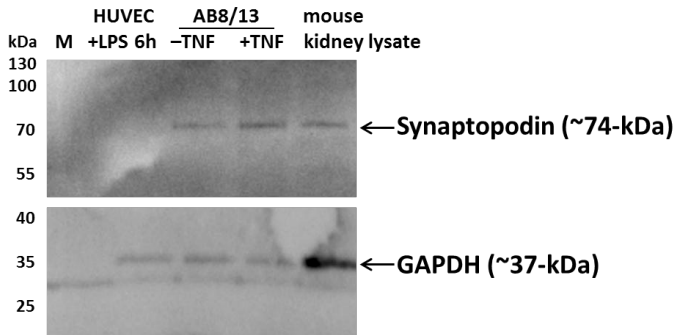


**Figure S2.** AB8/13 cells express the podocyte-specific marker synaptopodin. Synaptopodin detection on a Western blot loaded with cell lysates of AB8/13 cells, 15 days differentiated at 37°C in the absence (-) or presence(+) of TNF $\alpha$  for 24 h (10 ng/ml), respectively. The molecular mass (kDa) of pre-stained marker (M) is indicated at the left hand side of the blot. 6 h LPS-activated HUVEC cell lysate and mouse kidney lysate were used as negative and positive controls, respectively. Arrows indicate the bands of synaptopodin and GAPDH as loading control.

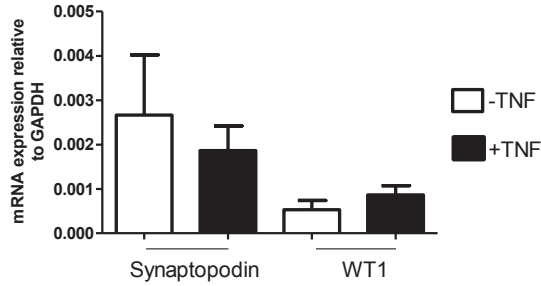


**Figure S3.** Mouse podocyte cell line (MPC-5) expresses podocyte markers. mRNA expression of mouse podocyte-specific markers synaptopodin and WT-1 in the absence (-) or presence (+) of TNF $\alpha$  (10 ng/ml; 24 h) relative to mouse GAPDH, as analyzed by RT-qPCR analysis. Data are presented as mean values  $\pm$  SD, n = 3 from three independent experiments.

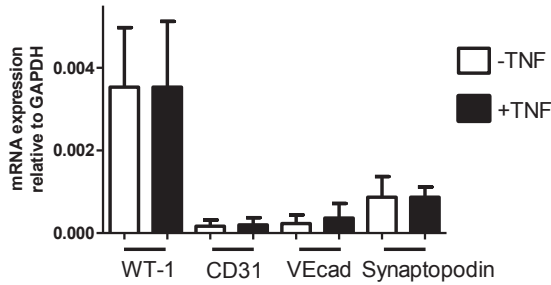


**Figure S4.** WT-1 and synaptopodin expression by primary mouse podocytes. RNA was isolated from the ICAM-2 negative glomerular cell fraction and analyzed for the mRNA expression of podocyte (WT-1 and synaptopodin) and endothelial (CD31 and VEcadherin) cell-specific markers, relative to mouse GAPDH, using RT-qPCR. Data are presented as mean values  $\pm$  SD, n=3 from three independent isolates.

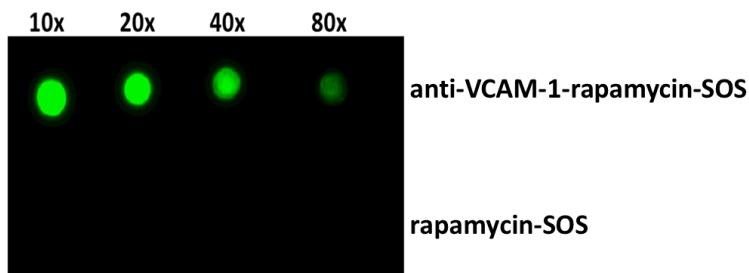


**Figure S5.** Dot-blot assay to demonstrate anti-VCAM-1 antibody conjugation to rapamycin- SAINT-O-Somes. Anti-VCAM-1-rapamycin- SAINT-O-Somes and rapamycin-SAINTO-Somes were loaded in dilutions ranging from 10x-80x. The successful coupling of anti-VCAM-1 antibody to rapamycin-SAINTO-Somes was confirmed using fluorescent secondary antibody detecting the anti-VCAM-1 antibody (green). Rapamycin-SAINTO-Somes without anti-VCAM-1 antibody conjugated did not yield a signal.

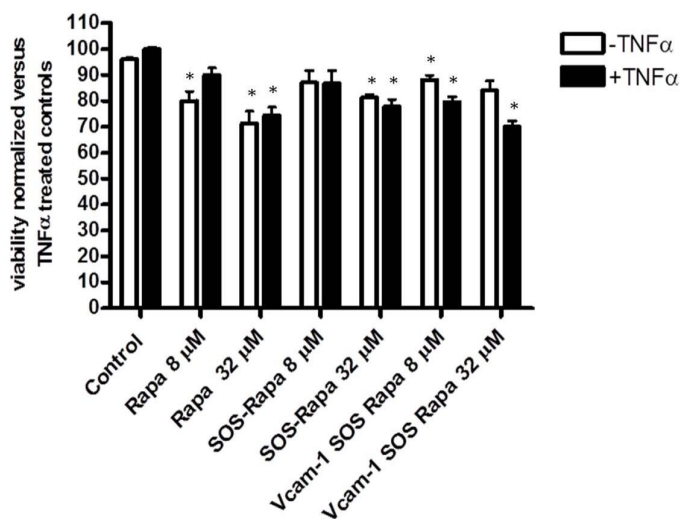


**Figure S6.** Effect of rapamycin on viability of AB8/13 cells. Cell viability of AB8/13 podocytes, 15 days differentiated at 37°C, incubated with rapamycin formulations for 24h. Cell viability was assessed by SRB staining and normalized to TNF $\alpha$  treated control cells. Data shown are mean  $\pm$ SEM (n = 3 for drug treated cells and n = 48 for controls). \* p < 0.05 versus resting or activated control podocytes.



## 6. References

1. Leeuwis JW, Nguyen TQ, Dendooven A, Kok RJ, Goldschmeding R. Targeting podocyte-associated diseases. *Adv Drug Deliv Rev.* 2010;62(14):1325-36.
2. Siddiqi FS AA. Endothelial-podocyte crosstalk: the missing link between endothelial dysfunction and albuminuria in diabetes. *Diabetes* 2013;62:3647-55.
3. Briganti EM RG, McNeil JJ, Atkins RC, Chadban SJ. . Risk of renal allograft loss from recurrent glomerulonephritis. *N Engl J Med* 2002;347:103-9.
4. Haraldsson B JM. Glomerular filtration barrier. *Curr Opin Nephrol Hypertens.* 2009;18:331-5.
5. Chiang WC GT, Altintas MM, Sever S, Ruiters MH, Reiser J Establishment of protein delivery systems targeting podocytes. *PLoS ONE.* 2010;5(e11837).
6. Hauser PV PJ, Kaiser C, Krofft RD, Brinkkoetter PT, Hudkins KL, et al. Novel siRNA delivery system to target podocytes in vivo. *PLoS ONE* 2010;5(e9463).
7. Canaud G BF, Viau A, Treins C, Baron W, Nguyen C, et al. AKT2 is essential to maintain podocyte viability and function during chronic kidney disease. *Nat Med.* 2013;19:1288-96.
8. Fogo AB, The targeted podocyte. *J Clin Invest.* 2011;121:2142-5.
9. Kowalski PS LL, Morselt HW, Leus NG, Ruiters MH, Molema G, et al. Anti-VCAM-1 and anti-E-selectin SAINT-O-Somes for selective delivery of siRNA into inflammation-activated primary endothelial cells. *Mol Pharm.* 2013;10:3033-44.
10. Adrian JE MH, Süß R, Barnert S, Kok JW, Asgeirsdóttir SA, et al. Targeted SAINTO-Somes for improved intracellular delivery of siRNA and cytotoxic drugs into endothelial cells. *J Control Release* 2010;144:341-9.
11. Saleem MA OHM, Reiser J, Coward RJ, Inward CD, Farren T, et al. A conditionally immortalized human podocyte cell line demonstrating nephrin and podocin expression. *J Am Soc Nephrol.* 2002;13:630-8.
12. Mundel P RJ, Zúñiga Mejía Borja A, Pavenstädt H, Davidson GR, Kriz W, et al. Rearrangements of the cytoskeleton and cell contacts induce process formation during differentiation of conditionally immortalized mouse podocyte cell lines. *Exp Cell Res.* 1997;236:248-58.
13. Jin E LJ, Suehiro J, Yuan L, Okada Y, Nikolova-Krstevski V, et al. Differential roles for ETS, CREB, and EGR binding sites in mediating VEGF receptor 1 expression in vivo. *Blood.* 2009;114:5557-66.
14. Böttcher CJF VgC. A rapid and sensitive sub-micro phosphorus determination. *Analytica Chimica Acta.* 1961;24:203-4.
15. Rouser G FS, Yamamoto A Two dimensional thin layer chromatographic separation of polar lipids and determination of phospholipids by phosphorus analysis of spots. *Lipids.* 1970;5:494-6.
16. Khattree N RL, Goldberg AFX., . Membrane curvature generation by a C-terminal amphipathic helix in peripherin-2/rds, a tetraspanin required for photoreceptor sensory cilium morphogenesis. *J Cell Sci* 2013;126:4659-70.

17. Vichai V KK. Sulforhodamine B colorimetric assay for cytotoxicity screening. *Nat Protocols*. 2006;1:1112–6.
18. Ricard I PM, Dupuis G VCAM-1 is internalized by a clathrin-related pathway in human endothelial cells but its alpha 4 beta 1 integrin counter-receptor remains associated with the plasma membrane in human T lymphocytes. *Eur J Immunol*. 1998;28:1708–18.
19. Sapra P AT. Internalizing antibodies are necessary for improved therapeutic efficacy of antibody-targeted liposomal drugs. *Cancer Res*. 2002;62:7190–4.
20. Vollenbröker B GB, Wolfgart M, Saleem MA, Pavenstädt H, Weide T mTOR regulates expression of slit diaphragm proteins and cytoskeleton structure in podocytes. *Am J Physiol Renal Physiol* 2009;296:F418–F26.
21. Kuldo JM ÁS, Zwiers PJ, Bellu AR, Rots MG, Schalk JA, et al. Targeted adenovirus mediated inhibition of NF- $\kappa$ B-dependent inflammatory gene expression in endothelial cells in vitro and in vivo. *J Control Release*. 2013;166:57–65.
22. Gao H-X CS, Burkly LC, Jakubowski A, Jarchum I, Banas B, et al. TNF-like weak inducer of apoptosis (TWEAK) induces inflammatory and proliferative effects in human kidney cells. *Cytokine*. 2009;46:24–35.
23. Kowalski PS ZP, Morselt HW, Kuldo JM, Leus NG, Ruiters MH, et al. Anti-VCAM-1 SAINT-O-Somes enable endothelial-specific delivery of siRNA and downregulation of inflammatory genes in activated endothelium in vivo. *J Control Rel*. 2014;176:64–75.
24. Asgeirsdóttir SA vSC, Kurniati NF, Zwiers PJ, Heeringa P, van Meurs M, et al. . Micro-RNA-126 contributes to renal microvascular heterogeneity of VCAM-1 protein expression in acute inflammation. *Am J Physiol Renal Physiol*. 2012;302:F1630–F9.
25. Ásgeirsdóttir SA ZP, Morselt HWM, Moorlag HE, Bakker HI, Heeringa P, et al. Inhibition of proinflammatory genes in anti-GBM glomerulonephritis by targeted dexamethasone-loaded AbEsel liposomes. *Am J Physiol: Renal Physiol*. 2008;294:F554–F61.

## **Chapter 5**

### **PLGA-PEG nanoparticles for targeted delivery of an mTOR/PI3kinase inhibitor, NVP-BEZ235, to inflamed endothelium**

Shima Gholizadeh, Wim E. Hennink, Jan. A. A. M. Kamps, Robbert J. Kok, submitted for publication.

**Abstract**

NVP-BEZ235 (also referred to as: 'BEZ235' or 'BEZ') is a novel dual mTOR/PI3K inhibitor, which can be considered as important drug candidate for the treatment of inflammatory disorders. The major drawback associated with the use of BEZ is its low systemic bioavailability when administered orally. This work focuses on formulation of BEZ-loaded nanoparticles composed of a blend of poly(D,L-lactide-co-glycolide) (PLGA) and poly(D,L-lactide-co-glycolide)-poly(ethylene glycol)-2000 (PLGA-PEG), decorated with an antibody that targets upregulated E-selectin on TNF- $\alpha$  activated endothelial cells. The aim of the study was to investigate whether the prepared targeted BEZ loaded NPs are able to bind and taken up by the activated endothelial cells for intracellular release of BEZ and subsequent inhibition of endothelial cell proliferation. The nanoparticles were prepared using oil/water emulsion solvent evaporation method, and were subsequently characterized for yield, encapsulation efficiency, morphology, particle size, drug-polymer interaction and *in vitro* drug release profiles. A targeted formulation was developed by conjugation of a SATA-modified mouse-anti human E-selectin antibody to the distal end of the SPDP-PEG groups present on the surface of the nanoparticles. Different formulation parameters were systematically varied in order to obtain nanoparticles with the desired characteristics. Our results show the successful preparation of spherical PLGA/PLGA-PEG nanoparticles loaded with BEZ. The particle size distribution showed a range from 250 to 360 nm with a high (>75%) BEZ encapsulation efficiency and around 35% of BEZ was released within 10 days at 37°C in a medium containing 5% BSA. Evaluation of efficacy of these BEZ-loaded nanoparticles was carried out in TNF- $\alpha$  activated endothelial cells. CLSM analysis showed that cellular uptake of the targeted nanoparticles and subsequent internalization was higher than that of similar nanoparticles without targeting ligands (i.e. non-targeted). Cell functional assays, including migration assay and western blot analysis, revealed that the targeted nanoparticles loaded with BEZ had a more pronounced effect on the activated endothelial cells compared to the non-targeted BEZ-loaded nanoparticles. In conclusion, E-selectin targeted nanoparticle-based formulation of BEZ has high potential in anti-inflammatory therapy.

## 1. Introduction

In many inflammatory disorders endothelial cells are the key players in induction and progression of the disease [1]. Upon inflammation, pro-inflammatory cytokines are secreted, which induce deregulation of various signaling pathways in endothelial cells [2-4]. One of these pathways is the PI3K/AKT/mTOR signaling cascade, deregulation of which causes proliferation, malfunctioning and morphological changes of endothelial cells (ECs), cumulating in fibrotic tissue formation as a long term consequence [4-7]. It is important to note that the PI3K pathway is involved in many different cellular functions under normal physiological conditions, including cell growth and proliferation, inhibition of apoptosis, cell metabolism, and intracellular signal transduction [8]. Many of these functions occur as a result of PI3K's interplay with its downstream effectors, Akt and mTOR, the latter being a kinase that is involved in the regulation of cell growth, angiogenesis, and metabolism [9].

Recently, kinases that act downstream of cytokine receptors (e.g. tyrosine kinase) have become new targets to tame inflammation. Small molecular inhibitors of intracellular signaling kinases are under investigation as chemotherapeutics for anti-inflammatory treatment [10]. However, many intracellular signaling molecules are involved in cellular functions both under normal and under pathological conditions. For this reason, application of a (tyrosine) kinase inhibitor that selectively blocks (tyrosine) kinases that are involved in the aberrant signaling can increase the potency and decrease the side effects compared to non-selective (tyrosine) kinase inhibitors [10-11]. Recent studies have shown that inhibition of activated PI3K/Akt and mTOR signaling in inflamed endothelial cells resulted in diminished immune responses by suppressing the secretion of pro-inflammatory cytokines [6, 12-13].

NVP-BEZ235 (BEZ) is a synthetic imidazoquinoline derivative with a hydrophobic character (LogP = 5.2) (Figure 1). It is a drug candidate under phase I/II clinical trials as an anti-cancer therapeutic with a highly selective, reversible inhibitory effect on class I PI3K, and mTORC complexes (mTORC1 and mTORC2)[14-18]. However, the clinical potential of BEZ is limited due to its low bioavailability

after oral administration and pharmacokinetic variability among patients [17, 19]. In order to increase the therapeutic efficacy and reduce side effects of (hydrophobic) drugs and drug candidates, various types of drug carrier systems have been developed over the past decade. Typical examples of such carrier systems are polymeric micro/nanoparticles, (polymeric) micelles, and liposomes [20-22]. Polymeric nanoparticles in particular have attracted a lot of interest in recent years [23-24]. Based on the polymer composition they can be used to dissolve/encapsulate (hydrophobic) drug molecules and biotherapeutics (e.g. pharmaceutical proteins and nucleic acid based drugs), which enables enhanced circulation time in the bloodstream, sustained drug release, and (active) targeting to specific sites in the body [23-25]. Poly(lactide-co glycolide) (PLGA) with and without a PEG block is frequently used for the design of drug carrier systems due to their good biocompatibility and biodegradability [26-28].

Nanoparticles with site-selective ligands bound to their surface have been shown to improve the desired site-selective drug delivery, while also increasing their active cellular uptake [29-30]. Out of the various types of targeting ligands (e.g. peptides, glycoproteins, carbohydrates, antibodies) that have thus far been used in targeted drug delivery, monoclonal antibodies (mAbs) are the most widely studied type of ligands [31].

During inflammation the secretion of cytokines, such as TNF- $\alpha$  and IL-1 $\beta$  by immune cells, induces an increase in the expression of several different adhesion molecules, such as selectins, vascular cell adhesion molecule-1 (VCAM-1), and intercellular adhesion molecule-1 (ICAM-1) on endothelial cells [32] of the above mentioned adhesion molecules, E-selectin in particular has been identified as a suitable adhesion molecule for drug or carrier system delivery to inflamed endothelial cells [33-34].

The aim of the present study was to formulate PEGylated PLGA nanoparticles loaded with the BEZ drug for active targeting of inflamed endothelial cells. First, various formulation parameters were evaluated to study their effects on the final nanoparticle characteristics such as size, morphology, BEZ encapsulation efficiency and release kinetics. Subsequently, a number of selected

nanoparticle formulations were surface functionalized with E-selectin antibody, in order to render them endothelial cell specific. The targeting (i.e. specific cell binding) capacity of such surface functionalized nanoparticles was evaluated by comparing nanoparticle formulations with varying surface antibody densities. Finally, the intracellular uptake and efficacy of the targeted BEZ loaded NPs were assessed on E-selectin (over)expressing HUVEC cells by cell migration assay, as well as western blot analysis on the PI3K and mTOR signaling pathways.

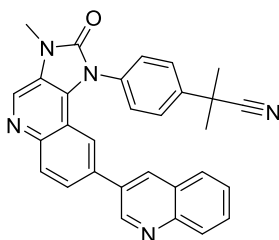


**Figure 1.** Molecular structure of dactolisib (NVP-BEZ235). Mw: 469.6 g/mol; logP: 5.2 (PubChem).

## 2. Materials and Methods

### 2.1. Materials

PLGA 5004A (molecular weight 20,000 Da), a copolymer of D,L-lactide and glycolide was obtained from Corbion Purac (Gorinchem, the Netherlands). Poly(ethylene glycol) monomethyl ether (molecular weight 2000 Da) was purchased from Sigma Aldrich (Germany). HO-PEG-NH<sub>2</sub> (Mw 2000 Da) was obtained from NOF corporations (Kyoto, Japan). Di-tert-butyl dicarbonate (Boc-o-Boc), poly(vinyl alcohol) (PVA; MW 13,000–23,000; 86–88% hydrolyzed), tin (II) 2-ethylhexanoate (SnOct<sub>2</sub>) and aldrithiol-2 were products of Sigma Aldrich. TNBSA (2,4,6-trinitrobenzene sulfonic acid) solution, succinimidyl 3-(2-pyridyldithio)propionate (SPDP), N-succinimidyl-S-acetylthioacetate (SATA) and rhodamine-NHS were obtained from Thermo scientific (Landsmeer, the Netherlands). Formaldehyde (4%) in PBS buffer was obtained from Fluka (Zwijndrecht, The Netherlands). NVP-BEZ235 was purchased from LC laboratories, USA. 4',6-Diamidino-2-phenylindole (DAPI) was

obtained from Roche (Penzberg, Germany). Phosphate buffer saline (PBS: NaCl 8.2 g, Na<sub>2</sub>HPO<sub>4</sub>·12H<sub>2</sub>O 3.1 g, NaH<sub>2</sub>PO<sub>4</sub>·2H<sub>2</sub>O 0.3 g in 1 L of water for injection, pH 7.4) was obtained from Braun (Melsungen AG, Germany). All other chemicals and reagents were obtained from Sigma Aldrich (Zwijndrecht, The Netherlands), unless otherwise mentioned.

## 2.2. Preparation of nanoparticles

A PEG-PLGA copolymer was synthesized by ring opening polymerization of D,L-lactide (1.44 g, 0.01 mol) and glycolide (1.16 g, 0.01 mol) using H<sub>3</sub>CO-PEG2000-OH (0.50 g, 0.25 mmol), and stannous octoate (0.05 g, 0.12 mmol) as initiator and catalyst, respectively (see supporting information). Nanoparticles (NPs) were prepared by a single emulsion solvent evaporation technique adapted from methods previously described by McCall *et al.*, [35] with some modifications. In short, the polymers (PLGA and PLGA-PEG, varying weight ratios of 100:0, 90:10, 80:20, 70:30, 50:50, 20:80, 0:100, respectively, were dissolved in chloroform to a final concentration of 5% w/v (0.10 g/2 ml). For BEZ loaded NPs, first a stock solution of BEZ in chloroform at concentration of 5 mg/ml was prepared. Next, 0.2, 1, or 2 ml of this solution were pipetted into vials containing 100 mg of blend polymers and volumed up to 2 ml with chloroform. Next, the obtained solutions were emulsified in an external aqueous phase (15 ml) containing poly(vinyl alcohol) 1% (w/v) in NaCl 0.9% (w/v) (filtered through a 0.2 µm Millipore filter), by an ultrasonic homogenizer (LABSONIC P, B. Braun Biotech) for 2 minutes at 45% amplitude to form an oil-in-water (o/w) emulsion. Chloroform was subsequently evaporated at 30 °C under reduced pressure for about 30 minutes, after which the resulting nanoparticle dispersion was kept under a nitrogen flow for 20 minutes at room temperature. The NPs were washed three times with 40 ml of PVA 1% (w/v) in NaCl 0.9% (w/v), by ultracentrifugation (J-26XP, Beckman Colter, Avanti) at 14000 g for 10 min, followed by resuspension in demineralized water, ultracentrifugation, and resuspension in HBS buffer (containing 10 mM Hepes and 135 mM NaCl, pH 7.4). Next, the samples were resuspended in demineralized water (2 - 3 ml), frozen with liquid nitrogen and freeze-dried overnight.



## 2.3. Nanoparticle characterization

### 2.3.1. Particle size determination

The freshly prepared NPs dispersions were 100 times diluted with 10 mM HEPES, pH 7.0 (concentration 50  $\mu\text{g}/\text{ml}$ ). The size of the NPs was measured using dynamic light scattering (DLS, Malvern Instruments, Malvern, UK). The intensity-weighted average (z-average) and the polydispersity index (PDI) of the samples were determined by analyzing the correlation function (cumulants analysis) using Malvern software. The measurements were performed at 25°C, at an angle of 90°.

### 2.3.2. Zeta potential determination

The  $\zeta$ -potential of the nanoparticles was analyzed using Malvern Zetasizer Nano-Z (Malvern instruments) with disposable folded capillary cells. Nanoparticle (NP) dilutions were prepared as described in the previous paragraph (see section 2-3-1). The zeta potential measurements were performed at 25°C, and analyzed using DTS Nano 4.20 software.

### 2.3.3. TEM analyses

The morphology and size of the nanoparticles were studied by Transmission Electron Microscopy (TEM, Tecnai 10, Philips, 100kV). Dilutions (100x) of nanoparticles (NPs) in HBS buffer (concentration 50  $\mu\text{g}/\text{ml}$ ) were prepared. Next, 25  $\mu\text{l}$  of the NP suspension was pipetted onto parafilm, and a formvar/carbon-coated copper grid was placed on top of the sample droplet for 2 minutes to allow the particles to adsorb on the grid. Excess liquid was gently removed with a filter paper. The grid was negatively stained by placing it on top of a 20  $\mu\text{l}$  droplet of 2% uranyl acetate in demineralized water supported on parafilm for 2 minutes. Excess liquid was gently removed by a filter paper and the grid was dried for 5 minutes at room temperature prior to the TEM analysis. Nanoparticles were visualized with 7-73k fold magnification and analyzed using MeasureIT software.

### 2.3.4. Yield measurement of nanoparticles

A 500  $\mu\text{l}$  sample from the original nanoparticle (NP) dispersion (10 mg/ml) in demineralized water was pipetted into a pre-weighed Eppendorf tube, and was subsequently freeze-dried. The nanoparticle yield was calculated as percentage of the weight of the obtained (recovered) product, divided by the total weight of the polymers and drug that was used to prepare the nanoparticles in the freeze-dried sample.

### 2.3.5. BEZ loading efficiency of the nanoparticles

The BEZ loading efficiency of the different NPs was determined by dissolving a sample of freeze dried, BEZ loaded NPs in DMSO, of which a known volume was taken and further diluted with acetonitrile, after which the concentration of BEZ was determined by UPLC. In detail, between 2 - 5 mg (accurately weighed) freeze-dried NPs was dissolved in 1 ml DMSO. Next, dilutions were made in acetonitrile (1/10 to 1/100), and samples were transferred into UPLC vials. Calibration was done by preparing serial dilutions in acetonitrile of a stock solution of BEZ in DMSO (concentration 1 mg/ml) in a concentration range of 0.05-100  $\mu\text{g}/\text{ml}$ . An Acquity UPLC <sup>®</sup>BEH C18, 1.7  $\mu\text{m}$  column (2.1  $\times$  50 mm) was used with a UV-detector (detection wavelength was 269 nm) for analysis. The gradient of the mobile phase (0.5 ml/min) was composed of 5% ACN in water with 0.05% TFA (solvent A) and 95% ACN in water with 0.05% of TFA (solvent B). Samples of 2  $\mu\text{l}$  were injected.

The BEZ encapsulation efficiency (EE) and loading capacity (LC) were calculated as follows:

$$\text{EE} = (\text{amount of measured BEZ} / \text{amount of BEZ added}) \times 100\%$$

$$\text{LC} = (\text{amount of measured BEZ}) / \text{amount of (measured BEZ + polymer added)} \times 100\%$$

### 2.3.6. $^1\text{H}$ NMR characterization of the formulated nanoparticles

Freeze dried non-loaded particles with varying wt% of PLGA and PLGA-PEG were dissolved in DMSO- $d_6$ , after which  $^1\text{H}$  NMR analysis was performed using a Gemini-300 MHz spectrometer (Varian Associates Inc., NMR Instruments, Palo Alto, CA, USA). From the  $^1\text{H}$  NMR spectra the PEG incorporation efficiency in the nanoparticles was calculated using the formulas given below (eq.(1)-(4)). To facilitate the analysis, the  $^1\text{H}$  NMR peak integrals ( $f$ ) were adjusted for the number of protons per monomer unit that contribute to the  $^1\text{H}$  NMR peak. For example, the numerical value of the PEG  $^1\text{H}$  NMR peak integral ( $f_{\text{PEG}}$ , 3.4 ppm) was divided by 4, to adjust for the 4 protons (i.e.  $2 \times \text{CH}_2$ ) per ethylene glycol unit that contributes to the peak in the  $^1\text{H}$  NMR. Similarly, the value of PLGA's glycolide  $^1\text{H}$  NMR peak integral ( $f_{\text{G}}$ , 4.8 ppm) was divided by 2, to adjust for the 2 protons (i.e.  $\text{CH}_2$ ) per glycolide monomer, while the value of the lactide  $^1\text{H}$  NMR peak integrals ( $f_{\text{L}}$ ) were divided by 3 (i.e.  $\text{CH}_3$  peak; 1.4 ppm) and 1 (i.e. CH peak; 5.3 ppm) respectively.

Based on the  $^1\text{H}$  NMR measurement of the PEG-PLGA copolymer, the PEG mol fraction in this PLGA-PEG co-polymer was calculated using equation 1:

$$[\text{PEG in PEG-PLGA}] = f_{\text{PEG}} / (f_{\text{G}} + f_{\text{L}} + f_{\text{PEG}}) \quad (1)$$

Where  $f_{\text{PEG}}$  is defined as the adjusted (see above) PEG  $^1\text{H}$  NMR peak integral;  $f_{\text{G}}$  is defined as the adjusted glycolide  $^1\text{H}$  NMR peak integral; and  $f_{\text{L}}$  is defined as the average value of the two adjusted lactide  $^1\text{H}$  NMR peak integrals (CH and  $\text{CH}_3$  peaks, see above).

The nanoparticles (NPs) used in this work were composed of a mixture of PLGA and PEG-PLGA. The weight fraction of PEG-PLGA in the NPs (see table 1) is converted to the respective mol fraction (X) of the PEG-PLGA copolymer. Combined with the PEG fraction that is known from equation 1 above, the fraction of PEG-PLGA (X) in the NPs can be used to calculate the theoretical PEG fraction in the NPs using equation 2:

$$[\text{PEG in NP, calc}] = [\text{PEG in PEG-PLGA}] * [(X)\text{PEG-PLGA}] \quad (2)$$

Where the fraction [PEG in PEG-PLGA] is the result of equation 1, and [(X)PEG-PLGA] is the mol fraction PEG-PLGA in the mixture (1-X)PLGA + (X)PEG-PLGA, used for the NP formulation, where the fraction (X) is a number between 0 and 1. Similar to equation 1, where the PEG fraction in PEG-PLGA is calculated from  $^1\text{H}$  NMR data of the copolymer, the PEG fraction in the formulated NPs is calculated from the  $^1\text{H}$  NMR data of the polymeric nanoparticles. Using the adjusted peak integrals from the NPs  $^1\text{H}$  NMR data, the PEG mol fraction in the NPs can be calculated using equation 3:

$$[\text{PEG in NP, exp}] = \int \text{PEG} / (\int \text{G} + \int \text{L} + \int \text{PEG}) \quad (3)$$

Comparison of the theoretical PEG fraction in the NP formulations, from equation (2), and the experimentally determined PEG fraction in the NP formulations, from equation (3), can be used to determine the percentage of PEG incorporation in the formulated NPs, as in equation 4:

$$[\text{PEG yield (\%)}] = [\text{PEG in NP, exp}] / [\text{PEG in NP, calc}] \times 100\% \quad (4)$$

Where [PEG in NP, exp] is the result from equation 3, and [PEG in NP, calc] is the result from equation 2, above.

### 2.3.7. XRD analyses

X-ray diffraction (XRD) patterns of BEZ, non-loaded and BEZ-loaded (8.1% w/w) NPs were recorded using a Bruker D2 Phaser powder X-ray diffractometer, equipped with a  $\text{Co-K}_{\alpha 1,2}$  source with  $k = 1.79026 \text{ \AA}$ . The XRD measurements were recorded at diffraction angles between 7–100 degrees  $2\theta$  (2 theta), using a step size of 0.05  $2\theta$  (2theta) and at a scan speed of 0.5 s.

### 2.3.8. Thermal analyses

The thermal behavior of formulated NPs was studied by differential scanning calorimetry, using a TA instruments DSC Q2000 machine. For polymers and freeze dried NPs, samples of 2 to 5 mg were accurately weighed and loaded into aluminum pans, which were subsequently closed. After equilibration at room temperature, the samples were heated to 100 °C (non-modulation) at a ramping rate of 2 °C/min under a nitrogen flow. Next, the samples were cooled down to -30 °C,

modulated ( $\pm 1$  °C every 30 seconds) at a ramping rate of 2 °C/min. Thereafter, the samples were heated to 100 °C modulated at a ramping rate of 2 °C/min. Two heating cycles were applied. The second heating cycle (modulated run) was used to determine the glass transition temperatures ( $T_g$ ). Glass transition temperatures ( $T_g$ ) are defined as the point of inflection of the step change observed in the heat flow curve.

#### **2.4. *In vitro* release of BEZ from NPs**

Freshly prepared nanoparticles (see section 2.2) were suspended in 5 ml HBS buffer (composed of 10 mM Hepes and 135 mM NaCl, pH 7.4) and 20  $\mu$ l samples of the homogeneous particle suspension were aliquoted into Eppendorf tubes and filled up to a total volume of 1 ml by adding 980  $\mu$ l of a HBS buffer in which BSA (50 mg/ml) was also dissolved. BSA was added to solubilize the released drug. For each batch aliquots were prepared in triplicate. Initial drug loading of the NPs was determined as described in section 2-3-5. The NP suspensions were incubated at 37 °C under mild agitation. At different time points samples were taken, which were subsequently centrifuged at 22,000 g for 10 min at 4 °C. The supernatant was collected for further analyses, and the pellets were resuspended in HBS buffer containing 50 mg/ml BSA. The collected supernatants were treated in the following way: 50  $\mu$ l of supernatant was taken per sample, to which 150  $\mu$ l acetonitrile was added. Next, the samples were vortexed for 10 s and kept at room temperature for about 1 h, followed by centrifugation for 10 min at 22,000 g at 4 °C to spin down precipitated BSA. A sample of the supernatant was injected into the UPLC system for analysis as described in section 2-3-5. The same pretreatment method was applied to BEZ standard solutions in the concentration range 0.4 to 200  $\mu$ g/ml, which were prepared in HBS buffer containing 50 mg/ml BSA. The percentage of released BEZ is reported relative to the loaded amount. The obtained BEZ release data were fitted using existing kinetic models (i.e. first order, zero order and Higuchi, assuming spherical particles) [36-37].

## 2.5. Preparation of placebo fluorescent labeled E-selectin targeted NPs

Nanoparticles (NPs) were prepared as described in section 2-2. Briefly, fixed 70 wt% PLGA and 30 wt% PLGA-PEG, with part of the PLGA-PEG functionalized with SPDP (synthesized as described in supporting information), was combined for formulation of the NPs. The varying weight ratios of PLGA-PEG-SPDP to PLGA-PEG were 100:0, 83:17, 50:50 and 0:100.

In order to prepare fluorescently labeled empty (i.e. placebo) NPs, 1 wt% of PLGA-PEG-rhodamine was added to the mixture. PLGA-PEG functionalized with rhodamine was synthesized as described in supporting information.

Mouse anti-human E-selectin (IgG2a) was purified from the supernatant of hybridoma H18/7 cells, kindly provided by Dr. M. Gimbrone Jr. (Harvard Medical School, Boston, MA), [38] and modified with S-acetylthioacetate (SATA) (8:1 SATA : Ab mol ratio) as described previously [39]. Prior to coupling, the SATA-modified E-selectin antibody (2 mg/ml in HBS buffer) was treated with deacetylation buffer (consisting of 0.5 M Hepes, 0.5 M hydroxylamine-HCl, and 25 mM EDTA at pH 7.4) at 1/10 (v/v) for 45 min at room temperature, [40] to deprotect the thioacetate groups and to subsequently allow (coupling-) reactions with the SPDP end groups on the nanoparticle surface. The solution with activated antibody was added to the NP suspension at a concentration of 10 µg Ab/mg polymer, and incubated overnight at 4 °C.

As negative control samples, rhodamine labeled NPs with 0:100 weight ratio of PLGA-PEG to PLGA-PEG-SPDP were prepared. The suspension was incubated with activated SATA modified human serum IgG (Sigma Aldrich, Germany) at a concentration of 10 µg protein/mg polymer as described in the previous paragraph. Next, the prepared NPs were centrifuged and washed with HBS buffer (pH 7.4). Finally, the NPs were suspended in HBS buffer, pH 7.4.

The size, charge and yield of the prepared targeted nanoparticles were analyzed as described in sections (2-3-1), (2-3-3) and (2-3-4).

## 2.6. Ab coupling efficiency determination

The antibody density on the surface of the NPs was determined using a micro-BCA protein assay kit (Pierce Biotechnology, Rockford, IL, USA) [41]. Calibration was performed using serial dilutions of mouse IgG (Sigma Aldrich, 0.16-50 µg/ml in HBS buffer). Coupling efficiency (CE %) is defined as the amount of Ab attached to NPs (measured with the micro-BCA assay) divided by the total amount of Ab added x 100%.

## 2.7. Flow cytometry analysis

HUVEC cells were seeded at 40,000 cells/well (96-well plates, Becton & Dickinson, Mountain View, CA, USA) and subsequently activated with TNF- $\alpha$  (10 ng/ml in EGM-2 medium) for 4 h at 37 °C [42]. Fluorescently labeled NPs with varying surface antibody densities (prepared as described in section 2-5) were diluted to concentrations of 0.1 - 8 mg polymer/ml in cell culture medium. The cells were incubated with the NPs for 1 h at 4 °C in the dark to avoid fluorochrome bleaching, after which they were washed three times with protein blocking agent (PBA) composed of 0.3% bovine serum albumin (BSA) in PBS. Finally, the cells were resuspended in 150 µl of PBA. The rhodamine fluorescence intensity of the different samples was determined using a BD FACSCanto (Becton & Dickinson). Typically, 10,000 events were acquired per sample prepared in triplicate. Data were analyzed using BD FACSDiva™ software (Becton & Dickinson) and results expressed as mean fluorescence intensity.

## 2.8. Confocal microscopy

30,000 Cells were seeded in FluoroDish (FD35-100, cell culture dish) and subsequently cultured overnight in EGM-2 medium at 37 °C. Next, the cells were activated with 10 ng/ml of TNF- $\alpha$  for 4 h at 37 °C, followed by incubation of the cells with fluorescently labeled targeted and non-targeted nanoparticles (NPs), at a concentration of 100 µg/ml polymer, for 3 h at 37 °C. Following incubation, the cells were detached with (trypsin/EDTA), [43] washed with plain medium, and the cells were then re-seeded in the FluoroDish plate. The cells were subsequently incubated for 1 h at 37 °C to

allow their attachment on the plate surface. Next, the medium was removed and the cells were washed with PBS after which they were fixed with 4% formaldehyde in PBS for 30 minutes at room temperature. For nuclear staining, the cells were washed and incubated with DAPI at a concentration of 1  $\mu\text{g}/\text{ml}$  for 5 minutes at room temperature. After three washing cycles, the petri dishes were dried and covered with FluorSave mounting agent (Calbiochem, San Diego, CA, USA) and kept at 4 °C for confocal analyses. The cellular uptake of NPs was visualized by a Z-axis scan of the sample using a Leica TCS-SP confocal laser-scanning microscope (Leica, Heidelberg, Germany) equipped with three lasers: 488 nm argon, 568 nm krypton, and 647 nm helium-neon. Scans were performed using steps of 0.8  $\mu\text{m}$ . The cells were visualized at 3 to 4  $\mu\text{m}$  Z-steps.

## 2.9. Effects of targeted BEZ loaded nanoparticles on cultured cells

BEZ loaded NPs were prepared using theoretical 9.1 wt% BEZ, 64.0 wt% PLGA and 27.0 wt% PLGA-PEG. The latter polymer was replaced by PLGA-PEG-SPDP when preparing the targeted formulation (see for more details section 2-2).

### 2.9.1. Wound healing assay

HUVEC cells were seeded in 12 well plates at a density of 40,000 cells per well in full EGM-2 medium and cultured for 24 h at 37 °C. Next, the cells were incubated with TNF $\alpha$  (10 ng/ml) for 4 h at 37 °C and subsequently dispersions of targeted BEZ loaded and control NPs as well as solution of free BEZ at concentrations of 10 and 50 nM were added to the cells and incubated for 12 h at 37 °C. Subsequently, a scratch was introduced in the cell monolayer using a p200 pipet tip with diameter of 1.8 mm. Thereafter, the cells were washed with PBS followed by the addition of plain medium (without TNF $\alpha$ ). The wound area was checked at time 0 (the moment of introducing scratch) and after 16 h incubation of the cells with plain medium at 37 °C. The wound surface area was analyzed using NIH Image J software. Wound closure was quantified by calculating the scratch wound area relative to surface area at t=0.



### 2.9.2. Western blot assay

HUVEC cells were seeded in 6 well plates at a density of 100,000 cells/well and allowed to adhere overnight, followed by activation with TNF- $\alpha$  at concentration of 10 ng/ml for 4 h at 37 °C. Subsequently, control and targeted NPs loaded with BEZ as well as free BEZ were added to the cells at concentrations of 10 and 50 nM. The cells were incubated for 16 h at 37 °C, followed by washing with cold PBS and subsequent lysis with radio immune precipitation assay buffer (RIPA), supplemented with phosphatase/kinase inhibitor cocktail (Thermo Fisher Scientific, Rockford, IL, USA) on ice for 30 min. The lysates were centrifuged at 4 °C for 15 min at 14,000 g and the obtained supernatants were stored at -20 °C. The protein concentration of the samples was determined using the micro-BCA assay (see section 2-6-1). The supernatants were subjected to SDS-PAGE analysis using 4-12% gradient NuPAGE Novex Bis-Tris mini-gels (Invitrogen, Breda, The Netherlands). Proteins were electro-transferred onto a nitrocellulose membrane via iBlot Dry Blotting system. The membranes were blocked with 5% BSA in Tris-Buffered Saline containing 0.1% Tween-20 (TBS-T) for 2 h at room temperature. The membranes were stained overnight at 4 °C with rabbit monoclonal antibody against S6 Ribosomal protein (5G10), phospho-S6 ribosomal protein (Ser240/244) (D68F8)XP, Akt (pan) (C67E7), p-Akt (S473) XP, P-PI3K p85(Y458)/ p55(Y199) and rabbit polyclonal antibody against  $\beta$ -actin (Cell Signaling Technology, Inc., Danvers, MA, USA). The antibodies were diluted 1:1000 (according to the manufactures protocol) in 5% BSA in TBS-T. After washing with TBS-T, the membranes were incubated for 2 h at room temperature with goat anti-rabbit horseradish peroxidase (HRP) conjugated secondary antibody (Cell Signaling Technology, Inc.), diluted 1:1000 in 5% BSA in TBS-T. The proteins were visualized and detected using supersignal west femto chemiluminescent substrate (Thermo Fischer Scientific) and a Gel Doc imaging system equipped with a XRS camera and Quantity one analysis software (Bio-Rad).

## 2.10. Statistical analysis

Statistical analysis of the data was performed by unpaired Student's *t*-test and one-way ANOVA. Values are represented as mean  $\pm$  SD. Differences were considered significant when  $p < 0.05$ . Data were analyzed with Graphpad prism (Graphpad software 5.0b, San Diego CA, USA).

## 3. Results and Discussion

### 3.1. Characterization of placebo nanoparticles with different PLGA-PEG weight fractions

Nanoparticles (NPs) were prepared by a single emulsion-solvent evaporation method. The formulated NPs containing less than 30 wt% of PLGA-PEG had comparable characteristics in terms of size, with a particle diameter as determined by DLS analysis between 250 and 360 nm (Table 1). TEM analysis of freshly prepared particles (Figure 2) showed that the NPs were spherical, with particle size ranging between 150 to 200 nm. The slightly larger diameter of the particles measured by DLS is likely due to the fact that DLS reports the hydrodynamic diameter of NPs in suspension, while the TEM data is based on freeze-dried NPs. Since the polymeric NPs used in this work are (slightly) swollen when suspended in water, and typically also contain a PEG hydration shell, it is likely that the DLS particle size will be higher than those observed by TEM. Furthermore, the polydispersity of the nanoparticles will result in an overestimation of the average particle size estimate in DLS [44-45]. The nanoparticles had a negative zeta potential ranging between -11 to -15 mV (Table 1), while no significant differences in zeta potential were observed between the various PLGA-PEG wt% contents in the NP formulations. NPs containing  $\geq 50$  wt% of PLGA-PEG had a clearly different morphology, with worm like structures being formed, in contrast to the spherical NPs that were formed at PLGA-PEG contents  $\leq 30$  wt% (Figure 2). Previously reported mechanistic studies on polymeric particle shape transformation have highlighted two main factors influencing the shape transformation kinetics of polymeric NPs. These are: 1) The viscoelastic properties of the applied polymer solutions, and 2) the interfacial tension between the polymer(-blocks) and the surrounding (aqueous-)medium [46-48]. However, the exact interplay between these factors is highly complex, and the exact nature

of these polymeric particle shape transformations would require a detailed investigation that is outside the scope of the present study. We further focused on spherical NPs formulations for use as drug (BEZ) carriers, and thus fixed the weight percentage of PLGA-PEG in the formulations at 30%.

Analysis of the various nanoparticles by  $^1\text{H}$  NMR spectroscopy (Figure 3) showed that within the experimental error PLGA-PEG was quantitatively incorporated in the formulation (Table 1, 64-101%).

**Table 1.** Characteristics of NPs prepared with different weight percentages of PLGA and PLGA-PEG copolymers

PLGA : PLGA-PEG (w/w)% in feed	DLS		TEM Size (nm) <sup>b</sup>	Zeta potential (mV)	PEG incorporation (%) <sup>e</sup>	T <sub>g</sub> (DSC) (°C) <sup>c</sup>	T <sub>g</sub> (Fox) (°C) <sup>d</sup>
	Size (nm)	PDI					
100:0	290 ± 10	0.10 ± 0.05	154 ± 34	-11.1 ± 4.0	-	48.1	-
90:10	368 ± 27	0.16 ± 0.05	182 ± 33	-11.5 ± 2.1	63.5	45.7	43.5
80:20	326 ± 32	0.12 ± 0.1	-	-14.2 ± 2.9	101.1	43.5	40.9
70:30	254 ± 18	0.14 ± 0.01	196 ± 33	-11.5 ± 4.9	82.2	41.2	38.4
50:50	345 ± 5	0.17 ± 0.02	184 ± 59	-11.7 ± 0.9	-	-	-
20:80 <sup>a</sup>	-	-	-	-15.6 ± 2.3	-	-	-
0:100 <sup>a</sup>	-	-	-	-15.3 ± 4.5	-	-	-

Data are presented as mean values ± SD of 2 preparations <sup>a</sup> The particles were non-spherical (see figure 2E,F), therefore DLS measurements were not reliable for these samples [44]. <sup>b</sup> Data represent average of 5 randomly selected particles from different areas on the grid. <sup>c</sup> Measured by DSC. <sup>d</sup> Predicted based on Fox equation:  $(1/T_g = W_1/T_{g,1} + W_2/T_{g,2})$ , in which  $W_1$  and  $W_2$  are the weight fractions and  $T_{g,1}$  and  $T_{g,2}$  are the glass transition temperatures of components 1 and 2 in the blend [51]. <sup>e</sup> Calculated from  $^1\text{H}$  NMR data (see figure 3)

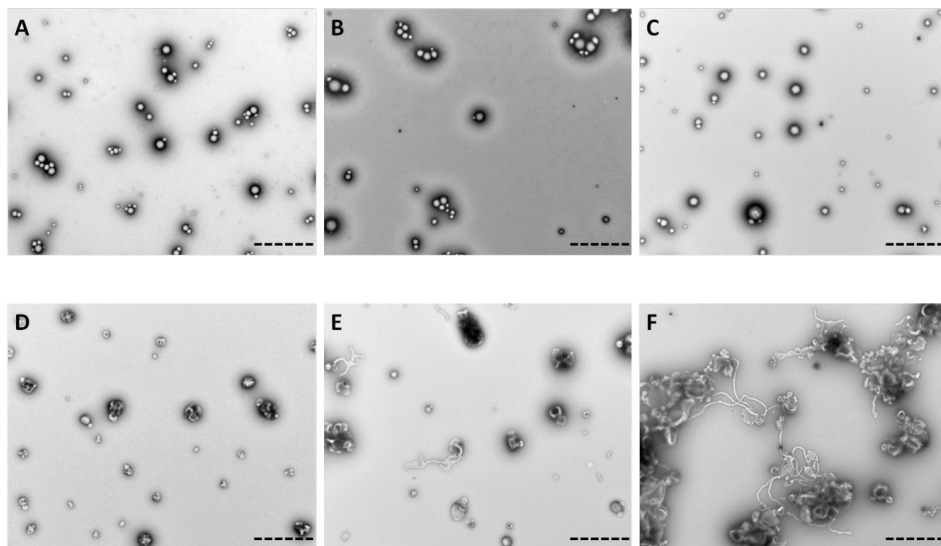


**Figure 2.** TEM images of NPs with different wt% of PLGA-PEG in the formulation ranging from 0 to 100%. (A) with 0 wt% PLGA-PEG (B) 10 wt% of PLGA-PEG (C) 30 wt% of PLGA-PEG (D) 50 wt% of PLGA-PEG (E) 80 wt% of PLGA-PEG (F) 100 wt% of PLGA-PEG. Scale bar represents 2  $\mu\text{m}$ .

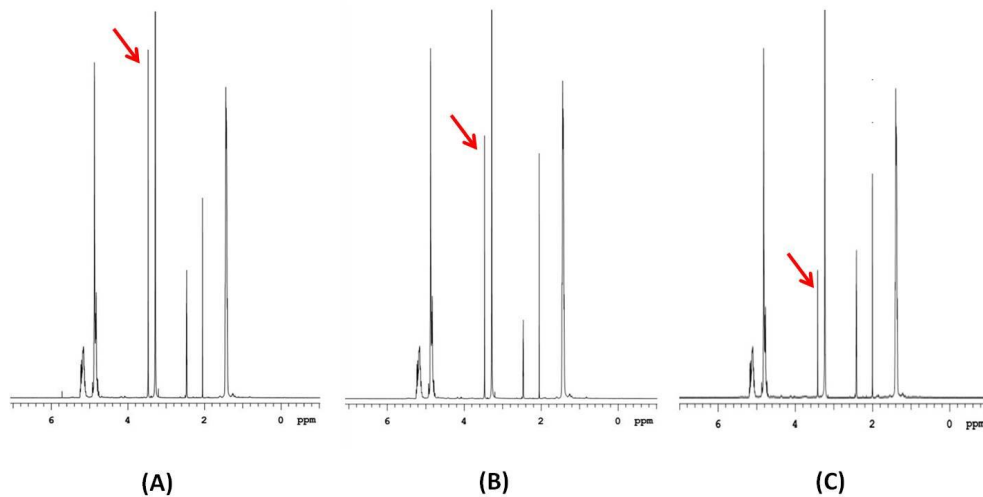


**Figure 3.** <sup>1</sup>H NMR spectra of freeze dried NPs with different wt% of PLGA-PEG dissolved in DMSO-d<sub>6</sub>. (A) NPs Formulation prepared with 30 wt% PLGA-PEG (B) with 20 wt% PLGA-PEG and (C) with 10 wt% of PLGA-PEG. The red arrows indicate the PEG signal at  $\delta$  3.4 ppm.

DSC analyses were performed in order to determine the glass transition temperatures ( $T_g$ ) of the obtained polymeric NPs. The DSC results showed that an increase in PLGA-PEG weight fraction from

0 to 30% results in a decrease of  $T_g$  from 48.1°C to 41.2°C (Table 1). The fact that only a single glass transition temperature was observed (see Figure S5) for the blend NPs demonstrates that the PEG and PLGA blocks are fully miscible in their solid state. These results are consistent with data reported in previous papers in which the miscibility of PLGA and PEG was demonstrated [49-50]. The high miscibility of the PEG and PLGA blocks is further supported by comparing the value of the experimentally observed  $T_g$  values with the ones calculated by the Fox equation for a blend of miscible polymers.

### 3.2. Characterization of BEZ loaded NPs

PLGA-PEG nanoparticles (NPs) were loaded with the drug NVP-BEZ235 (BEZ) using a single emulsion-solvent evaporation method as described in section 2-2. As can be seen in Table 2, the size of the BEZ-loaded NPs measured by DLS ranged from 290 to 342 nm with a polydispersity index (PDI) between 0.11 and 0.15. These values are comparable to the DLS-based sizes of the empty (i.e. non-loaded) NPs (Table 1). Table 2 also shows that the BEZ-loaded NPs have a negative zeta potential between -8 and -9 mV, which is the same as of the empty particles. From table 2 it can be further seen that the encapsulation efficiency of BEZ was high (80-90 %) and independent of the drug/polymer ratio in the feed, resulting in NPs with measured drug loadings varying between 0.9% and 8.1%. In order to gain insight into the physical state of BEZ in the NPs, XRD crystallography (Figure 4) was performed on the formulation with the highest drug load content (8.1%). BEZ as well as empty NP formulations were also measured for reference purposes. The X-ray diffractogram of BEZ showed sharp diffraction peaks at 12, 17 and 20 degrees  $2\theta$ , indicating high crystallinity. These diffractions were not observed for the BEZ-loaded NPs. In contrast, the XRD patterns of both the empty (i.e. non-loaded) and BEZ-loaded NP formulations did not show sharp diffraction peaks, which demonstrates that the drug-loaded NP formulations are either amorphous or containing only nanocrystalline domains that are below the XRD detection limits. To further investigate the physical state of BEZ and to check whether the drug is molecularly dissolved or dispersed in the polymer

matrix, DSC analysis was performed. The DSC thermogram of BEZ showed a melting peak at  $T_{m(\text{onset})} = 278$  °C, based on which its  $T_g$  was predicted to be around 85 °C, using the equation  $T_g = 0.67T_m$  [52], as no clear  $T_g$  for BEZ was detected in the thermogram. Since the (calculated)  $T_g$  of BEZ (~85 °C) is higher than that of the non-loaded blend NP (41.2 °C), it is expected that, when the drug is molecularly dissolved in the polymer matrix this would result in an increase in  $T_g$ . However Table 2 shows that within the experimental error the  $T_g$  of the drug-loaded NP is the same as that of the empty NPs. This means that the drug is dispersed in the form of small droplets (i.e. drug-rich domains) within the polymer matrix, rather than being molecularly dissolved in the polymer matrix.

**Table 2.** Characteristics of NPs formulated at 30 wt% of PLGA-PEG, with different BEZ loadings.

Formulation	DLC (%) <sup>a</sup>	DLS		Zeta Potential (mV)	Yield (%)	EE (%) <sup>b</sup>	DLC (%) <sup>c</sup>	$T_g$ (°C) <sup>d</sup>	$T_g$ (°C) <sup>e</sup>
		Size (nm)	PDI						
1	1.0 % (0.9 %)	317 ± 5	0.12 ± 0.05	-9.0 ± 0.3	71 ± 4	88.1 ± 3.4	0.87 ± 0.03	41.4	41.5
2	4.8 % (4.0 %)	290 ± 12	0.11 ± 0.03	-8.0 ± 0.2	75 ± 3	82.5 ± 3.7	4.0 ± 0.3	40.8	43.2
3	9.1 % (8.1 %)	342 ± 34	0.15 ± 0.02	-9.0 ± 0.5	72 ± 3	88.6 ± 5.9	8.1 ± 0.5	40.4	45.2

Data are presented as mean values ± SD for 3 preparations. <sup>a</sup> Theoretical drug (i.e. BEZ) load content and EE-corrected drug load content (corrected DLC value in brackets). <sup>b</sup> Encapsulation efficiency of the drug compound. <sup>c</sup> Drug loading capacity/content, corrected for EE. <sup>d</sup> Measured by DSC. <sup>e</sup> Predicted by Gordon-Taylor equation:  $T_g = (W_1T_{g1} + KW_2T_{g2}) / (W_1 + KW_2)$ , [53] in which  $W_1$  and  $W_2$  are the weight fractions of polymer and BEZ and  $T_{g,1}$  and  $T_{g,2}$  are the glass transition temperatures of the polymer and BEZ respectively, while  $K$  is defined as the ratio of the differences in expansion coefficient ( $\Delta\alpha$ ) at  $T_g$  of the drug and the polymer [54]. The measured  $T_g$  of the non-loaded blend NPs was 41.2 °C.

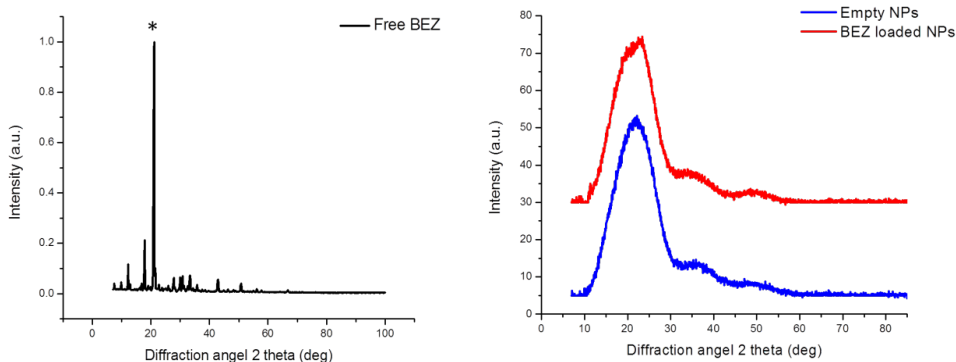


**Figure 4.** XRD pattern of free BEZ (left), BEZ loaded (8.1 wt%) NPs (right-side: top, red; Arbitrary y-axis offset), and empty NP (right side: bottom, blue) formulations. The XRD patterns have been background subtracted.

### 3.3. *In vitro* release of BEZ from nanoparticles

Figure 5 shows the *in vitro* release of BEZ from the NPs with different loadings (0.9 %, 4.0 % and 8.1%, see table 2). It is shown that that around 90% of the loaded BEZ was released from the NPs with a 0.9 % BEZ load content in 10 days. The NPs with 4.0% and 8.1% loading released 70 and 30 % of the content in the same timeframe.

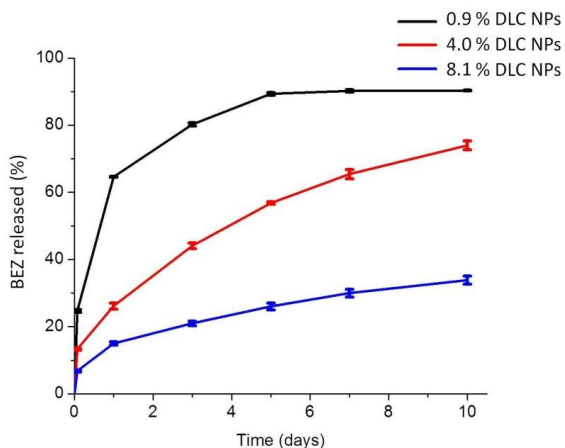


**Figure 5.** *In vitro* release of BEZ from NPs composed of 30 wt% of PLGA-PEG and varying weight percentages of BEZ in the formulations at 37°C in HBS buffer containing 5% BSA.

To further analyze the *in vitro* BEZ release data, shown in figure 5, and to gain more insight into the potential mechanism of drug release, the BEZ release curves of the three different nanoparticle formulations were fitted with three different simple kinetic (drug-release) models. The correlation of the experimental data and the fit of each of the kinetic models were compared for NP formulations with low (0.9 %), medium (4.0 %) and high (8.1%) drug load contents. The following three kinetic models were used to fit the BEZ drug release data:

Zero order kinetics:  $M_t = M_0 - k*t$  ; or:  $-dM/dt = k$

First order kinetics:  $M_t = M_0 * e^{-k*t}$  (alternatively:  $\ln(M_t/M_0) = -k*t$ ); or:  $-dM/dt = k*M_t$

Higuchi model (simplified):  $M_t/M_0 = k*(t^{1/2})$

Where  $M_0$  is the loaded amount of drug in the particles at time = 0,  $M_t$  is the amount of drug released from the particles at time =  $t$ , and  $k$  is the release rate constant. The three kinetic models each represent a fundamentally different type/mechanism of drug release from the polymeric NP formulations. As is clear from the respective equation, zero order kinetics assumes a (drug-) release rate that is constant over time. In principle, this would be ideal in cases where a constant drug concentration in the release medium is required during the release period. Instead, first order kinetics assumes an exponential correlation between time and amount of drug released (i.e. high initial release rate, decaying over time). Finally, the Higuchi model has been developed specifically to describe the release of drug molecules from a homogeneous (e.g. polymer) matrix in which the drug is dispersed. More details on the kinetic models used in this work can be found in the review of Siepmann et al [37].

The correlation coefficients ( $R^2$ ) of the fit of the three kinetic models to the experimental data are shown in table 3. It should be noted that the models fit reasonably well (correlation coefficients ( $R^2$ ) of >0.92) to the experimental data (with the exception of the zero-order model for the 0.9% DLC formulation). Although the correlation coefficients of all fits are reasonably close, in several cases the differences between are significant enough to allow the assignment of a preferred (i.e. best fitting) kinetic model. Out of the three kinetic models that were evaluated (Table 3), the first-order



model showed the best fit to the experimental drug release data from the formulation with 0.9% drug load content (DLC). For the formulation with 4.0% DLC, both first-order and Higuchi release models are excellent approximations ( $R^2 > 0.99$  for both models), while the release profile of the formulation with 8.1% DLC is best fitted by the Higuchi model. When combined with the DSC/XRD data described in previous paragraphs these results demonstrate that BEZ is mainly dispersed, and only a small fraction of BEZ is soluble in the polymer matrix. It is important to note that the Higuchi model in its simplified form disregards the effect of degrading (polymer) matrices on the drug release rate. This assumption was previously shown to be valid for PLGA NPs, since the degradation of PLGA heteropolymers start at approximately 2-6 weeks under similar conditions [55-57].

**Table 3.** Comparison of the correlation ( $R^2$ ) values for various release kinetic models fitted to experimental data shown in figure 5.

Formulation	DLC <sup>a</sup> (%)	Zero-order ( $R^2$ ) <sup>b</sup>	First-order ( $R^2$ ) <sup>c</sup>	Higuchi ( $R^2$ ) <sup>d</sup>
1	0.9%	0.784	0.955	0.928
2	4.0%	0.934	0.991	0.996
3	8.1%	0.919	0.945	0.997

<sup>a</sup> Drug loading content (DLC). <sup>b</sup> Zero-order fit: linear regression of percent drug retained (%Y) vs. time (t) plot. <sup>c</sup> First-order fit: linear regression of  $\ln(\%Y)$  vs. (t) plot. <sup>d</sup> Higuchi fit: linear regression of (%Y) vs. square root of time ( $t^{0.5}$ ) plot.

### 3.4. Characteristics of targeted nanoparticles with different surface antibody densities

Targeted NPs were prepared by a single emulsion solvent evaporation technique followed by antibody (Ab) coupling, as described in the section 2-5. The characteristics of the prepared particles are summarized in table 4. This table shows that by varying the weight fraction of PLGA-PEG-SPDP in the NPs from 0 to 30 wt%, the Ab coupling efficiency increased from 2 to 37 % (Table 4). The size of the targeted NPs ranged from 260 to 360 nm with a PDI of 0.08 to 0.16, and the particles had a negative zeta potential ranging between -11 to -30 mV (Table 4). The decrease in zeta potential (-11 to -30 mV) can be ascribed to an increase in antibody density on the surface of NPs, which can be explained by the negative charge of the anti-E-selectin monoclonal IgG Ab (pI: 5 to 6) at pH 7.4 [58].

**Table 4.** Characteristics of targeted nanoparticle formulations

Formulation	NP Composition X:Y:Z <sup>a</sup>	NP Composition Ab : SPDP <sup>b</sup>	DLS		ζ Pot (mV)	NP Yield (wt%) <sup>c</sup>	Ab coupled to NPs (wt%) <sup>d</sup>	Molecules Ab coupled / nanoparticle <sup>f</sup>	Ab coupling efficiency (%)
			Size (nm)	PDI					
1	30: 0: 70	N.A.	256	0.13	-11.4	73	0.03 <sup>e</sup>	5	2.0
2	25:05:70	9.2 : 1	297	0.08	-17.0	75	0.07	14	5.2
3	15:15:70	3.1 : 1	305	0.12	-24.9	72	0.27	54	19.4
4	0: 30: 70	1.5 : 1	347	0.16	-30.5	81	0.46	95	37.0

<sup>a</sup> X:Y:Z = PLGA-PEG: PLGA-PEG-SPDP: PLGA5004A weight ratio in formulated nanoparticles (NP). <sup>b</sup> Amount of antibody (Ab) added per formulation is constant at 1% of total polymer weight (=X+Y+Z). Calculated number is the theoretical antibody : SPDP-group weight ratio in the formulation. <sup>c</sup> Percentage of total polymer weight (=X+Y+Z) in the formulation recovered as nanoparticles after washing steps. <sup>d</sup> Calculated numbers are adjusted for NP yield. <sup>e</sup> Physically adsorbed. <sup>f</sup> Assuming NP density = 1.3 g/cm<sup>3</sup> and NP  $\phi$  = 200 nm, see main text.

To calculate the Ab density per particle, the average particle diameter was taken as 200 nm (average value based on TEM, see Table 1), and the density of PLGA/PLGA-PEG NPs was taken as 1.3 g/cm<sup>3</sup> [59]. As shown in table 4 the Ab density for the NP formulation with 30 wt% of PLGA-PEG-SPDP was 95 Ab molecules per nanoparticle, while for formulations with PLGA-PEG-SPDP weight fractions of 15, 5, and 0 percent, the Ab density decreased to 54, 14 and 5 Ab molecules per nanoparticle, respectively. These data indicate that the antibody molecules were mainly covalently attached (i.e. thiol linkage to the SPDP groups) to the surface of NPs, given the low a-specific adsorption of the antibody onto the NPs (i.e. 5 Ab/NP for particles without PLGA-PEG-SPDP).

### 3.5. Binding of antibody decorated nanoparticles to activated HUVEC cells

Figure 6 shows the binding of E-selectin targeted nanoparticles (NPs) to TNF- $\alpha$  activated endothelial cells as measured by flow cytometry analysis. The incubation time was fixed at 1 hour and the temperature at 4 °C to exclude internalization. The results demonstrate that NP formulations with the highest antibody density (95 Ab/NP) on their surface had mean fluorescence intensity (i.e. cell-binding) values that were 3 times higher than the values for the formulations with the lowest Ab density (5 Ab/NP). The NPs with intermediate antibody densities (54 Ab/NP and 14 Ab/NP) showed binding levels that were in between the values of the NPs with the highest and the lowest antibody densities, while the mean fluorescence intensity of the NPs with a Ab density of 54

Ab/NP was clearly higher than that of the NPs with a Ab density of 14 Ab/NP. The negative control NPs at the highest concentration, showed a binding comparable with the NPs (formulation #1) having lowest antibody density (5 Ab/NP) (data not shown). These results show that the extent of NP cell binding correlates directly with the number of amount of antibody molecules that are attached on their surface which is in agreement with previously reported findings [60]. For further *in vitro* cell uptake and functionality assays, the NP formulation with 70 wt % PLGA and 30 wt % of PLGA-PEG-SPDP was selected as targeted carrier system, focusing on the nanoparticle formulation with highest Ab density (95 Ab/NP).

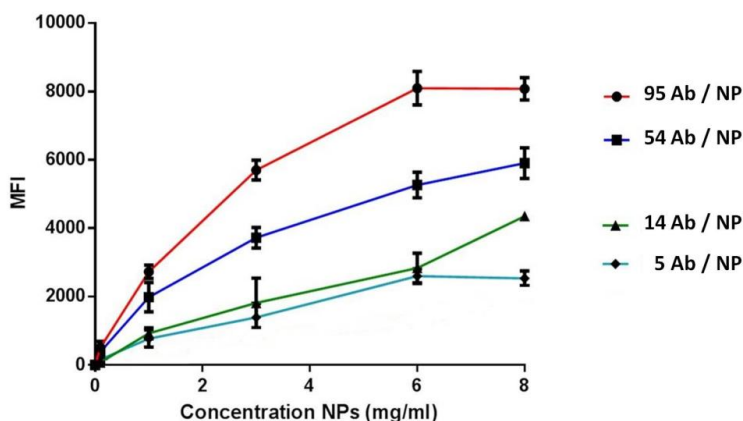


**Figure 6.** FACS analysis of TNF- $\alpha$  activated HUVEC cells incubated with NPs formulations containing different Ab densities on their surface for a time period of 1 h at 4 °C in the presence of serum.

### 3.6. Uptake of targeted nanoparticles by activated HUVEC cells

The uptake of E-selectin targeted rhodamine labeled NPs by TNF- $\alpha$  activated HUVEC cells was visualized using confocal microscopy (Figure 7). The cells were incubated with control (i.e. non-targeted) labeled NPs and targeted labeled NP formulations for 3 h at 37 °C, to allow for receptor mediated internalization of the targeted NPs. The targeted uptake process resulted in a distinct increase in intensity of the rhodamine fluorescence pattern compared to the cells that were

incubated with the non-targeted (control) NPs, as is shown in figure 7. These results suggest that targeted NPs are suitable carrier systems for active carrier system delivery to the cells.

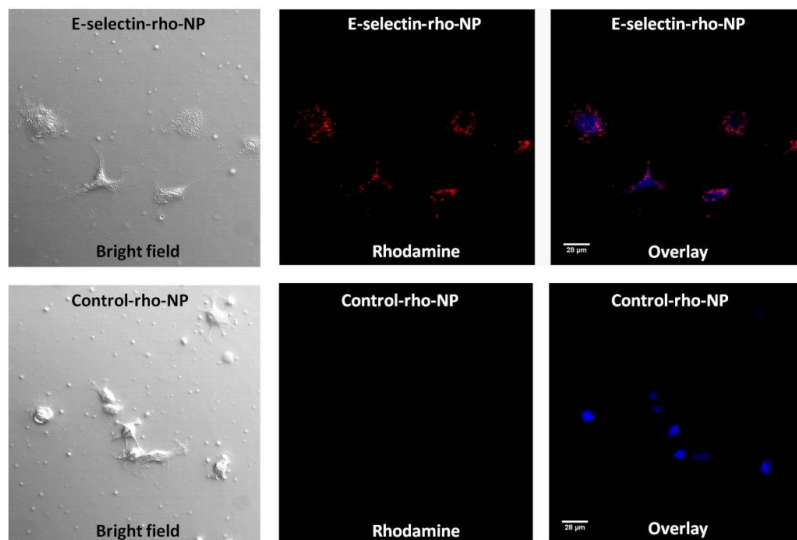


**Figure 7.** Confocal laser scanning microscope (CLSM) images of activated HUVEC cells after incubation with targeted and control rhodamine labeled NPs in serum for 3 h at 37°C. Scale bars in the figures represent 28 μm.

### 3.7. Characteristics of BEZ loaded nanoparticles applied for *in vitro* cell studies

Based on the results obtained from the previous sections regarding drug load content and antibody density on the surface of NPs, the final formulation to be tested for cell functional assays was composed of 70 wt % PLGA and 30 wt % PLGA-PEG-SPDP, functionalized with anti-E-selectin antibodies, and loaded with BEZ at 6.7% drug load content (c.f. Table 5). Similar formulation parameters were used for the control (i.e. non-targeted) BEZ loaded NPs, with one difference being that PLGA-PEG-SPDP was replaced by PLGA-PEG. The characteristics of both the targeted and non-targeted formulations are summarized in Table 5.

DLS analyses showed that the mean hydrodynamic diameter of both types of NPs was approximately 300 nm. The targeted BEZ-loaded NPs showed a higher (negative) zeta potential value

than the control BEZ-loaded NPs (-20.8 mV and -15.8 mV, respectively), which can be explained by the presence of negatively charged (at pH 7.4) antibody molecules (pI: 5 to 6) that are attached to the surface of the targeted NPs. Drug loading efficacies obtained for both targeted and control NP formulations were high (~ 75%), with Ab coupling efficiency being about 36% for the targeted formulation (Table 5).

**Table 5.** Characteristics of targeted and control NPs loaded with BEZ

Batch	Size (nm)	PDI	$\zeta$ Pot (mV) <sup>a</sup>	Yield <sup>b</sup> (%)	DLC (%) <sup>c</sup>	Drug loading efficiency (%)	Ab coupling efficiency (%)	Molecules Ab coupled / nanoparticle
Targeted BEZ NPs	324 ± 40	0.20 ± 0.04	-20.8 ± 6.0	74 ± 7	6.7 ± 0.3	75 ± 4	36 ± 5	100 ± 22
Control BEZ NPs	313 ± 42	0.16 ± 0.07	-15.8 ± 4.6	73 ± 10	6.8 ± 0.5	78 ± 7	N.A.	N.A.

Presented data are the average of 3 preparations. <sup>a</sup> Presented data are the average of 2 preparations <sup>b</sup> Yield is determined before Ab coupling to NPs. <sup>c</sup> Drug load content values corrected for drug loading efficiency.

### 3.8. Pharmacological activity of targeted BEZ-loaded nanoparticles

#### 3.8.1. Effect of targeted BEZ loaded nanoparticles in scratch wound assay

The mTOR and PI3K signaling cascades control a wide range of cellular responses, including cell motility and migration [61-62]. In previous studies it has been shown that TNF- $\alpha$  induced extracellular kinase signaling is involved in cell motility through Rho GTPase activity [63-64]. The PI3K pathway is also involved in Rho family signal transduction which indirectly affects cell migration [65-66].

To investigate the pharmacological characteristics of targeted NPs loaded with BEZ, the migration of endothelial cells was studied in a scratch wound assay as described in section (2-9-1). Semi-quantitative analysis of the scratch wound area revealed that non-treated, TNF- $\alpha$  activated endothelial cells (i.e. control) repopulated the cell-free area for more than 95% in 16 hours. Treatment with free BEZ reduced the closure of the scratch area in 16 hours to values of

approximately 30% and 15% at BEZ concentrations of 10 and 50 nM, respectively. BEZ loaded control (i.e. non-targeted) NPs also inhibited closure of the scratch wound area, although at a lesser extent compared to equivalent solutions of concentrations of free BEZ. Possible explanations for the observed effects of the control NPs can be either the non-specific cellular interaction of the (non-targeted) control NPs within the set exposure time, or (more likely) the release of BEZ from the control NPs into the surrounding medium during the incubation period. During 16 hours of incubation the amount of BEZ released from the control NPs into the medium would be equal to approximately 10 % of the total amount of BEZ present in the NP formulation, based on results discussed above in section 3-3.

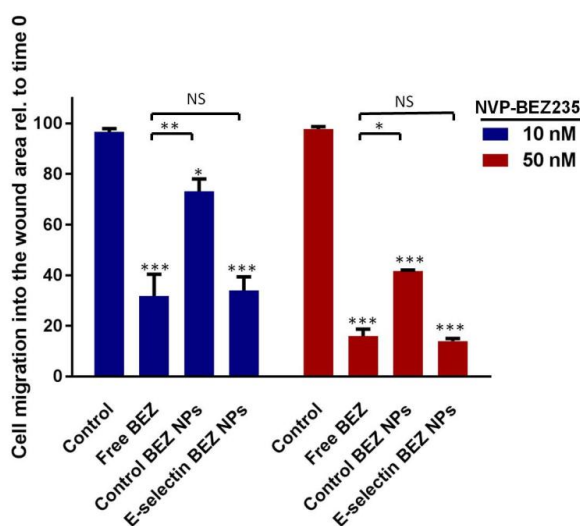


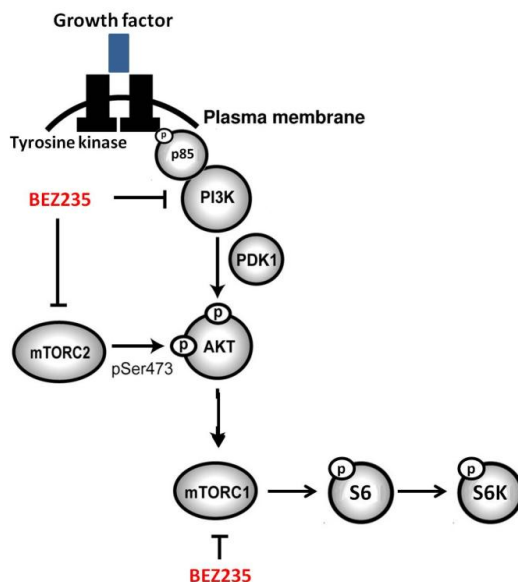
**Figure 8.** Semi-quantitative analysis of closure of the scratch wound area, as calculated from the images taken at t=0 h and t=16 h. Data are plotted as mean values  $\pm$ SEM of two individual experiments (n=2) with the same formulations; \*p<0.05, \*\*p<0.01, \*\*\*p<0.001 compared to TNF- $\alpha$  activated HUVEC cells (control), unless otherwise depicted. NS = not significant.

A more important result from figure 8 is that the E-selectin targeted BEZ-loaded nanoparticles showed a strong reduction in cell migration, similar to the values achieved by free BEZ. The targeted

formulations achieved a reduction of up to about 10% wound closure, corresponding to a 70% inhibition of cell migration at 10 nM BEZ concentrations and a 90% inhibition of cell migration at 50 nM BEZ concentrations (Figure 8). Given that only 10% of the total drug loading is released from the NPs into the medium during the 16 hour incubation period (see section 3-3) the equal cellular effects observed for targeted BEZ-loaded nanoparticles and free BEZ point to a superior efficacy of the targeted formulation.

### 3.8.2. Effects of targeted BEZ loaded nanoparticles on PI3K and mTOR signaling cascades

In a similar setup as described above for cell migration, the effects of BEZ-loaded targeted NPs on the mTOR/PI3K signaling cascades were studied. BEZ has inhibitory effects on both the mTOR and PI3K signaling cascades [67]. This can be visualized by determining the phosphorylation state of the downstream targets of these kinases, as shown in Scheme 1.



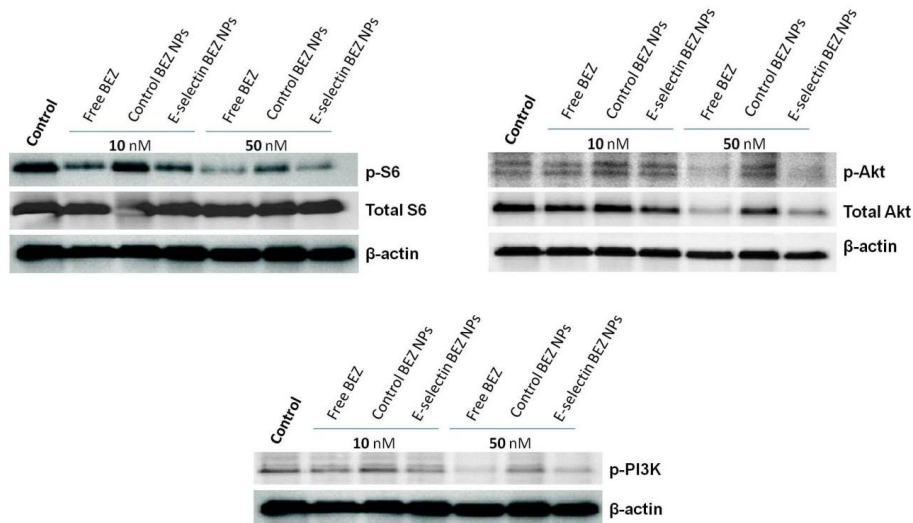
**Scheme 1.** Simplified representation of PI3K/mTOR-related signaling and ATP-competitive dual PI3K/mTOR inhibitor (i.e. BEZ235), which antagonize PI3K and both mTOR complexes. Adapted with permission from ref 68. Copyright 2011, The American Society of Hematology.

The direct effect of BEZ on the PI3K/mTOR signaling cascade was evaluated on total S6 ribosomal protein and its phosphorylated form at Ser240/244 residues, as well as on total Akt and its phosphorylated form at Ser473, while the indirect effect of the compound was analyzed on the phosphorylated form of PI3K at p85 (Tyr458)/ p55 (Tyr199) via immunoblotting. The total S6, Akt and  $\beta$ -actin were used as a control to show that the BEZ treatment does not affect total amount of S6, Akt and  $\beta$ -actin proteins isolated from cell lysates.

Both free BEZ and E-selectin targeted BEZ-loaded NPs inhibited phosphorylation of the S6 ribosomal subunit at BEZ concentrations of 10 nM (Figure 9A and B). The same figure also shows that at a BEZ concentration of 50 nM, the inhibitory effects for both treatments were more pronounced compared to the effects at a BEZ concentration of 10 nM.

The phosphorylation of Akt kinase also decreased upon treatment with free BEZ and E-selectin targeted BEZ-loaded NPs at BEZ concentrations of 10 and 50 nM (Figure 9A and B). However, a decrease in total Akt level was also observed for both treatments, which can be attributed to the inhibitory effect of BEZ on PI3K/Akt signaling pathway (67).

**A**





**B**

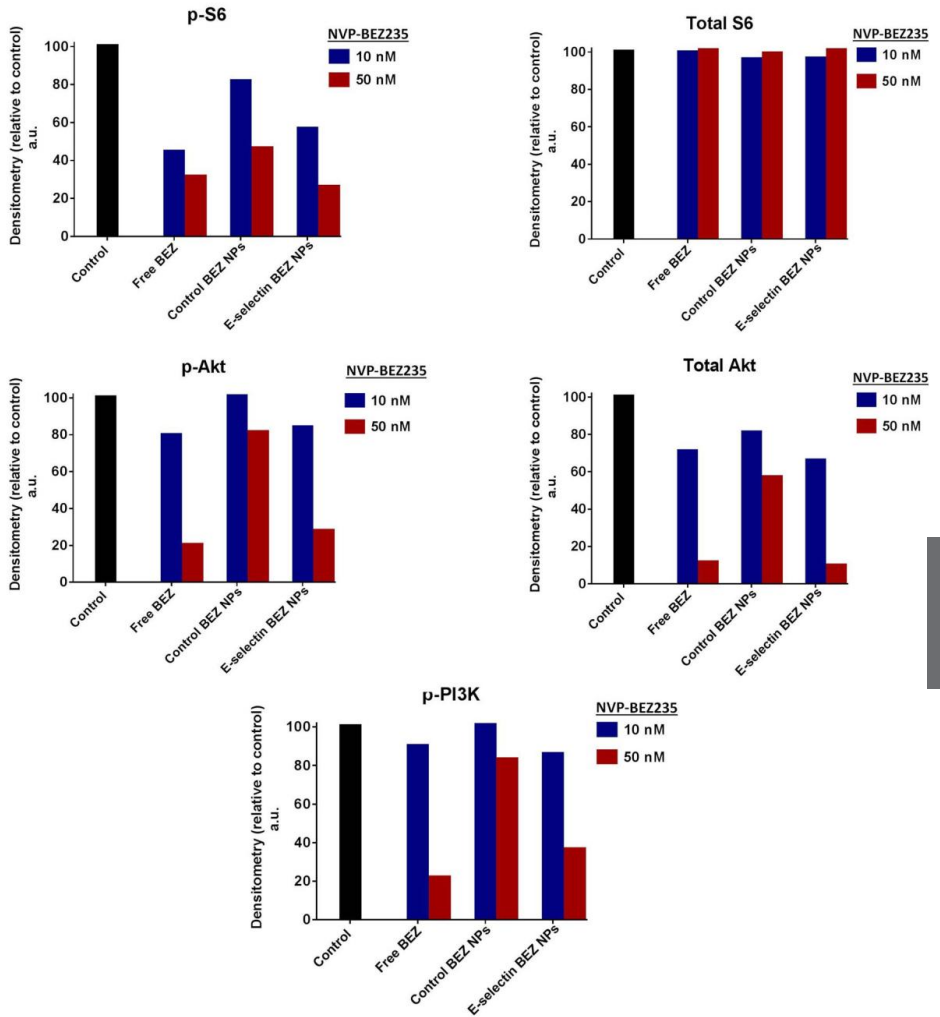


**Figure 9.** Effect of BEZ and its NP formulations (at 10 nM and 50 nM BEZ concentrations) on total protein expression or phosphorylation levels in PI3K and mTOR signaling pathways. **(A)** Representative Western blot bands of phosphorylation of S6 protein (Ser 240/244), Akt (Ser 473), PI3K (Tyr 199/458) and total protein expression levels.  $\beta$ -actin expression was analyzed as a loading control. **(B)** Densitometry of Western blot bands in the blots. Results are normalized as ratio of protein expression level in treated cells compared to TNF- $\alpha$  activated HUVEC cells (control).

Phosphorylation of the PI3K adaptor subunit (p85/p55) was analyzed to confirm the indirect effect of the free BEZ and the BEZ-loaded NP formulations on the PI3K signaling pathway. Free BEZ and E-

selectin targeted BEZ-loaded NPs at concentration of 10 nM and 50 nM indeed showed inhibition of phosphorylation of the PI3K adaptor subunit. In contrast, the control (i.e. non-targeted) BEZ-loaded NPs only showed (minor) inhibitory effects at the highest concentration of 50 nM (Figure 9A and B). The present data indicate that control (i.e. non-targeted) BEZ-loaded NPs did not achieve active intracellular BEZ delivery, and therefore failed to induce any significant inhibitory effect on cell migration and/or the PI3K/mTOR signaling cascade within the designated time period. On the other hand, the BEZ-loaded NPs that actively targeted E-selectin had an efficacy similar to that of the free BEZ, both concentrations of 10 nM and 50 nM. A similar trend was also observed in the cell migration assay discussed in the previous paragraph, confirming the efficient cellular uptake and subsequent cytoplasmic release of BEZ achieved by the targeted nanoparticles.

Although the initial *in vitro* results discussed in this work are promising, the question whether targeted BEZ-loaded NP formulations will be able to achieve an enhanced efficacy of BEZ *in vivo* still remains open. However, it is important to note that previously reported *in vivo* studies on E-selectin targeted nanomedicines (mainly liposome-based) have confirmed the high *in vivo* efficacy of the developed systems, as well as their capability to efficiently target the disease-affected endothelial cells that are primarily responsible for the inflammation [69-70]. Based on these promising *in vivo* results using targeted liposomal nanomedicines, the *in vitro* results of the E-selectin targeted BEZ-loaded NPs reported in this work can be viewed as a very encouraging starting point for future *in vivo* studies with targeted BEZ-loaded NP formulations.

It is important to note that the applied concentrations of 10 nM and 50 nM are above the half maximal inhibitory concentration ( $IC_{50}$ ) (see Figure S8). Based on the cell viability assay (MTS assay) about 80 to 90% cell viability was detected for the incubated cells in both the cell migration assay and the western blot analysis (see Figure S9).

#### 4. Conclusions

In this paper the formulation and characterization of E-selectin targeted BEZ-loaded polymeric nanoparticles (NPs) are presented, which were used for delivery of a mTOR/PI3kinase inhibitor (i.e. BEZ, structure shown in Figure 1) to TNF- $\alpha$  activated endothelial cells. The different BEZ-loaded NP formulations were composed of different ratios of PLGA and PLGA-PEG copolymers, where the PEG moiety of the latter was modified with an SPDP group to allow coupling of anti-E-selectin antibodies (Ab) when formulating targeted NPs. The nanoparticles were evaluated based on various characteristics, such as their particle size and morphology, BEZ loading, drug release kinetics, Ab coupling efficiency to NP surface, and the NP's ability to bind to activated endothelial cells. The most promising targeted BEZ-loaded nanoparticles were further tested *in vitro* using cell functionality assays, where they showed successful intracellular delivery and cytosolic release of the BEZ drug compound, achieving an efficacy that was comparable to the efficacy of an equivalent concentration of free BEZ. In contrast, the control (non-targeted) BEZ-loaded NPs showed an almost negligible efficacy, demonstrating that the targeting of E-selectin by functionalization of the NP surfaces with antibody molecules was critical to develop an effective BEZ nanocarrier. Further studies to evaluate the *in vivo* delivery of BEZ by E-selectin targeted nanoparticles are a logical next step to confirm their capacity to effectively inhibit inflammatory disorders.

#### 5. Acknowledgments

The authors would like to thank Dr. Jan A. A. Kamps (Rijks Universiteit Groningen/UMC Groningen) for supplying the SATA modified anti-E-selectin antibodies and Nazila Masoud (Utrecht University) for her assistance with the X-Ray diffraction measurements.

## Supplementary information

### 1. Supplementary materials and methods

#### 1.1. Synthesis of PLGA-PEG-O-CH<sub>3</sub>

H<sub>3</sub>CO-PEG2000-OH (0.5 g, 0.25 mmol), D,L-lactide (1.44 g, 0.01 mol) and glycolide (1.16 g, 0.01 mol) were introduced into a round bottomed-flask dried overnight in a vacuum oven. Tin (II) 2-ethylhexanoate (SnOct<sub>2</sub>) (0.05 g, 0.12 mmol) was dissolved in dried toluene and added to the flask.<sup>1</sup> Next, the flask was immersed in an oil bath of 140°C, and the melt was stirred vigorously overnight under an N<sub>2</sub> atmosphere. Next, the product was cooled to room temperature and the formed polymer was dissolved in 3-4 ml chloroform and subsequently precipitated in cold diethyl ether followed by centrifugation. This step was repeated 3 times. The final product was dried under vacuum overnight.

#### 1.2. Synthesis of PLGA-PEG-(SPDP/rhodamine)

The synthesis of PLGA-PEG-SPDP/rhodamine was performed in 4 steps as shown in scheme 1 based on a previously published method [2-3] with some slight modifications In detail:

##### 1.2.1. Boc protection of HO-PEG2000-NH<sub>2</sub>

In short, 1 g of HO-PEG2000-NH<sub>2</sub> (0.5 mmol) was dissolved in 10 ml of dried DCM (dichloromethane). Next, 218 mg di-tert-butyl dicarbonate (t-Boc) (1 mmol) was added to the solution. The reaction mixture was stirred at room temperature for 24 hours under an N<sub>2</sub> atmosphere. Next, DCM was partially evaporated under reduced pressure and the obtained product (Boc-NH-PEG-OH) was precipitated in 50 mL diethyl ether. Next, the product was dissolved in DCM and precipitated in diethyl ether (3 times) for purification.

##### 1.2.2. Synthesis of PLGA-PEG-NH-Boc

Boc-NH-PEG2000-OH (0.5 g, 0.25 mmol), D,L-lactide (1.44 g, 0.01 mol) and glycolide (1.16 g, 0.01 mol) were introduced into a round bottom flask and dried overnight in a vacuum oven. Tin (II) 2-

ethylhexanoate (SnOct2) (0.05 g) was dissolved in dry toluene and added to the round bottom flask. Next, the flask was immersed in an oil bath with a temperature of 140°C while stirring vigorously overnight under an N<sub>2</sub> atmosphere. Next, the product was cooled to room temperature. The formed polymer was dissolved in chloroform and precipitated in cold diethyl ether followed by centrifugation. This step was repeated 3 times. The final product was dried under vacuum overnight.

### 1.2.3. Deprotection of PLGA-PEG-NH-Boc

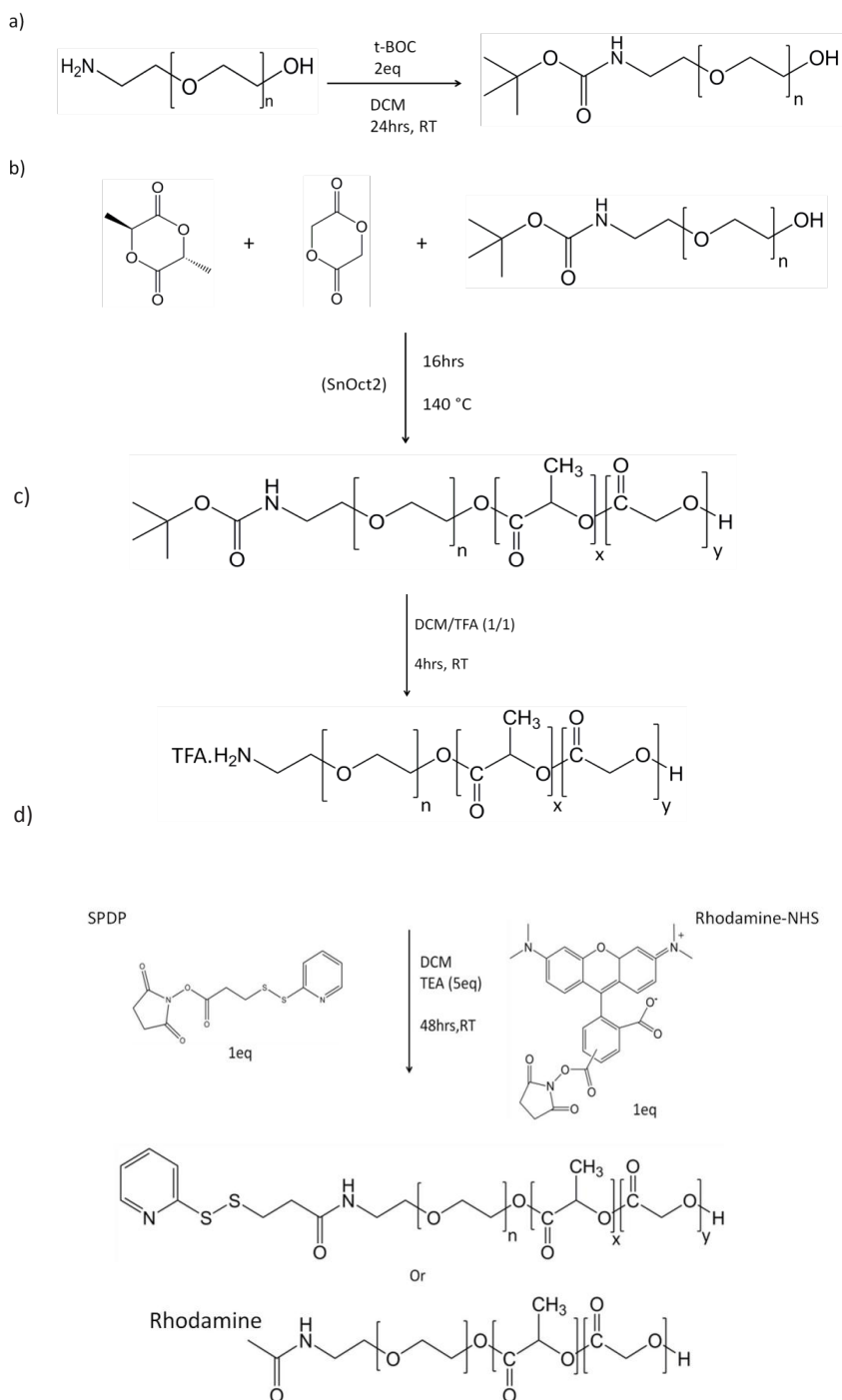
PLGA-PEG2000-NH-Boc (100 mg) was deprotected in a 1 ml DCM/TFA 1/1 (v/v) mixture for 4 hr at room temperature. This was followed by partial evaporation of the solvent under reduced pressure, after which the obtained product, TFA-NH<sub>2</sub>-PEG-PLGA, was precipitated in cold diethyl ether, followed by dissolution in DCM and re-precipitation in diethyl ether (3 times)

### 1.2.4. Synthesis of PLGA-PEG-SPDP

A stock solution of SPDP (0.156 g, 0.5 mol) was prepared in 1 ml of pre-dried DCM, 17 μl (8.5 μmol, 1eq) of this stock solution was pipetted into a glass vial and 5 eq triethylamine in DCM was subsequently added. Next, a solution of PLGA-PEG-NH<sub>2</sub>.TFA (100 mg, 8.5 μmol, 1 eq) in 2 ml DCM was slowly added to this reaction mixture while stirring at room temperature. The reaction was allowed to proceed for 48 hours under an N<sub>2</sub> atmosphere in the dark. The final product was precipitated in diethyl ether, followed by dissolution in DCM and re-precipitation in diethyl ether (3 times).

### 1.2.5. Synthesis of PLGA-PEG-Rhodamine

A stock solution of rhodamine-NHS (0.01 M) was prepared in dry DCM, and 428.5 μl (4.28 μmol, 1 eq) of this stock solution was pipetted into a glass vial followed by the addition of 5 eq triethylamine in DCM. Next, a solution of PLGA-PEG-NH<sub>2</sub>.TFA (50 mg, 4.28 μmol, 1 eq) in 1 ml DCM was slowly added.



Scheme S1. Synthesis of PLGA-PEG-SPDP and PLGA-PEG-rhodamine

The reaction was allowed to proceed for 48 hours under an N<sub>2</sub> atmosphere in the dark. The final product was precipitated in diethyl ether, followed by dissolution in DCM and re-precipitation in diethyl ether (3 times).

### 1.3. UV-VIS spectra of PLGA-PEG, PLGA-PEG-SPDP and PLGA-PEG-rhodamine

The UV-VIS spectra (200-700 nm) of PLGA-PEG, PLGA-PEG-SPDP and PLGA-PEG-rhodamine polymers, dissolved in DMSO (concentration 1 mg/ml) were recorded on a Shimadzu UV-2450 UV-VIS spectrophotometer ('s-Hertogenbosch, The Netherlands) with 1 cm quartz cuvette.

### 1.4. Gel permeation chromatography (GPC) characterization of polymers

Analyses of the polymers were performed using a Waters System (Water Associates Inc., Milford, MA) equipped with Waters 2414 refractive index (RI) detector, combined with Waters 2478 UV detector. UV absorption wavelength was set at 280 nm and 552 nm for detection of the polymers with of SPDP and Rhodamine end groups, respectively. Two serial PLgel 5 μm MIXED-D columns fitted with a guard column (Polymer Laboratories, Mw range 0.2-400 kDa) and DMF containing 10 mM LiCl as eluent were used. The flow rate was 1 ml/min (30 minutes run time) and the column temperature was 65 °C. Polystyrene standards (Agilent EasiCal) were used to calibrate the column. The results were analyzed using Empower software v.2 (Waters, USA) to calculate the number and weight average molecular weight ( $M_n$ ,  $M_w$ ) and polydispersity index (PDI; ( $M_w/M_n$ )).

To quantify the molarity of SPDP end groups per polymer chain, calibration was performed using 0.1-2.5 μmol/ml aldrithiol-2 solutions in DMF containing 10 mM LiCl. PLGA-PEG-SPDP (see section 2-3-4) was dissolved in DMF/LiCl and 50 μl of this sample was injected onto two serial PLgel 5 μm MIXED-D columns. The Areas under the peak of standards and samples were measured by using waters alliance system equipped with Waters refractive index (RI) detector and UV detector (absorption wavelength was 280 nm). The same procedure was used to quantify the molarity of Rhodamine end

groups per polymer chain. Calibration was performed using 0.03-1.0  $\mu\text{mol/ml}$  Rhodamine-NHS solutions in DMF/LiCl. Area under the peak of standards and samples were measured with UV detector (absorption wavelength was 552 nm, combined with RI detection). Coupling efficiency (CE) of SPDP or Rhodamine to the polymers was determined as following:

Coupling efficiency (CE) % = (amount of coupled [SPDP or Rhodamine] / amount of added [SPDP or Rhodamine])  $\times$  100 %

### 1.5. $^1\text{H}$ NMR characterization of the polymers

The copolymers were dissolved in DMSO- $d_6$  and  $^1\text{H}$  NMR analysis was performed using a Gemini 300 MHz spectrometer at 298 K (Varian Association Inc. USA). The copolymer composition, number-average molecule weight ( $M_n$ ) and PEG content of the different copolymers were determined by  $^1\text{H}$  NMR as follows: (a) the value of the integral of the mPEG protons (at  $\delta$  3.4 ppm) divided by 180 (the average number of protons per one mPEG chain,  $M_n=2000$ ) gives the integral value for one mPEG chain, and (b) the number of the lactide and glycolide units in the polymers were determined from the ratio of the integral of the aliphatic protons of lactide ( $\delta$  1.4 ppm,  $\text{CH}_3$ ) or ( $\delta$  5.3 ppm, CH) or aliphatic protons of glycolide ( $\delta$  4.8 ppm,  $\text{CH}_2$ ) to the integral of one mPEG chain. (c) The  $M_n$  of the polymers was calculated from the resulting number of lactide and glycolide units. The mol percentage of the mPEG, lactide and glycolide in the copolymer was calculated from the resulting number of mPEG, Lactide and Glycolide units based on following equations:

$$M_n = [(M_{\text{Lactide}} + M_{\text{Glycolide}}) \times \int \delta_{5.3}] + 2000 \text{ (g/mol)}$$

$$\text{Mol \% of lactide} = \int L / (\int \text{PEG} + \int G + \int L) \times 100$$

$$\text{Mol \% of glycolide} = \int G / (\int \text{PEG} + \int G + \int L) \times 100$$

$$\text{Mol \% of mPEG} = \int \text{PEG} / (\int \text{PEG} + \int G + \int L) \times 100$$



Where  $\int\delta_{5.3}$ ,  $\int\delta_{4.3}$  and  $\int\delta_{3.4}$  are the values of the integrals at 5.3, 4.3 and 3.4 ppm, respectively.

$M_{\text{Lactide}}$  and  $M_{\text{Glycolide}}$  are the molar masses of lactide and glycolide, respectively. The number of protons for the 2000 Da PEG block at  $\delta_{3.4}$  was set at 180.

Where  $\int_{\text{PEG}}$ ,  $\int_{\text{G}}$  and  $\int_{\text{L}}$  are the peak integrals per proton of each monomer unit, and  $f$  number is the integral obtained from the NMR spectra at the indicated peak signals (ppm).

### 1.6. Differential scanning calorimetry

In order to determine the melting point of BEZ, differential scanning calorimetry (DSC) was applied using a TA instruments Discovery DSC. Sample of approximately 4 mg was accurately weighed and loaded into the aluminum pans, after which the pan was closed. After equilibration at room temperature, the sample was first cooled down to -30 °C, followed by heating at the rate of 10 °C/min up to 300 °C. Melting temperature ( $T_m$ ) was derived from the onset of endothermic peak.

### 1.7. IC50 determination of BEZ

10,000 cells per well were added in 96 well plates. After overnight incubation at 37 °C, the medium was replaced with either TNF- $\alpha$  containing medium at concentration of 10 ng/ml or plain medium for resting (non-activated) cells. This was followed by additional incubation for 4hrs at 37°C. Next, 50  $\mu$ l of BEZ dilutions in medium prepared from stock solution of BEZ in DMSO was added to the cells, corresponding to a final concentration of 1-1000 nM. After 48 h of incubation, MTS cell proliferation assay (Promega, Wisconsin, USA) was performed according to manufactures' protocol.

### 1.8. Cell toxicity

10,000 cells per well were added in two 96 well plate. After overnight incubation at 37 °C, the medium was replaced with TNF- $\alpha$  containing medium at concentration of 10 ng/ml, followed by incubation of cells for 4 hours at 37°C. Two concentrations of BEZ compound (10 nM and 50 nM), were added to the activated cells. Two different experimental set ups were followed. One experimental set up was adapted based on western blot analyses, including 16 h of continuous

exposure to BEZ and its formulations. The other set up was adapted based on wound healing assay, including 12 h of continuous exposure to BEZ and its formulations, followed by washing step with PBS and incubation of cells in plain medium for an additional 16 h. MTS cell proliferation assay was performed according to manufacturer's protocol.

## 2. Supplementary data

**Table S1.** Overview of the characteristics of the polymers used for NPs preparation as determined by GPC, and  $^1\text{H}$  NMR.

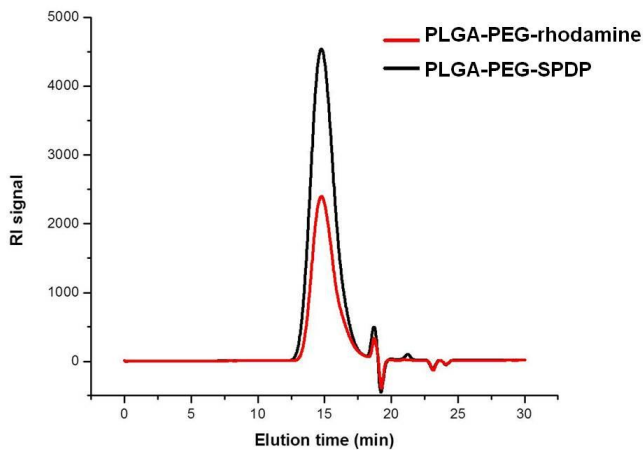
Polymer	Composition x:y:z <sup>a</sup>		Molecular weight (kDa)					Yield (%)	T <sub>g</sub> (°C) <sup>c</sup>
	Feed ratio	Polymer ratio (NMR)	GPC			NMR	Theoretical		
			M <sub>n</sub>	M <sub>w</sub>	PDI	M <sub>n</sub>	M <sub>n</sub> <sup>b</sup>		
PLGA-PEG <sub>2000</sub>	22:39:39	33:31:36	12.4	21	1.7	12.9	12.4	91	21.5
PLGA-PEG <sub>2000</sub> -rhodamine		34:39:27	7.0	11	1.6	11.0	12.4	82	-
PLGA-PEG <sub>2000</sub> -SPDP		31:40:29	7.3	12	1.6	12.1	12.4	84	-
PLGA 5004A	50:50 <sup>c</sup>	47:53 <sup>d</sup>	22.3	50.6	2.2	-	-	-	46.2

<sup>a</sup> x:y:z denotes the molar ratio of PEG/D, L-lactide/glycolide. <sup>b</sup> Based on the PEG/monomers (D,L-lactide and glycolide) molar ratio. <sup>c</sup> Measured by DSC analysis. <sup>d</sup> The molar ratio of D,L-lactide /glycolide (specification from the supplier).

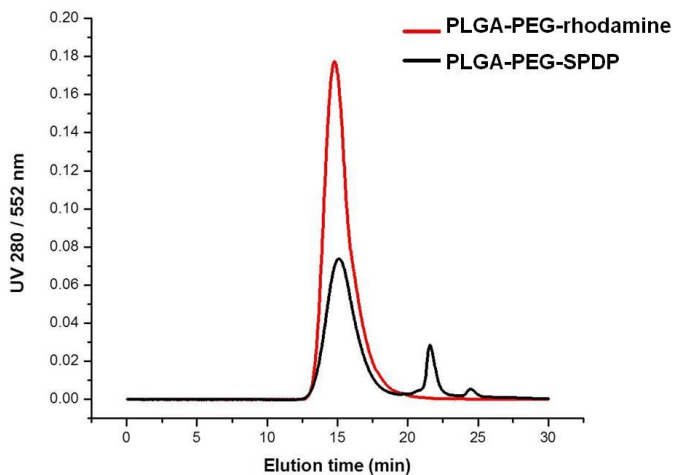
**Table S2.** Overview of coupling efficiencies of SPDP/rhodamine to PLGA-PEG-SPDP and PLGA-PEG-rhodamine, determined by  $^1\text{H}$  NMR and GPC.

Polymers	SPDP / rhodamine CE <sup>a</sup> (%)	
	$^1\text{H}$ NMR	GPC
PLGA-PEG <sub>2000</sub> -rhodamine	92.8 ± 5.5	92.1 ± 2.8
PLGA-PEG <sub>2000</sub> -SPDP	91.0 ± 1.4	81.0 <sup>*</sup>

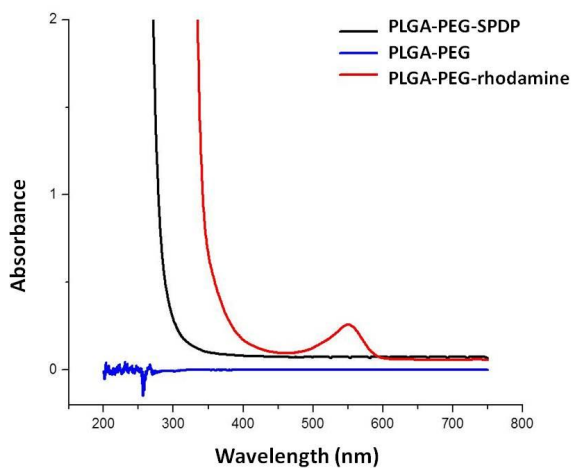
'Free' (non-functionalized) PLGA-PEG<sub>2000</sub> showed no absorbance at the chosen wavelengths. Data are presented as means of 2 independently synthesized polymer batches unless otherwise mentioned. <sup>a</sup> CE = coupling efficiency. \*Measurement was done once.



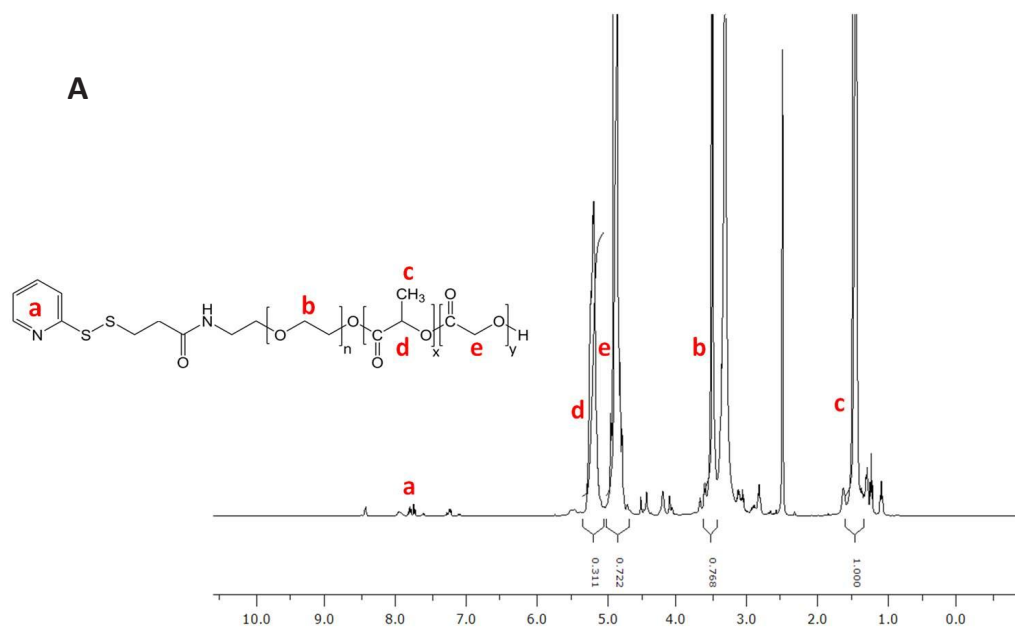
**Figure S1.** GPC chromatograms (RI detection) of PLGA-PEG-SPDP and PLGA-PEG-rhodamine



**Figure S2.** GPC chromatograms of PLGA-PEG-SPDP/rhodamine. Detection (UV-VIS) wavelength set at 280 nm for PLGA-PEG-SPDP polymer and at 552 nm for PLGA-PEG-rhodamine polymer, which are their respective absorption maxima as determined by separate UV-VIS measurements (see figure S3).



**Figure S3.** The UV-VIS absorption spectra of PLGA-PEG, PLGA-PEG-SPDP and PLGA-PEG-rhodamine polymers dissolved in DMSO. An absorption maximum for PLGA-PEG-Rhodamine at 552 nm is clearly observed.



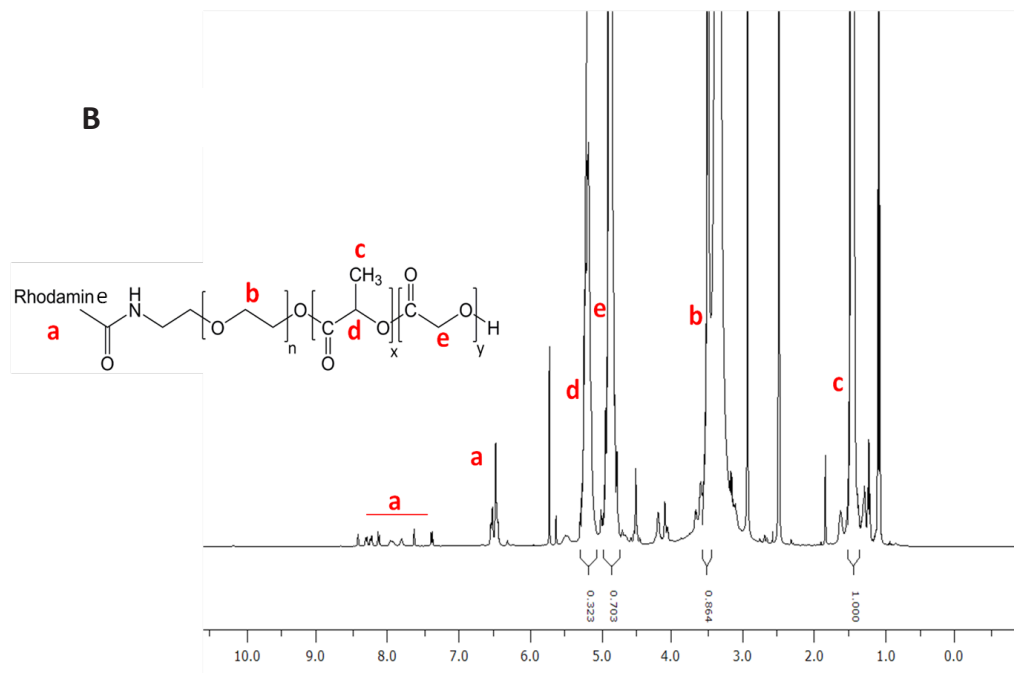


**Figure S4.**  $^1\text{H}$  NMR spectra of (A) PLGA-PEG-SPDP and (B) PLGA-PEG-rhodamine in deuterated DMSO.

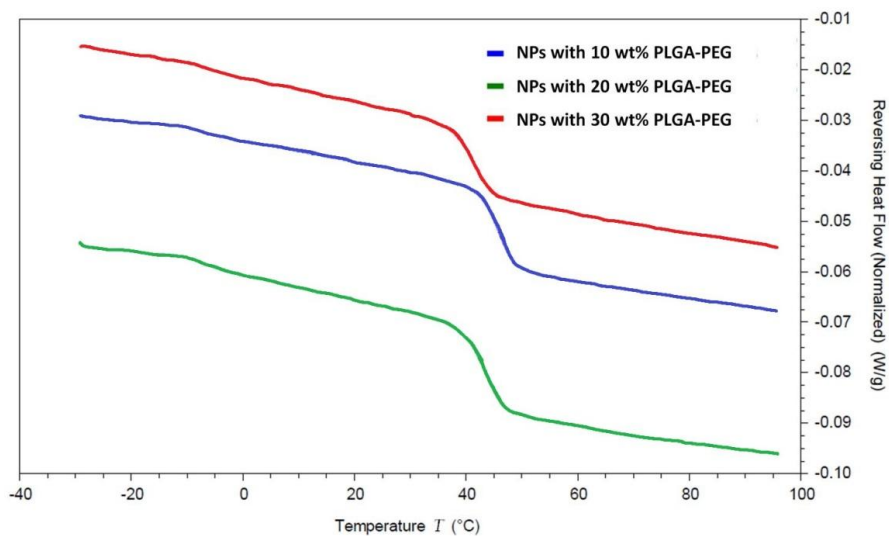


**Figure S5.** DSC thermograms (modulated, 2<sup>nd</sup> heating ramp) of NP formulations with varying wt% of PLGA-PEG.

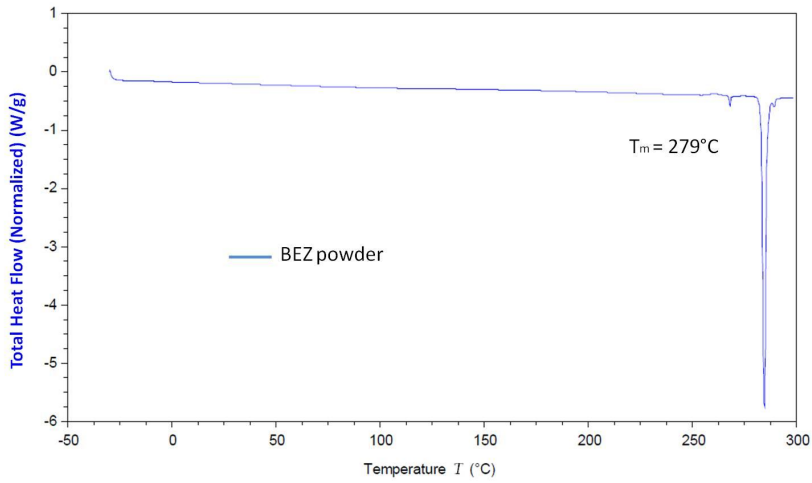


**Figure S6.** DSC thermogram of free BEZ at a heating rate of 10°C/min.

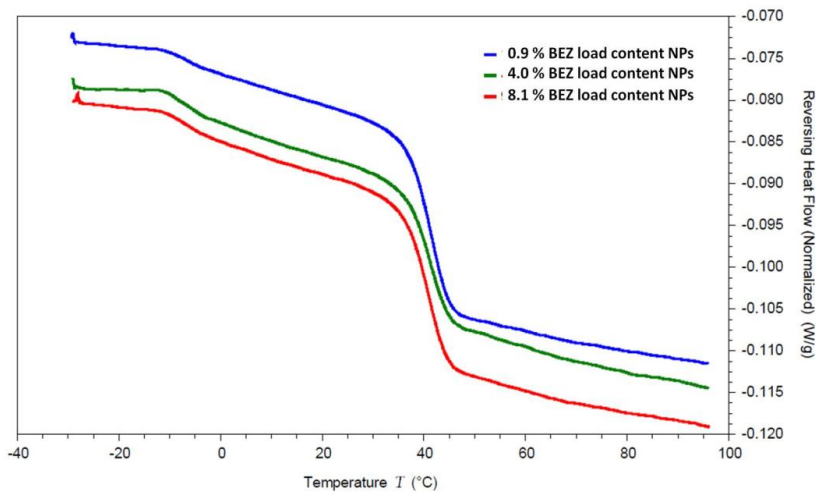


**Figure S7.** DSC thermograms of NP formulations (modulated, 2<sup>nd</sup> heating ramp) with varying BEZ loadings.

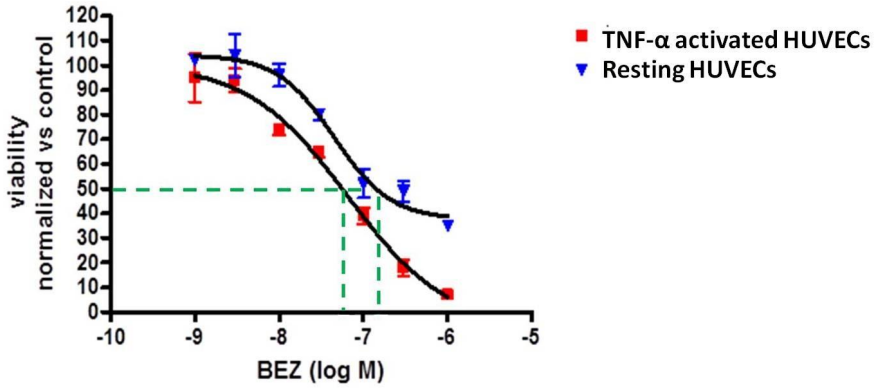


**Figure S8.** MTS cell toxicity assay on activated and resting HUVEC cells (incubation period of 48hrs). The  $IC_{50}$  values were determined by a sigmoidal curve fit (Graph pad Prism). Results are presented as mean  $\pm$  SD (n=3). Dashed green line indicates estimated  $IC_{50}$ .  $IC_{50}$  of ~80nM and ~100nM was detected for activated and non-activated cells, respectively.

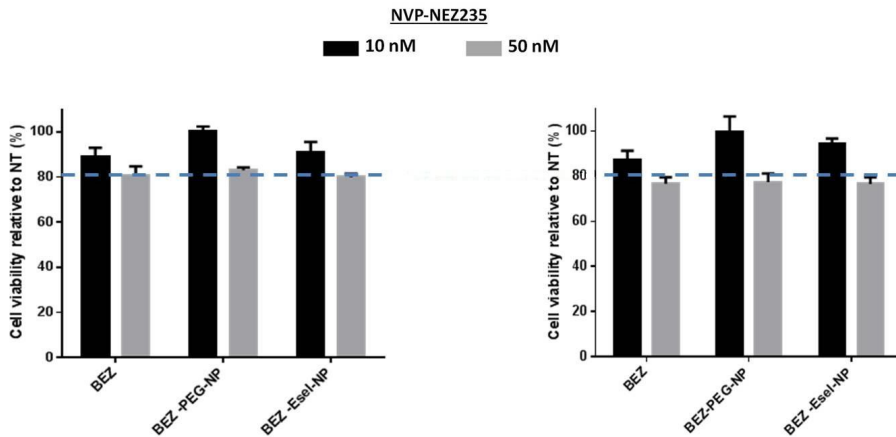


**Figure S9.** MTS cell toxicity assay to determine the effect of BEZ at concentrations of 10 and 50nM on viability of activated HUVEC cells. The graph on the left side shows the cell viability based on protocol used for Western blot analyses (16 h continues exposure to BEZ and its formulations). The graph on the right side shows the cell viability based on protocol used for Wound healing assay (12 h continues exposure to BEZ and its formulations plus 16 h recovery period). Results are presented as mean  $\pm$  SD (n=3)

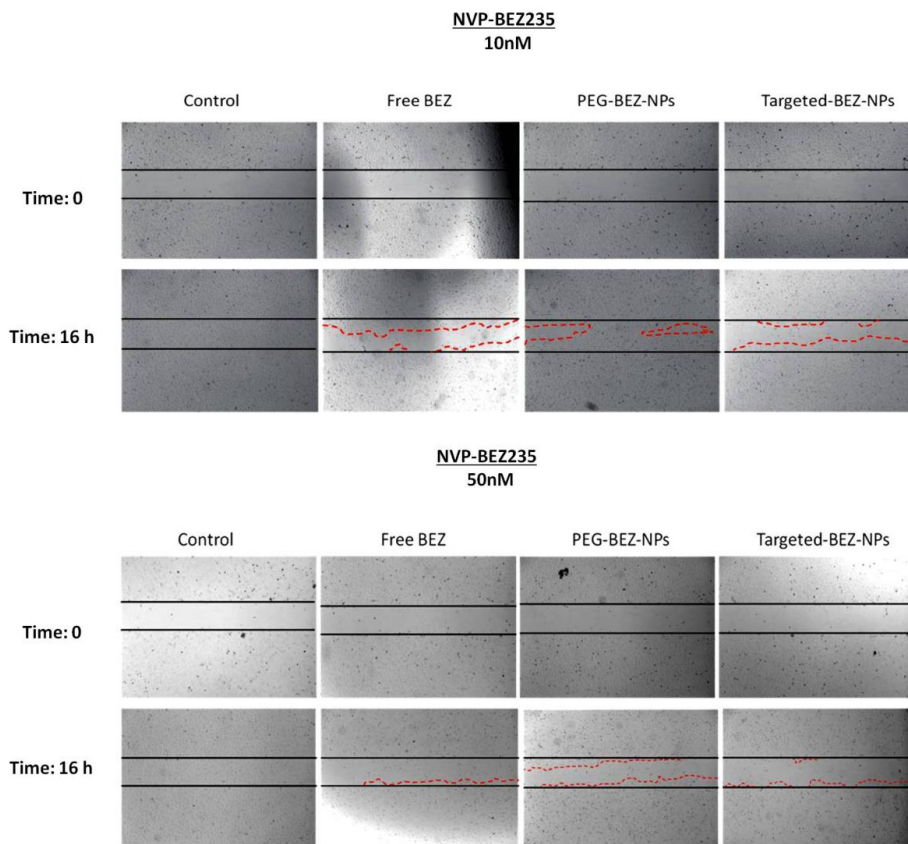


**Figure S10.** Effect of BEZ loaded NPs on migration of TNF- $\alpha$  activated endothelial cells. Repopulation of endothelial cells in a scratch wound was investigated with TNF- $\alpha$  activated HUVEC that had been pre-incubated with BEZ formulations at 10 and 50 nM concentrations for 12 h. Images were taken immediately after the wound scratch (T=0) and 16 h after scratching (T=16). Wound closure was quantified by analysis of the scratch wound area with Imaj software.

### References (S1)

1. McCall RL, Sirianni RW. PLGA Nanoparticles Formed by Single- or Double-emulsion with Vitamin E-TPGS. *J Vis Exp.* 2013, 82, 1-8
2. Novo L, Mastrobattista E, van Nostrum CF, Hennink WE. Targeted decationized polyplexes for cell specific gene delivery. *Bioconjugate Chem.* 2014, 25(4), 802–12.
3. Talelli M, Rijcken CJ, Oliveira S, et al. Nanobody-shell functionalized thermosensitive core-crosslinked polymeric micelles for active drug targeting. *J Control Release.* 2011, 151(2), 183-92.



## 6. References

1. Pober JS, Sessa WC. Evolving functions of endothelial cells in inflammation. *Nat Rev Immunol.* 2007; 7: 803-15.
2. Arango Duque G, Descoteaux A. Macrophage Cytokines: Involvement in Immunity and Infectious Diseases. *Front Immunol.* 2014; 5 (491): 1-12
3. Grivennikov SI, Greten FR, Karin M. Immunity, Inflammation, and Cancer. *Cell.* 2010; 140(6): 883–99.
4. Karar J, Maity A. PI3K/AKT/mTOR Pathway in Angiogenesis. *Front Mol Neurosci.* 2011; 4(51) : 1-8
5. Maeshima Y, Makino H. Angiogenesis and chronic kidney disease. *Fibrogenesis & Tissue Repair.* 2010; 3(13): 1-17.
6. Fokas E, Yoshimura M, Prevo R, et al. NVP-BEZ235 and NVP-BGT226, dual phosphatidylinositol 3-kinase/mammalian target of rapamycin inhibitors, enhance tumor and endothelial cell radiosensitivity. *Radiation Oncology.* 2012; 7(48): 1-13.
7. Liu P, Cheng H, Roberts TM, Zhao JJ. Targeting the phosphoinositide 3-kinase (PI3K) pathway in cancer. *Nat Rev Drug Discov.* 2009; 8: 627–44.
8. Engelman JA, Luo J, Cantley LC. The evolution of phosphatidylinositol 3-kinases as regulators of growth and metabolism. *Nature Reviews Genetics.* 2006; 7: 606-19.
9. Dy GK, Adjei AA. Emerging therapeutic targets in non-small cell lung cancer. *Proceedings of the American Thoracic Society.* 2009; 6:218-23.
10. Dinarello CA. Anti-inflammatory agents: Present and Future. *Cell.* 2010;140:935-50.
11. Fleur Broekman EG, and Godefridus J Peters. Tyrosine kinase inhibitors: Multi-targeted or single-targeted? *World J Clin Oncol.* 2011;2(2):80–93.
12. Bhatt AP, Bhende PM, Sin SH, et al. Dual inhibition of PI3K and mTOR inhibits autocrine and paracrine proliferative loops in PI3K/Akt/mTOR-addicted lymphomas. *Blood.* 2010; 115(22): 4455-63
13. Liang M, Lv J, Chu H, et al. Vertical inhibition of PI3K/Akt/mTOR signaling demonstrates in vitro and in vivo anti-fibrotic activity. *Dermatological Science.* 2014; 76(2): 104–11.
14. Maira SM, Stauffer F, Brueggen J, et al. Identification and characterization of NVP-BEZ235, a new orally available dual phosphatidylinositol 3-kinase/mammalian target of rapamycin inhibitor with potent in vivo antitumor activity. *Mol Cancer Ther.* 2008; 7(7): 1851–63.
15. Baumann P, Mandl-Weber S, Oduncu F, Schmidmaier R. The novel orally bioavailable inhibitor of phosphoinositol-3-kinase and mammalian target of rapamycin, NVP-BEZ235, inhibits growth and proliferation in multiple myeloma. *Exp Cell Res.* 2009; 315(3): 485–97.
16. Liu TJ, Koul D, LaFortune T, et al. NVP-BEZ235, a novel dual phosphatidylinositol3-kinase/mammalian target of rapamycin inhibitor, elicits multifaceted antitumor activities in human gliomas. *Mol Cancer Theranostics.* 2009; 8(8): 2204–10.

17. Bendell JC, Kurkjian C, Infante JR, et al. A phase 1 study of the sachet formulation of the oral dual PI3K/mTOR inhibitor BEZ235 given twice daily (BID) in patients with advanced solid tumors. *Invest New Drugs*. 2015; 33: 463–71.
18. Polivka J Jr, Janku F. Molecular targets of cancer therapy in the PI3K/AKT/mTOR pathway. *Pharmacology and Therapeutics*. 2014 ;142 :164-75.
19. Burris H, Rodon J, Sharma S, et al. First-in-human phase I study of the oral PI3K inhibitor BEZ235 in patients (pts) with advanced solid tumors. *J Clin Oncol*. 2010; 28(15) (suppl ; abstr 3005).
20. Zhang L, Gu FX, Chan JM, et al. Nanoparticles in medicine: therapeutic applications and developments. *Clin Pharmacol Ther*. 2008; 83(5): 761-9.
21. Farokhzad OC, Langer R. Impact of nanotechnology on drug delivery. *Acs Nano*. 2009;3(1):16-20.
22. Deng C, Jiang Y, Cheng R, Meng F, Zhong Z. Biodegradable polymeric micelles for targeted and controlled anticancer drug delivery: Promises, progress and prospects. *Nanotoday*. 2012; 7(5): 467–480.
23. Duncan R and Gaspar R. Nanomedicine(s) under the Microscope. *Mol Pharmaceutics*. 2011; 8 (6): 2101–41.
24. Kamaly N, Yameen B, et al. Degradable Controlled-Release Polymers and Polymeric Nanoparticles: Mechanisms of Controlling Drug Release. *Chem Rev*. 2016; 116: 2602–63.
25. Lammers T, Kiessling F, Hennink WE, Storm G. Nanotheranostics and image-guided drug delivery: current concepts and future directions. *Mol Pharm*. 2010; 7(6): 1899-912.
26. Cho EJ, Holback H, Liu KC, Abouelmagd SA, Park J, Yeo Y. Nanoparticle characterization: state of the art, challenges, and emerging technologies. *Mol Pharm*. 2013; 10(6):2093-110.
27. Zhang K, Tang X, Zhang J, Lu W, Lin X, et al. PEG-PLGA copolymers: their structure and structure-influenced drug delivery applications. *J Control Release*. 2014; 183:77-86.
28. Anderson JM, Shive MS. Biodegradation and biocompatibility of PLA and PLGA microspheres. *Adv Drug Deliv Rev*. 2012; 64: 72–82.
29. Laquintana V, Denora N, Lopalco A, Lopodota A, Cutrignelli A, Lasorsa FM, Agostino G, Franco M. Translocator protein ligand-PLGA conjugated nanoparticles for 5 fluorouracil delivery to glioma cancer cells. *Mol Pharm*. 2014; 1(3): 859-71
30. Ambade AV, Savariar EN, Thayumanavan S. Dendrimeric micelles for controlled drug release and targeted delivery. *Mol Pharm*. 2005; 2(4): 264-72.
31. Van der Meel R, Vehmeijer LJ, Kok RJ, Storm G, van Gaal EV. Ligand-targeted particulate nanomedicines undergoing clinical evaluation: current status. *Adv Drug Deliv Rev*. 2013; 65(10): 1284-98.
32. Sprague AH, Khalil RA. Inflammatory cytokines in vascular dysfunction and vascular disease. *Biochem Pharmacol*. 2009; 78(6): 539–52.
33. Asgeirsdóttir SA, Kok RJ, et al. Delivery of pharmacologically active dexamethasone into activated endothelial cells by dexamethasone-anti-E-selectin immunoconjugate. *Biochem Pharmacol*. 2003; 65(10): 1729-39.

34. Jubeli E, Moine L, Nicolas V, Barratt G. Preparation of E-selectin-targeting nanoparticles and preliminary in vitro evaluation. *Int J Pharm.* 2012; 426(1-2): 291-301.
35. McCall RL, Sirianni RW. PLGA Nanoparticles Formed by Single- or Double-emulsion with Vitamin E-TPGS. *J Vis Exp.* 2013; 82: 1-8.
36. Siepmann J, Siepmann F. Modeling of diffusion controlled drug delivery. *J Control Release.* 2012; 161(2): 351-62.
37. Siepmann J, Peppas NA. Higuchi equation: Derivation, applications, use and misuse. *Int J Pharm.* 2011; 418(1): 6–12.
38. Spragg DD, Alford DR, Greferath R, Larsen CE, Lee KD, Gurtner GC, Cybulsky MI, Tosi PF, Nicolau C, Gimbrone MA Jr. Immunotargeting of liposomes to activated vascular endothelial cells: a strategy for siteselective delivery in the cardiovascular system. *Proc Natl Acad Sci USA.* 1997; 94(16): 8795-800
39. Everts M, Koning GA, Kok RJ, Asgeirsdóttir SA, Vestweber D, Meijer DK, Storm G, Molema G. In vitro cellular handling and in vivo targeting of E-selectin-directed immunoconjugates and immunoliposomes used for drug delivery to inflamed endothelium. *Pharm Res.* 2003; 20(1): 64-72.
40. Oliveira S, Schiffelers RM, van der Veeken J, van der Meel R, Vongpromek R, van Bergen en Henegouwen PM, Storm G, Roovers RC. Downregulation of EGFR by a novel multivalent nanobody-liposome platform. *J Control Release.* 2010; 145(2): 165-75.
41. Wiechelmann KJ, Braun RD, Fitzpatrick JD. Investigation of the bicinchoninic acid protein assay: Identification of the groups responsible for color formation. *Anal Biochem.* 1988; 175: 231-7.
42. Kowalski PS, Lintermans LL, Morselt HW, Leus NG, Ruiters MH, Molema G, Kamps JA. Anti-VCAM-1 and anti-E-selectin SAINT-O-Somes for selective delivery of siRNA into inflammation-activated primary endothelial cells. *Mol Pharm.* 2013; 10(8): 3033-44.
43. Visweswaran GR, Gholizadeh S, Ruiters MH, Molema G, Kok RJ, Kamps JA. Targeting Rapamycin to Podocytes Using a Vascular Cell Adhesion Molecule-1 (VCAM-1)-Harnesses SAINT-Based Lipid Carrier System. *PLoS One.* 2015; 10(9): 1-17
44. Bhattacharjee S. DLS and zeta potential - What they are and what they are not?". *J Control Release.* 2016; 235: 337-51.
45. Filipe V, Hawe A, Jiskoot W. Critical evaluation of Nanoparticle Tracking Analysis (NTA) by NanoSight for the measurement of nanoparticles and protein aggregates. *Pharm Res.* 2010; 27(5): 796-810.
46. Williford JM, Ren Y, et al. Shape transformation following reduction-sensitive PEG cleavage of polymer/DNA nanoparticles. *J Mater Chem B.* 2014; 2: 8106-9.
47. Chien MP, Rush AM, et al. Programmable shape-shifting micelles. *Angew Chem Int Ed Engl.* 2010; 49(30): 5076-80.
48. Blanzas A, Armes SP, Ryan AJ. Self-Assembled Block Copolymer Aggregates: From Micelles to Vesicles and their Biological Applications. *Macromol Rapid Commun.* 2009; 30(4-5): 267-77.

49. Jackson JK, Hung T, Letchford K, Burt HM. The characterization of paclitaxel-loaded microspheres manufactured from blends of poly(lactic-co-glycolic acid) (PLGA) and low molecular weight diblock copolymers. *Int J Pharm.* 2007; 342: 6-17.
50. Samadi N, van Steenberg MJ, van den Dikkenberg JB, Vermonden T, van Nostrum CF, Amidi M, Hennink WE. Nanoparticles based on a hydrophilic polyester with a sheddable PEG coating for protein delivery. *Pharm Res.* 2014; 31(10): 2593-604.
51. Brostow W, Chiu R, Kalogeras IM, Vassilikou-Dova A. Prediction of glass transition temperatures: Binary blends and copolymers. *Materials Letters.* 2008; 62(17-18): 3152-5.
52. Alzghoul A, Alhalaweh A, Mahlin D, Bergström CA. Experimental and Computational Prediction of Glass Transition Temperature of Drugs. *J Chem Inf Model.* 2014; 54(12): 3396-403.
53. Van den Mooter G, Wuyts M, Bleton N, Busson R, Grobet P, Augustijns P, Kinget R. Physical stabilisation of amorphous ketoconazole in solid dispersions with polyvinylpyrrolidone K25. *Eur J Pharm Sci.* 2001; 12(3): 261-9.
54. Gordon M, Taylor JS. Ideal copolymers and the second-order transitions of synthetic rubbers. I. Non-crystalline copolymers. *J Appl Chem.* 1952; 2: 493-501.
55. Zweers ML, Engbers GH, Grijpma DW, Feijen J. In vitro degradation of nanoparticles prepared from polymers based on DL-lactide, glycolide and poly(ethylene oxide). *J Control Release.* 2004; 100(3): 347-56.
56. Belbella A, Vauthier C, Fessi H, Devissaguet J-P and Puisieux F. In vitro degradation of nanospheres from poly(D,Llactides) of different molecular weights and polydispersities *Int. J. Pharm.* 1996; 129: 95-102.
57. Español L, Larrea A, Andreu V, Mendoza G, Arruebo M, Sebastian V , Aurora-Prado MS, Kedor-Hackmann E, Santoro MI, Santamaria J. Dual Encapsulation of Hydrophobic and Hydrophilic Drugs in PLGA Nanoparticles by a Single-Step Method: Drug delivery and cytotoxicity assays. *RSC Advances.* 2016; 6(112): 1-11.
58. <http://www.agrisera.com/en/info/molecular-weight-and-isoelectric-point-of-various-immunoglobulins.html>.
59. Saha B, Evers TH, Prins MW. How antibody surface coverage on nanoparticles determines the activity and kinetics of antigen capturing for biosensing. *Anal Chem.* 2014; 86 (16): 8158-66.
60. Gu F, Zhang L, Teply BA, Mann N, Wang A, Radovic-Moreno AF, Langer R, Farokhzad OC. Precise engineering of targeted nanoparticles by using self-assembled biointegrated block copolymers. *PNAS.* 2008; 105(7): 2586-91.
61. Berven LA, Willard FS, Crouch MF. Role of the p70(S6K) pathway in regulating the actin cytoskeleton and cell migration. *Exp Cell Res.* 2004; 296: 183-95.
62. Castellano E, Molina-Arcas M, Krygowska AA, East P, Warne P, Nicol A, Downward J. RAS signalling through PI3-Kinase controls cell migration via modulation of Reelin expression. *Nat Commun.* 2016; 7(11245): 1-13.

63. Pollock CB, Shirasawa S, Sasazuki T, Kolch W, Dhillon AS. Oncogenic K-RAS is required to maintain changes in cytoskeletal organization, adhesion, and motility in colon cancer cells. *Cancer Res.* 2005; 65: 1244–50.
64. Vial E, Sahai E, Marshall CJ. ERK-MAPK signaling coordinately regulates activity of Rac1 and RhoA for tumor cell motility. *Cancer Cell.* 2003; 4: 67–79.
65. Jiménez C, Portela RA, Mellado M, Rodríguez-Frade JM, Collard J, Serrano A, Martínez-A C, Avila J, Carrera AC. Role of the PI3K regulatory subunit in the control of actin organization and cell migration. *J Cell Biol.* 2000; 151: 249–62.
66. Toliaf KF, Cantley LC, Carpenter CL. Rho family GTPases bind to phosphoinositide kinases. *J Biol Chem.* 1995; 270: 17656–9.
67. Kim KW, Myers CJ, Jung DK, Lu B. NVP-BEZ-235 enhances radiosensitization via blockade of the PI3K/mTOR pathway in cisplatin-resistant non-small cell lung carcinoma. *Genes & Cancer.* 2014; 5: 7-8.
68. Shortt J, Martin BP, Newbold A, Hannan KM, Devlin JR, Baker AJ, Ralli R, Cullinane C, Schmitt CA, Reimann M, Hall MN, Wall M, Hannan RD, Pearson RB, McArthur GA, Johnstone RW. Combined inhibition of PI3K-related DNA damage response kinases and mTORC1 induces apoptosis in MYC-driven B-cell lymphomas. *Blood.* 2013; 121(15): 2964-74.
69. Asgeirsdóttir SA, Zwiers PJ, Morselt HW, Moorlag HE, Bakker HI, Heeringa P, Kok JW, Kallenberg CG, Molema G, Kamps JA. Inhibition of proinflammatory genes in anti-GBM glomerulonephritis by targeted dexamethasone-loaded AbEsel liposomes. *Am J Physiol Renal Physiol.* 2008; 294(3): F554-61.
70. Kowalski PS, Zwiers PJ, Morselt HW, Kuldo JM, Leus NG, Ruiters MH, Molema G, Kamps JA. Anti-VCAM-1 SAINT-O-Somes enable endothelial-specific delivery of siRNA and downregulation of inflammatory genes in activated endothelium in vivo. *J Control Release.* 2014; 176: 64-75.

## **Chapter 6**

**Anti-GD2 immunoliposomes for delivery of the survivin inhibitor  
Sepantronium bromide (YM155) to neuroblastoma tumor cells**

Shima Gholizadeh, Emmy M. Dolman, Rolf W. Sparidans, Wim E. Hennink, Robbert J. Kok, Submitted for publication.

## Abstract

The current study focuses on the preparation and characterization of immunoliposomes (targeted liposomes) for specific delivery of YM155 to neuroblastoma. Recurrent neuroblastoma express high levels of anti-apoptotic proteins which increases their resistance to anticancer therapeutics. Sepantronium bromide (YM155) is a potent inhibitor of the survivin anti-apoptotic protein with a very short plasma half-life. Administration as nanomedicine formulation that can accumulate in neuroblastoma cells can improve the dosing schedule (i.e. bolus injections with low frequency) and the therapeutic potential of YM155 treatment.

YM155 was loaded into PEGylated liposomes composed of DPPC, cholesterol and DSPE-PEG<sub>2000</sub> via passive film-hydration and extrusion over polycarbonate filters. Targeted liposomes were prepared by liposome surface functionalization with monoclonal antibodies that recognize disialoganglioside (GD2) antigen, a known marker for neuroblastoma cells. Stability analysis of formulated liposomes (targeted and non-targeted control) revealed no leakage of liposomal YM155 for the time period of 4 weeks at 4°C in HBS buffer. Roughly 70% of the loaded YM155 was retained in the liposomal formulations after incubation in HBS buffer containing 50% serum for 24 hours at 37°C. Binding and internalization of the immunoliposomes by GD2 expressing neuroblastoma type cells (i.e. IMR32 and KCNR) was confirmed by flow cytometry analysis and confocal microscopy studies with fluorescently labeled liposomes. Immunoliposomes loaded with YM155 were less cytotoxic than free YM155 when incubated with GD2-positive KCNR cells *in vitro*, which is most likely due to the lower internalization of liposomes as compared to the free drug, which undergoes cation carrier mediated transport. A pilot pharmacokinetic evaluation of YM155 loaded liposomes (both GD2-targeted immunoliposomes and PEGylated control liposomes) showed prolonged blood circulation and a significantly increased half-life of YM155 in tumor tissue for the liposomal formulations, as compared to a bolus injection of free YM155. Collectively, these data demonstrate that YM155 has been successfully encapsulated in neuroblastoma-targeted immunoliposomes, which can improve the circulation time and tumor accumulation of this anti-apoptotic drug.

## 1. Introduction

Neuroblastoma (NB) is an aggressive malignancy of the sympathetic nervous system and is the most frequently occurring type of solid extracranial tumor in children [1]. Although the survival rate in low-risk patients is currently over 90%, children with high-risk neuroblastoma currently have a very poor prognosis. For these patients, the 5-year disease free survival rate is between 25%-35%, despite many patients undergoing aggressive multi-modality therapies (i.e. combination of chemotherapy, surgery, stem cell rescue and radiation therapy) [2]. This highlights the urgent need for new therapeutic strategies [1, 3, 4].

The pathology of neuroblastoma (as well as most other types of cancer) is complex and differs between individual patients. Anti-apoptotic proteins have been shown to play a role in tumor development, thus making such proteins promising drug targets. One of these proteins is survivin, which is encoded by the 'baculoviral inhibitor of apoptosis repeat-containing 5' (BIRC5) gene. Over-expression of this surviving-encoding gene has been shown to correlate strongly to a poor patient prognosis, metastatic spread and (increased) resistance to chemotherapy [5]. Hence, survivin inhibitors could potentially be used in neuroblastoma treatment, especially for high risk patients with poor prognosis [6, 7]. Anti-BIRC5 antisense based therapies such as gataparsen sodium (LY2181308) and small molecular inhibitors of anti-apoptotic proteins are currently being tested in phase I/II clinical trials [8-10].

One of the promising small molecular inhibitors of survivin is sepantronium bromide (YM155), the structure of which is shown in figure 1 [11]. Recent phase I/II 'single agent' clinical trials have shown acceptable toxicity in patients with advanced solid malignancies [10, 12]. The physicochemical and pharmacological properties of YM155 are listed in table 1. Due to the hydrophilicity and permanent cationic charge on one of the nitrogen atoms of the molecule, YM155 is rapidly eliminated via organic cation transporter (OCT) mediated excretion in bile and urine. Because of this, YM155 has a short plasma half-life of approximately 1-2 hours, as determined in pharmacokinetic measurements



in mice and rats [13, 14]. The rapid elimination of YM155 dictates administration as intravenous infusion rather than intravenous bolus injection [12, 15].

Nano-encapsulation technologies and application of the resulting so-called nanomedicines in health care have received much attention in recent years, in particular for application in cancer therapy [16, 17]. Long circulating nanomedicines such as PEGylated liposomes can improve tumor drug delivery by virtue of the enhance permeability and retention (EPR) effect, i.e. the accumulation and retention of nanocarriers in the tumor site due to differences between normal vasculature and tumor blood vessels [18]. Thus, the rapid elimination of YM155 and its poor pharmacokinetic properties can potentially be improved by encapsulating the YM155 molecules in a nanocarrier that can prevent renal excretion of the compound. In recent studies, such a PEGylated liposomal dosage form of YM155 has been introduced and studied in rodent cancer models for tumor drug uptake and efficacy [19, 20]. We now propose a novel immunoliposomal formulation for YM155, which can further improve its delivery to neuroblastoma.

Targeted liposomes (immunoliposomes) have been modified with ligands such as antibodies (Ab) that bind to cell-surface exposed receptors on target cells. Such a binding of the nanomedicine to receptors can be an efficient strategy to facilitate the intracellular delivery of drugs into target cells, which can further enhance their specificity for the targeted cell type [21, 22]. Disialoganglioside GD2 is an attractive target for an immunoliposome based strategy since GD2 is extensively expressed by neuroblastoma tumor cells [23-26], while it is virtually absent in nonmalignant tissues outside the central nervous system (CNS)(27). GD2-positive tumor cells can be recognized specifically by anti-GD2 antibodies (Ab) or anti-GD2 Ab functionalized nanoparticles [28]. Chimeric and humanized anti-GD2 antibodies have been investigated for immunotherapy, tumor vaccination and as targeting ligand for drug delivery purposes [29]. Although GD2 is expressed in neurons, the human brain is protected from parenteral anti-GD2 Ab and anti-GD2 decorated nanoparticles by the blood-brain barrier.

In this study, we investigate the formulation of YM155 in GD2-targeted immunoliposomes for the specific delivery of YM155 to neuroblastoma tumor cells. The obtained formulation was evaluated for their *in vitro* stability and YM155 release kinetics at different release conditions. The cell specific binding and uptake of the liposomal formulations (i.e. targeted and non-targeted control) were analyzed in cultured NB tumor cells (i.e. KCNR and IMR32), followed by an *in vitro* efficacy evaluation of the formulated liposomes and free YM155. Finally, a pharmacokinetic pilot study was conducted to investigate the plasma half-life and tumor accumulation of the targeted immunoliposomes.

**Table 1.** Characteristics of YM155 compound

<b>Mw</b>	443,33 g/mol
<b>XLogP</b>	0,77 ( $\pm 1,88$ )
<b>pKa</b>	-0,33
<b>IC50</b>	At low nM range for most NB cell lines
<b>LogD</b>	-2,1
<b>Solubility in water</b>	At least 0,5 mg/ml

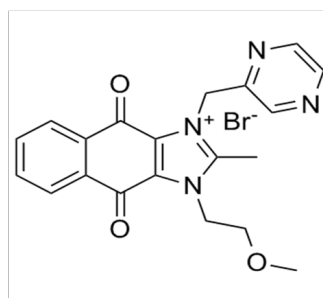


**Figure 1.** Molecular structure of Sepantronium bromide (YM155)

## 2. Materials and Methods

### 2.1. Materials

The lipids 1,2-dipalmitoyl-*sn*-glycero-3-phosphocholine (DPPC), 1,2-distearoyl-*sn*-glycero-3-phosphoethanolamine-N-[maleimide(polyethylene glycol)-2000] (DSPE-PEG<sub>2000</sub>-Mal), 1,2-distearoyl-*sn*-glycero-3-phosphoethanolamine-N-[methoxy(polyethylene glycol)-2000] (DSPE-PEG<sub>2000</sub>) and 1,2-dimyristoyl-*sn*-glycero-3-phosphoethanolamine-N-(lissamine rhodamine-B sulfonyl) (Rho-PE) were purchased from Avanti Polar Lipids (Alabaster AL, USA). Cholesterol (Chol) was obtained from Sigma Aldrich (St. Louis MO, USA). Sepantronium bromide (YM155) was purchased from Bio-connect (Huissen, The Netherlands). Anti-disialoganglioside GD2 (Anti-GD2) antibody was obtained from BD Pharmingen (Alphen aan den Rijn, The Netherlands). N-succinimidyl S-acetylthioacetate (SATA) and Hoechst 33342 Fluorescent Stain were obtained from Thermo Fischer Scientific (Landsmeer, The Netherlands). 4',6-Diamidino-2-phenylindole (DAPI) was obtained from Roche (The Netherlands). FluorSave mounting agent was obtained from Merck Millipore (San Diego, CA, USA). All chemicals used were analytical grade unless otherwise stated. Cell culture media and supplements were obtained from Gibco laboratories (Gaithersburg, United states). Foetal calf serum (FCS) was obtained from Sigma Aldrich.

### 2.2. Preparation of liposomes

Targeted liposomes were prepared from a mixture of DPPC, Cholesterol, DSPE-PEG<sub>2000</sub> and DSPE-PEG<sub>2000</sub>-Mal in molar ratios of 1.36:1.36:0.14:0.14. Control liposomes consisted of DPPC, Cholesterol and DSPE-PEG<sub>2000</sub> in molar ratios of 1.36:1.36:0.28. Fluorescently labeled liposomes were prepared by adding rhodamine-PE to the lipid mixture at 0.2 mol% of total lipid (TL). Lipids were dissolved in chloroform: methanol (9:1, v/v) and to a final concentration of 90 mM TL. YM155 was co-dissolved with the lipid mixture at a concentration of 0.25  $\mu\text{mol}/\mu\text{mol}$  TL. Organic solvents were removed using a rotary evaporator and subsequent drying under a nitrogen flow. The resulting drug-lipid film was hydrated by adding 3 ml of HBS buffer pH 7.4 (10 mM Hepes containing 135 mM NaCl).

Unilamellar liposomes were prepared by multiple extrusion steps over polycarbonate membranes (Nuclepore, Pleasanton, CA, USA) at decreasing pore size range (from 0.4 to 0.1  $\mu\text{m}$ ). Next, targeted liposomes (but not control liposomes) were reacted with Sata-anti-GD2 antibody at a final concentration of 30  $\mu\text{g}/\mu\text{mol}$  TL (2 mg/ml antibody) that had been deprotected with hydroxylamine 0.5 M for 45 minutes prior to its addition to the liposomes. Coupling of S-acetylthioacetyl (SATA) to anti-GD2 (8:1 SATA:Ab mol:mol ratio) was performed as described previously [30]. Remaining non-reacted antibody and non-encapsulated YM155 were removed by ultracentrifugation at 60,000 g at 4°C for 30 minutes and resuspension of liposomes in 3 ml HBS which was repeated three times. After the final purification step, liposomes were stored under nitrogen atmosphere at 4°C in the dark for a maximum of 4 weeks prior to usage.

### 2.3. Characterization of liposomes

Liposome size and polydispersity was measured using dynamic light scattering (DLS) on a ALV CGS-3 system (Malvern Instruments, Malvern, UK). Zeta- $(\zeta)$  potential of liposomes was measured using a Malvern Zetasizer Nano-Z (Malvern Instruments, Malvern, UK) with universal ZEN 1002 dip cells and DTS (Nano) software. The total lipid concentration was determined according to Rouser (31). YM155 content of the liposomes was determined from 100  $\mu\text{l}$  aliquots which were disrupted by diluting in 300  $\mu\text{l}$  of acetonitrile (ACN). YM155 content was measured with a UPLC Waters Acquity system (Waters Corporation, Milford, MA, USA) equipped with Acquity UPLC  $^{\circ}$ BEH C18, 1.7  $\mu\text{m}$  column (2.1  $\times$  50 mm) thermostated at 50 °C and a UV detector operated at 252 nm. The gradient mobile phase was operated at a flow rate of 0.5 ml/min and consisted of 5% ACN in water containing 0.1% trifluoroacetic acid (solvent A) and 100% ACN containing 0.1% trifluoroacetic acid (solvent B). YM155 encapsulation efficiency (EE %) was calculated from the determined YM155/TL ratio versus the initial drug/TL ratio. Conjugation of anti-GD2 to DSPE-PEG<sub>2000</sub>-Mal was confirmed by western blotting using anti-mouse IgG immunodetection. In brief, reduced samples were subjected to SDS-PAGE using 4-12% gradient NuPAGE Novex Bis-Tris mini-gel (Thermo Fischer Scientific). Samples

were electrotransferred onto a nitrocellulose membrane via an iBlot Dry Blotting system (Invitrogen). Next, the membrane was blocked with 5% BSA in Tris-buffered saline containing 0.1% Tween-20 (TBS-T) and incubated with goat-anti mouse-IgG secondary antibody conjugated to horseradish peroxidase (HRP) (Thermo Fischer Scientific), diluted 1:1000 in 5% BSA in TBS-T. Proteins were visualized and detected using SuperSignal West Femto Chemiluminescent Substrate (Thermo Fischer Scientific) and a Gel Doc imaging system equipped with a XRS camera and Quantity One analysis software (Bio-Rad, Hercules, CA, USA). Coupling of antiGD2 to targeted liposomes was quantified and further characterized by micro-BCA assay (Pierce Biotechnology, Rockford, IL, USA) using mouse IgG (Sigma Aldrich) as calibration standards. Antibody coupling degree (antibody/liposome;  $p$ ) was calculated using geometric arguments according to Adrian [32] using the following formula:  $p = \pi/6 \times C_{Ab} \times (3d_{bl} \times R^2 - 3R \times d_{bl}^2 + d_{bl}^3) \times M_{ab}^{-1} \times V_{LS}^{-1}$ , in which ( $C_{Ab}$ ) is the measured concentration of coupled antibody (g/mol TL), ( $M_{Ab}$ ) is the molecular mass of the antibody, ( $R$ ) is the average diameter of liposomes (nm) of the spherical liposomes and ( $V_{LS}$ ) and ( $d_{bl}$ ) represent the specific lipid volume and lipid bilayer thickness, respectively.

#### 2.4. Storage stability of YM155 loaded liposomes

The storage stability of YM155 loaded liposomal formulations (targeted and non-targeted control liposomes) was studied at 4 °C for a total duration of 4 weeks on samples diluted in HBS buffer. At 0, 5, 10, 20 and 30 days samples were collected in duplicate. Released (non-encapsulated) YM155 was separated from liposomal YM155 by ultrafiltration using Vivaspin centrifugal concentrators with a molecular weight cut-off membrane of 10 kDa (Sartorius AG, Aubagne, France) for 5 minutes at 4000 g at 4°C. YM155 was determined in both the filtrate (free YM155, released fraction) and the remaining fraction in the upper compartment of the Vivaspin device (total YM155, free and liposomal fraction) which represented at least 70% of the starting volume. The collected samples (both fractions) from each time point were stored in the dark at 4 °C for further analysis. Aliquots of 50  $\mu$ l were taken and diluted in 150  $\mu$ l ACN, centrifuged at 22000 g for 10 minutes at 4°C and

subjected to UPLC analysis as described above. Experiments were repeated two times with individually prepared batches of liposomes.

### 2.5. *In vitro* release of YM155 from liposomes

Release studies were conducted under conditions reflecting cell culture and animal experiments, to study the influence of serum proteins and temperature on stability of YM155 loaded liposomes. Aliquots of anti-GD2 targeted and control liposomes with a final YM155 concentration of 25-30  $\mu\text{M}$  were prepared by diluting the stock solutions prepared for each batch with incubation media consisting of either HBS buffer, 5% bovine serum albumin (BSA) in HBS buffer, or pooled female mouse serum containing *EDTA-disodium* (Seralab Laboratories, Haywards Heath, UK) diluted 1:1 with HBS buffer. Samples were incubated at either 37°C or 4°C while gently shaking on a roller bench for a total duration of 24 hours. At pre-determined time periods of 0, 6, 12 and 24 hours, samples were removed from the incubators and concentrations of released YM155 and total YM155 were determined as described above. Experiments were repeated two times with individually prepared batches of liposomes.

The YM155 release data were fitted with zero-order or first order kinetic models, thereby using the following formulas:

Zero-order kinetics:  $M_t/M_0 = -k*t$

First-order kinetics:  $M_t/M_0 = e^{-k*t}$

Where  $M_0$  is the amount of encapsulated YM155 at the start of the incubation and  $M_t$  is the amount of encapsulated YM155 at each time point;  $k$  is the release rate constant. The release rate constants ( $k$ ) reported in this work are calculated from first-order kinetics fits to experimental release data, and are thus expressed in units of (1/hour, or  $\text{h}^{-1}$ ). The calculated release rate constants allow for a quantitative comparison of the experimental YM155 release profiles of the (liposomal) formulations under the various conditions.

## 2.6. Culturing of tumor cell lines

Tumor cell lines KCNR, IMR32 (Neuroblastoma tumor cells) and WiDR (human *colon adenocarcinoma tumor cells*) were obtained from ATCC<sup>TM</sup>. Cells were cultured in Dulbecco's Modified Eagle's Medium (DMEM) containing D-glucose (4.5 g/L) and 2mM glutamate, without pyruvate, and supplemented with 10% fetal calf serum (FCS), 1% MEM Non-Essential Amino Acids (NEAA) and 1% L-Glutamine. Cells from passage 5 to 7 were seeded one day before the experiment in culture flasks (T-75 cm<sup>2</sup>) at 2-4 x 10<sup>6</sup> cell densities, unless stated differently.

## 2.7. Assessment of GD2 expression in neuroblastoma cell lines

Neuroblastoma cell lines were studied for GD2 expression levels by flow cytometry. Cells from each cell line were trypsinized and re-suspended at a concentration of approximately 4 x 10<sup>6</sup> cells/ml in 10 ml of PBS supplemented 6.6% FCS and 20 mM EDTA (flow cytometry buffer). Cells were incubated with either anti-GD2 Ab or mouse isotype control Ab (Thermo Fischer Scientific) as a negative control, at a 1:200 dilution for 45 minutes at room temperature. Next, cells were washed three times with flow cytometry buffer by centrifugation for 5 minutes at 300 g and resuspension in buffer. After the final washing step, cells were suspended in flow cytometry buffer FACS containing FITC-labeled Goat-anti-Mouse IgG (H+L) secondary antibody (Thermo Fischer Scientific) at a dilution of 1:960, followed by incubation at room temperature in the dark for 20 minutes. Next, the cells were washed as explained earlier. Gates were set for GD2-positive and negative fluorescence signals, based on the fluorescence intensity obtained from cells as measured by the Accuri<sup>TM</sup> C6 Flow Cytometer (BD Biosciences, Erembodegem, Belgium). The analysis was based on both living and dead cells. Generally, 10,000 events were acquired per sample. Data were analyzed with CFlow Plus software.

## 2.8. Binding and uptake studies with rhodamine labeled liposomes

The binding of rhodamine labeled GD2-targeted and control liposomes to GD2 positive (i.e. IMR32) and GD2 negative (i.e. WiDR) tumor cells was studied by flow cytometry, using an average of

40 x 10<sup>3</sup> cells/ml in flow cytometry buffer. Cells were incubated with liposomes for 1 hour at 4 °C in the dark at different lipid concentrations ranging from 0.1 to 2 mM TL. Cells were washed three times with FACS buffer as described in the previous section after which mean fluorescence intensity (MFI) of the rhodamine signal was determined using the Accuri™ C6 Flow Cytometer. Generally, 10,000 events were acquired per sample. Data were analyzed with CFlow Plus software.

The uptake of rhodamine-labeled liposomes was studied using KCNR neuroblastoma cells by fluorescence microscopy using a Leica TCS-SP confocal laser-scanning microscope (Leica, Heidelberg, Germany). KCNR cells were seeded at a concentration of 40 x 10<sup>4</sup> cells/ml on FluoroDish™ glass bottom petri-dishes and allowed to adhere overnight. Cells were incubated with rhodamine labeled liposomes at a TL concentration of 1 mM for 4 hours at 37 °C, followed by washing with cold PBS. Cells were fixed (4% formaldehyde in PBS; 30 minutes at room temperature) and nuclei were stained using Hoechst 33342 (5 min at room temperature). After washing with cold PBS the petri-dishes were dried and covered with FluorSave mounting agent and kept at 4 °C until confocal microscopy analysis. *Z-stack* of optical sections (11.5 µm in total thickness) was captured with a 20x objective, using 10 sections with a step size of 1.15 µm. In order to illustrate cell uptake, 2D images were captured from the middle section of the Z-stack (i.e. 5<sup>th</sup> section).

## 2.9. In vitro effects of YM155 loaded liposomes

Efficacy of YM155 loaded liposomes (targeted and non-targeted control liposomes) was studied on KCNR by alamarBlue viability assay (Thermo Fischer Scientific, Landsmeer, The Netherlands), according to the supplier's instruction. KCNR cells were seeded at 20 x 10<sup>3</sup> cells/well in 96 well plates in complete DMEM medium and allowed to adhere overnight. The medium was replaced by cell culture medium supplemented with YM155 or YM155 liposomal formulations at concentrations ranging from 0.8 to 100 nM, after which the cell culture were incubated for 24 hours at 37 °C. Control experiments included incubations with empty liposomes (i.e. without YM155) at equivalent TL concentrations in the range of 0.08-11 µM TL. After 24 hours of incubation, medium was replaced



with drug-free medium containing alamarBlue reagent (10 vol %), after which cells were incubated for an extra 3 hours at 37 °C. Fluorescence was quantified with a microplate reader (Mithras LB940) and used to calculate the relative percentage of living cells normalized against control cells that had not been treated with YM155. IC<sub>50</sub> values were calculated by curve fitting using non-linear regression in Graph Pad Prism 6.0.

### **2.10. Pharmacokinetic pilot study**

Animal experiments were conducted in compliance with the national regulations and have been approved by the local ethical committee for animal experimentation. NMRI nu/nu female mice (25 g, Charles River, Massachusetts, United States) were housed in a temperature-controlled room (approximately 22 °C) with 55 to 65 % relative humidity, a photoperiod of 12/12 h with free access to water and pelleted rodent food. The mice were challenged with KCNR neuroblastoma (passage 1-2) derived from DAG102776 by serial xenotransplantation in both flanks. When the tumor growth reached the size of approximately 8x8 mm, mice were randomly divided in three groups that were injected intravenously with either free YM155 dissolved in HBS (1 mg/kg, n= 13), YM155 loaded anti-GD2-immunoliposomes (3 μmol TL/kg diluted in HBS, equivalent to 1 mg/kg YM155, n=11), or an equivalent dose of YM155 loaded control liposomes (n=12). At indicated time points, mice were sacrificed and blood samples (approximately 0.5 ml per sampling time point) were collected in tubes containing EDTA as anticoagulant. Blood samples and excised tumors were stored at -80 °C until analysis of their YM155 concentration by liquid chromatography-tandem mass spectrometry (LC-MS/MS) method. All samples (liposomal YM155 and free YM155) were treated and analyzed by LC-MS using the methodology described previously [33].

### **2.11. Pharmacokinetic and statistical analyses**

Pharmacokinetic analysis of the in vivo data was performed using the Pk Solver 2.0 add-in template for Microsoft Excel, as described previously [34]. Pharmacokinetic parameters were

determined by non-compartmental analysis (NCA) using linear-logarithmic trapezoidal model fitting, or by compartmental analysis (CA) using 1-compartment model fitting.

Statistical significance was analyzed using two-tailed unpaired Student's t-test. A p-value < 0.05 was considered statistically significant.

### 3. Results and discussion

#### 3.1. Preparation and characterization of liposomes

YM155 loaded liposomes were prepared by drug/lipid film hydration and extrusion, and subsequently purified by three cycles of ultracentrifugation and re-dispersion of the pelletized liposomes in HBS. SATA-modified anti-GD2 was conjugated to the maleimidyl anchor of DSPE-PEG<sub>2000</sub>-Mal before the ultracentrifugation procedure, thus avoiding an additional purification process to remove non-conjugated anti-GD2 from the final immunoliposomes. The physicochemical properties of the different types of liposomes are given in table 2. The average liposome size determined by DLS was in the range of 140-170 nm, with a corresponding polydispersity index of about 0.1. The prepared liposomes had a slightly negative zeta-potential of around -10 mV. Attachment of anti-GD2 antibody to the surface of the liposomes did not significantly alter their size or surface zeta potential as compared to control liposomes, and neither did the inclusion of YM155. The average YM155 encapsulation efficiency was found to be around 14 %, resulting in an average loading content of approximately 0.8 mg/ml (0.035 mM; see table 2). Quantification by microBCA showed an anti-GD2 coupling efficiency of around 60% for both YM155-loaded and empty liposomes, which corresponds to an average of approximately 33  $\mu\text{g Ab}/\mu\text{mol TL}$ . Assuming an average liposomal size of 140 nm, this results in a calculated 16 to 19 antibody molecules coupled per single liposomal particle (see table 3).

**Table 2.** Physicochemical properties of liposomal formulations loaded with YM155 and/or containing GD2 antibody on the surface.

Batch	Size (nm)	PDI	Charge (mV)	TL ( $\mu\text{mol/ml}$ )	Lipid Yield (%)	Encapsulated YM155 ( $\mu\text{mol/ml}$ )	Drug / Lipid ratio <sup>a</sup>	YM155 EE (%) <sup>b</sup>
(empty) control liposomes	140 $\pm$ 1	0.10 $\pm$ 0.01	-10.0 $\pm$ 5.2	56.3 $\pm$ 16.6	62.5 $\pm$ 18.4	-	-	-
(empty) anti-GD2 immunoliposomes	147 $\pm$ 14	0.10 $\pm$ 0.03	-9.0 $\pm$ 1.4	56.6 $\pm$ 22.5	62.8 $\pm$ 24.9	-	-	-
YM155-loaded control liposomes	161 $\pm$ 14	0.05 $\pm$ 0.01	-8.1 $\pm$ 2.1	52.7 $\pm$ 13.3	58.7 $\pm$ 11.5	1.85 $\pm$ 0.24	0.036 $\pm$ 0.010	14.3 $\pm$ 4.8
YM155-loaded anti-GD2 immunoliposomes	171 $\pm$ 10	0.10 $\pm$ 0.03	-9.6 $\pm$ 0.5	52.5 $\pm$ 14.4	60.2 $\pm$ 12.3	1.77 $\pm$ 0.29	0.035 $\pm$ 0.010	13.9 $\pm$ 5.0

Data are presented as mean values of 3-5 preparations  $\pm$  SD, <sup>a</sup> Drug/Lipid ratio determined after liposomal disruption. The initial YM155/Lipid ratio prior to liposomal formulation was determined to be 0.25, see paragraph 2.2 in main text. <sup>b</sup> YM155 encapsulation efficiency is defined as: [liposomal drug/lipid ratio (see note a)] / [initial drug/lipid ratio (=0.25, see paragraph 2.2 in main text)]

**Table 3.** Efficiency of anti-GD2 antibody coupling to liposomes

	GD2-YM155 liposomes	GD2 liposomes (empty)
$\mu\text{g Ab} / \mu\text{mol TL}$	35.7 $\pm$ 9.9	30.9 $\pm$ 9.8
Ab coupling efficiency (%) <sup>a</sup>	60.1 $\pm$ 5.5	58.7 $\pm$ 7.8
Ab / liposome <sup>b</sup>	19 $\pm$ 5	16 $\pm$ 5

Data are presented as mean values of 3 preparations  $\pm$  SD, <sup>a</sup> Antibody (Ab) coupling efficiency (%) = (amount of Ab coupled to liposomes/initial amount of Ab added)  $\times$  100%, <sup>b</sup> Number of Ab molecules coupled per liposome, assuming all recovered Ab is attached covalently to liposomes, and assuming an average liposome size of 140 nm.

To confirm that anti-GD2 had indeed been coupled covalently to the liposomal surface, (i.e. by thioether bond resulting from the reaction of SATA-anti-GD2 with the maleimidyl-PEG-DSPE lipids) immunoblotting was performed as described in section 2-3. SATA-modified anti-GD2 Ab (SATA-GD2) migrated as two bands of approximately 25 and 55 kDa, which correspond to the respective light and heavy chains of the antibody (Figure 2, left). Control (i.e. non-targeted) non-loaded liposomes (L) and control YM155 loaded liposomes (YM155-L) did not display any bands, while both GD2-targeted

empty (non-loaded) liposomes (GD2-L) and GD2-targeted YM155 loaded liposomes (GD2-YM155-L) displayed several bands between 25 and 80 kDa corresponding to the molecular weight of anti-GD2 Ab heavy or light chains coupled to one or multiple DSPE-PEG<sub>2000</sub>-Mal anchors (2.9 kDa per unit). Since not all of the anti-GD2 subunits had been modified with SATA and/or conjugated to the maleimidyl-PEG anchor, the immunoliposomal formulations also contained bands that migrated in parallel to the subunits of the parent anti-GD2 protein (i.e. around 25 and 55 kDa).

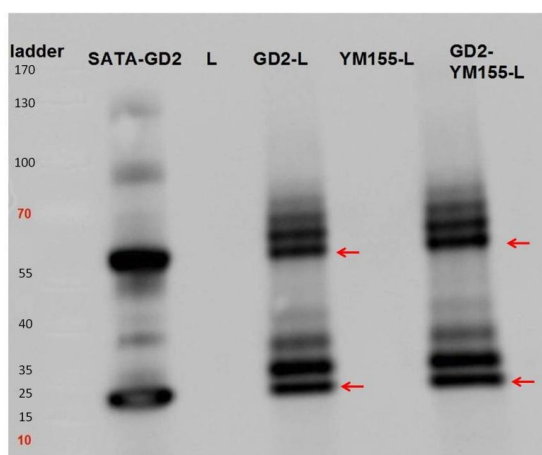


**Figure 2.** SDS-PAGE (reducing conditions) of: SATA modified anti-GD2 antibodies (**SATA-GD2**), empty (YM155-free) control liposomes (**L**), empty (YM155-free) GD2-targeted immunoliposomes (**GD2-L**), (non-targeted) control YM155 loaded liposomes (**YM155-L**) and GD2-targeted YM155 loaded immunoliposomes (**GD2-YM155-L**) from left to right, respectively. Red arrows indicate the location of bands corresponding to antibody subunits not modified with maleimidyl-PEG-DSPE anchor (see also corresponding bands in SATA-GD2) in liposomal formulations. Protein bands with either 1 or 2 attached PEGylated lipids are clearly visualized at higher MWs. See main text for details.

### 3.2. Stability and release of YM155 from liposomes at different conditions

The results of the stability tests of GD2-targeted immunoliposomes and control liposomes loaded with YM155 are shown in figure 3. The conditions of these experiments were chosen to reflect cell culture or *in vivo* conditions (50% serum, 37 °C) and conditions in which effects of either temperature on bilayer stability or serum proteins can be demonstrated. Both control liposomes and anti-GD2 immunoliposomes released approximately 20-30% of the encapsulated drug over the

studied 24 hour time period when incubated in 50% serum at 37 °C (Figure 3B). The observed leakage of the liposomes could be largely attributed to temperature-related changes in liposomal stability (Figure 3C vs. 3D, showing release in HBS buffer at 37 °C vs. 4 °C) while the presence of either serum albumin or 50% serum increased the release rate of YM155 only marginally (see table 4 and figure 3A + 3B vs. 3C, showing YM155 release at 37 °C in HBS buffer containing 5% BSA or 50% serum, versus pure HBS buffer).

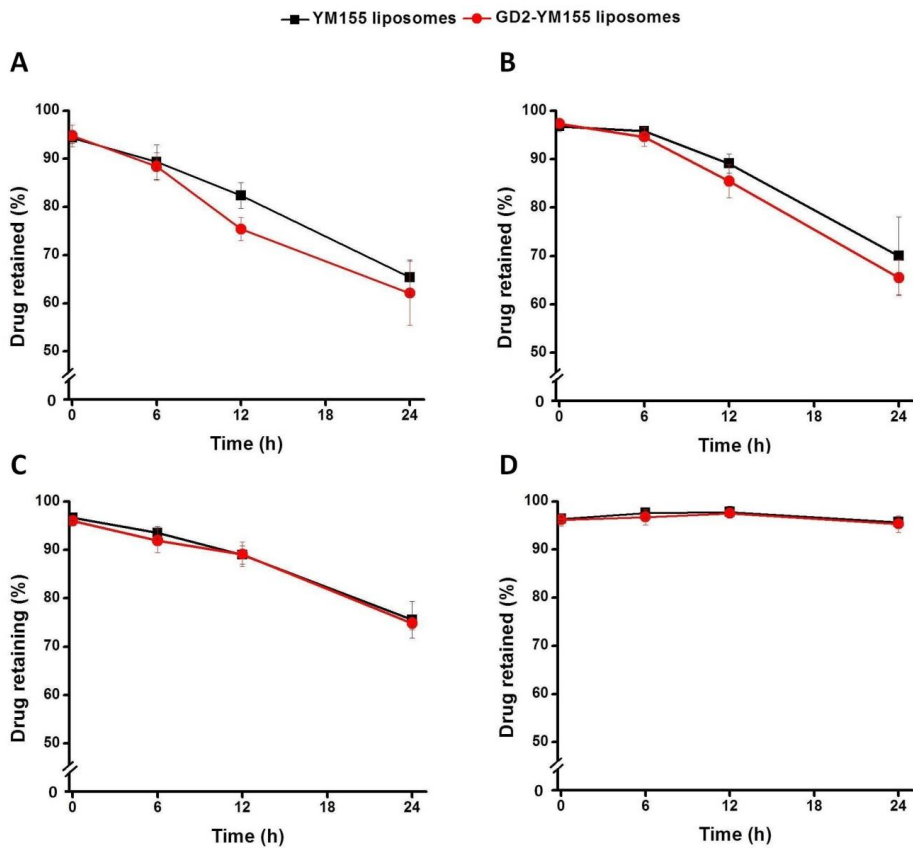


**Figure 3.** Release experiments were performed at different conditions. **(A)** at 37 °C in 5% BSA in HBS buffer, **(B)** at 37 °C in 50% serum in HBS buffer, **(C)** at 37 °C in only HBS buffer and **(D)** at 4 °C in 5% BSA in HBS buffer. Each value represents the mean value ( $\pm$  S.D) of two independent experiments performed in duplicate.

**Table 4.** Comparison of the first-order rate constants  $k$  ( $\text{h}^{-1}$ ), based on fitting of the *in vitro* YM155 release profiles shown in figure 3, showing the effects of temperature and medium composition on the YM155 release rates.

Conditions		$k$ ( $\text{h}^{-1}$ ) <sup>a</sup>	
Temp. (°C)	Medium	Control liposomes	Targeted liposomes
37	HBS + 5% BSA	0.018	0.018
37	HBS + 50% serum	0.018	0.021
37	HBS	0.012	0.011
4	HBS + 5% BSA <sup>b</sup>	-	-

**a)** Value of  $k$  equals the slope of the linear fit ( $R^2 > 0.99$  in all cases) of the semi-logarithmic plot [(YM155 retained in liposomes) versus time] (not shown), extrapolated from the experimental release profiles shown in figure 3A-D. **b)** YM155 release from the liposomes in HBS + 5% BSA at 4 °C remained unchanged (< 5% for all samples) during a 24 hour period, indicating the YM155-containing liposomes are stable in the medium at low temperatures.

Comparison of first-order release rates (Table 4) confirms a slight increase in the YM155 release rate at 37 °C in the presence of serum albumin. The data in figure 3 and table 4 also shows that there is no significant difference in YM155 release rate between the control liposomes and the anti-GD2 modified immunoliposomes, regardless of the release medium and temperature. Furthermore, it was shown that the YM155 release in the presence of HBS buffer + 5% BSA could be halted for at least 24 hours if the temperature was dropped to 4 °C, as can be seen in figure 3D. Additional stability tests (see figure S3) have shown that the YM155-loaded liposomes were stable for at least 3 weeks at 4 °C in HBS buffer (no BSA).

A plausible explanation for the increased YM155 release at higher temperatures is an increase in fluidity of the lipid bilayer at 37 °C [35, 36]. Overall, it can be concluded that YM155 liposomes have moderate stability at body temperature, while neither the presence of proteins (i.e. serum or BSA) in the medium, nor the coupling of anti-GD2 to the liposomal surface appear to greatly influence the stability of the liposomes. The observed release of YM155 from liposomes can be important in the interpretation of other results concerning efficacy and pharmacokinetics, in which free YM155 and encapsulated drug may undergo different uptake and clearance routes. For potential *in vivo* applications of YM155-loaded PEGylated liposomes their instability and the related release of the encapsulated drug is not necessarily problematic, as has been reported by Shakushiro and coworkers

[19]. In their study, YM155-loaded liposomes with various lipid compositions were extensively studied and tested for antitumor activity. Among the investigated formulations DSPC/AS liposomes were shown to be the most stable formulation, based on *in vitro* YM155 release study. The YM155 release rate from DSPC/AS liposomes reported by Shakushiro and coworkers is comparable to the YM155 release rate of the formulations described here in the present work. However, Shakushiro *et al.* reported that the optimal formulation which demonstrated most potent *in vivo* antitumor activity was in fact the DSPC/BP liposomes, which showed a higher YM155 *in vitro* release rate than the DSPC/AS formulation mentioned earlier. The difference in YM155 release rates between the optimum formulations found previously by Shakushiro *et al.* and the formulations used in this work can be explained by the different nanomedicine targeting approaches in both studies.

Generally, both passively and actively targeting nanomedicine accumulate in the tumor tissue via the enhanced permeability and retention (EPR) phenomenon. When passively targeting nanomedicine accumulates in the target tissue, the encapsulated drug molecules need to be released from their delivery system so that they can be taken up by the target cells. Thus, their release rate needs to be precisely engineered, as described by Shakushiro *et al.* However, for actively targeting nanomedicine direct endosomal uptake of the nanomedicine is facilitated by the presence of (surface) targeting moieties (e.g. anti-GD2 antibody), which is then followed by cytosolic release of the encapsulated drug molecules. Since this study aims to use actively targeting nanomedicine formulations for the delivery of YM155, the more stable liposomal formulations are expected to be most suitable.

### 3.3. GD2 expression in various neuroblastoma cell lines

GD2 expression levels in neuroblastoma tumor cell lines were measured by flow cytometry as explained in section 2-7. KCNR (and IMR32) neuroblastoma showed relatively high levels of GD2 expression (i.e. about 95% and 86%, respectively), while WiDr colon carcinoma cells showed negligible fluorescent signal at the pre-determined gate settings, confirming the lack of GD2

expression on this cell line (data not shown). WiDr cells were further used in flow cytometry experiments as negative control cells.

### 3.4. Cell binding and uptake of liposomes

The ability of GD2-targeted immunoliposomes to recognize GD2 positive cells (IMR32) was demonstrated by incubating rhodamine labeled liposomes with the cells at 4 °C, after which cell-associated liposomes were detected by flow cytometry. A four-fold increase in binding of GD2-targeted immunoliposomes to IMR32 cells was observed in comparison to non-targeted control liposomes (Figure 4A). Moreover, both formulations showed similar low binding to GD2-negative WiDr cells (Figure 4B), thus confirming the GD2-dependency of liposomal binding.

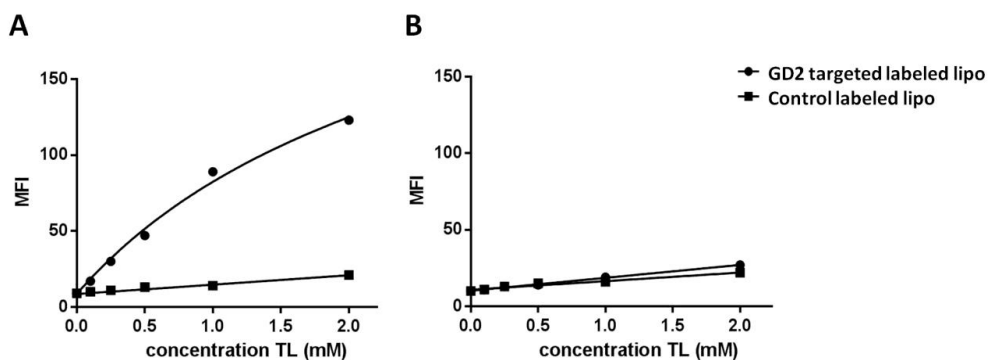


**Figure 4.** Binding of liposomal formulations to (A) IMR32 cells and (B) WiDr cells. The data points are aligned (fitted) by non-linear regression. MFI = Mean Fluorescence Intensity; TL=total lipids.

The binding and internalization of GD2-targeted immunoliposomes by KCNR cells was studied by confocal microscopy (Figure 5). Incubation of cells with liposomal formulation for 4 hours at 37 °C allowed binding and receptor mediated internalization of immunoliposomes, which was detected by a distinct increase in captured fluorescent intensity at the middle section of z-axis, which was not observed for control liposomes. The obtained results confirm the active (cellular) uptake of GD2-targeted immunoliposomes by KCNR cells.



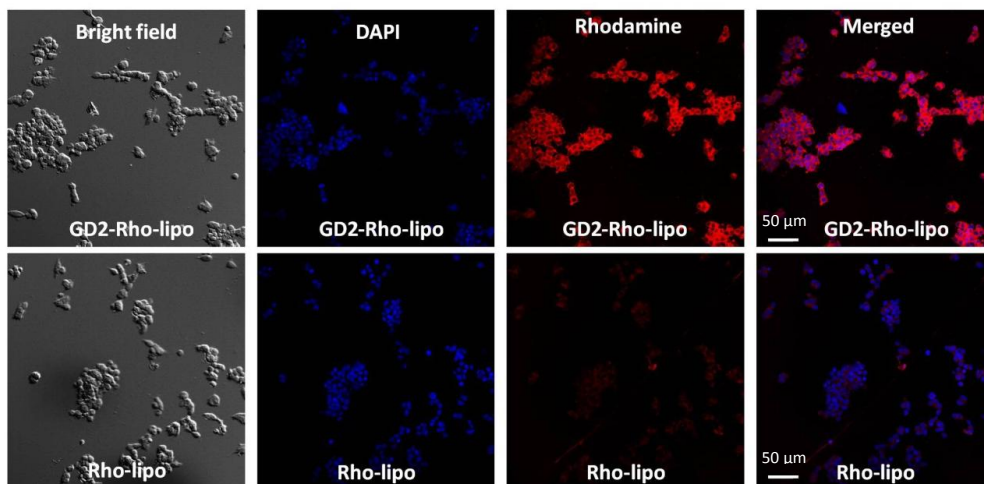


**Figure 5.** Confocal laser scanning microscope (CLSM) images of KCNR cells incubated with either GD2-targeted labeled liposomes (GD2-Rho-lipo) or with non-targeted control labeled liposomes (Rho-lipo). Blue staining (DAPI) represents cell nuclei. Red staining (rhodamine) represents liposomes. Scale bars in the figures represent 50  $\mu\text{m}$ .

### 3.5. *In vitro* evaluation of GD2 targeted loaded liposomes in cell culture

The *in vitro* efficacy of YM155 loaded liposomes was studied in KCNR cells by incubating the cells for 24 hours with the developed formulations. Inhibition of survivin by YM155 will change the balance between cell survival and apoptosis, which means that the efficacy of YM155 can be determined indirectly by a cell viability assay (AlamarBlue assay). Dose response curves shown in figure 6A have been analyzed by non-linear curve fitting to determine  $\text{IC}_{50}$  values of each formulation.  $\text{IC}_{50}$  values of 27, 60 and 83 nM were calculated for free YM155, anti-GD2 immunoliposomes loaded with YM155, and control liposomes loaded with YM155, respectively. Liposomes not containing YM155 did not induce cell toxicity at the concentrations examined in this work (Figure 6B). The overall data suggest that treatment of neuroblastoma cells (KCNR) with free YM155 is more effective compared to the treatment of cells with liposomal formulations (targeted or control), although YM155 loaded GD2-targeted immunoliposomes showed an increased (around 20%) efficacy compared to the non-targeted YM155-loaded control liposomes.

Amphiphilic small molecular inhibitors generally diffuse rapidly through cellular membranes, which enables small molecules to effectively inhibit intracellular molecular targets. However, YM155 is a positively charged small molecule not capable of passive diffusion over lipid membranes. Instead, its intracellular accumulation is actively mediated by cell specific influx transporter channels [37]. Apparently, the active uptake of free YM155 is very efficient, outperforming the intracellular delivery as effectuated by GD2-targeted liposomes. Other processes that can diminish the efficacy of liposomal formulated YM155 are the slow liberation of YM155 from the liposomal nanocarriers, and the absence of transporters in the endosomal and lysosomal membrane. It should thus be noted that part of the effects observed for the liposomal formulations might be due to a fraction of YM155 that is released from the liposomal formulations during the 24 hours incubation in protein containing cell culture media at 37 °C and which is subsequently transported over the cell membrane similar to free YM155. However, the absence of sample agitation means that YM155 released from the liposomes during the incubation period is likely to be lower than the corresponding YM155 release in the stability tests shown in figure 3. More importantly, the difference in efficacy observed between the anti-GD2 immunoliposomes and the non-targeted control liposomes clearly shows that a significant part of the total YM155 is taken up by the cells while remaining encapsulated in the liposomal nanocarrier system. Figure 7 schematically depicts the available uptake routes of YM155 upon its addition to the cells as liposomal formulation or free drug.

Our experiments show no toxicity of the anti-GD2 antibodies attached to the surface of liposomes on KCNR cells. However, toxic effects of free anti-GD2 antibodies were previously reported by Gottstein *et al.* on IMR32 cells [38]. One cause for these alternate observations regarding anti-GD2 toxicity can be the difference in sensitivity of the neuroblastoma cell types (i.e. IMR32 and KCNR) to anti-GD2 antibody. Another explanation is that Gottstein *et al.* observed toxic effects because in their work the IMR32 cells were exposed to concentrations of anti-GD2 antibody ( $IC_{50}$  1.5  $\mu\text{g/ml}$ ) that were much higher than the concentrations of anti-GD2 antibody that the liposomal surfaces were exposed to in this work. The highest concentration of anti-GD2 (coupled to a liposomal surface)

that was added to the cell culture media in our experiments was 0.08  $\mu\text{g/ml}$ , which is well below the above mentioned  $\text{IC}_{50}$  value of 1.5  $\mu\text{g/ml}$ .

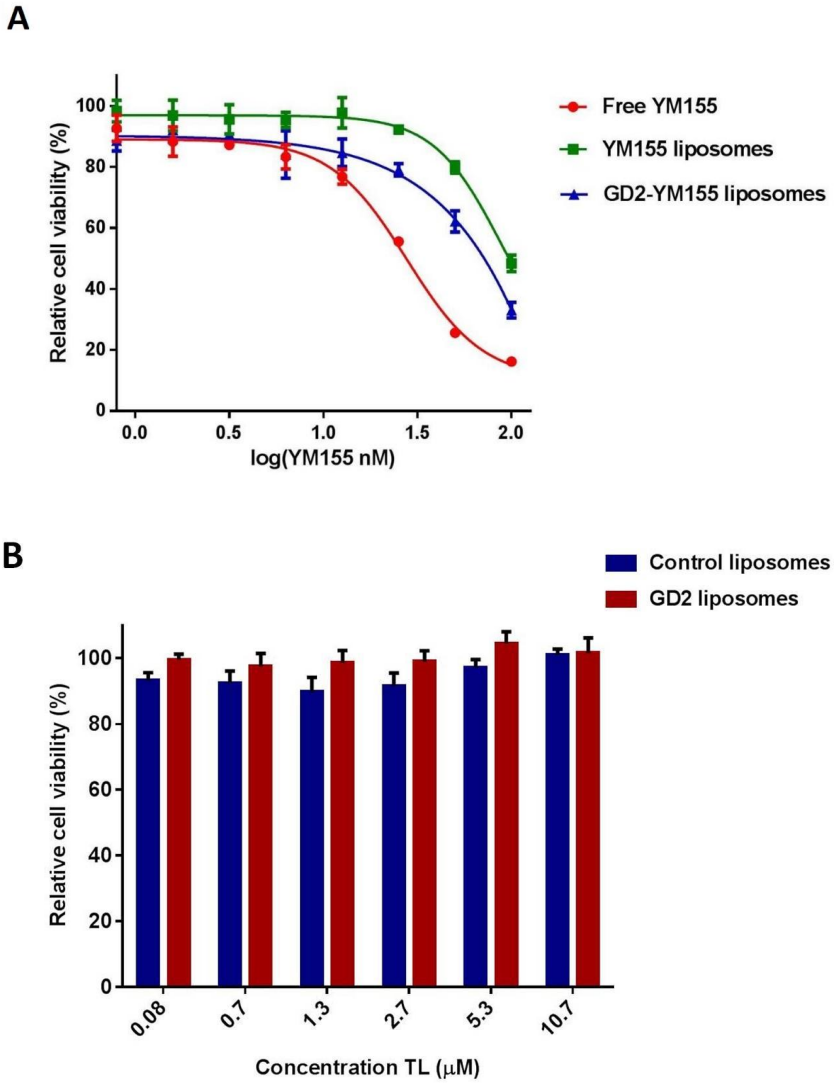


**Figure 6.** Cell toxicity was determined in neuroblastoma cells (KCNr) via MTS assay after 24 hours of total incubation period. **(A)** Semi-logarithmic plot of the cells exposed for 24 hours to YM155 loaded liposomal formulations and free YM155. The  $\text{IC}_{50}$  values were determined with Graph Pad Prism 6.0. (non-linear regression model was used for curve fitting). **(B)** Cells were exposed for 24 hours to non-loaded liposomal formulations. Data are plotted as mean values  $\pm$  SEM ( $n = 3$ ).

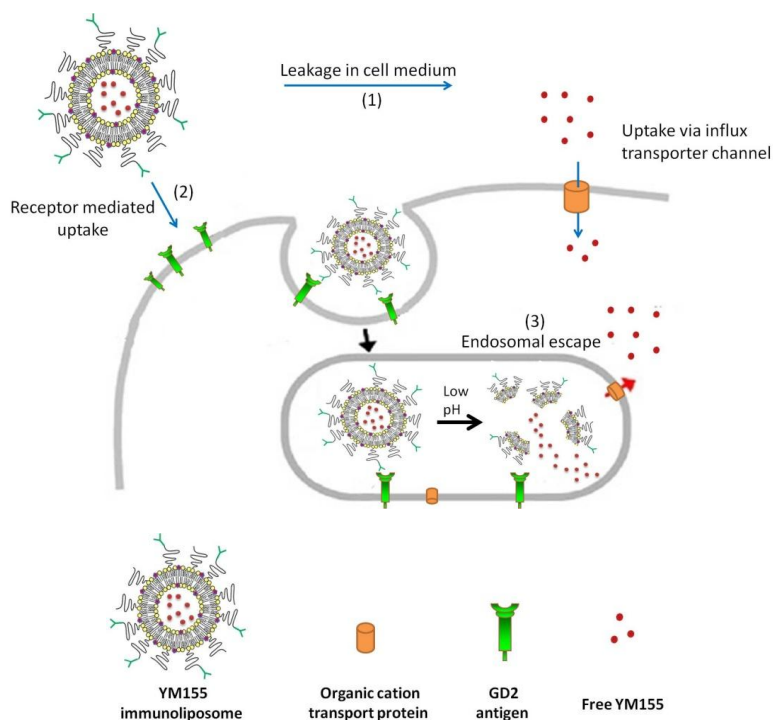


**Figure 7.** Uptake routes for cytosolic delivery of YM155. Receptor mediated uptake delivers GD2-targeted YM155 liposome into endosomal and eventually lysosomal vesicles. Cytosolic delivery of liberated YM155 is facilitated by passive diffusion (possibly as in complex with an organic anion or via organic cation transporters (OCT) when they are present in the lysosomal membrane). Cytosolic delivery of free YM155 is facilitated via organic cation transport (OCT) channels at the cell membrane. Adapted with permission from ref (39). Copyright 2006, Springer.

### 3.7. Pharmacokinetic profiles of free YM155 and its liposomal formulations

The distribution kinetics of YM155-loaded liposomes was evaluated in nude mice with subcutaneously implanted neuroblastoma tumors. Upon intravenous injection of either targeted or control liposomes or free YM155, plasma and tumor samples were collected over a time period of 5 minutes till 3 days and analyzed for YM155 by LC-MS. Figure 8 shows the YM155 plasma concentration versus time curves of free YM155 (Figure 8A), YM155-loaded control liposomes (Figure 8B), and YM155-loaded anti-GD2 immunoliposomes (Figure 8C). The calculated

pharmacokinetic (PK) parameters for free YM155 and liposomal YM155 presented in table 5 have been determined by non-compartmental analysis (NCA) using a linear-logarithmic trapezoidal method, in which linear interpolation is used if drug concentrations are increasing or constant ( $C_{i+1} \geq C_i$ ), while logarithmic interpolation is used if drug concentrations are decreasing ( $C_{i+1} < C_i$ ). The slope of the drug concentration versus time curve in the terminal phase ( $\lambda_z$ ) was determined by linear regression on a semi-logarithmic scale, and  $\lambda_z$  was then used to derive pharmacokinetic parameters such as drug half-life ( $t_{1/2}$ ) and volume of distribution in the terminal phase ( $V_z$ ). PK parameters were also determined by compartmental analysis (CA), in which the YM155 plasma concentration versus time curve is fitted using a 1-compartment model. The small scale of this in vivo pilot study resulted in a relatively low amount of data points (3 to 5) in the terminal phase of the YM155 plasma concentration versus time curves (see figure 8). Combined with the large error margins in some of the data points, this lowers the reliability of the fitted results and the related PK parameters listed in table 5. Thus, the results from the pharmacokinetic analyses listed in table 5 should be treated as estimates when comparing them with pharmacokinetic results from other studies. Within this work however, the PK parameters listed in table 5 are an excellent way to quantify the differences between the three different formulations (i.e. free YM155, Liposomal YM155, and GD2-liposomal YM155). As expected, mice treated with free YM155 showed very low YM155 plasma levels ( $< 0.7 \mu\text{g/mL}$ ) already shortly after injection (i.e. within the first 5 min before collection of the first blood samples) which is reflected in the large distribution volume of YM155 (see table 5). Moreover, free YM155 was rapidly eliminated from the circulation, and the plasma levels were detectable only for about 8 hours post- i.v. administration (Figure 8A). In contrast, liposomal formulations of YM155 (targeted and control) showed drastically reduced distribution volume as compared to free YM155, which can be expected for PEGylated nanocarriers as these prevent free distribution and cellular uptake of the drug into cells. Both liposomal formulation were able to sustain elevated plasma levels of YM155 for at least a 3 day time period (Figure 8B-C). The increased longevity of the liposomal YM155 in blood plasma can be attributed to the small hydrodynamic size and stealth properties

provided by PEG chains, which allow liposomal formulations to escape recognition and subsequent clearance by the mononuclear phagocyte system (MPS) [40, 41]. Moreover, the normal clearance of free YM155 is also prevented when the drug is still retained in the liposomal nanocarriers.

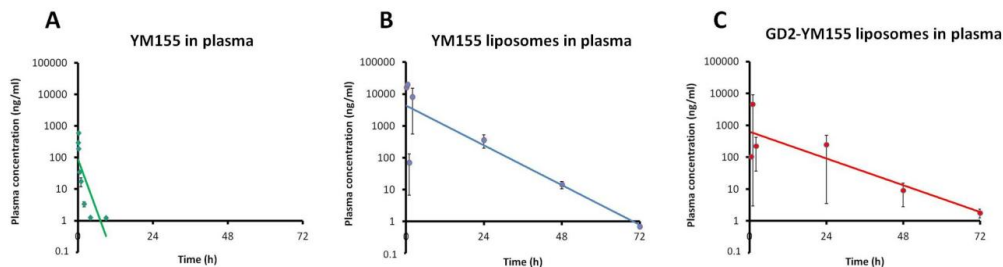


**Figure 8.** Semi-logarithmic YM155 plasma concentration vs. time plots, following single i.v. administration of **A:** free YM155 (1 mg/kg) or liposomal YM155 (**B:** control and **C:** targeted) (1 mg/kg) in mice. Data are expressed as the mean  $\pm$  SEM (n=2). Each dataset has been fitted using linear regression, with the inclusion of all data points in the fit. The fit in figure 8A (free YM155 in plasma) is a result of the tailing data points at  $t > 2$ h. Note that these data points have been excluded from the fit (not shown) used in the pharmacokinetic analysis of the free YM155 data. See main text for details.

**Table 5.** Pharmacokinetic evaluation for total YM155 levels in whole blood after a single i.v. administration to female mice

	Free YM155 (2h) <sup>a</sup> (1mg/kg)	YM155 liposomes (1mg/kg)	GD2-YM155 liposomes (1mg/kg)
$t_{1/2}$ (h)	0.4	5.3	6.8
$AUC_{0-\infty}$ (ng/mL*h)	136	71473	37787
$C_L$ (mL/h)	7337	12	26
$V_z$ (mL/kg)	4653	90	258
$V_{ss}$ (mL/kg)	2466	75	98
$MRT_{0-\infty}$ (h)	0.34	6.4	3.7

The PK values are calculated by non-compartmental analysis using a linear-logarithmic trapezoidal method.

$C_0$  = concentration at  $t=0$ , extrapolated,  $t_{1/2}$  = elimination half-life,  $AUC_{0-\infty}$  = extrapolated area under the curve from zero to infinity,  $C_L$  = plasma clearance,  $V_z$  = volume of distribution during terminal phase, derived from slope ( $\lambda_z$ ) in terminal phase,  $V_{ss}$  = volume of distribution at steady state,  $MRT_{0-\infty}$  = mean residence time.

**a)** PK analysis for free YM155 is based on data points until  $t=2$ h. Inclusion of the  $t > 2$ h data points will result in an unrealistic estimate of the terminal slope  $\lambda_z$  due to the negligible (difference in) YM155 concentrations in these  $t > 2$ h data points (see also figure 8A).

The difference between free YM155 and liposomal YM155 formulations is also clear when examining their difference in rate of YM155 elimination from the blood plasma, and the related YM155 half-life ( $t_{1/2}$ ) values. The samples' ( $t_{1/2}$ ) values derived from the NCA fitting model are listed in table 5, together with other related PK parameters. Clearly, the half-life of free YM155 in blood plasma is significantly shorter (0.4 h) than that of the control liposomes and the GD2-immunoliposomes loaded with YM155 (5.3 and 6.8 h respectively). As mentioned above, these ( $t_{1/2}$ ) values have been derived from the terminal slope ( $\lambda_z$ ), which in turn is determined by the linear fit of the last 3 data points of the semi-logarithmic (YM155 concentration in blood plasma vs. time) plots. However, when examining the data in figure 8, it becomes clear that YM155 plasma concentration in the first few data points (i.e.  $t \leq 2$  h) appears to decrease with a different exponential decay rate as compared to the exponential decay rate in the last 3 data points of the terminal phase. This effect is particularly pronounced for free YM155 when comparing the 0-2 hour period and the 2-8 hour time period, though the YM155 plasma concentration in the liposomal formulations also shows different exponential decay rates in the 0-2 hour period as compared to the subsequent 2-72 hour period. These different exponential decay rates could be explained by differences between a distribution phase and an elimination (termination) phase during the YM155 clearance from the blood plasma. However, in the present *in vivo* pilot study there are not enough data points available per formulation to be able to draw reliable conclusions regarding this topic. To illustrate the difference in initial and terminal YM155 clearance rates in the different formulations, the pharmacokinetic evaluation was also performed by compartmental analysis (CA), using a 1-compartment model (data not shown). Contrary to NCA, which determines the YM155 half-life from the fitted terminal slope, CA (1-compartment model) fits a first-order exponential decay function to the dataset to determine the PK parameters. The ( $t_{1/2}$ ) values of the YM155 concentration in plasma derived from the NCA and CA methods are listed for comparison in table 6. It should be noted that the CA used a 1-compartmental model, which means that the fit results are only meaningful for the initial period of rapid decline in YM155 plasma concentration that occurs in the first two hours. Instead, the more

gradual decline in the terminal period that can go up to  $t=72$  h is accurately described by the NCA fit results.

**Table 6.** Comparison of half-life values for YM155 concentration in blood plasma determined by non-compartmental (NCA) and compartmental analysis (CA).

	NCA $t_{1/2}$ (h)	CA $t_{1/2}$ (h)
Free YM155 (2h) <sup>a</sup>	0.4	0.20
YM155 Liposomes	5.3	1.94
YM155 GD2-Liposomes	6.8	0.23

Half-life values determined by non-compartmental analysis (NCA) using linear-logarithmic trapezoidal model, and compartmental analysis (CA) using a 1-compartment model. <sup>a</sup> PK analyses of free YM155 are based on data points until  $t=2$  h. See also table 5 and main text.

Free YM155 samples (data points until  $t=2$ h included in both CA and NCA analyses) in fact showed little difference between the NCA and CA results, as can be seen in table 6. This was expected, since both NCA and CA fit only the rapid decay in YM155 blood plasma concentrations that was observed during the first 2 hours. Since the free YM155 samples already had an almost negligible YM155 concentration remaining at  $t=2$ h ( $3.3 \pm 0.9$  ng/mL), the inclusion of the additional data points at  $t>2$ h, with YM155 plasma concentrations around 1 ng/mL, would have severely skewed the resulting fit and related free YM155 PK parameters, as can be seen in figure 8A.

Instead, for the liposomal samples a significant fraction of the YM155 remains detectable in the blood plasma for a long period of time of up to 72 hours (see figure 8B-C). Not surprisingly, the NCA and CA fits result in very different half-life values for the YM155 concentration in blood plasma. The difference is most pronounced for the GD2-liposomes loaded with YM155, for which the rapid decrease observed in YM155 plasma concentration during the first 2 hours results in a CA half-life estimate that is even comparable to that of free YM155 (0.23 and 0.20 hours, respectively). In contrast, after 2 hours the remaining YM155 concentration in blood plasma that originated from the GD2-liposomes is more sustainable, with trace YM155 (1.8 ng/mL) being detectable in the blood plasma even after 72 hours, resulting in a NCA (terminal) half-life estimate of 6.8 hours.



### 3.8. Tumor accumulation of free YM155 and its liposomal formulations

As can be observed in figure 9, intratumor levels of YM155 could be detected up to 24 hours post injection for free YM155, or up to three days post injection for liposomal YM155. It is important to notice that free YM155 was eliminated more slowly from tumor tissue than from the circulation (half-life of 6 hours in tumor, as compared to a half-life of 0.4 hours in plasma, determined by NCA of YM155 concentration in tumor samples vs. time plot, using a linear-logarithmic trapezoidal model), which can be attributed to the cation-transporter mediated uptake of the drug and its subsequent intracellular retention. Furthermore, tumor accumulation of liposomal encapsulated YM155 was delayed and sustained as compared to free YM155 (Figure 9A), which can be attributed to accumulation of nanocarriers via leaky tumor blood vessels, i.e. by EPR, and the prolonged residence of the nanocarriers in the circulation [42, 43]. Lastly, comparing anti-GD2 immunoliposomes and non-targeted control liposomes for the intratumor delivery of YM155 showed a reduced tumor AUC for the GD2-targeted formulation (AUC<sub>0-∞</sub> values of 13194 and 3803 (ng/mL\*h) for control- and GD2-liposomes respectively). A major limitation of the present pharmacokinetic study is the high variation in detected YM155 levels, in both plasma and tumor homogenates. These variations can be due to problems in the extraction of YM155 from the tissues, which could not be solved during the duration of this project, or other technical problems associated with the pilot animal experiment. Alternatively, the lower tumor AUC measured after injection of YM155-loaded anti-GD2 immunoliposomes can be due to faster elimination of YM155 from the tumor site as compared to YM155 control liposomes. Several scientific arguments can support this, such as the receptor mediated uptake and intracellular processing of anti-GD2 liposomes, which will liberate YM155 from the liposomal carrier. However, arguments such as differences in plasma YM155 concentrations and YM155 leakage are not supporting the higher tumor AUC for anti-GD2 immunoliposomes, as these values (e.g. plasma concentrations) are quite comparable for both liposomal carriers. Although this was not possible in the context of this pilot study, it would be very interesting to compare the anti-

tumor effects of both liposomal formulations, in order to assess the added value of anti-GD2 immunoliposomes over conventional long-circulating PEG-liposomes for the delivery of YM155.

Liposomal formulations of YM155 have been previously studied, for example in papers by Kawana *et al.* [20] and Shakushiro *et al.* [19]. In the study by Kawana and coworkers, the authors developed a liposomal YM155 formulation composed of DSPC, cholesterol and DSPE-PEG<sub>2000</sub> lipids using phosphate buffer as liposomal 'inner' phase. The reported blood circulation half-life ( $t_{1/2}$ ) was 14.6 and 26.5 hours for YM155 formulations at a dosage of 3 and 9 mg/kg, respectively [20]. In another study by Shakushiro and coworkers, the authors mainly focused on evaluating the effect of different liposomal formulations on the pharmacokinetics and efficacy. They reported a  $t_{1/2}$  of 24 hours at 3 mg/kg dose for a liposomal YM155 formulation composed of DPPC, cholesterol and DSPE-PEG<sub>2000</sub>, and a  $t_{1/2}$  of 48 hours at 3 mg/kg dose for a formulation composed of DSPC, cholesterol and DSPE-PEG<sub>2000</sub>, both containing phosphate buffer as liposomal inner phase [19]. These results are comparable to the results obtained with the liposomes in this work, in which a  $t_{1/2}$  of 5.3 and 6.8 hours was found for non-targeted and targeted liposomal YM155 formulations respectively (table 5), at an administration dose of 1 mg/kg. It is plausible to assume that similar  $t_{1/2}$  values would have been found when applying the 3 mg/kg dose, as was done in the work by Kawana *et al.* and Shakushiro *et al.* referenced above.

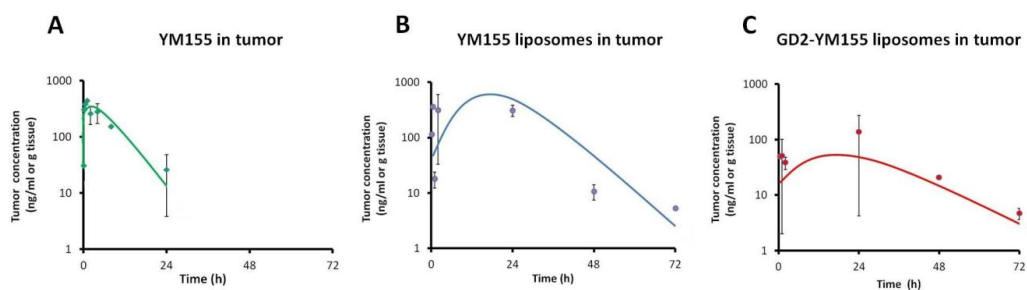


**Figure 9.** YM155 tumor levels vs. time plots after single i.v. administration of free YM155 (1 mg/kg) or liposomal YM155 (targeted and control) (1 mg/kg) in mice. Data are expressed as the mean  $\pm$  SEM ( $n=2$ ). Trend lines are added to guide the eye.

#### **4. Conclusions**

The present study reports on the encapsulation of the surviving inhibitor YM155 in immunoliposomes directed to neuroblastoma cancer cells. Surface bound anti-GD2 antibodies render the liposomes neuroblastoma cell specific (i.e. targeted) which has been confirmed by binding and uptake studies with GD2 expressing tumor cells. Both the immunoliposomes and the non-targeted control liposomes showed similar stability under all conditions, excluding detrimental effects of the surface-conjugated antibodies on liposome stability. The liposomal formulations were studied in a pilot pharmacokinetic experiment which demonstrated their long-circulating character and capability to accumulate intra-tumor. When compared to free YM155 after single bolus intravenous (i.v.) injection, prolonged intratumoral levels were obtained. A clear added value of using anti-GD2 immunoliposomes could not be assessed in the conducted pilot study. Further studies are required to evaluate the pharmacological effects (efficacy) of YM155-loaded anti-GD2 immunoliposomes at different YM155 dose ranges which may disclose more details on the potential of the liposomal YM155 formulations for clinical therapeutic applications.

#### **5. Acknowledgments**

The authors would like to thank Rebeca Wieriks and Charlene Ogu for their help with the experiments.

## Supporting information

### 1. Supplementary materials and methods

#### 1.1 Determining the functionality of SATA-modified anti-GD2 antibody

The functionality of SATA-modified anti-GD2 antibody (Ab) was assessed by FACS analysis on KCNR cells. For this study, cells at concentration of  $4 \times 10^6$  cells/ml were incubated with native and SATA modified anti-GD2 Ab at 1:200 dilution in FACS buffer. Cells were incubated for 45 minutes at room temperature followed by 3 washing steps with FACS buffer as explained in section 2-8. Next, cells were incubated for 20 minutes at room temperature with FITC labeled goat anti-mouse Ab at 1:960 dilution, followed by washing steps. At the final step, cells were resuspended in FACS-buffer and the fluorescence intensity was measured by Accuri™ C6 Flow Cytometer (BD Biosciences, Erembodegem, Belgium). The analysis was based on both living and dead cells. Generally, 10,000 events were acquired per sample. Data were analyzed with CFlow Plus software.

### 2. Supplementary data

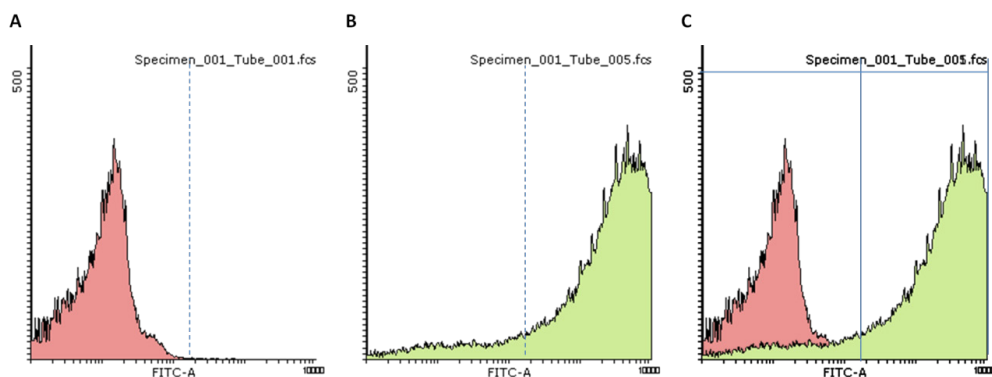


**Figure S1.** Example of flow-cytometry analysis to evaluate GD2 expression on IMR32 cells. **(A)** The staining with control isotype antibody is shown as the solid red profile. **(B)** The staining with the anti-GD2 antibody is shown as solid green profile. **(C)** An overlay of histograms. The percentage of positive expression is based on the area under the curve for the green histogram, on the right side of the blue lined set border.

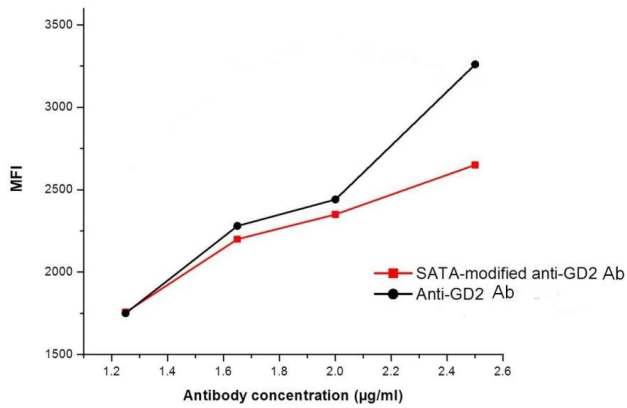


**Figure S2.** Modification of the anti-GD2 antibody with SATA only had a moderate influence the binding capacity of the antibody to GD2-positive cells.

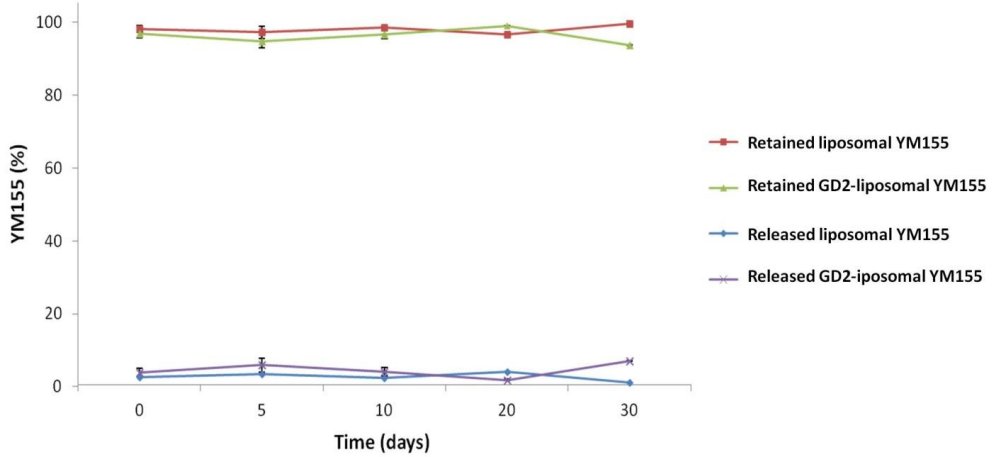


**Figure S3.** Results of the stability study on liposomes at 4 °C in HBS buffer (Each value represents the mean ( $\pm$  S.D) of two independent experiments.

## 6. References

1. Maris JM. Recent advances in neuroblastoma. *N Engl J Med.* 2010; 362: 2202–11.
2. <http://www.acco.org/treating-high-risk-neuroblastoma-at-the-turn-of-the-century/>
3. Morgenstern DA BS, Irwin MS. Current and future strategies for relapsed neuroblastoma: challenges on the road to precision therapy. *J Pediatr Hematol Oncol.* 2013;35(5):337-47.
4. Julia E. Heck BR, Rayjean J. Hung, Mia Hashibe and Paolo Boffetta. The epidemiology of neuroblastoma: a review. *Paediatr Perinat Epidemiol.* 2009;23(2):125-43.
5. Rauch A HD, Schäfer C, Wirth M, Marx C, Heinzel T, Schneider G, Krämer OH. Survivin and YM155: how faithful is the liaison? *Biochim Biophys Acta.* 2014;1845(2):202-20.
6. Lamers F, van der Ploeg I, Schild L, Ebus ME, Koster J, Hansen BR, et al. Knockdown of survivin (BIRC5) causes apoptosis in neuroblastoma via mitotic catastrophe. *Endocrine-related cancer.* 2011;18(6):657-68.
7. Lamers F SL, Koster J, Versteeg R, Caron HN, Molenaar JJ. Targeted BIRC5 silencing using YM155 causes cell death in neuroblastoma cells with low ABCB1 expression. *Eur J Cancer* 2012;48(5):763-71.
8. Ryan BM, O'Donovan N, Duffy MJ. Survivin: A new target for anti-cancer therapy. *Cancer Treat Rev.* 2009; 35: 553-62.
9. Tanioka M, Nokihara H, et al. Phase I study of LY2181308, an antisense oligonucleotide against survivin, in patients with advanced solid tumors. *Cancer Chemother Pharmacol.* 2011; 68(2): 505-11.
10. Satoh T, Okamoto I, et al. Phase I study of YM155, a novel survivin suppressant, in patients with advanced solid tumors. *Clin Cancer Res.* 2009; 15(11): 3872-80.
11. Lamers F, Schild L, et al. Targeted BIRC5 silencing using YM155 causes cell death in neuroblastoma cells with low ABCB1 expression. *Eur J Cancer.* 2012; 48(5): 763-71.
12. Tolcher AW, Mita A, Lewis LD, et al. Phase I and pharmacokinetic study of YM155, a small-molecule inhibitor of survivin. *J Clin Oncol.* 2008; 26(32): 5198-203.
13. Nakahara T, Kita A, et al. YM155, a novel small-molecule survivin suppressant, induces regression of established human hormone-refractory prostate tumor xenografts. *Cancer Research.* 2007; 67(17): 8014-21.
14. Minematsu T, Sonoda T, et al. Pharmacokinetics, distribution and excretion of YM155 monobromide, a novel small-molecule survivin suppressant, in male and pregnant or lactating female rats. *Biopharm Drug Dispos.* 2012; 33(3): 160-9.
15. Aoyama Y, Katashima M, Sawamoto T. Lack of differences in the pharmacokinetics of sepantronium bromide (YM155) between US and Japanese patients with advanced solid tumors or non-Hodgkin lymphoma. *Biopharm Drug Dispos.* 2013; 34(2): 137-40.
16. Farokhzad OC, Langer R. Nanomedicine: developing smarter therapeutic and diagnostic modalities. *Adv Drug Deliv Rev.* 2006; 58(14): 1456-9.

17. Dan Peer, Jeffrey M. Karp, et al. Nanocarriers as an emerging platform for cancer therapy. *Nature Nanotechnology*. 2007; 2: 751 - 60.
18. Bae YH, Park K. Targeted drug delivery to tumors: myths, reality and possibility. *J Control Release*. 2011; 153(3): 198-205.
19. Shakushiro K, Kawano H, et al. Formulation design and evaluation of liposomal sepantronium bromide (YM155), a small-molecule survivin suppressant, based on pharmacokinetic modeling and simulation. *Pharm Res*. 2015; 32(1): 238-47.
20. Kawano H, Shakushiro K, et al. Antitumor efficacy and biodistribution of liposomal sepantronium bromide (YM155), a novel small-molecule survivin suppressant. *Eur J Pharm Biopharm* 2014; 88(1): 283-9.
21. Allen TM, Moase EH. Therapeutic opportunities for targeted liposomal drug delivery. *Adv Drug Del Rev*. 1996; 21: 117-33.
22. Lu J, Zhao W, Huang Y, et al. Targeted Delivery of Doxorubicin by Folic Acid-Decorated Dual Functional Nanocarrier. *Mol Pharmaceutics*. 2014; 11: 4164–78.
23. Mujoo K, Cheresch DA, et al. Disialoganglioside GD2 on human neuroblastoma cells: target antigen for monoclonal antibody-mediated cytotoxicity and suppression of tumor growth. *Cancer Res*. 1987; 47: 1098-104.
24. Schulz G, Cheresch DA, et al. Detection of ganglioside GD2 in tumor tissues and sera of neuroblastoma patients. *Cancer Res*. 1984; 44: 5914-20.
25. Frost JD, Hank JA, Reaman GH, et al. A phase I/IB trial of murine monoclonal anti-GD2 antibody 14.G2a plus interleukin-2 in children with refractory neuroblastoma: a report of the Children's Cancer Group. *Cancer Biol Ther*. 1997; 80: 317-33.
26. Uttenreuther-Fischer MM, Huang CS, Yu AL. Pharmacokinetics of human-mouse chimeric anti-GD2 mAb ch14.18 in a phase I trial in neuroblastoma patients. *Cancer Immunol Immunother* . 1995; (41): 331-8.
27. Lammie G, Cheung N, et al. Ganglioside gd(2) expression in the human nervous-system and in neuroblastomas - an immunohistochemical study. *Int J Oncol*. 1993; 3(5): 909-15.
28. Baiu DC, Artz NS, McElreath MR, et al. High specificity targeting and detection of human neuroblastoma using multifunctional anti-GD2 iron-oxide nanoparticles. *Nanomedicine (Lond)*. 2015; 1-23.
29. Suzuki M, Cheung NK. Disialoganglioside GD2 as a therapeutic target for human diseases. *Expert Opin Ther Targets*. 2015; 19(3): 349-62
30. Everts M, Koning GA, et al. In vitro cellular handling and in vivo targeting of E-selectin-directed immunoconjugates and immunoliposomes used for drug delivery to inflamed endothelium. *Pharm Res*. 2003; 20(1): 64-72.
31. Rouser G, Fkeischer S, Yamamoto A. A Two dimensional thin layer chromatographic separation of polar lipids and determination of phospholipids by phosphorus analysis of spots. *Lipids*. 1970; 5: 494–6.

32. Adrian JE, Kamps JA, et al. A novel lipid-based drug carrier targeted to the non-parenchymal cells, including hepatic stellate cells, in the fibrotic livers of bile duct ligated rats. *BBA Biomembranes*. 2007; 6: 1430-9
33. Dolman ME, den Hartog IJ, et al. Liquid chromatography-tandem mass spectrometric assay for the light sensitive survivin suppressant sepantronium bromide (YM155) in mouse plasma. *J Pharm Biomed Anal*. 2014; 92: 144-8.
34. Gabrielsson J, Weiner D. Non-compartmental analysis. *Methods Mol Biol*. 2012; 929: 377-89.
35. Kneidl B, Peller M, et al. Thermosensitive liposomal drug delivery systems: state of the art review. *Int J Nanomedicine*. 2014; 9(1): 4387-4398.
36. Jones MN, Nicholas AR. The effect of blood serum on the size and stability of phospholipid liposomes. *Biochim Biophys Acta*. 1991; 11165(2): 145-1.
37. Iwai M, Minematsu T, et al. Utility of P-glycoprotein and organic cation transporter 1 double-transfected LLC-PK1 cells for studying the interaction of YM155 monobromide, novel small-molecule survivin suppressant, with P-glycoprotein. *Drug Metab Dispos*. 2011; 39(12): 2314-20.
38. Gottstein C, Schön G, et al. Anti disialoganglioside Ricin A-Chain Immunotoxins Show Potent Antitumor Effects in Vitro and in a Disseminated Human Neuroblastoma Severe Combined Immunodeficiency Mouse Model. *Cancer Res*. 1994; 45(23): 6186-93.
39. Boeckle S, Wagner E. Optimizing targeted gene delivery: chemical modification of viral vectors and synthesis of artificial virus vector systems. *AAPS J*. 2006; 8(4): 31-42.
40. Hobbs SK, Monsky WL, et al. Regulation of transport pathways in tumor vessels: Role of tumor type and microenvironment. *Proc Natl Acad Sci U S A*. 1998; 95(8): 4607-12.
41. Maeda H, Wu J, et al. Tumor vascular permeability and the EPR effect in macromolecular therapeutics: a review. *J Control Release*. 2000; 65(1-2): 271-84.
42. Maeda H, Sawa T, Konno T. Mechanism of tumor-targeted delivery of macromolecular drugs, including the EPR effect in solid tumor and clinical overview of the prototype polymeric drug SMANCS. *J Control Release*. 2001; 74(1-3): 47-61.
43. Immordino ML, Dosio F, Cattel L. Stealth liposomes: review of the basic science, rationale, and clinical applications, existing and potential. *Int J Nanomedicine*. 2006; 1(3): 297-315.



# **Chapter 7**

## **Summary and Perspectives**

## Summary

Diseases of modern life such as type II diabetes, cardiovascular diseases and cancer have a chronic inflammatory process at its base as described in introduction section. The apparent link between such diseases and chronic inflammation can provide new modalities of chemotherapeutic interventions. Although treatment of chronic inflammation may not necessarily lead to a (complete) cure, it can act synergistically with other treatment modalities that are currently applied [1, 2]. Many different potent small drug molecules that can be of benefit in the treatment of inflammatory disorders have been identified. However, these established or potential drugs typically have a substantial set of adversary (side-) effects, especially upon chronic use. Therefore, it is of great importance to suppress and/or avoid such adverse effects as much as possible. A technology that has shown some promise in this regard has been the application of targeted nanomedicines, which can direct potent drug molecules away from certain tissues or cell types, while they also can accumulate locally within tumors or inflamed tissues [3-5].

Colloidal nanomedicines based on e.g. lipids or amphiphilic block copolymers have emerged in the past decades as an exciting domain that can help to solve a number of problems linked to unsatisfactory therapeutic responses [6]. Such colloidal nanomedicines have been reported to lead to enhanced drug solubility and stability. Their hydrophilic shell and hydrodynamic size (100-300 nm) allow colloidal nanomedicines to act as a vector with prolonged *in vivo* circulation kinetics, which thereby allows potential passive targeting to their site of action via the enhanced permeability and retention (EPR) effect [7, 8]. Moreover, the conjugation of targeting ligands to generate actively targeted nanomedicines is strategy aimed to increase target cell recognition and uptake into the target cell to ultimately increase the therapeutic efficacy of drug molecules loaded in such nanocarriers systems.

At present, a variety of lipid and polymer based nanomedicines systems have entered clinical trials and some formulations are on the market and used in clinical practice [9-11]. However, clinical translation of actively targeting drug carrier systems is limited to several approved antibody drug

conjugates but no actively targeting lipid or polymer based carrier systems have successfully passed clinical trials yet [12, 13].

Here in this thesis, we aimed to develop and evaluate several different lipid and polymer based nanomedicines (drug carrier systems) for targeted (active) delivery of small drug molecules to specific cell types.

**Chapter 1** provides a general introduction to inflammatory disorders and neuroblastoma, together with different nano-therapeutic modalities applied for treatment of each (*in vitro* and *in vivo*). Further, the current challenges in clinical applications of active pharmaceutical ingredients (small drug molecules) are described. Colloidal nanomedicines are discussed as a potential solution for these challenges, with a particular focus on lipid and polymer based carrier systems. In particular, actively targeted nanomedicines are discussed, as these aim to increase target cell recognition and consequently increase the therapeutic efficacy of the nanomedicine.

**Chapter 2** summarizes the evidence for a diverse population of myofibroblast progenitors in kidney fibrosis. The relative contributions of the different factors and cellular sources to the formation of renal myofibroblasts are described in detail.

Based on the pivotal role of myofibroblasts in the production of pro-fibrotic mediators, the application of different targeting therapeutic strategies in order to manipulate their activities has been reviewed. In addition, examples are given of different pre-clinical and clinical trials using systemic therapy in order to inhibit myofibroblast accumulation and thereby attenuate kidney fibrosis.

**Chapter 3** describes the preparation, and characterization of E-selectin targeted immunoliposomes loaded with an mTOR inhibitor (rapamycin), which were used for targeted delivery of rapamycin to TNF- $\alpha$  activated HUVEC cells. Modification of liposomal surface PEG chains with anti E-selectin antibody resulted in the creation of immunoliposomes, which showed binding and uptake by the activated endothelial cells. The results obtained from cell functionality assays including (inhibition of) cell migration, proliferation, gene expression and western blot analyses, all

of which revealed an enhanced pharmacologic effect of targeted rapamycin loaded immunoliposomes compared to the free drug and control (i.e. non-targeted) rapamycin loaded liposomes. The data presented in this work clearly demonstrate that the use of rapamycin loaded immunoliposomes effectuates higher intracellular concentrations of rapamycin compared to an equivalent dose of free rapamycin.

**Chapter 4** describes a conceptual proof that VCAM-1 could be applied as a molecular target for nanocarrier systems directed to podocytes, a cell type that is abundantly present in the glomeruli of the kidney. We demonstrated that VCAM-1 is overexpressed in podocytes activated by TNF- $\alpha$  and that we could employ the overexpression of VCAM-1 to deliver rapamycin to podocytes. In previous studies it was shown that VCAM-1 expression is upregulated in vascular endothelial cells under inflammatory conditions [14-16]. Hence, one can expect that rapamycin loaded anti-VCAM-1-SAINTOsomes will be internalized by inflammation activated endothelial cells, similar to previously reported siRNA loaded anti-VCAM-1-SAINTOsomes [14, 17]. The expression of VCAM-1 on (subsets of) endothelial cells and on activated podocytes has implications for targeted drug delivery. Thus, rapamycin loaded anti-VCAM-1-SAINTOsomes were developed for targeted delivery of rapamycin to activated podocytes. The characteristics of the developed formulation together with its cell (podocyte) binding and pharmacological effect were assessed *in vitro*. Based on the obtained results, it is clear that an anti-VCAM-1-coated nanocarrier is an interesting option to therapeutically address more than one cell type under inflammatory conditions in kidney related inflammatory disorders.

**Chapter 5** describes a rationally designed formulation of E-selectin targeted nanoparticles (NPs) loaded with mTOR/PI3K inhibitor BEZ, which was used for targeted delivery of BEZ to TNF- $\alpha$  activated endothelial cells. Upon varying different formulation parameters such as polymer composition, drug loading content and antibody coupling density, a promising combination of characteristics for the targeted NP formulation loaded with BEZ was identified and evaluated using cultured endothelial cells.

The different formulations were screened and evaluated based on various characteristics, such as their particle size and morphology, BEZ loading and release kinetics, and their ability to bind to activated endothelial cells. The most promising targeted BEZ-loaded nanoparticles were further tested *in vitro* using cell functionality assays, where they showed successful intracellular delivery and cytosolic release of BEZ, while achieving an efficacy that was comparable to the efficacy of an equivalent dose of free BEZ.

**Chapter 6** describes the preparation of YM155 loaded liposomes that were functionalized with surface bound anti-GD2 antibodies in order to render them specific for neuroblastoma tumor cells. The formulated liposomes (targeted and non-targeted control) were evaluated for their size, charge, Ab coupling density, drug (YM155) loading, and YM155 release rates *in vitro* under different conditions (i.e. varying release medium and temperature).

Further, the binding and uptake capabilities of immunoliposomes were studied *in vitro*. Although the formulated immunoliposomes showed *in vitro* cell toxicity on KCNR cells, they failed to achieve the levels of toxicity that were achieved by free YM155 under similar conditions.

The liposomal formulations were also studied *in vivo*, in which it was shown that liposomal YM155 formulations (targeted and non-targeted control) had the desired physicochemical characteristics to obtain a significantly improved blood circulation half-life ( $t_{1/2}$ ), as well as improved tumor accumulation, compared to free YM155 after single bolus intravenous (i.v.) injection. In addition, the *in vivo* results showed that the addition of targeting antibodies on the surface of the liposomes did not induce significant changes in the observed tumor accumulation of the formulated liposomes at the applied dose.

Finally, **Chapter 7** summarizes the results described in this thesis and provides perspectives on the biopharmaceutical characteristics of prepared targeted nanomedicines, together with a brief discussion on nanomedicine technology assessment and risk analysis of nanoencapsulated therapeutics.

## Perspectives

### Nanomedicine development

On a lab scale, lipid or polymer based targeted carrier systems were developed. For lipid based carrier systems, drug/lipid film hydration followed by sonication/extrusion steps was applied and for polymeric nanoparticles single an oil-in-water emulsification technique was applied. The pharmaceutical properties of (drug-entrapped) liposomes/polymeric nanoparticles were analyzed and evaluated with respect to their particle size, charge, yield, drug loading efficiency, drug release kinetics and antibody coupling efficiency.

### Tailored pharmaceutical properties

The targeted nanomedicines presented in this thesis can be considered as platform technology in which pharmaceutical properties have been tailored based on specific medical need and application. As described in **Chapter 5**, the pharmaceutical properties of polymeric nanoparticles (NPs) loaded with BEZ were tailored with respect to particle size and morphology, drug loading content and drug release kinetics. Different sizes and morphologies of the polymeric nanoparticles (NPs) were achieved by varying the weight ratio of the PLGA and PLGA-PEG<sub>2000</sub> polymers. The drug release rates were modified by varying the drug (BEZ) load content in the polymeric formulations. Further in **Chapter 6** the effect of release medium properties and its composition (e.g. temperature, protein concentration) on release kinetic of YM155 loaded liposomes (targeted and control) were investigated. Next, the *in vivo* release kinetics of developed nanomedicine should be investigated, to have a more realistic opinion on stability of the formulated nanomedicines.

### Surface modification and targeting to specific cells or organs

Enhanced permeability and retention (EPR) mediated drug delivery is considered to be a passive targeting approach. However, besides utilizing the EPR effect, drug targeting can be enhanced by active targeting which is achieved by the use of targeting ligands, such as small molecules [18],

peptides [19], antibodies or their fragments [20, 21] and aptamers [22] on the surface of nanocarriers.

In previous studies of Kowalski *et al.*, it was shown that conjugation of an E-selectin antibody to the surface of liposomes resulted in a greater binding and uptake of such liposomes by E-selectin over-expressing endothelial cells compared to their non-targeted (control) counterparts [14]. Also, it has previously been shown that surface modification of dexamethasone or siRNA loaded liposomes with anti E-selectin antibodies improved the *in vivo* efficacy of liposomes in both inflammatory tissue and tumor xenograft [17, 23]. These promising results corroborate the use of active targeting by functionalization of hydrophilic PEG block of lipids or block co-polymers with for example maleimide, SPDP or azide groups, as (surface) anchor points for the attachment of targeting moieties [24]. As described in **Chapter 3 to 6** of this thesis, antibodies directed to different surface-exposed receptors were applied for targeted delivery of formulated lipid or polymer based nanomedicines. These targeting modalities are specific for certain types of receptors that are over-expressed on the surface of specific cell types under diseased conditions such as inflammation and cancer. The *in vitro* studies showed successful binding and intercellular delivery of drug loaded nanomedicine. These pilot studies can be considered as first steps toward achieving the final goal that is development of cell-specific delivery systems that can be applied in the clinic.

### **Control of ligand surface density**

Thus far, the reported density of ligands attached to the surface of the nanosized carrier systems (lipid or polymer based) has been varied in many studies [9]. The large differences between the reported nanocarrier surface ligand densities in the scientific literature can be due to various parameters (besides differences in preparation conditions), such as the characteristics of the applied ligand itself (i.e. binding affinity towards its receptor), or receptor molecule density on the target tissue [25]. According to the research performed by Farokhzad *et al.*, the optimal ligand density can be defined as the minimal number of targeting ligands on the surface of the carrier system required

for maximal targeted cellular uptake, in order to avoid unnecessary masking of the carrier surface (e.g. PEG chains) by excess of targeting ligands [26].

With this in mind, in **Chapter 5** the surface density of the anti E-selectin antibody attached to the NPs was systematically modified by changing the ratio of the PLGA-PEG-SPDP co-polymer applied in the formulation. The *in vitro* results showed a linear correlation between cell binding capacity and antibody density on nanoparticles. Further *in vivo* studies are necessary to better optimize the developed targeted nanomedicine described in **Chapter 5**.

### **Pharmacokinetics and biodistribution**

Previous studies have shown that PEGylated nanocarrier systems can have a relatively long residence time in the systemic circulation after i.v. administration due to their small hydrodynamic size and stealth properties [27-29]. The prolonged circulation in turn allows the targeted delivery of the entrapped payloads to the tumor or inflammatory tissues, owing to the EPR effect. However, further analysis on the *in vivo* nanoparticle biodistribution revealed that the major part of “in tumor accumulated” nanoparticles in fact resided on the (blood) vessel wall surface or in close proximity to the blood vessels [30-34], which does not exclude their washout back to the blood circulation.

Targeting has a major effect on preventing the washout of the smaller nanoparticles from the extravascular compartment [33, 35], especially in tissues with low blood flow [35]. Therefore, strong binding of nanocarriers with the target cell is considered to be one of the main causes of the superior tumor residence time of targeted nanomedicines [25].

In **Chapter 6** targeted nanomedicines (i.e. GD2-targeted liposomes loaded with YM155) were formulated and their functionality were evaluated *in vitro*. Subsequently, the *in vivo* applicability of the GD2-targeted liposomes loaded with YM155 was evaluated in a pilot study using mouse neuroblastoma xenograft model following i.v. administration of formulated liposomes. More extensive and complete *in vivo* experiments including efficacy studies are highly recommended. This



way, we can better evaluate the pharmacokinetics and efficacy of formulated targeted YM155 liposomes compared to control formulation or free YM155.

### **Nanomedicine technology assessment**

Nano-therapeutic products have an unusual nature (specific complexity and characteristics) compared to traditional drug products, and therefore require new research and development guidelines at the industrial level. Size, complexity, and stability are major developmental issues for nano-therapeutic products [36, 37]. Pharmacokinetic studies of nanomedicine are often complicated by analytical challenges, since preservation of their colloidal structures (i.e. intact assembly of lipid bilayer or self-assembled polymers) is an important issue [37]. To date, a notable number of different nanomedicine have gained market authorization by the Food and Drug Administration (FDA) and European Medicines Agency (EMA) [36, 38]. Nanomedicine such as liposomal formulations, iron-based preparations, or drug nanocrystals in oral dosage forms are considered as first-generation products, whose effectiveness and safety have been substantiated for long-term clinical use [36].

An example of a more complex nanomedicine (second generation product) with clinical scale manufacturing, is targeted polymeric poly(lactic-co-glycolic acid) (PLGA) nanoparticles loaded with docetaxel (DTX), also known as BIND-014 [39]. Another example is the polymeric micelle-based formulation of paclitaxel, so called Genexo<sup>®</sup>-PM (Samyang Biopharmaceuticals, Seoul, South Korea), which has been explored extensively for use in anticancer therapy and is currently in preclinical and clinical development [40, 41].

### **Scale up and manufacturing**

As mentioned in previous paragraphs, nanomedicine (i.e. nanoparticles) are complex multicomponent structures, in contrast to conventional drug products. Therefore, a full understanding of the components and their interactions during early development is an essential step to tailor and define the key characteristics of the final product. This understanding will in turn

help to better define critical steps in larger scale manufacturing. The formulation of nanomedicine (e.g. liposomal or polymeric drug formulations) usually involves the use of organic solvents, high speed homogenization and sonication, followed by emulsification, evaporation of the organic solvent, centrifugation, filtration and freeze drying. During the early development process in the lab (small scale), it is important to take into the consideration critical formulation and processing conditions (parameters) that can play a significant role in the quality of the scaled up (final) drug product. These parameters may involve the ratio of polymers and/or drugs, the type of organic solvent and emulsifier/stabilizer/cross-linker, the oil-to-water phase ratio, mixing, temperature, pressure, and the pH [42]. Therefore, the manufacturing plan needs to define acceptable limits or specifications for key nanomedicine attributes and identify process parameters that are critical to achieve these key attributes.

Liposomes provide a good example to illustrate issues of stability, scale-up and importance of critical process parameters. The FDA has highlighted the importance and challenges in maintaining a close control over the scale-up manufacturing process in a draft guidance for liposome drug products, stating that “liposome drug products are sensitive to changes in the manufacturing parameters such as scale, shear force, and temperature. These are parameters need to be considered during the development process” [43].

### **Health and environmental risk assessment**

Many scientists consider nanotechnology as the next logical step in science, as a tool which integrates engineering with biology, chemistry, medicine, and physics [44-46]. However, on the nanoscale, typically within the range of 1-100 nm in at least one dimension, the properties of materials can be different from those on a larger scale [47]. The manufactured nanomaterials with medical or non-medical applications are increasingly being used in commercial applications. An example of medical nanomaterial applications are gold-nanoparticles (Au-NPs) used as a contrast

agent [48] and an example of nanomaterial application in a non-medical product is carbon nanotubes, which are being applied in electronics [49].

Increases in nanomaterial production raise questions regarding potential unintended hazards to both humans and the environment [50]. A debate is taking place in the scientific community whether nanomaterials need special regulation to assess and deal with potential related risks [50, 51].

In order to determine and understand the potential toxic effects of nanomaterials, strategies need to be devised to efficiently gather and analyze relevant data, while also taking into account the long term effects of nanomaterial bio-accumulation.

So far, applied biological models to determine potential toxicological effects of chemicals are composed of cells in culture, aquatic organisms including embryonic zebrafish (*Danio rerio*), and whole-animal tests such as rodents [52, 53]. A brief look through toxicity studies of nanoparticles that have been carried out by different research groups already reveals an inconsistency in cell lines, culturing conditions and incubation times that are being used in these studies, thus making it even more difficult to compare results between research groups and to determine whether the observed cytotoxicity is physiologically relevant or not [50]. In general there are two main problems regarding in depth risk assessment: 1) Currently, our basic knowledge in understanding the toxic effects of nanomaterials is limited: 2) The large, ever increasing variety of existing nanomaterials makes it even more difficult to generate a risk matrix in order to conduct risk assessment [54]. Taken together, it seems that currently there is insufficient data available to conduct an in depth risk assessment. Therefore, there is an urgent need for a responsible and harmonized approach to ensure that potential safety issues are being addressed by toxicity studies related to nanomaterials at the same time as the technology is developing [54, 55].

In this context, it worth to mention that the organization for Economic Cooperation and Development (OECD) assists countries with the implementation of national policies that guarantee the responsible development of nanotechnologies/nanomaterials. As such, part of its work is

focused on the evaluation and safety assessment of manufactured nanomaterials, to ensure human health and environmental safety. Within this organization there is the so called Working Party on Manufactured Nanomaterials (WPMN), which is mainly concentrated on human health and environmental safety implications of manufactured nanomaterials (limited mainly to the chemicals sector). Its program mainly seeks to promote international co-operation regarding human health and environmental safety of manufactured nanomaterials, and as such it is also involved in the safety testing and risk assessment of manufactured nanomaterials [55].

### Conclusions

In the present thesis, the feasibility of applying lipid or polymer-based nanocarrier systems for the targeted (intracellular) delivery of small drug molecules has been demonstrated both *in vitro* and *in vivo*. Anti E-selectin, anti-VCAM-1 and anti-GD2 antibodies were coupled to the surface of the nanocarrier systems as targeting moieties. Several analyses, together with efficacy studies, have been carried out, including physicochemical characterization of the targeted nanomedicines and *in vitro* analysis of their binding to and internalization by activated endothelial cells or tumor cells. An *in vivo* pharmacokinetic pilot study was performed, evaluating immunoliposomes loaded with YM155. Collectively, the obtained results, demonstrated the suitability and potential of targeted nanomedicine formulations for further *in vivo* efficacy studies.

### References

1. Medzhitov R. Origin and physiological roles of inflammation. *Nature*. 2008; 454: 428-35.
2. Farkona S, Diamandis EP, Blasutig IM. Cancer immunotherapy: the beginning of the end of cancer? *BMC Med*. 2016;14(73): 1-9.
3. Riehemann K, Schneider SW, Luger TA, Godin B, Ferrari M, Fuchs H. Nanomedicine – challenge and perspectives. *Angew Chem Int Ed Engl*. 2009;48(5):872–97.
4. Ventola CL. The Nanomedicine Revolution. *Pharmacy and Therapeutic*. 2012;37(9):512-7.
5. Lammers T, Kiessling F, Ashford M, Hennink W, Crommelin D, Storm G. Cancer nanomedicine: is targeting our target? *Nat Rev Mater*. 2016;1(9):1-4.

6. Mariana Beija, Nancy Lauth-de Viguier, Jean-Daniel Marty. Colloidal systems for drug delivery: from design to therapy. *Trends in Biotechnology*. 2012;30(9):485–96.
7. Matsumura Y, Maeda H. A new concept for macromolecular therapeutics in cancer chemotherapy: mechanism of tumorotropic accumulation of proteins and the antitumor agent. *Cancer Research*. 1986; 46: 6387-92.
8. Maeda H, Wu J, Sawa T, Matsumura Y, Hori K. Tumor vascular permeability and the EPR effect in macromolecular therapeutics: a review. *Journal of Controlled Release*. 2000; 65: 271-84.
9. Pérez-Herrero E, Fernández-Medarde A. Advanced targeted therapies in cancer: Drug nanocarriers, the future of chemotherapy. *Eur J Pharm Biopharm*. 2015; 93: 52-79.
10. Rizzo LY, Theek B, Storm G, Kiessling F, Lammers T. Recent progress in nanomedicine: therapeutic, diagnostic and theranostic applications. *Curr Opin Biotechnol* 2013; 24(6): 1159-66.
11. Wang R, Billone PS, and Mullett WM. Nanomedicine in Action: An Overview of Cancer Nanomedicine on the Market and in Clinical Trials. *Journal of Nanomaterials*. 2013: 1-12.
12. Kim EG, Kim KM. Strategies and Advancement in Antibody-Drug Conjugate Optimization for Targeted Cancer Therapeutics. *Biomol Ther*. 2015;23(6):493–509.
13. van der Meel R, Vehmeijer LJ, Kok RJ, Storm G, van Gaal EV. Ligand-targeted particulate nanomedicines undergoing clinical evaluation: current status. *Adv Drug Deliv Rev*. 2013; 65(10): 1284-98.
14. Kowalski PS, Lintermans LL, Morselt HW, Leus NG, Ruiters MH, Molema G, Kamps JA. Anti-VCAM-1 and anti-E-selectin SAINT-O-Somes for selective delivery of siRNA into inflammation-activated primary endothelial cells. *Mol Pharm*. 2013; 10: 3033–44.
15. Kuřdo JM, Ásgeirsdóttir SA, Zwiers PJ, et al. Targeted adenovirus mediated inhibition of NF- $\kappa$ B-dependent inflammatory gene expression in endothelial cells in vitro and in vivo. *J Control Release*. 2013; 166: 57–65.
16. Gao HX, Campbell SR, Burkly LC, et al. TNF-like weak inducer of apoptosis (TWEAK) induces inflammatory and proliferative effects in human kidney cells. *Cytokine*. 2009; 46: 24–35.
17. Kowalski PS, Zwiers PJ, Morselt HW, et al. Anti-VCAM-1 SAINT-O-Somes enable endothelial-specific delivery of siRNA and downregulation of inflammatory genes in activated endothelium in vivo. *J Control Rel*. 2014; 176: 64–75.
18. Zhang Z, Yao J. Preparation of irinotecan-loaded folate-targeted liposome for tumor targeting delivery and its antitumor activity. *AAPS PharmSciTech*. 2012; 13(3): 802-10.
19. Amin M, Mansourian M, Koning GA, Badiee A, Jaafari MR, ten Hagen TL. Development of a novel cyclic RGD peptide for multiple targeting approaches of liposomes to tumor region. *J Control Release*. 2015;28(220):308-15.
20. Leserman LD, Barbet J, Kourilsky F, Weinstein JN. Targeting to cells of fluorescent liposomes covalently coupled with monoclonal antibody or protein A. *Nature*. 1980; 288: 602–4.
21. Arias JL, Unciti-Broceta JD, Maceira J, et al. Nanobody conjugated PLGA nanoparticles for active targeting of African Trypanosomiasis. *J Control Release*. 2015; 10(197): 190-8.

22. Xiao Z, Farokhzad O. Aptamer-Functionalized Nanoparticles for Medical Applications: Challenges and Opportunities. *ACS Nano*. 2012; 6: 3670–6.
23. Asgeirsdóttir SA, Zwiers PJ, Morselt HW, Moorlag HE, et al. Inhibition of proinflammatory genes in anti-GBM glomerulonephritis by targeted dexamethasone-loaded AbEsel liposomes. *Am J Physiol Renal Physiol*. 2008; 294(3): 554-61.
24. Spanedda MV, De Giorgi M, Hassane FS, Schuber F, Bourel-Bonnet L, Frisch B. Coupling of Ligands to the Liposome Surface by Click Chemistry. *Methods Mol Biol*. 2017; 1522: 93-106.
25. Durymanov MO, Rosenkranz AA, Sobolev AS. Current Approaches for Improving Intratumoral Accumulation and Distribution of Nanomedicines. *Theranostics* 2015; 5(9): 1007-20.
26. Frank Gu, Zhang L, Benjamin A, et al. Precise engineering of targeted nanoparticles by using self-assembled biointegrated block copolymers. 2008; 105(7): 2586–91.
27. De Jong WH and Borm PJ. Drug delivery and nanoparticles: Applications and hazards. *Int J Nanomedicine*. 2008; 3(2): 133–49.
28. Perry JL, Reuter KG, Kai MP, Herlihy KP, Jones SW, et al. PEGylated PRINT nanoparticles: the impact of PEG density on protein binding, macrophage association, biodistribution, and pharmacokinetics. *Nano Lett*. 2012; 12(10): 5304-10.
29. Xu X, Ho W, Zhang X, Bertrand N, Farokhzad O. Cancer Nanomedicine: From Targeted Delivery to Combination Therapy. *Trends Mol Med*. 2015; 21(4): 223–32.
30. Durymanov MO, Slastnikova TA, Kuzmich AI, et al. Microdistribution of MC1R-targeted polyplexes in murine melanoma tumor tissue. *Biomaterials*. 2013; 34: 10209-16.
31. Dreher MR, Liu W, Michelich CR, Dewhirst MW, Yuan F, Chilkoti A. Tumor vascular permeability, accumulation, and penetration of macromolecular drug carriers. *J Natl Cancer Inst*. 2006; 98: 335-44.
32. Popović Z, Liu W, Chauhan VP, Lee J, et al. A nanoparticle size series for in vivo fluorescence imaging. *Angew Chem Int Ed Engl*. 2010; 49: 8649–52.
33. Lee H, Fonge H, Hoang B, Reilly RM, Allen C. The effects of particle size and molecular targeting on the intratumoral and subcellular distribution of polymeric nanoparticles. *Mol Pharm*. 2007; 7: 1195-208.
34. Campbell RB, Fukumura D, Brown EB, et al. Cationic charge determines the distribution of liposomes between the vascular and extravascular compartments of tumors. *Cancer Res*. 2002; 62: 6831-6.
35. Toy R, Hayden E, Camann A, Berman Z, et al. Multimodal in vivo imaging exposes the voyage of nanoparticles in tumor microcirculation. *ACS Nano*. 2013; 7: 3118-29.
36. Ehmann F, Sakai-Kato K, Duncan R, et al. Next-generation nanomedicines and nanosimilars: EU regulators' initiatives relating to the development and evaluation of nanomedicines. *Nanomedicine (Lond)*. 2013; 8(5): 849–56.
37. Hafner A, Lovrić J, Lakoš GP, Pepić I. Nanotherapeutics in the EU: an overview on current state and future directions. *Int J Nanomedicine*. 2014; 9: 1005-23.

38. Weissig V, Pettinger TK, Murdock N. Nanopharmaceuticals (part 1): products on the market. *Int J Nanomedicine*. 2014; 9 : 4357-4373
39. Hrkach J, Von Hoff D, Mukkaram Ali M, et al. Preclinical development and clinical translation of a PSMA-targeted docetaxel nanoparticle with a differentiated pharmacological profile. *Science Translational Medicine*. 2012; 4: 128-139.
40. Min Y, Caster JM, Eblan MJ, Andrew, Wang Z. Clinical translation of nanomedicines. *Chemical reviews*. 2015; 115(19): 11147–11190.
41. Cabral H, Kataoka K. Progress of drug-loaded polymeric micelles into clinical studies. *J Control Release* 2014; 28(190): 465-76.
42. Feng SS, Mu L, Win KY, Huang G. Nanoparticles of biodegradable polymers for clinical administration of paclitaxel. *Curr Med Chem*. 2004; 11(4): 413–24.
43. <https://www.fda.gov/downloads/Drugs/GuidanceCompliance/RegulatoryInformation/Guidances/ucm070570.pdf>.
44. Vo-Dinh T. *Nanotechnology in Biology and Medicine: Methods, Devices, and Applications*. CRC Press. 2007.
45. Stewart ME, Anderton CR, Thompson LB, et al. Nanostructured plasmonic sensors. *Chem Rev* 2008; 108: 494–521.
46. Dahl JA, Maddux BL, Hutchison JE. Toward greener nanosynthesis. *Chem Rev*. 2007; 107: 2891–959.
47. <https://www.nano.gov/nanotech-101/special>
48. Sun IC, Eun DK, Na JH, Lee S. Heparin-coated gold nanoparticles for liver-specific CT imaging. *Chemistry*. 2009; 15(48): 13341-7.
49. Peng LM, Zhang Z, Wang S. Carbon nanotube electronics: recent advances. *materialstoday*. 2014; 17(9): 433–42.
50. Ray PC, Yu H, Fu PP. Toxicity and environmental risks of nanomaterials: challenges and future needs. *J Environ Sci Health C Environ Carcinog Ecotoxicol Rev*. 2009; 27(1): 1-35.
51. Taylor D. *The Pharmaceutical Industry and the Future of Drug Development*. Pharmaceuticals in the Environment. 2015; eISBN:978-1-78262-234-5.
52. Den Boer D, Rip A, Speller S. Scripting possible futures of nanotechnologies: A methodology that enhances reflexivity. *Technology in Society*. 2009; 31: 295–304.
53. Hare JI, Lammers T, Ashford MB, Puri S, Storm G, Barry ST. Challenges and strategies in anti-cancer nanomedicine development: An industry perspective. *Adv Drug Deliver Rev*. 2017; 108: 25–38.
54. Miller G, Wickson F. *Big questions about risk assessment of nanomaterials*. The conversation 2015.
55. <https://www.oecd.org/science/nanosafety/47104296.pdf>

## **Appendices**

Nederlandse samenvatting

Acknowledgement

Curriculum vitae

List of publications



## Nederlandse Samenvatting

Chronische inflammatoire processen staan aan de basis van vele moderne aandoeningen zoals suikerziekte (diabetes type II), hart- en vaatziekten, en kanker. De correlatie tussen zulke ziektes en chronische ontstekingen kan wellicht een aanknopingspunt bieden om de behandelingen op een andere manier te gaan benaderen. Hoewel een behandeling van de chronische ontsteking niet noodzakelijkerwijs tot een (volledig) herstel leidt, kan het wel synergetisch werken met andere soorten van therapie. Momenteel zijn er al veel verschillende kleine moleculen geïdentificeerd als potentiële geneesmiddelen met een krachtige ontstekingsremmende werking. De reeds ontwikkelde geneesmiddelen hebben echter vrijwel allemaal een flinke hoeveelheid nadelige bijwerkingen, zeker bij chronisch gebruik. Het is daarom van groot belang om bijwerkingen zoveel mogelijk te onderdrukken en/of voorkomen. Een methode die in dit opzicht veelbelovend lijkt, is de toepassing van zogeheten '(doel-)gerichte' nano-medicijnen, welke idealiter een werkzaamheid hebben die vergelijkbaar is met het oorspronkelijke geneesmiddel, maar vrijwel geen van de gebruikelijke bijwerkingen.

Colloïdale nano-medicijnen, met als basis een bolvormige samenstelling van lipiden of amfifiele blok-copolymeren waarin het geneesmiddel zich bevindt, zijn in de afgelopen decennia uitgegroeid tot een belangrijk onderzoek domein, waarin men oplossingen hoopt te vinden voor problemen die gerelateerd zijn aan tegenvallende therapeutische responses van de oorspronkelijke geneesmiddelen. Zulke colloïdale medicijnen staan erom bekend te leiden tot een verbeterde oplosbaarheid en stabiliteit ten opzichte van het oorspronkelijke geneesmiddel. De hydrofiele buitenschil en deeltjes grootte van 100-300 nanometer (inclusief buitenste hydratatie schil) geven dergelijke colloïdale nano-medicijnen de mogelijkheid om gedurende lange periodes in vivo te circuleren, hetgeen de kans verhoogt dat de geneesmiddelen passief bij hun doelwit geraken volgens het 'verhoogde permeabiliteit en retentie' effect. Verder is het door koppeling van specifieke liganden ook mogelijk om 'gerichte' nano-medicijnen te creëren die een specifiek doelwit kunnen herkennen. Door middel van verbeterde cel herkenning en verbeterde opname door de doelwit

cellen, kan gerichte nano-medicatie dan de intrinsieke werkzaamheid van de kleine geneesmiddel moleculen verbeteren.

Momenteel zijn er klinische tests gestart voor een aantal van dergelijke op lipiden of polymeren gebaseerde gerichte moleculair bezorg systemen. Tot op heden is het echter nog lastig gebleken om het concept van actieve gerichte moleculaire drager systemen succesvol te vertalen naar een klinische behandeling. Hoewel er wel al verscheidene antilichaam-geneesmiddel verbindingen zijn goedgekeurd, zijn er tot op heden nog geen actieve gerichte moleculaire bezorg systemen door klinische tests heen gekomen die gebaseerd zijn op lipiden of polymeren.

Het doel van dit proefschrift is het ontwikkelen en evalueren van verschillende op lipiden of polymeren gebaseerde gerichte nano-medicijnen (geneesmiddel drager systemen) die typerend zijn voor actieve gerichte bezorging van kleine geneesmiddel moleculen bij specifieke soorten cellen.

**Hoofdstuk 1** begint met een algemene introductie over ontstekingen en neuroblastoom, en de verschillende therapeutische mogelijkheden voor behandeling van elk van beiden. Verder worden de huidige uitdagingen voor de klinische toepassing van farmaceutisch actieve ingrediënten (kleine geneesmiddel moleculen) beschreven. Colloïdale nano-medicijnen worden besproken als een mogelijke oplossing voor deze uitdagingen, met daarbij een speciale aandacht voor (moleculaire) drager systemen gebaseerd op lipiden en polymeren. In het bijzonder worden actieve gerichte nano-medicijnen besproken, aangezien het streven naar verbeterde herkenning van doelwit cellen waarschijnlijk ook zal zorgen voor een verhoogde therapeutische werkzaamheid van het nano-medicijn.

**Hoofdstuk 2** geeft een overzicht van het bewijs voor een diverse populatie van myofibroblast progenitor cellen bij nier fibrose. De relatieve bijdragen van de verschillende (cellulaire) factoren aan de vorming van nier-myofibroblasten wordt in detail beschreven. Ook werden verscheidene gerichte therapeutische strategieën geëvalueerd om de activiteit van myofibroblasten te manipuleren, vanwege de zeer belangrijke rol die myofibroblasten spelen bij de productie van pro-fibrotische *mediators*. Verder worden er voorbeelden gegeven van verschillende klinische en pre-klinische

behandelingen waarin systeem therapie wordt gebruikt om ophoping van myofibroblasten te stoppen, en daardoor de nier fibrose te verminderen.

**Hoofdstuk 3** beschrijft de bereiding en karakterisering van E-selectin gerichte immunoliposomen, beladen met een mTOR inhibitor (rapamycin). Deze immunoliposomen werden gebruikt voor de gerichte bezorging van rapamycin in TNF- $\alpha$  geactiveerde HUVEC cellen. De immunoliposomen werden gevormd door middel van een modificatie van de buitenste liposomale PEG (polyethyleenglycol) ketens met anti-E-selectin antilichamen. Deze immunoliposomen vormden een sterker binding met, en werden beter opgenomen door, de geactiveerde endotheel cellen. De resultaten van cel functie essays, waaronder cel migratie, proliferatie, gen expressie, en 'western blot' analyses, toonden allen duidelijk een verhoogd farmacologisch effect van gerichte met rapamycin beladen immunoliposomen ten opzichte van het oorspronkelijke rapamycin geneesmiddel, en ook ten opzichte van controle (niet-beladen) gerichte immunoliposomen. De resultaten van deze studie laten duidelijk zien dat het gebruik van gerichte met rapamycin beladen immunoliposomen leidt tot hogere intracellulaire rapamycin concentraties dan het oorspronkelijke rapamycin geneesmiddel wanneer gelijke hoeveelheden aan het cel medium wordt toegevoegd. Verder laat deze studie ook duidelijk de toegevoegde waarde zien van elk van de gebruikte cel-gerelateerde experimentele technieken voor het bestuderen en begrijpen van de farmacologische effecten van de gerichte immunoliposomen.

**Hoofdstuk 4** beschrijft resultaten die aantonen dat VCAM-1 gebruikt zou kunnen worden als een moleculair doelwit om therapeutische middelen te bezorgen bij TNF- $\alpha$  geactiveerde podocyt cellen (met VCAM-1 over-expressie). In eerdere studies is aangetoond dat tijdens ontstekingen upregulatie van VCAM-1 expressie in endotheel vaatcellen plaatsvindt. Het is dus te verwachten dat rapamycin beladen anti-VCAM-1-SAINT-O-Somes zullen worden geïnternaliseerd door ontstoken endotheel cellen, vergelijkbaar met de eerder beschreven siRNA beladen anti-VCAM-1-SAINT-O-Somes. De expressie van VCAM-1 op (delen van) endotheel cellen en geactiveerde podocyt cellen geeft mogelijkheden voor gerichte geneesmiddel bezorging. Derhalve werden er rapamycin beladen anti-

VCAM-1-SAINT-O-Somes ontwikkeld voor de gerichte bezorging van rapamycin in geactiveerde podocyt cellen. De farmacologische en cel (podocyt) binding eigenschappen van de ontwikkelde formulering werden in vitro beoordeeld. Op basis van de behaalde resultaten lijken anti-VCAM-1-gecoate nanodragers een mogelijkheid te bieden om tijdens een nier ontsteking meerdere soorten cellen therapeutisch aan te kunnen spreken.

**Hoofdstuk 5** beschrijft een geoptimaliseerde formulering van E-selectin gerichte nanodeeltjes die beladen zijn met de mTOR/PI3K inhibitor BEZ, die worden gebruikt voor de gerichte bezorging van het BEZ geneesmiddel in TNF- $\alpha$  geactiveerde HUVEC cellen. Verschillende formulering parameters, zoals polymeer samenstelling, geneesmiddel belading, en antilichaam koppelingsdichtheid, werden gevarieerd en getest, zodat de meest veelbelovende samenstelling van de gerichte BEZ beladen nanodeeltjes kon worden gevonden. De verschillende formuleringen werden getest en geëvalueerd met behulp van verscheidene criteria, zoals hun deeltjes grootte en vorm, BEZ belading, geneesmiddel afgifte kinetiek, en hun capaciteit om te binden aan geactiveerde endotheel cellen. De meest veelbelovende gerichte BEZ beladen nanodeeltjes werden verder getest in vitro met behulp van cel functie essays. Daarin toonden de gerichte BEZ beladen nanodeeltjes succesvolle intracellulaire bezorging en afgifte in het cytosol van het BEZ geneesmiddel, met een werkzaamheid die vergelijkbaar was met die van een gelijke hoeveelheid van het originele BEZ geneesmiddel.

**Hoofdstuk 6** beschrijft de bereiding van liposomale YM155 formuleringen, waarbij sommige van de formuleringen aan hun oppervlak gemodificeerd werden met covalent gebonden anti-GD2 antilichamen, om ze op die manier specifiek te maken voor neuroblastoom (KCNR) cellen. De geformuleerde liposomen (gericht en niet-gerichte controle) werden geëvalueerd op hun grootte, lading, antilichaam koppeling, geneesmiddel (YM155) belading, en hun YM155 afgiftesnelheid in vitro onder een aantal verschillende afgifte condities (variërende media en temperaturen). Vervolgens werden de binding en opname mogelijkheden van de immunoliposomen in vitro bestudeerd. Hoewel de geformuleerde immunoliposomen in vitro cel toxiciteit voor KCNR cellen toonden, behaalden ze niet de toxiciteit die het oorspronkelijke YM155 geneesmiddel toonde onder

vergelijkbare condities. De liposomale formuleringen werden ook in vivo bestudeerd. De in vivo experimenten toonden aan dat bij een directe toediening van een enkele dosis in de bloedbaan de liposomale YM155 formuleringen (zowel gerichte als niet-gerichte controle formuleringen) de gewenste fysiochemische eigenschappen hadden om een significant hogere bloed circulatie halfwaardetijd ( $t_{1/2}$ ) te bereiken, alsmede een verbeterde accumulatie in de tumor, ten opzichte van het oorspronkelijke YM155 geneesmiddel. De in vivo resultaten lieten verder zien dat bij de gebruikte dosering de aanwezigheid van gerichte antilichamen op het oppervlak van de liposomen geen significante invloed had op de gemeten accumulatie van de liposomen in de tumor.

**Hoofdstuk 7**, tot slot, geeft een samenvatting van de resultaten die in dit proefschrift beschreven worden, alsmede een perspectief op de biofarmaceutische eigenschappen van de geprepareerde nano-medicijnen. Dit hoofdstuk bevat ook een korte algemene discussie over nano-(medische)technologie, samen met een risico analyse.

## **Acknowledgement**

Since I moved to the Netherlands I have met many intelligent, kind and good people that made my journey toward the achievement of this academic milestone incredible. Nothing would be possible without (you). Thank you for helping me persevere during the tough times, and for brightening my mood during the good times.

Also I want to mention my colleagues and friends at the department of pharmaceutical sciences. My thanks and appreciations to all of you whom I've had the pleasure to work with over the years, and of course the very best of luck to those who still have their struggles ahead of them.

Many thanks to all my climbing friends, for all the fun and great moments we spent at Boulderhal 'Sterk'!

Marco, thanks for the awesome times in Utrecht and the great trip to Sicily! Happy times at the social events, where we all could unwind after a hard day's work. Riccardo, thanks for always being a good and loyal friend to me. I wish you all the best with your scientific career.

Yasi and Samaneh, I was very lucky to get to know you girls. Thanks for good company, nice talks and all the fun times we had together.

I would like to express my gratitude to my beloved mother and father who, despite being far away, have always been very supportive and helpful in any moment.

My beautiful sister Sama, being far from you during these whole years was more difficult for me than completing the PhD research. Thanks for being there for me when I needed in the most. Thanks for always supporting my decisions and for visiting me in Utrecht.

I would like to spend the last words of this manuscript to thank you, Daniel, for being such a great, kind, gentle person, for all your support, help and encouragement, for all the valuable moments together. Achieving this PhD would have been much more difficult without your support. I am certain that together we can overcome all future challenges.

Shima

12/08/2017

Utrecht

---

**Curriculum Vitae**

I was born on June 27<sup>th</sup>, 1985 in Urmia, a small town located on north-west of Iran. In fall 2003, after a selective admission test, I enrolled in a 6 years program of veterinary medicine at Urmia University, faculty of veterinary medicine. In 2009 I was awarded with doctor of veterinary medicine (D.V.M) degree. During the same year, I enrolled in master program "Drug Innovation" at Utrecht University, majoring in development of targeted drug delivery systems. In 2010, I spent a semester in Nijmegen, at their University center for Bioinformatics, where I developed in-silico skills in structural homology modeling and docking approaches for drug discovery. After graduation from Utrecht University in September 2011, I started work in Utrecht as a research associate on microsphere project sponsored by Nanomi B.V. In February 2012, I started my PhD project under the supervision of Prof. Wim Hennink and Dr. Robbert Jan Kok. During this PhD project I focused upon the development of targeted nanomedicine, specifically targeted liposomal and polymeric nanoparticles, loaded with different types of drug molecules. The results of the research are presented in this thesis.

**List of publications:**

Mahmoodzadeh H, Nikibakhsh A, Karamyyar M, Gheibi S, **Gholizadeh S**, Hooshmand H. Idiopathic hypercalciuria in children with vesico ureteral reflux and recurrent urinary tract infection. *Urol J*. 2010. 10; 7(2): 95-8.

Venselaar H, Camilli F, **Gholizadeh S**, Snelleman M, Brunner HG, Vriend G. Status quo of annotation of human disease variants. *BMC Bioinformatics*. 2013 4; 14: 352.

Falke LL, **Gholizadeh S**, Goldschmeding R, Kok RJ, Nguyen TQ. Diverse origins of the myofibroblast—implications for kidney fibrosis. *Nat Rev Nephrol*. 2015 Apr; 11(4):233-44.

Visweswaran GR, **Gholizadeh S**, Ruiters MH, Molema G, Kok RJ, Kamps JA. Targeting rapamycin to podocytes using a vascular cell adhesion molecule-1 (VCAM-1)-harnessed SAINT-based lipid carrier system. *PLoS One*. 2015 Sep 25;10 (9).

**Gholizadeh S**, Shehata Draz M, Zarghooni M, Sanati-Nezhad A, Ghavami S, Shafiee H, Akbari M. Microfluidic approaches for isolation, detection, and characterization of extracellular vesicles: Current status and future directions. *Biosens Bioelectron*. 2017 May 15; 91: 588-605.

**Gholizadeh S**, Visweswaran GR, Storm G, Hennink WE, Kamps JA, Kok RJ, submitted for publication. E-selectin targeted immunoliposomes for rapamycin delivery to activated endothelial cells. Submitted for publication (2017).

**Gholizadeh S**, Hennink WE, Kamps JA, Kok RJ. PLGA-PEG nanoparticles for targeted delivery of an mTOR/PI3kinase inhibitor, NVP-BEZ235, to inflamed endothelium. Submitted for publication (2017).

**Gholizadeh S**, Dolman ME, Sparidans RW, Hennink WE, Kok RJ. Anti-GD2 immunoliposomes for delivery of the survivin inhibitor Sepantronium bromide (YM155) to neuroblastoma tumor cells. Submitted for publication (2017).



